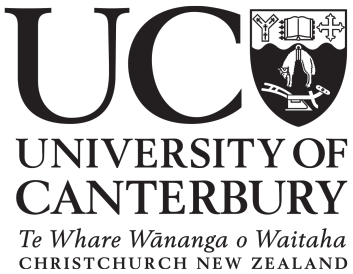

School of Physical and Chemical Sciences
University of Canterbury

Ring Laser Gyroscopes: Using Optical Frequency to Vary the Scale Factor

Author:
Dian Zou

Supervisor:
Prof. Jon-Paul R. Wells

Co-Supervisor:
Prof. Michael F. Reid

Submitted in Partial Fulfilment of the Requirements for the Degree of
Doctor of Philosophy in Physics

2021

I confirm that the content of this thesis is original and I have documented all sources and material used.

Christchurch, New Zealand, 2021 Dian Zou

Acknowledgments

First of all, I am deeply grateful to those who have provided me help and guidance throughout my PhD. The most sincere gratitude goes to my two supervisors, Professors Jon-Paul Wells and Mike Reid, for the opportunity to be a part of the ring laser program. Without your encouragement, support and wonderful insights, I would not have made it this far in my scientific career, nor gain confidence in my research ability. My genuine appreciation goes to Dr. Bob Hurst, who spent his precious time explaining the in-depth physics of ring lasers to me.

My special thanks go to Mr. Robert Thirkettle, who has provided continual help in the endless mirror cleanings and cavity alignments. I am equally grateful to Mr. Graeme MacDonald, who has supported me in tackling the electronic issues. I feel really lucky to work with them, not only for their tremendous technical help, but also for the optimism and joy they provided during my experimental works. To the most supportive colleagues throughout my PhD career: Caroline Anyi and Sangeetha Balabhadra, thank you both for always backing me up like real sisters and family. To my other fellow group members: Nick, Yashar, Pratik, Sagar and Jamin, thank you all for bringing me a warm, joyful and supportive environment. It has been a great pleasure for me to work with these intelligent, creative and hard-working fellows.

My thanks also goes to Professor Ulrich Schreiber, for allowing me to work on the 'G' and ROMY ring lasers in Germany. I have gained better understandings and scientific insights into the overall ring laser project after this research visit. Also, I want to show my appreciation to Dr. Jan Kodet for his help during my stay at the Wettzell Observatory in the Bavarian forest. I wish to give my special thanks to Dr. André Gebauer for offering me many bright ideas in data analysis and bringing me motivations to investigate more about the geoscientific applications of ring lasers. Finally, I want to thank the Dodd-Walls Centre for offering a PhD scholarship, and the University of Canterbury for providing all types of resources, support and working places.

In the end, I wish to dedicate this thesis to my parents, Joe and Hong. Thank you Joe for showing me the charms of optics, and cultivating my enthusiasm in the general sciences and to Hong for her unconditional love and encouragement. I feel forever blessed for being raised by you two in this family full of love, joy and support.

Abstract

An active ring laser gyroscope is a highly sensitive interferometer for the direct measurement of instantaneous inertial rotation via the optical beats generated from two frequency-shifted beams counterpropagating along a common enclosed path. In this thesis, the two He-Ne gas lasers called 'Physics Ring 1' (PR-1) and 'Ernest Rutherford 1' (ER-1) are utilised as large ring laser gyroscopes. They are designed for applications in the geosciences and civil engineering field as well as for tests of fundamental physics.

The research presented in this thesis focuses on several possible schemes for improving gyroscopic performance regarding rotational sensitivity and long-term stability. Feasible techniques include geometrical-upscaling of the ring cavity, the use of higher optical frequencies, implementation of a perimeter stabilisation system, and correction of systematic errors were utilised to maximise the useful resolution of the ring laser gyros.

A multi-wavelength laser gyro that can operate at 611.8, 604.6, and 593.9 nm has been developed. The initial results predict that simultaneous stable operation on multiple neon transitions having dissimilar gains is achievable when the intra-cavity supermirrors provide appropriate, unequal loss for each wavelength output. The success of stable multi-wavelength operation would ultimately benefit schemes for systematic calibration of dispersion-induced null-shift errors. In particular, the 611.8 nm laser yielded stable optical beats having frequencies of about 117.4 Hz due to the Earth rotation and obtained a usable resolution of 8.8 nrad/s ($1.2 \times 10^{-4}\Omega_E$, where Ω_E is the Earth's rotation rate of 7.2921159×10^{-5} rad/s) for an optimised gas fill and a cavity Q of 1.2×10^{11}. Furthermore, the 2.56 m^2 PR-1 laser has been configured with commercially sourced standard laser mirrors to operate at 1152.3 nm. The outcome demonstrates that this rotational sensor can unlock on Earth's rotation.

A new ring laser (denoted as ER-1) having a perimeter of 10 m and beam paths which enclose an area of 6.25 m^2 has been developed and used to demonstrate sensor functionality using operation on three different neon transitions in the visible region. It is found that the 632.8, 611.8, and 543.4 nm operating wavelengths can offer the highest rotational resolutions of 36 prad/s ($4.9 \times 10^{-7}\Omega_E$), 80 prad/s ($1.1 \times 10^{-6}\Omega_E$), and 226 prad/s ($3.1 \times 10^{-6}\Omega_E$) respectively in Earth rotation measurement. Various excitation systems (gain tube, RF transmitter) and mirror configurations have been applied and compared to identify the optimal operational conditions for frequency-upscaled gyroscopic operation. The average sensor resolution of ER-1 is two orders of magnitude higher than that of PR-1. The critical factor which accounts for this improvement is the increase in the cavity size and geometric stability.

Other significant measurements using ER-1 include the successful detection of marine microseisms and precise measurement of earthquake-induced ground rotational motions. The ocean-generated microseismic signals observed were in the 150 - 250 mHz frequency band. Two earthquakes (epicentres at a similar distance to the ER-1 site) of different magnitudes (M) at 5.4 and 5.8 have generated the highest local ground rotation rate at 78 and 254 nrad/s, respectively. The phase velocities for the S-waves and Love waves inferred from the observation were calculated at about 4.3 km/s and 3.4 km/s, respectively. These measured values fit into the expected range provided by common seismology.

Contents

List of Figures

List of Tables

1 Introduction

Ring laser gyroscopes (RLGs) are highly sensitive optical interferometers, having the unique feature of measuring absolute rotation that is self referenced to the rotation axis in question. They are found in a diverse range of applications such as inertial navigation, tests of fundamental physics, measurements in the geosciences field, and civil engineering. The principle of gyroscopic operation and rotational sensing relies on the Sagnac effect demonstrated in 1913 [1]. Georges Sagnac was the first to measure and interpret the interference fringe patterns produced from the rotation of a ring interferometer (mounted on a turntable). The formation of optical interference via this mechanism is named the Sagnac effect. Sagnac's original experiment used an external light source which was split into two beams to propagate along the same polygonal-shaped closed path in opposite directions. Fringe shifts were observed after recombination of the two beams as the two beams returned to the entry point with different phases due to the differential travel time. The phase shift was demonstrated to measure the angular speed of the interferometer since it was found proportional to the imposed rotation rate.

In 1925 Michelson, Gale and Pearson repeated the Sagnac experiment using a 613 m $\times$ 339 m rectangular ring interferometer and successfully measured the Earth's rotation rate ($\approx 7.3 \times 10^{-5}$ rad/s) through an observed relative fringe shift of 0.230 ± 0.005 [2]. This revolutionary achievement laid the scientific foundation for the externally excited passive resonant ring gyroscopes (PRRGs) developed in the laser era. In 1963 Macek and Davis demonstrated the first ring laser gyroscope soon after the development of the helium-neon laser [3]. This ring laser consisted of four corner mirrors and four sealed gain tubes (each located on a different side of the ring) and formed a square-shaped cavity (having 20 intra-cavity surfaces) of 1 m^2 enclosed area. It was an active ring laser operating at a wavelength of 1152.3 nm using the helium-neon gain medium. The PRRGs were developed after the success of active ring laser gyroscopes.

One prerequisite to enhance the sensitivity of laser based rotation sensors is to increase the optical round-trip path length (or scale-factor) of the ring interferometer. Fibre-optic gyroscopes (FOGs) are the most successful phase-sensitive PRRGs given by their inherent advantage - these portable and cost-effective devices utilise many turns of the optical fibre to increase their sensitivity [4]. Due to improvements in fabrication techniques for low-loss single-mode fibres, FOGs have achieved a rotational resolution three orders of magnitude below the Earth rotation rate (10^{-8} rad/s). However, the bias stability is still limited. The bias related to the polarisation and birefringence in the fibre as well as the backscattered waves from Rayleigh scattering are two significant technical problems. They are associated

with temperature fluctuations and mechanical stresses and give rise to noise, instability, and drift of the measured results [5, 6]. Nowadays, active ring lasers are the most mature and advanced technique for precise measurements in low rotation rates.

For any active ring laser whose body experiences an externally imposed rotation, the two counter-propagating beams experience different round-trip path lengths. In a laser cavity the implied phase shift becomes converted to frequency shift since laser oscillation requires an integer number of wavelengths around the cavity. Simultaneous observation of these two frequency-shifted laser beams would result in observable beat notes with the optical beat frequency proportional to the angular velocity about the normal vector to the cavity body. The Sagnac Equation for the active ring laser system is given by:

$$\delta f_s = \frac{4A}{\lambda P}\vec{n} \cdot \Omega, \tag{1.1}$$

where A is the area enclosed by the cavity, P is the perimeter of the laser cavity, $\vec{n}$ is the normal vector of the ring laser gyro relative to the orientation of the rotation axis in the inertial frame, and Ω is the angular velocity of the rotation axis. The conversion of the phase shift read-out in a classical interferometer into the beat frequency detection in an active ring laser gyroscope can considerably improve the sensitivity and accuracy of measurement.

Free space solid-state ring laser gyroscopes (SSRLGs) and gas ring laser gyroscopes (GRLGs) are the two types of active gyros investigated the most. The most common solid-state laser medium is Nd: YAG, while other solid-state materials such as the Nd: YVO4 crystal and Er^{3+}-Yb^{3+} phosphate glass, have also been employed to construct SSRLGs [7, 8]. In most cases, solid-state ring lasers are of no practical use in high-performance applications because of strong mode competition between the counter-propagating beams which arises due to the absence of the Doppler laser line-broadening effect. Another problematic situation is that standing waves (denoted as 'gain grating') are formed in the solid-state lasing medium due to the reflection of a small fraction of one beam into the other beam. This causes additional coupling between the clockwise and counter-clockwise beams. At the current stage, practical solutions for suppressing the mode competition encountered by SSRLGs are still under exploration [9]. The large ring laser gyroscopes dedicated for measurements of small rotational signals in the geosciences are all constructed as helium-neon-based GRLGs, as the He-Ne lasing medium can offer high coherence, superior spectral purity, good beam quality, and stable centre wavelength in the visible region [10, 11].

1.1 Large Ring Lasers and Applications

Small ring lasers having an area ≤ 0.02 m^2 are used for inertial navigation systems, while large ring lasers are purposely built for applications in geodesy and geophysics with particular emphasis on Earth rotation and seismological observations [10]. Large RLGs use customised

Ring Laser	Year	A	P	FSR	δf_s	Ω/Ω_E	Location
-	-	(m^2)	(m)	(MHz)	(Hz)	-	-
C–I	1988	0.748	3.84	78.13	76.1	-	New Zealand
C–II	1995	1	4	75	79.4	4×10^{-7}	New Zealand
G-0	1998	12.25	14	21.43	288.2	9×10^{-6}	New Zealand
Grossring	2001	16	16	18.75	384.5	3×10^{-9}	Germany
PR-1	2003	2.56	6.4	46.875	113.5	9×10^{-5}	New Zealand
UG-1/3	2000/2008	367.5	77	3.896	1512.8	6×10^{-8}	New Zealand
UG-2	2005	834.34	121.4	2.48	2177.1	4.5×10^{-8}	New Zealand
GEOsensor	2005	2.56	6.4	46.875	102.6	-	USA
G-Pisa	2008	1.82	5.4	53.6	111.1	2×10^{-5}	Italy
GINGERino	2014	12.96	14.4	20.83	280.4	$\sim 10^{-6}$	Italy
ROMY	2017	62.4/53.9	36/33.5	8.3/8.9	303-553	$\sim 10^{-7}$	Germany
ER-1	2019	6.25	10	30	198.3	10^{-7} - 10^{-6}	New Zealand

Table 1.1: A summary of typical large He-Ne ring lasers constructed since the 1980s. The table lists the name, the year of construction or operation, the laser area (A) and perimeter (P), the free spectral range (FSR), the Sagnac frequency (δf_s), the rotational resolution normalised to Earth's rotation rate (Ω/Ω_E), and the location of the ring laser. These gyroscopic parameters obtained from 632.8 nm operation are extracted from the data summarised in refs [10, 12–22].

cavity mirrors with a reflectivity of more than 99.999% and have a high-quality cavity of reinforced mechanical design. They are commonly constructed in thermal-and-pressure stabilised laboratories and operate in a quiet and nearly static environment. Representative large ring lasers worldwide developed over the last 30 years are summarised in Table 1.1.

Irregularities of Earth's rotation such as dynamic variations in the orientation of the rotation axis and the angular velocity, are visible as long-period drifts in Earth Orientation Parameters (EOP). They originate from the re-distribution of mass either inside or on the Earth (sea currents, tides, and large-scale earthquakes) and Earth's atmosphere dynamic [23]. Additionally, the gravitational force of the sun and the moon excite global phenomenon such as diurnal polar motion and solid Earth tide with astronomical frequencies of about 12 hours, 24 hours, and two weeks, and so on. It is of great importance to accurately measure the angular rotation speed and the orientation of the Earth rotation axis, as they are linking quantities between the terrestrial and the celestial reference frames. Currently, Earth Orientation Parameters such as the length of day (LOD) and pole coordinates are derived from space geodetic observations by Very-Long-Baseline Interferometry (VLBI) coupled with the Global Navigation Satellite System (GNSS), Satellite Laser Ranging (SLR), and Lunar Laser Ranging (LLR) [24]. The combination of these comprehensive observations gives an absolute reference frame for the derivation of EOP and therefore provides the orientation of Earth's rotation axis relative to inertial space and its rotational velocity.

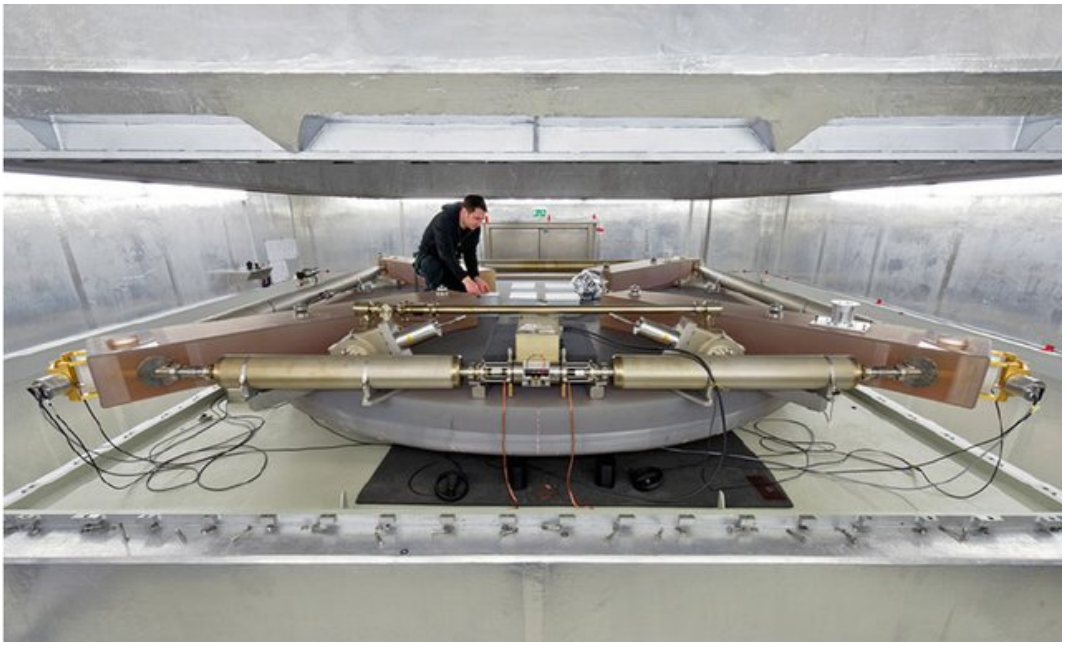

Figure 1.1: The semi-monolithic G ring laser gyroscope located at Geodetic Observatory Wettzell, Germany. The photo is sourced from ref [10].

VLBI uses a worldwide network of radio telescopes to measure the noise of distant astronomical radio sources such as quasars (considered as a set of 'static' markers – fixed stars in the inertial space) which are millions to billions of light-years away. As each radio telescope observes noise signals independently, the correlation process in the analysis centres requires the physical transport of data information (terabytes) recorded from each measurement position. The VLBI technique does not directly measure the real-time Earth's rotation axis but uses a theoretical precession-nutation model to predict EOP. VLBI achieves an uncertainty for the Earth's pole position of 0.5 nrad and for the Length of Day (LOD) less than 10 μs, acquired with an integration time of about one day [25]. Large ring lasers that are directly linked to the rotation axis of Earth can be viable tools for continuous observations of the instantaneous Earth orientation and rotation without data latency. However, a network of instruments is still required.

The 0.748 m^2 'Canterbury-1' (C–I) constructed in Christchurch (New Zealand) during 1988 - 1990 was the first ring laser (see Figure 1.2 (a)) that successfully unlocked on Earth's rotation and demonstrated the potential usage of large ring lasers in geodetic measurements [26]. Nowadays, the 16 m^2 Grossring laser ('G-ring') located at the Geodetic Observatory Wettzell (Germany) can routinely measure polar motion, tidal tilt effect, and Chandler and annual wobble with a resolution (0.164 prad/s, on the order of 10^{-9} of Earth rotation rate) only one order of magnitude lower than that provided by VLBI over an averaging time interval of few hours [27, 28]. Furthermore, Nilsson *et al*. have demonstrated that the accuracy of parameter estimations is improved by 16% for y-pole and 12% for Universal Time (UT) via

combining the VLBI analysis and the G-ring data[29]. As shown in Figure 1.1, the G-ring is a semi-monolithic square-shaped ring laser, constructed on a monolithic Zerodur block of low thermal expansion and housed in a thermally-stabilised underground laboratory (temperature drifts about 5 mK/day). It is the most stable large ring laser worldwide mostly due to its construction from a large zerodur telescope blank.

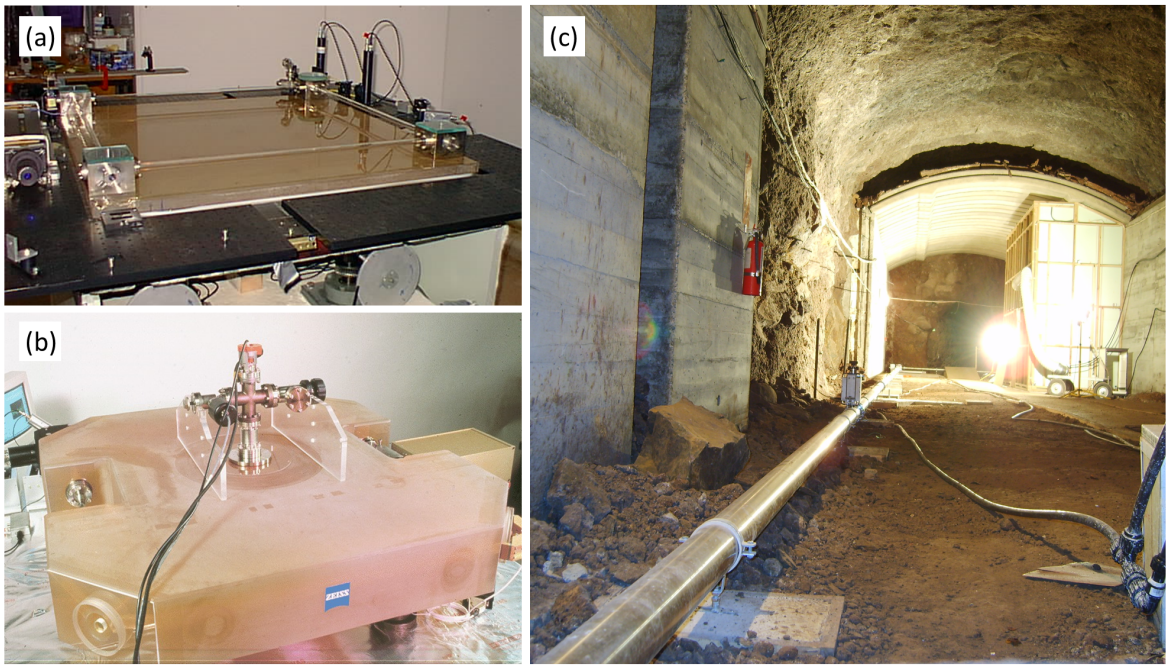

Figure 1.2: Canterbury ring laser gyroscopes: (a) C–I; (b) C–II; (c) UG-2.

Apart from the G ring laser, other two large ring lasers housed in the Cashmere Cavern (Christchurch, New Zealand), called 'Canterbury-2' (C–II) and 'UltraGrossring-1' (UG-1), have also demonstrated the capability to measure diurnal polar motions as well as solid Earth tides [30]. As shown in Figure 1.2 (b), C–II is a 1 m^2 large ring laser using a monolithic construction as its entire cavity is drilled out of an 18 cm thick Zerodur slab. Despite having a scale factor 16 times smaller than that of the G-ring, the C–II ring laser can perform well with a high rotational resolution of less than 1 part in 10^7 over weeks and months owning to the far superior mechanical rigidity and mirror design (using a set of supermirrors with nominal losses of 4 parts per billion per mirror) [14]. Unlike the G and C–II ring lasers that are built upon high-stability materials, UG-1 having a rectangular area of 367.5 m^2 (21.0 m $\times$ 17.5 m) is configured by stainless steel vacuum tubes with its whole cavity constructed upon the basalt rock floor (of the cavern) [31]. The ultra-large ring cavity prominently reduces the backscatter effects and compensates for the disadvantage of mechanical instability induced by the heterolithic construction to some extent. UG-1 can resolve a highest rotation rate of 10^{-8} Ω_E at about 5000 s of integration time [10]. The largest ring laser ever built is an enlarged version of UG-1 called 'UltraGrossring-2' (UG-2), having a cavity of 834 m^2 in area

occupying the entire Cashmere cavern floor, as shown in Figure 1.2 (c) [32]. It is by far the most sensitive ring laser ever constructed as it obtains the highest raw sensitivity of the order of 10^{-12} rad/s/$\sqrt{\text{Hz}}$. However, its stability is inferior to that of the UG-1 ring laser due to a much larger heterolithic cavity.

Single-component, horizontally-placed ring lasers having appropriate resolutions can accurately measure Earth's rotation. They provide a rotational component (scalar) about the normal vector of the cavity plane projected on Earth's rotation axis. A multi-dimensional ring laser integrating at least three optimally-oriented cavity components can reconstruct the complete rotation vector of Earth and thus permit rotational measurements with much higher accuracy [15].

The first large three-dimensional ring laser in the world, called ROMY (ROtational Motion in SeismologY), is installed 15 m underground at the Geophysical Observatory Fürstenfeldbruck, 20 km west of Munich, Germany [33]. As can be seen from Figure 1.3 (a) - (f), ROMY has a tetrahedral shape as it consists of four equilateral, triangular-shaped ring laser components. It has the apex pointing downward and the whole 3D structure built upon a massive concrete monument. Three of the four components have a cavity side length of 12 m, and that in the horizontal plane has a cavity arm of 11.1 m. All laser corners from one cavity plane are rigidly attached to those from the adjacent planes. ROMY ring laser can be a highly desired complement to VLBI once its precision matches (or outperforms) that required for the LOD measurements.

Earthquakes mainly release four different seismic waves: Primary waves (P-waves), Secondary waves (S-waves), Love waves, and Rayleigh waves. The first two types are body waves which generate translational (linear) ground acceleration, whereas the last two are surface waves which introduce ground rotational motion in the horizontal and vertical planes, respectively. For a long time in the past, only the translational motion observable by a conventional seismometer and the strain has been studied systematically in seismology. With the ongoing development of large ring lasers, the rotational components become accessible for seismological investigation. The rotation rates expected in seismology span at least ten orders of magnitude, ranging from 10^{-11} rad/s observed for large earthquakes at teleseismic distances to 10^{-1} rad/s observed near seismic sources [34].

As large ring lasers are insensitive to translational motion and are sensitive enough to detect rotation at the microradian level, they are currently the most reliable tools to accurately measure ground rotation rates over such a wide range [35]. The signal responses for seismic waves are in a dominant frequency band of 0 - 10 Hz [36, 37]. The combination of translational and rotational seismograms would improve the understanding of comprehensive earthquake source processes and seismic wavefields and allow the characterisation of permanent ground displacement from seismic events [38]. ROMY coupled with classic broadband seismometers would permit observations of seismically-induced ground motions in all six degrees of free-

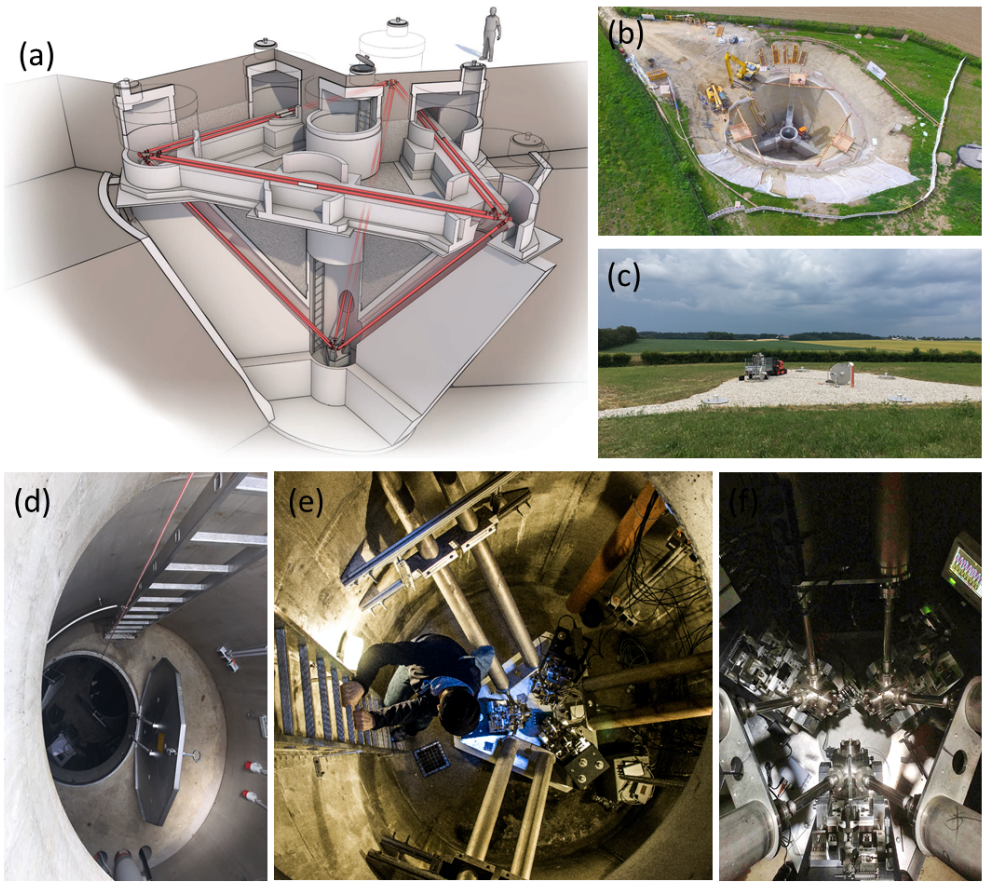

Figure 1.3: Demonstration of the ROMY ring laser, where (a) shows a schematic drawing of the design of the 3D structure; (b) shows the construction work 15 m underground at the Geophysical Observatory Fürstenfeldbruck; (c) shows the surface condition of the completed construction site; (d) shows one of the access to the underground laboratory; (e) and (f) show the apex located at the bottom of the monument. Components (a) and (b) are sourced from Science Magazine: https://www.science.org/content/article/buried-lasers-will-sense-earths-spin-and-quakes-doing-twist; (e) is sourced from refs [15, 17]; (c), (d), and (f) photos are taken by D. Zou.

dom and quantify the movements of the ground with unprecedented accuracy [17].

GEOsensor (Figure1.4) and PR-1 (Figure 3.1) are two identical ring lasers with both having a heterolithic and square-shaped cavity of 2.56 m^2 area (1.6 m $\times$ 1.6 m). GEOsensor was developed for measurements of the seismic events in seismically active regions [21]. PR-1 was designed for the measurement of building dynamics. GEOsensor is mounted on a rigid concrete slab in an underground laboratory at the Piñon Flat Seismological Observatory in Southern California, USA, whereas PR-1 was vertically mounted on the wall in a second-story laboratory at the University of Canterbury, Christchurch, New Zealand. For this type of ring laser, a relocatable, compact, and flexible mechanical structure is the prioritised design principle since long-term gyroscopic stability is not required for seismological observations. GEOsensor demonstrates that a less sophisticated and low-cost ring laser is also capable of offering valid information of the ground rotational motions induced from both local earthquakes and teleseismic events [39].

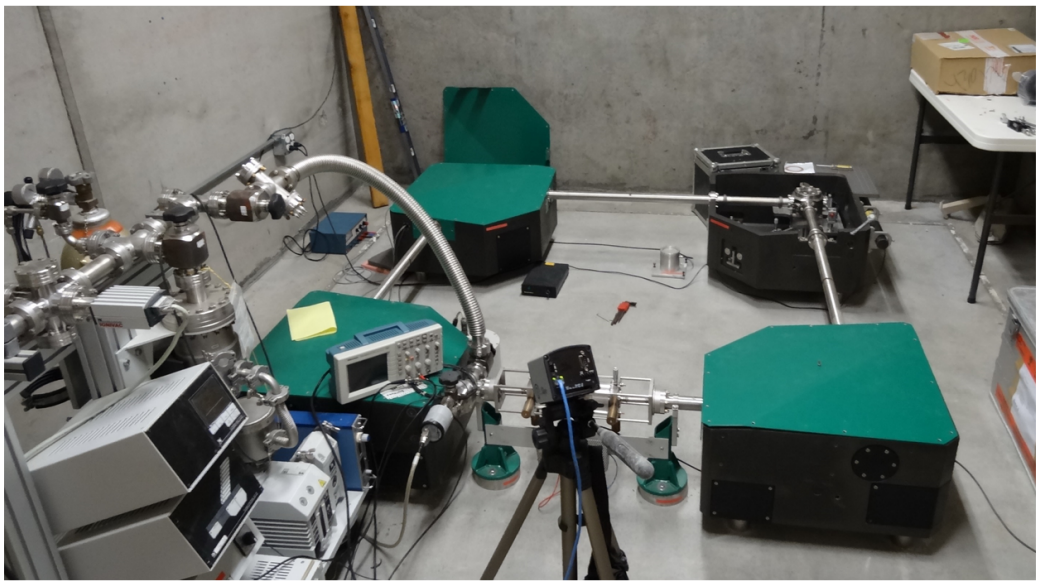

Figure 1.4: The medium-scale GEOsensor ring laser (photo: A. Gebauer). Four intra-cavity mirrors are located inside the mirror chambers attaching to the solid corner boxes. The ring cavity is sealed by connecting one gain tube and multiple stainless steel tubes.

1.2 Research Motivation and Objectives

Over three decades, an international collaboration effort on large ring lasers has aimed to increase the rotational sensitivity via construction of the laser cavity with upscaled dimen-

sions [26]. Ring laser gyros with an area larger than 1 m^2 are normally constructed in a heterolithic or semi-monolithic structure due to the lack of a massive and intact Zerodur block and the expensive cost of this delicate glass ceramic material [10]. Currently, it is known that ring lasers having the largest scale-factor do not necessarily have the highest usable laser sensitivity, as the gyroscopic potential of an ultra-large laser (such as UG-2) would be inevitably limited by the mechanical instability induced from a large heterolithic cavity structure. The optimal geometrical scale factor remains to be determined. The proposed scale of a ring laser can affect many decisions in selecting sensor location, construction materials, laser assembly technique, peripheral systems, and laboratory environment. To push the rotational resolution further towards 10^{-9} Ω_E, operation using upscaled optical frequencies might present great measurement potential and provide new insights into the methodology used for gyroscopic improvement. One unparalleled advantage inherited in the frequency-upscaling approach is that no additional cavity development is required. Under such condition, the only work required is to employ appropriate resonant mirrors that permit laser oscillation at a wavelength shorter than 632.8 nm (in the case of using the He-Ne gain medium).

Rotational signals obtained by a ring laser can contain systematic errors introduced from various mechanisms. In an active ring laser system, dispersion provided by the gain medium varies according to the change in optical frequency and plasma temperature and gas flow, giving rise to dynamic null-shift errors in the signal read-outs [40, 41]. The biases introduced by the dispersion effect are insignificant when considering their small scale, but they become critical and non-negligible when the goal is to achieve 'absolute' rotation rate measurement [42, 43]. The backscatter-coupling effect is known to be the primary source for data read-out biases [44, 45]. In most cases, ring lasers having a longer cavity length experience a reduced backscatter effect [46]. Studies using the 'G-ring' reveal that a thorough correction of backscatter perturbations is not possible when the backscatter-induced intensity modulations on the single beam output are too small to be measured precisely [11, 47]. As for the UG-series ring lasers, they do not have measureable frequency pulling at all as the backscatter magnitude is far below the noise level [32].

A non-monolithic ring laser can be easily subject to ambient thermal-and-pressure fluctuations. Given such a cavity structure, an active perimeter stabilisation technique is crucial for sustaining a stable optical path length to achieve long-term operation on a consistent mode index. A well-stabilised ring laser cavity also helps to minimise perimeter-dependent backscatter phase and amplitude variations. This thesis aims to establish practical techniques for improving gyroscopic sensitivity and mechanical stability of the laser cavity. Our main goals can be outlined as follows:

(1) Developing a multi-wavelength ring laser (using the 2.56 m^2 PR-1 as a test-bed) which permits simultaneous lasing on three neon transitions of $3s_2 \rightarrow 2p_6$, $3s_2 \rightarrow 2p_7$, and $3s_2 \rightarrow 2p_8$ (611.8, 604.6, and 593.9 nm); achieving stable operation on a minimum of two wavelengths

with either a single-mode or a phase-locked structure. The purpose for exploring the potential of a stable multi-oscillator operation is that the Sagnac time series yielded from one wavelength can be used to make corrections for dispersion when compared to the signal from the other wavelength. A successful simultaneous operation at multiple wavelengths helps in examining the mathematical model developed for the dispersion correction. This is because the rotation rate inferred at any wavelength should reduce to the same value at any measurement time.

(2) Constructing a new large ring laser with a proposed area of 6.25 m^2 on a 3 m thick concrete foundation in a purpose-built laboratory on the ground floor of the Ernest Rutherford Building, at the Ilam campus of the University of Canterbury in Christchurch, New Zealand; implementing a self-referenced perimeter stabilisation scheme on this 10 m long laser cavity by operating the laser in a phase-locked mode configuration and using the beat frequency induced from the two longitudinal modes as a feedback signal; applying an appropriate numerical solution to correct the backscatter-induced frequency errors in the raw Sagnac data obtained by the new laser gyro. Our purpose is to explore the best gyroscopic sensitivity and stability obtainable by a heterolithic ring laser housed in a building and built for the measurement of Earth rotation rate and seismically-induced ground rotational motions.

(3) Developing the 6.25 m^2 ring laser for operation at the 611.8 and 543.4 nm wavelengths and optimising the operational conditions for these two neon transitions. The purpose is to investigate the feasibility of the frequency-upscaling approach for gyroscopic improvement.

1.3 Thesis Outline

- Chapter 2
  This chapter provides all the relevant information required to understand the fundamental theories, operation mechanisms, and functionality of an active He-Ne ring laser gyroscope. We review the principles and measurement objective of the helium-neon gas laser in the context of a ring laser system. Later on, we introduce core parameters that determine the gyroscopic capability in rotational sensing. The origin of the systematic biases of a non-ideal gyro sensor and practical solutions for error reductions via data post-processing are described. Finally, we present an analytical method for frequency noise processing.

- Chapter 3
  This chapter begins with an overview of the technical details and operation specification of PR-1, in order to give a brief introduction of the general operational procedures applied to any active laser gyro system. Following this, we present two independent experiments conducted on this test cavity. In the first part, we detail the experimental work for constructing a system that permits simultaneous laser action at 611.8, 604.6

and 593.9 nm, and report the laser behaviour at each wavelength under such operation. For the second part, we configured the PR-1 cavity using a set of barely explored, commercially polished laser mirrors to operate the ring laser at the 1152.3 nm near-infrared region. The overall gyroscopic behaviour is investigated.

- Chapter 4
  At the beginning of this chapter, we present the construction procedures and technical details of an upgraded ring laser called ER-1. Following this, we describe the experimental set-up for initial operation at the standard 632.8 nm wavelength. We also present the development and implementation of a self-referenced perimeter stabilisation technique. Afterwards, the backscatter correction process is introduced. Then we evaluate laser stability and rotational resolution. Finally, we outline ER-1's potential in geoscience presenting the results measured from marine microseisms and earthquake activities.

- Chapter 5
  This chapter is devoted to exploring gyroscopic performance using operation at wavelengths shorter than 632.8 nm. We construct ER-1 to operate at 611.8 nm using two sets of supermirrors that have a different radius of curvature of 3 m and 10 m, respectively. We investigate the beam stability and sensor resolution acquired from each type of cavity to obtain the optimal mirror configuration for a geometry-and-frequency-upscaled ring laser.

- Chapter 6
  This chapter presents ER-1's operation on the highest operable frequency (552 THz) available from the helium-neon gain medium. We describe the preparatory works performed on a standard 632.8 nm laser system for proposed operation on 543.4 nm, a low-gain neon transition. Two long gain tubes (with the same effective length of 400 mm) having different inner diameters at 3 mm and 4 mm are used in turn to explore the optimal cavity configuration for achieving maximum gain. Investigations of the operational conditions, laser efficiency, and gyroscopic performance are performed thoroughly. Finally, we discuss the overall sensor behaviour obtained and specify the limitations and technical challenges typically encountered by operation with such a low gain transition.

- Chapter 7
  This chapter concludes the thesis with a summary of the significant results obtained from each experiment and outlines some future approaches for further technical improvement of the ER-1 laser.

2 Active Ring Lasers Fundamentals

A measurement tool using an invariant wavelength standard can yield reproducible and repeatable results. Therefore it is beneficial for interferometric metrology. Active ring laser gyroscopes have widely adopted the helium-neon system as the gain medium. An attractive feature of the He-Ne laser is the availability of standardized wavelengths, owing to the immutable properties of the neon atoms [48]. Another significant attribute of the He-Ne laser is its highly monochromatic output. For the 632.8 nm emission, the lowest ratio of linewidth to the frequency was characterised at the order of 10^{-16} with the linewidth limit determined by the spontaneous emission [49].

In this chapter, the fundamental laser physics background and the essential criteria for the characterisation of ring laser performance is demonstrated. In the beginning, the helium-neon gain medium with the associated linewidth broadening phenomena and the laser excitation mechanisms are introduced. Additionally, the Sagnac effect is reviewed for a better understanding of active laser gyro operation. Later, the gain curve profile and the hole-burning effect are illustrated to explain the operational regime in a more comprehensible way. Following this, the chapter describes the quality factor Q, intra-cavity bias and non-reciprocities in detail as they play crucial roles in the determination of the ultimate sensor resolution. Finally, a practical scheme for the correction of systematic bias as well as comprehensive criteria used for the assessment of sensor stability and resolution is presented.

2.1 Helium-Neon Gain Medium and Mechanisms of Laser Linewidth Broadening

Optical linewidth broadening of spontaneous emission has a direct effect on the interaction of the gain medium and the incident field in a cavity. Therefore the broadening mechanisms influence the probabilities of the stimulated absorption and emission among atomic energy levels and eventually affect the laser gain. In general, linewidth broadening is categorized into homogeneous broadening and inhomogeneous broadening, which are often characterised by the Lorentzian and the Gaussian functions respectively.

2.1.1 Homogeneous Broadening

Homogeneous broadening affects all particles equally and as such they have the same lineshape, linewidth and centre frequency.

Natural Broadening

The natural linewidth is determined by the probability of spontaneous emission (A_{ki}) between two energy states, which essentially depends on the average lifetime of the excited energy level. The average lifetime of particular excited states can be interpreted as the time uncertainty for the atomic measurement. This is given by the uncertainty principle which relates the lifetime and the energy of an excited state, as:

$$\Delta E \Delta t \geqslant \hbar/2, \tag{2.1}$$

where $\hbar$ is the reduced Planck constant ($\hbar = h/2\pi$). This results in a lifetime broadening width of $\Delta\nu_l$:

$$\Delta\nu_l = \frac{1}{2\pi}(\frac{1}{\tau_k} + \frac{1}{\tau_i}), \tag{2.2}$$

where τ_k and τ_i are the average lifetimes of the upper and lower energy states.

Collision Broadening

In a gaseous gain medium, homogeneous broadening of the spectral linewidth is mainly determined by stochastic atomic collisions, which dynamically alter the energy states of the helium and neon atoms. Atomic collisions can introduce a chaotic and random modulation of the radiative phase of the optical field, and also give rise to a faster radiative decay rate, in terms of shortening the average lifetime of the excited states.

The magnitude of the collision broadening is proportional to the average atomic collision rate. If the average time interval for collisions between the luminescent atoms and other atoms is τ_c, then the averaged atomic collision rate or the radiative energy decay rate is $1/\tau_c$. The spectral lineshape given by the collision broadening can be expressed by a Lorentzian function:

$$g_c(\nu, \nu_0) = \frac{2}{\pi\Delta\nu_c}\frac{1}{1 + (\frac{\nu-\nu_0}{\frac{\Delta\nu_c}{2}})^2}, \tag{2.3}$$

where ν_0 is the centre frequency and $\Delta\nu_c$ is the full width at half maximum of the collision broadening lineshape. The broadening linewidth is denoted as $\Delta\nu_c = \frac{1}{2\pi\tau_c}$.

Generally, the collision rate ($1/\tau_c$) correlates with the gas pressure, temperature and the cross-section for atomic collisions. However, experimental results imply a linear relation between the broadening linewidth and the gas pressure (P): $\Delta\nu_c = \alpha P$. Note that α is the pressure broadening coefficient. Considering that the gain medium is composed of both helium (h) and neon (n) atoms, the linear relation above is extended to the form:

$$\Delta\nu_c(n) = \alpha_{nn}P_n + \alpha_{nh}P_h, \tag{2.4}$$

where P_n and P_h are the gas pressures of neon and helium respectively and α_{nn} and α_{nh} are the pressure broadening coefficients for neon-neon and helium-neon collisions. The pressure broadening factors, for neon-neon and helium-neon atomic collisions for different neon transitions are listed in Table 2.1.

Wavelength, λ (nm)	α_{nn} (MHz/mbar)	α_{nh} (MHz/mbar)
1152.3	7 ± 2	21 ± 1
632.8	70 ± 8	94 ± 4
611.8	58 ± 9	100 ± 5
604.6	80 ± 8	97 ± 5
593.9	-	100 ± 6
543.4	61 ± 10	98 ± 5

Table 2.1: The variation of broadening width (full width at half maximum) in response to variations of gas pressure for different neon transitions [50–52].

2.1.2 Inhomogeneous Broadening

In a gaseous gain medium, there are additional contributions to the lineshape due to the distribution of atomic velocities. In the laboratory coordinate system, we define the radiative centre frequency of the luminescent atom as ν_0, measured when the atom is stationary relative to the photodetector. As the luminescent neon atoms move with a velocity component of v_z relative to the photodetector ($v_z/c \ll 1$), the emitted frequency ν_0 is shifted to ν_0', where

$$\nu_0' = \nu_0(1 + \frac{v_z}{c}), \tag{2.5}$$

this Doppler shift ($\Delta\nu$) in optical frequency is given by:

$$\Delta\nu = \nu_0' - \nu_0 = \nu_0\frac{v_z}{c}. \tag{2.6}$$

Referring to the probability (Maxwellian) distribution of particle speeds, the velocities of the neon atoms (v) in the upper excited states, should follow a distribution function of the form:

$$f(v) = \sqrt{\frac{m}{2\pi K_B T}} \cdot e^{-\frac{mv_z^2}{2K_B T}}, \tag{2.7}$$

where K_B is Boltzmann's constant, T is the thermodynamic temperature, and m is the atomic mass of the neon atoms. The spectral lineshape yielded by the Doppler broadening mechanism, can be interpreted as the probability distribution function of the observed frequency ν_0'. Therefore the derived Doppler broadening contribution to the spectral lineshape is:

$$g_D(\nu,\nu_0) = \frac{c}{\nu_0}\sqrt{\frac{m}{2\pi K_B T}}\cdot e^{-\frac{mc^2}{2K_B T\nu_0^2}(\nu-\nu_0)^2}, \tag{2.8}$$

with a Doppler linewidth of:

$$\Delta\nu_D = 2\nu_0\sqrt{\frac{2K_B T}{mc^2}\cdot \ln 2} \approx 7.16\times 10^{-7}\nu_0\sqrt{\frac{T}{M}}, \tag{2.9}$$

where M is the relative atomic mass of the neon isotope, $M = m/(1.66\times 10^{-27}kg)$. Equation 2.8 therefore can be re-written in the form:

$$g_D(\nu,\nu_0) = \frac{2}{\Delta\nu_D}\cdot\sqrt{\frac{\ln 2}{\pi}}e^{-\ln 2\cdot[\,2(\nu-\nu_0)/\Delta\nu_D\,]^2}. \tag{2.10}$$

2.1.3 A Resultant Total Lineshape

The convolution of two Lorentzian functions $g_l(\nu,\nu_0)$[1] and $g_c(\nu,\nu_0)$, yields a homogeneously broadened lineshape that also has a Lorentzian profile:

$$g_H(\nu,\nu_0) = \frac{2}{\pi\Delta\nu_H}\frac{1}{1+(\frac{\nu-\nu_0}{\frac{\Delta\nu_H}{2}})^2}, \tag{2.11}$$

where the theoretical homogeneous broadening linewidth $\Delta\nu_H$ can be calculated from Equation 2.2 and Equation 2.4, since $\Delta\nu_H = \Delta\nu_l + \Delta\nu_c$. As discussed previously, the lifetime ($\Delta\nu_l$), collision ($\Delta\nu_c$) and Doppler ($\Delta\nu_D$) linewidth broadening mechanisms co-exist together and determine the emission profile of the gain medium. The overall lineshape has therefore both homogeneous and inhomogeneous contributions. The probability that the emitted frequency lies in the range ν to $\nu+\Delta\nu$, therefore is given by:

$$g(\nu,\nu_0)d\nu = \int_{-\infty}^{\infty} g_D(\nu_0',\nu)g_H(\nu,\nu_0')d\nu_0' = g_D(\nu,\nu_0) * g_H(\nu,\nu_0). \tag{2.12}$$

This convolution of Gaussian and Lorentzian distributions yields a probability distribution having a Voigt profile[2] (see Figure 2.1). The linewidth of the Voigt profile can be estimated by the equation [53]:

$$\Delta\nu_{Voigt} \approx 0.5346\Delta\nu_H + \sqrt{0.2166\Delta\nu_H^2 + \Delta\nu_D^2}. \tag{2.13}$$

[1] $g_l(\nu,\nu_0)$: the spectral lineshape defined by the lifetime (natural) broadening mechanism.

[2] The maximum probability of stimulated emission is achieved when the incident light has a frequency of ν_0. As the optical frequency ν of the incident field is detuned from the emitted centre frequency (ν_0), the chance of stimulated laser transition decreases following the line-broadening function (Voigt profile).

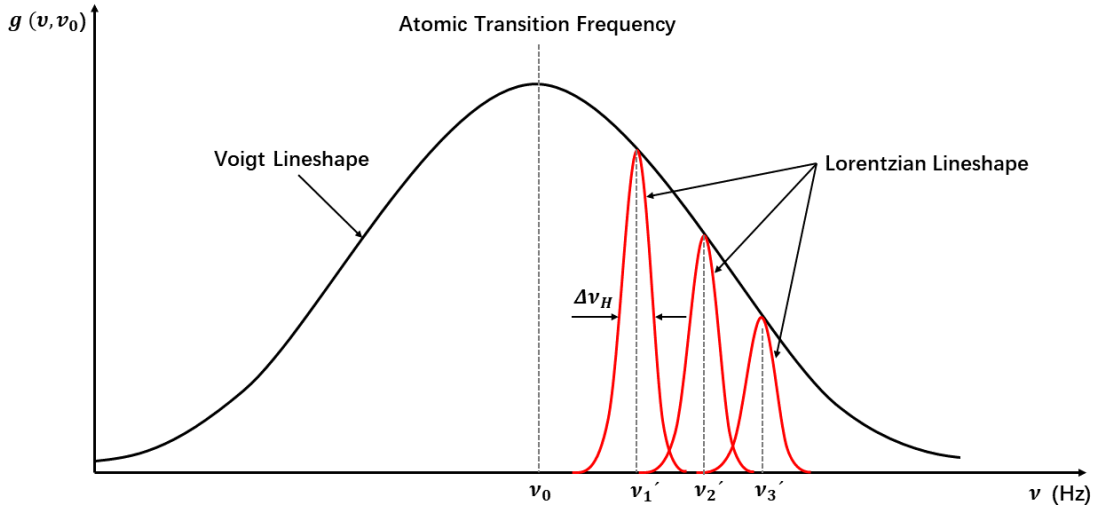

Figure 2.1: The Voigt lineshape profile, which is the convolution of the homogeneously (Lorentzian function) and the inhomogeneously (Gaussian function) broadened lineshapes.

2.2 Principles of the He-Ne Laser

The essential laser operating mechanism is demonstrated via a schematic of the laser excitation given in Figure 2.2. The atomic energy levels are in electron volts, and the excited states are denoted using the Paschen classification for simplicity.

2.2.1 Excitation of the Gain Medium

In a radio-frequency gas discharge, free electrons accelerate and collide with the un-excited helium atoms in the ground state (denoted as $1s^2,^1S_0$). The inelastic collisions lift helium atoms from the $1s^2$ level to reach higher energy at the metastable levels of $1s2s$ via

$$He(1s^2,^1S_0) + e \rightarrow He(1s2s,^1S_0/^3S_1), \tag{2.14}$$

where the energy of the $^1S_0$ and $^3S_1$ states are about 20.61 eV and 19.8 eV higher than that of the ground level. Shown in Figure 2.2, the energy gaps between the meta-stable helium atoms and the excited neon atoms of $2p^55s$ and $2p^54s$ states are reasonably small, which allow a high possibility of resonant transfer of energy. The neon atoms at the base level of $2p^6$ receive kinetic energy from collisions with the excited helium atoms, and transit to the upper laser levels via:

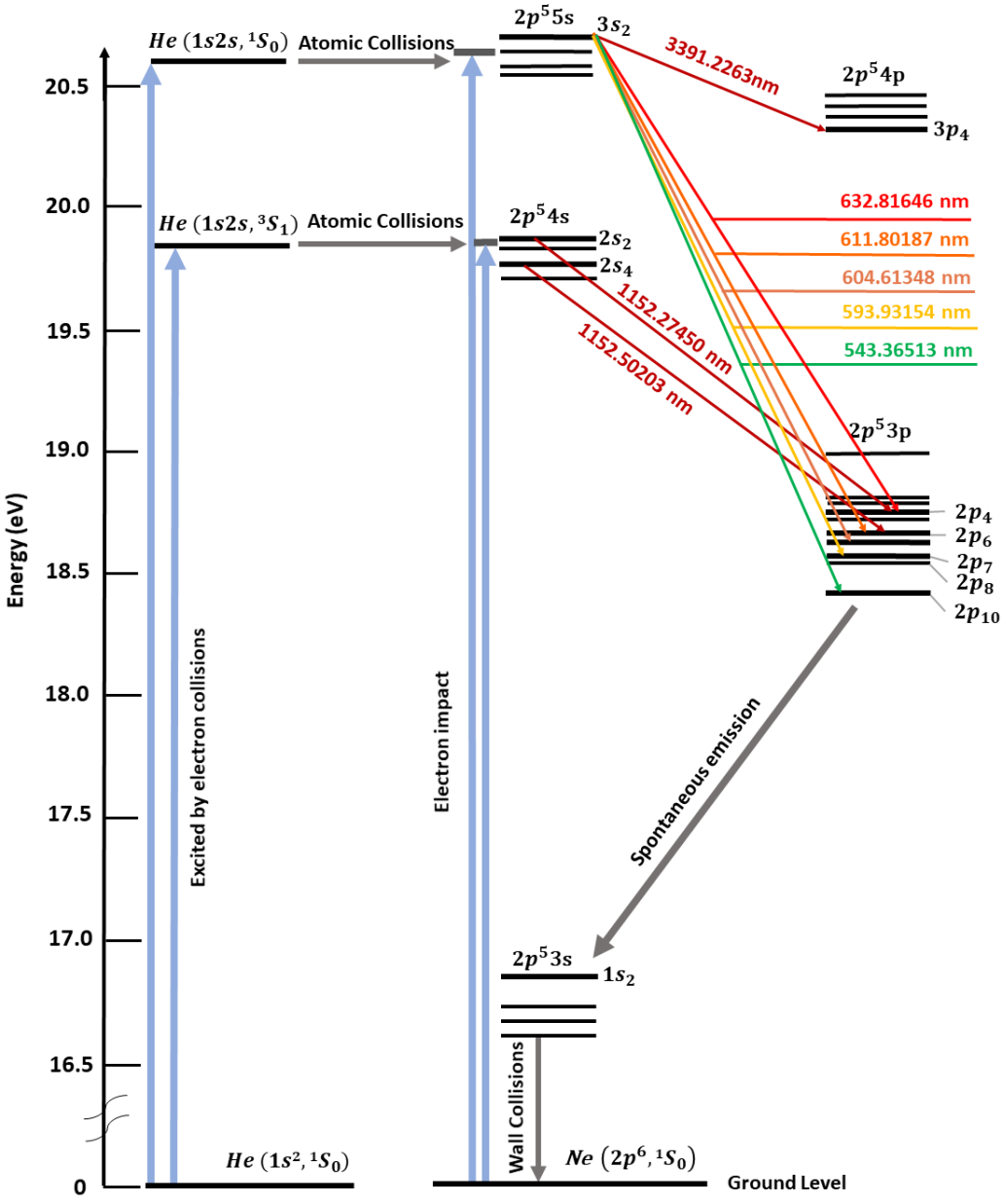

Figure 2.2: Principle of He-Ne laser excitation; the diagram illustrates the energy transfer during the atomic collisions and the population inversions of the neon atoms.

$$He(1s2s,^1S_0) + Ne(2p^6,^1S_0) \rightarrow He(1s^2,^1S_0) + Ne(2p^5 5s) + \Delta E_1, \tag{2.15}$$

or,

$$He(1s2s,^3S_1) + Ne(2p^6,^1S_0) \rightarrow He(1s^2,^1S_0) + Ne(2p^5 4s) + \Delta E_2, \tag{2.16}$$

where ΔE_1 and ΔE_2 are the small energy differences between the metastable helium and excited neon atoms. Without the 'catalytic' helium atoms, the collisions between the neon atoms and the accelerated electrons can directly promote the neon atoms from the ground level to the excited states. However, the excitation of upper energy levels is not efficient using this electron-neon collision scheme. By referring to the Table 2.2, excited helium atoms have very long lifetimes, which are several orders of magnitude higher than all the relevant lifetimes of neon atoms. This implies that helium atoms can efficiently populate the neon atoms. As the neon atoms do not persist in the high energy regime for a long time (< 200 ns), natural decay from the upper levels of $3s$ or $2s$ to the lower level of $3p$ or $2p$ occurs. This process is accompanied by fluorescent radiation at certain wavelengths, denoted as spontaneous emission. The radiative lifetimes of the excited neon $3s$ levels are higher than that of the $3p$ and $2p$ levels and the lifetimes of the $2s$ levels are also high compared to that of the $2p$ levels. These lifetime differences between the upper (E_k) and the lower (E_i) energy levels, paves the way for the laser amplification process, which will be elaborated in the next section 2.2.2.

2.2.2 Laser Amplification

Assume that an initial atomic number density in the E_k level is n_k and the total number of neon atoms involved in spontaneous emissions is dn_{ki} for a given time of (dt), therefore:

$$dn_{ki} = A_{ki} n_k dt, \tag{2.17}$$

where A_{ki} is the Einstein coefficient for spontaneous emissions, symbolising the probability of spontaneous neon transitions per unit time. The radiation intensity (I) from the spontaneous emission can be calculated via

$$I = n_k A_{ki} h\nu_{ki}, \tag{2.18}$$

where $h\nu_{ki}$ defines the emitted photon energy by $h\nu_{ki} = E_k - E_i$.

Spontaneous emission releases photons of stochastic phases, irregular polarisation and propagating directions in a broad spectral range. However, equipped with a well-aligned high finesse laser cavity, the phases, propagations, polarisation and the frequencies of the emitted photons can be regulated for the subsequent laser amplification process.

Atoms	States	Energy Levels, E (eV)	Lifetimes, τ (ns)
	$1s^2\ ^1S_0$	0	-
He	$1s2s\ ^3S_1$	19.8	2.04×10^6
	$1s2s\ ^1S_0$	20.61	5×10^3
	$2p_6\ ^1S_0$	0	-
	$1s^5$	16.6214312	-
	$1s^4$	16.6731888	22
	$1s^3$	16.7177544	-
	$1s^2$	16.8504468	16
	$2p^{10}$	18.3842028	< 20
	$2p^9$	18.557716	17
Ne	$2p^8$	18.5788208	16
(E_i)	$2p^7$	18.6153264	<13
	$2p^6$	18.6394072	13
	$2p^5$	18.6959884	<11
	$2p^4$	18.706702	12
	$2p^3$	18.7140056	<13
	$2p^2$	18.7290096	<10
	$2p^1$	18.9686148	<8
	$3p^4$	20.3001144	120
	$2s^5$	19.6667844	110
	$2s^4$	19.690952	98
	$2s^3$	19.7633556	160
Ne	$2s^2$	19.7825384	96
(E_k)	$3s^5$	20.5629324	78
	$3s^4$	20.5734352	26
	$3s^3$	20.6594292	10
	$3s^2$	20.665654	55

Table 2.2: The energy levels and related natural lifetimes of particular interest. The upper and the lower energy levels are denoted as E_k and E_i respectively, results are provided by [54]; The lifetimes are given in [55–57].

Neon Transition	Wavelength, λ (nm)	Einstein Coefficient, A_{ki} (s^{-1})
$3s_2 \rightarrow 3p_4$	3391.2263	1.07×10^6
$2s_2 \rightarrow 2p_6$	1152.50203	5.37×10^6
$2s_2 \rightarrow 2p_4$	1152.27450	1.07×10^7
$3s_2 \rightarrow 2p_4$	632.81646	3.39×10^6
$3s_2 \rightarrow 2p_6$	611.80187	6.09×10^5
$3s_2 \rightarrow 2p_7$	604.61348	2.26×10^5
$3s_2 \rightarrow 2p_8$	593.93154	2.00×10^5
$3s_2 \rightarrow 2p_{10}$	543.36513	2.83×10^5

Table 2.3: Einstein coefficient for spontaneous emission among different energy levels. The results are recorded from the NIST neon spectra database.

As the photons are guided to travel along the cavity axis, neon atoms in the excited states interact and absorb energy from the incident photons ($h\nu_{ki}$), thereafter decaying from a high energy level to a lower one. These stimulated neon transitions radiate photons whose propagating direction, polarisation and energy are consistent with those of the incident photons. The atomic number density of neon (dn_{ki}) engaged in stimulated emission per unit time can be expressed by

$$dn_{ki} = B_{ki}\rho(\nu)n_k dt, \tag{2.19}$$

where $\rho(\nu)$ is the radiation energy density of the incident field at frequency ν, and B_{ki} is the Einstein coefficient for stimulated emissions. Since neon transitions for stimulated emission and stimulated absorption are of equal probability ($B_{ki} = B_{ik}$), population inversion ($n_k \gg n_i$) is a key factor to achieve stimulated emission and laser amplification.

As shown in the Figure 2.2, spontaneous emission also occurs between the energy levels of $2p$ and $1s$, and neon atoms in the $1s$ states deplete to the ground level via wall-collisions. To increase the population inversion, the capillary for gain medium excitation is designed with a small diameter. For ring laser gyros, most of the gain tubes are of diameter 3-6 mm. This enhances the population inversion. Self-amplification of the intra-cavity laser power (P), can be derived from the equation:

$$P = h\nu_{ki}g(\nu)\rho(\nu)B_{ki}(\Delta n), \tag{2.20}$$

where $g(\nu)$ is the spectral lineshape of the incident field, Δn is the difference of atomic distribution between the upper and the lower energy level ($\Delta n = n_k - n_i$). As shown in Table 2.3, in the visible region the 632.8 nm transition has the highest probability of spontaneous emission. It implies that the highest laser gain can be achieved with the operation at the strong neon transition of $3s_2 \rightarrow 2p_4$.

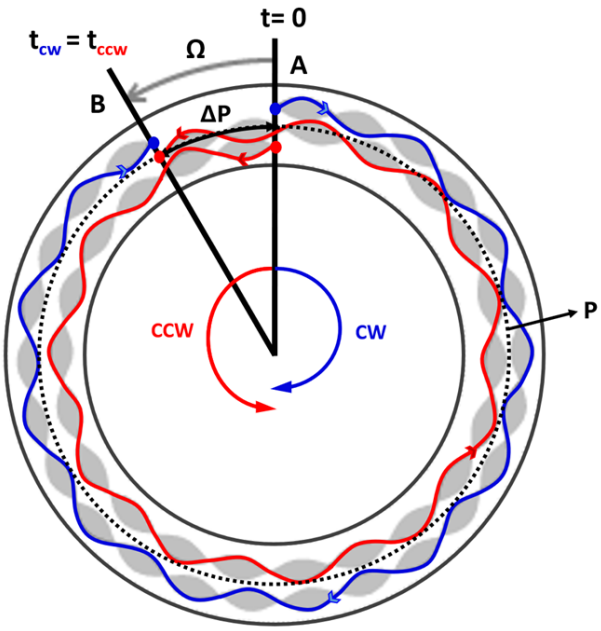

Figure 2.3: A simplified circular interferometer for the illustration of Sagnac effect. If the device is rotating in the CCW manner, then the CCW beam (shown as the red path) travels a further distance to fulfil one complete circuit in comparison to the CW beam (the blue path).

2.3 The Sagnac Effect

The working mechanism of a ring laser is based on the Sagnac effect first demonstrated by George Sagnac in 1913 [1, 58]. The Sagnac effect in an active ring laser gyro can be explained by a simplified ring interferometer as shown in Figure 2.3. The light separates into two bi-directional beams from point A. In the presence of an externally imposed rotation, the two counter-propagating beams travel with different path-lengths to complete one cycle of the mechanical frame to reach point B.

In a linear resonant cavity, the prerequisite for laser oscillation is that an integer number of wavelengths fits into the length of the cavity. This also applies to a ring cavity, where an integer number of wavelength is required in both directions, even when the ring interferometer is rotating. If each beam must travel different path-lengths in either direction, it gives a wavelength shift (or a frequency shift) of the resonant beams. As long as the frequency disparity of two beams is small and the amplitudes of two beams are fairly equal, an optical beat denoted as the Sagnac frequency (δf_s) can be observed when two counter-propagating beams are combined.

2.3.1 Sagnac Formula for a Circular Active Ring Cavity

As illustrated in Figure 2.3, a rotating ring interferometer shifts the position of the starting point (initially at position A) for either beam. The counter-clockwise (CCW) beam, propagating in the same direction as the rotation, needs to travel for a longer time to reach the starting point (now shifted to position B) in comparison to the opposite beam, since it travels an extra length ΔP with respect to the perimeter of the ring (P). The path-length of the CCW beam (P_+) for a complete circuit is $P_+ = P + \Delta P$, and the duration of the path is t_+. The angular rotation rate is Ω and the radius of the ring interferometer is R. Therefore,

$$2\pi\ R + (\Omega\pi)t_+ = ct_+, \tag{2.21}$$

where $R\Omega$ is the tangential velocity (v). After rearranging Equation 2.21 the unknown ΔP can be canceled, and the journey time of CCW beam is $t_+ = \frac{P}{c-v}$. The same rationale applies to the other beam (CW), which has a travel distance of $P_- = P - \Delta P$ and a path-length travel time of $t_- = \frac{P}{c+v}$. The time difference, Δt between the two beams, for travelling one circuit is given by

$$\begin{aligned} \Delta t = t_+ - t_- &= \frac{P}{c-v} - \frac{P}{c+v} = \frac{2Pv}{c^2 - v^2} \\ &= \frac{4\pi R^2\Omega}{c^2}(1 - \frac{R^2\Omega^2}{c^2})^{-1} \approx \frac{4A\Omega}{c^2}, \end{aligned} \tag{2.22}$$

where $A = \pi R^2$ is the enclosed area of the beam-path (area of the ring). As $R^2\Omega^2 \ll c^2$, therefore the Equation 2.22 can be simplified to $\Delta t \approx \frac{4A\Omega}{c^2}$. Then this equation is useful to calculate the overall path-length difference of two beams (ΔL):

$$\Delta L = P_+ - P_- = 2\Delta P = c \cdot \Delta t = \frac{4A\Omega}{c}. \tag{2.23}$$

Therefore the shift of the position from A to B, ΔP, is

$$\Delta P = \frac{2A\Omega}{c}. \tag{2.24}$$

The resonant frequency shift $\Delta\nu$ induced by the path-length change of ΔP has:

$$\frac{\Delta\nu}{\nu} = \frac{\Delta P}{P}. \tag{2.25}$$

As for the generated Sagnac beat frequency δf_s, it can be represented as:

$$\delta f_s = 2 \cdot \Delta\nu = 2\Delta P \cdot \frac{\nu}{P} = \frac{4A}{\lambda P} \cdot \Omega. \tag{2.26}$$

This derived result presents an analysis of a circular ring laser which is rotating about its centre. A derivation of the Sagnac effect for a general polygonal path was provided by R. B. Hurst et al. [59]. A treatment of laser gyros with an arbitrary loop (ring) and any (constant) rotation axis, is analysed in detail by S. F. Jacobs and R. Zanoni via Stoke's theorem

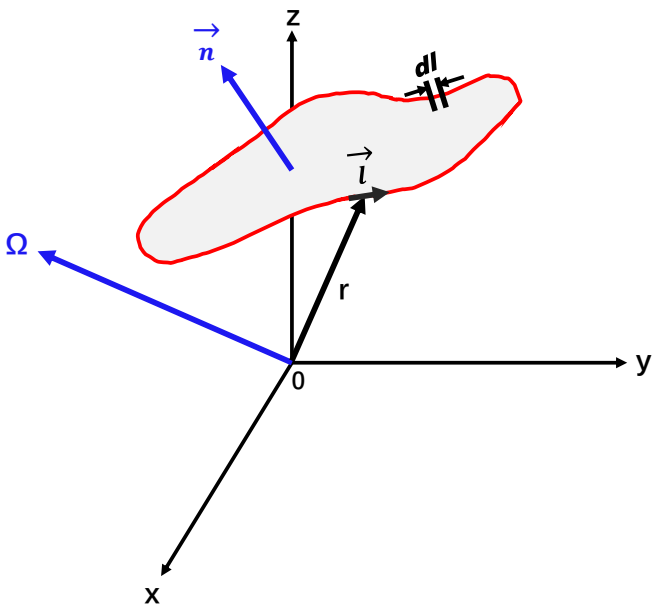

Figure 2.4: A ring laser with an arbitrary-shaped cavity that rotates with angular velocity Ω.

[60]. All their work proved that the Sagnac beat frequency is of geometrical dependence (A/P).

2.3.2 Sagnac Equation Derivation for Laser Gyros of Arbitrary Shape and Rotation Axis

Real ring laser gyros do not have circular beam paths or rotate conveniently about their centre [60]. Hence, by using Stokes theorem, a general derivation with respect to a gyro of arbitrary shape and rotation axis, is outlined in this section. Figure 2.4 simulates the circumstance where a ring laser with an irregular shape is rotating with an angular velocity of Ω about some axis.

As mentioned earlier, laser oscillation is possible when an integer number (n) of wavelengths span the cavity. Therefore for each beam path:

$$P = n\lambda = \oint_{ring} d\vec{l}, \tag{2.27}$$

where P is the perimeter of the ring cavity of any arbitrary shape.

The path integral (δP) is the product of the velocity component (v_{path}) along the propagation direction and the time required (dt) for the beam to propagate a path element dl, therefore dt is given by

$$dt = \frac{dl}{c}. \tag{2.28}$$

The velocity component (v_{path}) of a point in the propagating path is

$$v_{path} = (\vec{\Omega} \times \vec{r}) \cdot \vec{l}, \tag{2.29}$$

where $\vec{l}$ is a unit vector tangential to the beam path of a certain point (x, y, z). Defining $\vec{x}$, $\vec{y}$, $\vec{z}$ as unit vectors along with the x, y, z axes, the angular velocity of the rotating axis $\vec{\Omega}$ can be written as:

$$\vec{\Omega} = \Omega_x \vec{x} + \Omega_y \vec{y} + \Omega_z \vec{z}, \tag{2.30}$$

where $\vec{r}$ is the position vector of a point along the path in the resonant cavity, whose coordinates are (x, y, z):

$$\vec{r} = x\vec{x} + y\vec{y} + z\vec{z}. \tag{2.31}$$

Therefore the path integral δP can be represented as

$$\delta P = \oint_{ring} [(\vec{\Omega} \times \vec{r}) \cdot \vec{l}] \frac{dl}{c} = \frac{1}{c} \oint_{ring} (\vec{\Omega} \times \vec{r}) \cdot d\vec{l}, \tag{2.32}$$

where the vector $d\vec{l}$ is $d\vec{l} = \vec{l}\, dl$. The average velocity component along the beam path can be obtained from

$$\overline{v} = \oint_{ring} (\vec{\Omega} \times \vec{r}) \cdot d\vec{l} / \oint_{ring} d\vec{l} = \frac{1}{P} \oint_{ring} (\vec{\Omega} \times \vec{r}) \cdot d\vec{l}, \tag{2.33}$$

and the time required for a beam to propagate around the cavity is

$$t = \frac{1}{c} \oint_{ring} d\vec{l} = \frac{P}{c}. \tag{2.34}$$

The path-length change, ΔP, induced by the inertial frame rotation, is given by the product of the average velocity component along the path and the time for the beam to propagate the cavity:

$$\Delta P = \overline{v} \cdot t = \frac{1}{c} \oint_{ring} (\vec{\Omega} \times \vec{r}) \cdot d\vec{l}. \tag{2.35}$$

By comparison this ΔP agrees with the result in Equation 2.32.

With reference to Stokes theorem, there is

$$\oint_{ring} (\vec{\Omega} \times \vec{r}) \cdot d\vec{l} = \iint_A [\mathrm{curl}(\vec{\Omega} \times \vec{r}) \cdot \vec{n}] dA = \iint_A [\nabla \times (\vec{\Omega} \times \vec{r})] \cdot d\vec{A}, \tag{2.36}$$

where the A is the enclosed area formed by the ring with an arbitrary shape and $\vec{n}$ is the normal vector at any point to the area surface. Thus, the path-length shift ΔP can be written

as:

$$\Delta P = \frac{1}{c} \iint_A [\nabla \times (\vec{\Omega} \times \vec{r})] \cdot d\vec{A}. \tag{2.37}$$

The curl of the product of two vector fields ($\vec{\Omega}$ and $\vec{r}$), can be evaluated via [61]

$$\nabla \times (\vec{\Omega} \times \vec{r}) = (\nabla \cdot \vec{r})\vec{\Omega} - (\vec{\Omega} \cdot \nabla)\vec{r} + (\vec{r} \cdot \nabla)\vec{\Omega} - (\nabla \cdot \vec{\Omega})\vec{r}. \tag{2.38}$$

In case of an invariant rotation axis ($\vec{\Omega}$ = constant), the divergence of $\vec{\Omega}$ is

$$\nabla \cdot \vec{\Omega} = 0. \tag{2.39}$$

Also there are

$$(\vec{r} \cdot \nabla)\vec{\Omega} = \vec{r} \cdot (\nabla\vec{\Omega}) = (x\vec{x} + y\vec{y} + z\vec{z}) \cdot (\vec{x}\frac{\partial}{\partial x} + \vec{y}\frac{\partial}{\partial y} + \vec{z}\frac{\partial}{\partial z})\vec{\Omega} = 0, \tag{2.40}$$

and,

$$(\nabla \cdot \vec{r})\vec{\Omega} = (\frac{\partial x}{\partial x} + \frac{\partial y}{\partial y} + \frac{\partial z}{\partial z})\vec{\Omega} = 3\vec{\Omega}, \tag{2.41}$$

and,

$$\begin{aligned}
(\vec{\Omega} \cdot \nabla)\vec{r} &= \vec{\Omega} \cdot (\nabla\vec{r}) \\
&= \vec{\Omega} \cdot [(\vec{x}\frac{\partial}{\partial x} + \vec{y}\frac{\partial}{\partial y} + \vec{z}\frac{\partial}{\partial z})(x\vec{x} + y\vec{y} + z\vec{z})] \\
&= (\Omega_x\frac{\partial}{\partial x} + \Omega_y\frac{\partial}{\partial y} + \Omega_z\frac{\partial}{\partial z})(x\vec{x} + y\vec{y} + z\vec{z}) \\
&= \Omega_x\vec{x} + \Omega_y\vec{y} + \Omega_z\vec{z} \\
&= \vec{\Omega}.
\end{aligned} \tag{2.42}$$

Hence, by combining Equation 2.38 to 2.42 there is

$$\nabla \times (\vec{\Omega} \times \vec{r}) = 3\vec{\Omega} - \vec{\Omega} = 2\vec{\Omega}. \tag{2.43}$$

By referring to Equation 2.37 and 2.43, for a constant angular velocity,

$$\Delta P = \frac{1}{c} \iint_A 2\vec{\Omega} \cdot d\vec{A} = \frac{2\vec{A}}{c} \cdot \vec{\Omega}. \tag{2.44}$$

Finally, combining Equation 2.37 and 2.44, there is

$$\frac{\Delta\nu}{\nu} = \frac{\Delta P}{P} = \frac{2\vec{A}}{c} \cdot \vec{\Omega}, \tag{2.45}$$

consequently, the optical frequency shift of each beam ($\Delta\nu$) can be written as

$$\Delta\nu = \frac{2\vec{A}}{\lambda P} \cdot \vec{\Omega}. \tag{2.46}$$

Thus we have:

$$\delta f_s = \frac{4A}{\lambda P}\vec{n} \cdot \Omega, \tag{2.47}$$

where $\vec{n}$ is the normal vector of the ring laser gyro relative to the orientation of the rotation axis, in the inertial frame. This Sagnac equation can be applied to all planar ring lasers of arbitrary shape and rotation axis, while the previously derived Equation 2.26 contains no directional dependence.

2.4 Steady-State Laser Gain and Spectral Hole Burning Effects in a Two Isotope Travelling Wave Cavity

The laser gain coefficient (G) is a parameter for measuring the amplification of an incident radiation field. A monochromatic light wave with a frequency of ν, travels along the cavity in a direction z, and passes through the gain medium with a cross-sectional area A and a length l. Due to excitation of the gain medium, the incident field gets magnified during a round-trip of the cavity. If the light intensity at a position of z is $I(z)$ and at the position of $z + dz$ is $I(z) + dI(z)$, we can simply express the laser gain coefficient as:

$$G(z) = \frac{1}{I(z)}\frac{dI(z)}{dz}. \tag{2.48}$$

The $G(z)$ symbolises a varying rate of the light intensity per unit distance.

2.4.1 Laser Gain with Linewidth Broadening Effect

Unsaturated Gain Calculation

In a steady-state laser amplification process, where the laser excitation power is a constant, the population inversion Δn, reaches equilibrium with $d(\Delta n)/dt = 0$ and $\Delta n \ll n$. Note that n represents the total atomic number density of the ground and the excited states, and $\Delta n = n_2 - \frac{g_2}{g_1}n_1$, where n_1, n_2 are the respective atomic number densities of the ground and the excited states, and g_1, g_2 are the corresponding degeneracy factors. When the incident field is at an intensity far smaller than the saturation intensity[3], the unsaturated gain coefficient, $G^0(\nu)$, can be calculated via:

$$G^0(\nu) = \Delta n^0 \frac{\lambda_0^2}{8\pi} A_{ki} g(\nu, \nu_0), \tag{2.49}$$

[3]By definition the saturation intensity is the intensity when the gain drops to exactly half of the small-signal gain, however, numerically it can be calculated via Equation 2.51.

where $g(\nu, \nu_0)$ is a Voigt profile, Δn^0 is the population inversion under an incident field of low intensity and λ_0 is the centre wavelength of the emission. Equation 2.49 demonstrates that the unsaturated laser gain as a function of the incident frequency is purely determined by the wavelength, lineshape function of the spontaneous emission, and the population inversion.

Gain Saturation Phenomenon

Under ideal conditions, the laser excitation power is always maintained at a low value. With such conditions, the population inversion (Δn) is approximately linearly dependent upon the excitation power. However, there exists a threshold for the saturation of population inversion (Δn). The saturation effect of the population inversion occurs when the neon atoms are depleted in the atomic ground state and bottleneck in the upper energy level. The population inversion is expressed as:

$$\Delta n = \frac{\Delta n^0}{1 + \frac{I_\nu}{I_{sat}}}, \tag{2.50}$$

where I_ν is the stable intra-cavity laser intensity and I_{sat} is the saturation intensity of a specific neon transition. Equation 2.50 indicates that a higher intensity of the incident field depletes the population inversion by a greater amount. A stronger saturation effect (greater decrease of Δn) is found with a smaller saturation parameter (intensity) I_{sat} calculated via [62]

$$I_{sat} = \frac{h\nu}{\sigma_{ki}\tau_k}, \tag{2.51}$$

where σ_{ki} is the stimulated emission cross-section, and τ_k is the average lifetime of the upper level of the neon transition. The stimulated emission cross-section (σ_{ki}) can be calculated by

$$\sigma_{ki} = \frac{B_{ki} h\nu g(\nu, \nu_0')}{c} \approx \frac{\lambda_0^2}{8\pi} A_{ki} g(\nu, \nu_0'). \tag{2.52}$$

Therefore the saturation intensity at the emitted centre frequency ($\nu = \nu_0$) is:

$$I_{sat}(\nu_0') = \frac{4\pi^2 h(\nu_0')^3 \Delta\nu_H}{c^2 A_{ki}\tau_k} \approx \frac{4\pi^2 h\nu_0^3 \Delta\nu_H}{c^2 A_{ki}\tau_k}, \tag{2.53}$$

where $\Delta\nu_H$ is the laser linewidth induced by homogeneous broadening.

2.4.2 Hole-Burning of the Gain Curve

When an incident beam with a frequency of ν_1 (intensity denoted as $I_{\nu 1}$) interacts with the gain medium, the strongest saturation of the population inversion occurs where the luminescent neon atoms yield an observed frequency of $\nu_0' = \nu_1$. Based on Equations 2.5 and 2.6, the neon atom group having a velocity component of $v_z = c(\nu_1 - \nu_0)/\nu_0$ will maximally interact with the incident field, leading to the strongest saturation of neon atoms in this

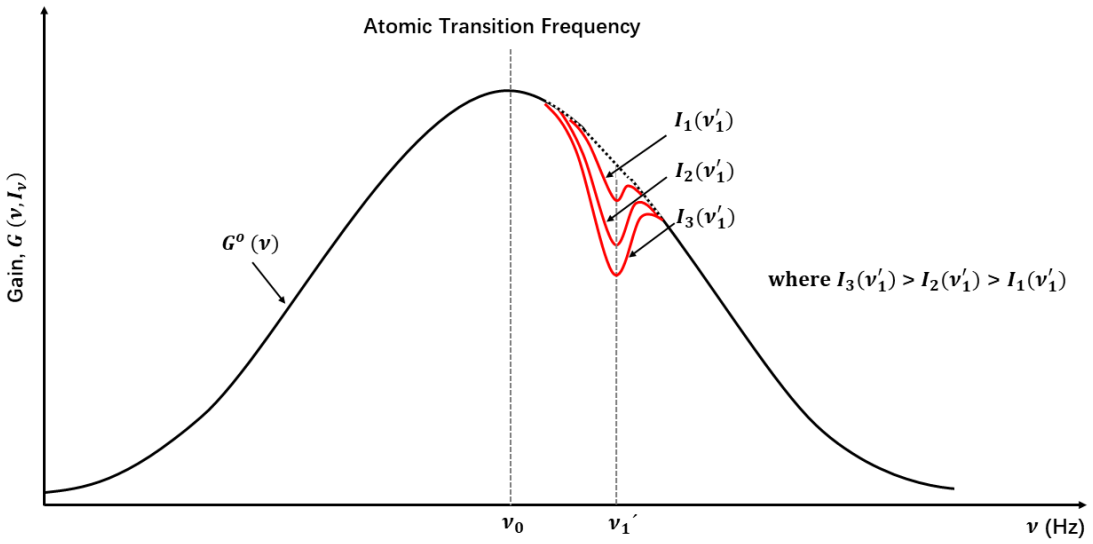

Figure 2.5: The hole burning effect occurs near the centre frequency ν_0; the partial gain saturation at the operating frequency ν_1' gets higher as $I_(\nu_1')$ increases, yielding a wider and deeper 'burnt' hole.

velocity ensemble. For the neon atoms with a Doppler-shifted atomic frequency (ν_0') further away from ν_1, a higher incident intensity ($I_{\nu 1}$) is required, to generate a saturation effect which is equivalent to the saturation at the observed frequency of ν_1. Therefore a high laser operating power (intra-cavity power) decreases the gain coefficient, by an intense depletion of the fractional population inversion at the atomic frequency nearby ν_0. This uneven gain saturation mechanism ultimately introduces 'hole-burning' in the gain curve (shown in Figure 2.5).

In bi-directional ring laser operation, two counter-propagating beams oscillate on a common longitudinal laser mode (having mode number: $N_{ccw} = N_{cw} = q$). When the frequencies of the two beams match the condition $\nu_{ccw,cw} \neq \nu_0$, the oppositely directed beams simultaneously interact with two groups of excited neon atoms, whose velocity vectors are opposite to each other [63]. Therefore the population depletion holes contributed by the two identical beams, are symmetrically located about the atomic transition frequency (ν_0), in each side of the gain curve. In the special case where the frequency is tuned to the centre of the Doppler broadened gain curve, one of the two independent beams will be extinguished due to intense mode competition [64]. Under this circumstance, the two burnt holes completely overlap in the gain curve, as the counter-travelling waves compete for the same group of excited neon atoms whose thermal motion are at $v_z = 0$.

To avoid beam extinction due to strong mode competition close to the atomic line centre (as it would occur in a single-isotope gain medium), ring laser operation utilizes two isotopes of neon: ^{20}Ne and ^{22}Ne [65, 66]. As a result, the gain curve versus velocity ensemble is composed of two velocity-distribution functions, given by the two neon isotope groups. Each neon isotope contributes its own gain curve. In each curve, there are two 'burnt' holes which are of different depth and are located at different distances from the $v_z = 0$ axis. Note that the two gain curves do not completely overlap as their atomic line centres are 200-1000 MHz apart from each other (the exact isotope shift is dependent on the neon transition). Therefore the overall gain curve versus frequency is the convolution of two identical gain curves from the two neon isotopes, with the operating frequency located in the centre.

The spectral holes reflect the homogeneous linewidth and therefore have a Lorentzian profile of a certain width. In general, the hole burning effect reduces mode competition among adjacent modes, and enables multiple longitudinal modes to sustain stable oscillation at the same time. As shown in Equation 2.53, a higher saturation parameter corresponds to a wider and a deeper hole-burning. Therefore the pressure-dependent saturation intensity (I_{sat}) becomes larger for laser operation at higher gas pressures.

2.5 Ring Laser Operational Regimes

Ring laser gyroscopes can achieve precise rotational sensing for operation on either a single-mode or in a 'phase-locked' stable multi-mode regime. The experimental results indicate that for laser operation on either of the two mode configurations, there is no significant difference in gyroscopic performance [67]. Due to the pressure dependence of the saturation intensity and the 'burnt hole' width, varying the cavity gas pressure can alter the output powers available for the single-mode and stable 'phase-locked' mode regimes.

2.5.1 Single Mode

Single-mode operation is widely-adopted as the main approach for rotation sensing, due to the convenience of a direct translation between operating frequency and Sagnac beat frequency. Single-mode oscillation is obtained via gain starvation, where the laser power is maintained just above the lasing threshold, to ensure that only one longitudinal mode survives in the mode competition and obtains the maximum gain. The single-mode operation regime is sustained via servo-controlled RF excitation of the laser intensity. However, ring lasers with a large perimeter (scale factor) potentially present a difficulty in gain starvation for mono-mode oscillation, because they have a small cavity free spectral range (FSR) given by:

$$\nu_{FSR} = \frac{c}{nP}, \tag{2.54}$$

where P is the cavity perimeter and n is the refractive index of the gain medium. Thus the larger the cavity perimeter, the smaller the frequency spacing between two modes. Correspondingly the maintenance of single-mode lasing is challenging, as the gain difference between adjacent modes becomes smaller. However, this issue can be addressed using laser operation at high gas pressure. The wider homogeneous broadening associated with higher gas pressure, broadens the gain curve with a reduced curvature at the saturation point, allowing for a greater detuning without the possibility of a 'mode-hop' even if the cavity length is perturbed. Therefore, laser operation at high pressure is a key factor for single-mode operation, as weak saturation can persist for higher intra-cavity intensities.

2.5.2 Phase-Locked Stable Multi-Mode

When the intra-cavity laser power is increased above the multi-mode threshold, multiple longitudinal modes can oscillate simultaneously. The amplitude and initial phase of each mode are generally unrelated as the different oscillating modes are generated by photons originating from the spontaneous emission process. In a 'free-running' multi-mode regime, the laser output generated from the incoherent superposition of multi-longitudinal mode oscillations yields an irregular, unstable power over time. However, in gas lasers, a 'self-mode-locking' phenomenon can arise as a result of the nonlinear susceptibility of the gain medium, if the intensities of the combination tones contributed by different oscillating modes are tuned to fall within a certain boundary [68–70]. A stable mode-locking can occur spontaneously at specific power levels without the need for external modulation, with all different longitudinal modes exhibiting a well-defined and constant phase relationship [71–73].

As a mode-locked (also denoted as 'phase-locked') configuration also yields a stable laser output, stable Sagnac waveforms are observable under this operational regime. The derived FFT spectrum, is an average of the Sagnac beat frequencies as introduced by different pairs of oscillating modes. Typical phase-locked operation on a central dominant mode accompanied by several pairs of minor modes yields an output power 10-30 times greater than that obtained with single-mode operation. The phase-locked mode structure is more sensitive to cavity geometric variations compared to the single-mode operation. As the relative mode amplitudes vary owing to geometric instability, the extinction of weak side-modes and their occurrence at different FSR away from the centre mode can be observed on a longer time scale. Therefore, this mode structure can affect long-term sensing stability. However, a useful advantage of stable multimode operation is that the occurrence of 'mode splitting'[4] (also denoted as split-mode operation) does not necessarily cause complete loss of Sagnac signal, even if the main mode of one beam is instantly shifted to a consecutive mode number [67]. The Sagnac beat signal might be still observable, albeit with a reduced amplitude as the main mode of one beam can still heterodyne with the side modes of the opposite travelling beam.

[4]Mode splitting is defined by the case where the two counter-propagating beams operate on different longitudinal mode numbers.

2.6 Quality Characterisation of the Ring Cavity

Optical loss is a significant parameter for the evaluation of a ring cavity as it determines not only the resonance threshold and the operable laser output, but also the cavity Q and therefore the rotational sensitivity. In the following, we detail the mechanisms which introduce the overall cavity-loss and the parameters that symbolise the optical quality of the ring cavity.

2.6.1 Cavity Loss Mechanisms

Loss from Absorption, Scattering and Transmission

Advanced ring lasers utilise Bragg stack supermirrors to construct a high Q resonator of low transmission loss of parts per million. A Bragg supermirror consists of multiple dielectric layers of alternating materials[5] with varying high and low refractive index coated on a highly polished glass substrate. The partial reflection of an optical wave caused by each layer boundary will combine yielding constructive interference as long as the layers designed have an optical thickness at a quarter of the incident wavelength ($\lambda/4$, at 45° angle of incidence). For a laser cavity employed with this type of supermirrors absorption and scattering loss is greatly reduced, consequently, the finesse of the cavity and intra-cavity photon flux are increased.

Diffraction Loss

The cavity mirrors are all limited in size, with small reflection areas. As the light wave travels around the cavity, cavity loss is generated by diffraction effects at the edge of the free aperture. If the cavity contains other optical elements, more diffraction loss can occur. Therefore, all active ring laser cavities are equipped only with the cavity mirrors to reduce undesired diffraction loss. However, the gain tube functions as a small aperture and is a significant source of unwanted loss. In particular, this type of loss is affected by the waist of the Gaussian beam which is dependent on the geometric parameters of the cavity (each arm length), the radii of curvature (ROC) of the mirrors and the order of the transverse mode, as well as the diameter and the length of the gain tube.

2.6.2 Average Photon Lifetime

To quantify the optical loss introduced by the mechanisms listed above, the attenuated laser intensity after a single round-trip is written as:

$$I = I_0 e^{-\delta}, \tag{2.55}$$

[5]The conventional design for the stack uses titanium dioxide (n ≈ 2.5) and silica (n ≈ 1.5).

where the coefficient δ is the optical loss per round-trip, and I_0 is the initial laser intensity. If the laser intensity is I_0 when $t = 0$, at a given time (t) the number of round-trips that the laser beam travels, m, is expressed by:

$$m = \frac{t}{nP/c}, \tag{2.56}$$

where n is the refractive index (which is close to 1) of the gas medium and P is the cavity perimeter. Hence, the Equation 2.55 can be expressed as

$$I_m(t) = I_0 e^{-\delta m} = I_0 e^{-t/\tau}, \tag{2.57}$$

where τ is the average photon lifetime in the cavity, also denoted as the cavity ring-down time, having $\tau = nP/\delta c$. As such, the ring-down time τ is a significant parameter, symbolising the time required for the intensity to be attenuated to $1/e$ of the initial intensity I_0. The ring-down time is affected by the optical loss coefficient δ. The higher the optical loss, the faster the photon decay.

2.6.3 Quality Factor Q and Cavity Linewidth

The quality factor Q is a dimensionless physical factor for analysing the quality of the ring laser oscillator. It is defined as the ratio of the stored energy to the energy dissipated over one radian of oscillation. Therefore, a higher Q indicates a lower rate of energy loss and a longer oscillation period. The universal definition of quality factor Q is:

$$Q = 2\pi\nu \frac{E}{P} = 2\pi\nu \frac{E}{-dE/dt}, \tag{2.58}$$

where E is the energy stored and P ($P = -dE/dt$) is the energy dissipated per cycle, and ν is the optical frequency. It follows from Equation 2.58 that:

$$E = E_0 e^{-2\pi\nu t/Q}, \tag{2.59}$$

where E_0 is the initial energy storage, equivalent to the number of photons times the energy associated with each photon. When $t = \frac{Q}{2\pi\nu}$, the stored energy has decayed to $1/e$ of the initial energy. Therefore the photon lifetime in the cavity is given by $\tau = Q/2\pi\nu$. The quality factor Q of the ring laser can be written as:

$$Q = 2\pi\nu\tau = 2\pi\nu \frac{nP}{\delta c}. \tag{2.60}$$

The laser linewidth limit[6] determined by the line-broadening from spontaneous emission is of great significance for interferometric metrology. The laser outputs with high spectral purity are immensely desired as they enable ring lasers to measure the rotational signals with good frequency stability and therefore high resolution. However, the actual cavity linewidth,

[6] See Equation 2.83.

denoted as $\Delta\nu_R$, can be larger than the laser linewidth expected from quantum noise. The cavity linewidth is influenced by environmental disturbances such as plasma oscillations and cavity structural vibrations [74]. For example, air-or-ground-borne vibrations in the laboratory can perturb the cavity length. According to the Equation 2.57, the amplitude of the optical field, $A(t)$, can be written as:

$$A(t) = A_0 e^{-t/\tau}, \tag{2.61}$$

therefore the monochromatic light waves can also be written in a complex form:

$$u(t) = A(t)e^{-i2\pi\nu t} = A_0 e^{-t/\tau} \cdot e^{-i2\pi\nu t}. \tag{2.62}$$

Given by a Fourier transform, the decay of optical field expressed in Equation 2.62 yields the cavity linewidth $\Delta\nu_R$:

$$\Delta\nu_R = \frac{1}{2\pi\tau} = \frac{\delta c}{2\pi n P}. \tag{2.63}$$

Equation 2.63 denotes that the a narrower cavity linewidth is given by a lower cavity loss and a longer photon lifespan. Merging Equation 2.63 to Equation 2.60, there is:

$$Q = \frac{\nu}{\Delta\nu_R}. \tag{2.64}$$

Equation 2.60 and Equation 2.64 denote that a higher cavity factor Q corresponds to a longer photon lifetime τ, a smaller cavity loss δ and a better capability of the cavity in storing energy. A cavity with a high Q factor has a narrower cavity linewidth and therefore yields the Sagnac frequency with greater accuracy. This can be achieved by better cavity alignment which reduces the geometrical loss, the employment of highly-reflective mirrors of better quality for a lower mirror loss, and the elimination of the optical elements in the cavity for a lower diffraction loss.

2.7 Measurement Errors of a Non-Ideal Ring Laser and Backscatter Correction

Ideally, the Sagnac beat frequency induced by an external rotation strictly follows Equation 2.47. However, intra-cavity biases and non-reciprocities can give rise to offsets to the measured frequency. Any geometrical variation of the cavity, plasma dispersion, null shifts and backscatter-coupling are contributing factors for a deviated Sagnac beat frequency δf_s. The bias (Δf_s) introduced by the systematic errors can be written as:

$$\Delta f_s = K\vec{n} \cdot \vec{\Omega} + \Delta f_0 + \Delta f_{bs}, \tag{2.65}$$

where K is a constant term given by the scale factor shift, Δf_0 is the null-shift error representing the frequency difference for zero rotation rate, and Δf_{bs} is the error signal arising from

backscatter perturbations.

2.7.1 Perturbations Introduced by Scale Factor Shifts

Geometrical shifts are the simplest examples of scale factor variation, which commonly occur in ring lasers of heterolithic or semi-monolithic design. Environmental instabilities like air pressure and temperature changes lead to thermal expansion and compression of the ring laser cavity, and therefore variation of the optical paths of the two counter-propagating beams. This dimensional variation gives rise to variation of the laser operating frequency via 'mode-hops' and 'mode splitting'. In the mode-hop phenomenon, the operating modes in both laser beams simultaneously change to the adjacent mode number in the same direction, yielding a sudden step-up and step-down of the Sagnac frequency. Mode splitting is the most undesired configuration. It causes complete loss of the Sagnac signal when the two counter-propagating modes are shifted to different mode indices.

Another type of scale factor shift is the change in optical frequency (or wavelength) of the counter-travelling beams, due to plasma dispersion. Plasma dispersion varies approximately linearly with the optical frequency which is close to the centre of the lasing transition. Near the peak of the gain curve, the neighbouring modes are pulled closer to each other, and therefore reduce the effective Sagnac beat signal. The easiest method for estimating the optical frequency pulling $\Delta\nu$ is given by the Siegman Equation [62]:

$$\Delta\nu \approx \frac{c}{\lambda} \cdot \frac{G_0 \nu_{FSR}}{2\pi l_w}, \tag{2.66}$$

where G_0 is the single-pass gain of the operating frequency, ν_{FSR} is the FSR frequency of the ring cavity, l_w is the width of composite gain curve (Lorentzian profile). The dispersion-induced systematic error lowers the expected Sagnac frequency by a small amount.

2.7.2 Null Shifts Arising from Non-Reciprocities

A null-shift bias (Δf_0) is deviation from absolute rotation rate sensing. This arises mainly from a net flow of gas (Langmuir flow) in a particular direction [40]. As a consequence, the ions and electrons moving with a net flow velocity in a guided direction give rise to an offset in the Doppler broadened velocity distribution. Eventually, the shifted gain curve influences the operating frequency, and differential mode pulling and pushing of the two counter-propagating beams introduces an offset in the Sagnac frequency.

Langmuir flow occurs typically in a DC excited plasma as the gas circulation is created between cathode and anode, with a gas flow rates of about 100 mm/s reported by Podgorski and Aronowitz [75]. Ring lasers using RF excitation can minimise such null shifts since the excitation process does not (in principle) generate a net travel direction. However, net travel

velocities can also be generated by the temperature differences as gas flow is generated from any thermal gradient along the tube walls [76, 77]. Hence, low power inputs are highly desirable.

2.7.3 Backscatter Coupling and Lock-In Phenomenon

Induced by the substrate, interface imperfections and defects in the cavity mirrors, the backscattering effect gives rise to both a deviation from absolute rotation sensing as well as a time varying error component. This special case where the radiation scatters into the incident direction of the counter-propagating beam, is known as the backscatter-coupling effect (see Figure 2.6 (a)), and is the dominant systematic error in a laser gyroscope [78]. Backscatter-coupling introduces both amplitude and phase variations of either beam, and thereby leads to frequency pulling.

As shown in Figure 2.6 (b), the phasor E_0 represents the electric field of a single beam (also denoted as a 'monobeam') and correspondingly $|E_0|$ is the amplitude of the sinusoidal waveform. A much smaller phasor E_{bs} denotes the electric field of the backscattered light. Assuming that the clockwise and counterclockwise beams are of equal intensity, the phasor E_{bs} has an amplitude of $\sqrt{\frac{r}{r_s}}|E_0|$, where r is the fractional amplitude of each beam that contributes to the opposite beam and r_s is the total scattering amplitude. The phasor E_p represents the resultant electric field of the laser beam which is affected by the backscattered light E_{bs}. The spatial superposition of electromagnetic waves E_{bs} and E_0, results in the phasor E_p with a 'pulled' angular frequency relative to that of E_0. Noticeably, the backscatter perturbation modifies both the intensity and optical frequency of the laser beam. Correspondingly the 'pulled' frequencies of the two laser beams give rise to an error signal Δf_{bs} to the Sagnac beat frequency.

In extreme cases, strong coupling between the two counter-propagating beams eliminates the Sagnac beat frequency, as the 'pulled' oscillating modes of each beam lock to a common frequency [46, 79]. This is denoted as the 'lock-in' behaviour, which completely suppresses the Sagnac effect and turns the ring laser into an inoperative rotation sensor. It occurs when the Sagnac frequency drops below a threshold value of f_L. The lock-in frequency defined from the backscattering amplitude can be calculated as in [80–82]:

$$f_L = r \cdot \nu_{FSR} = \frac{rc}{P}, \tag{2.67}$$

where r is the fractional amplitude of backscatter coupling, ν_{FSR} is the FSR frequency of the cavity, c is the speed of light and P is the perimeter of the ring laser cavity.

A fraction of the total scattering intensity r_s^2 can be scattered in any direction within a solid angle of 4π steradians. If the scattering degree is assumed to be uniform at each angle, only a portion $d\Omega/4\pi$ of the scattering intensity r_s^2 can be coupled into the oppositely directed beam.

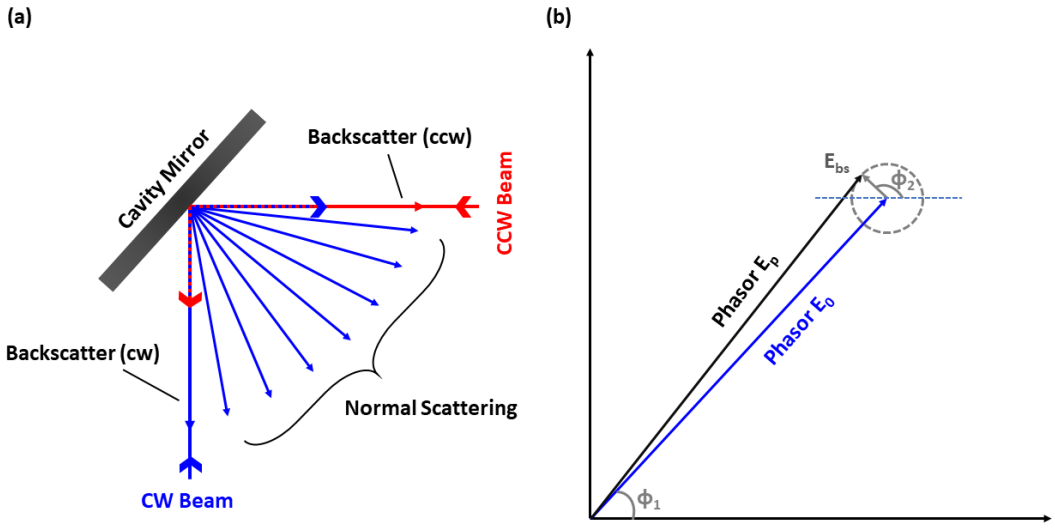

Figure 2.6: Schematic diagrams with: (a) the normal scattering and backscatter-coupling effect; (b) the backscatter-induced frequency pulling (also denoted as 'Adler pulling'), where ϕ_1 and ϕ_2 are the phase angles of E_0 and E_{bs}, respectively.

The $d\Omega$ is the acceptance solid angle of the other beam having $d\Omega = \pi\theta^2$, where θ is the diffraction angle of the Gaussian beam profile determined by $\theta = 2\lambda/\pi d$, and d represents the beam diameter at the waist. The relation between the total scattering intensity and the backscatter fractional intensity can be expressed by [83, 84]:

$$\frac{r^2}{r_s^2} = \frac{\lambda^2}{\pi^2 d^2}. \tag{2.68}$$

Thus we can write:

$$f_L = \frac{c\lambda r_s}{\pi d P}. \tag{2.69}$$

By linking the lock-in frequency f_L to the Sagnac equation, the corresponding lock-in threshold for the rotation rate of the ring laser can be estimated via:

$$\Omega_L = \frac{c\lambda^2 r_s}{4\pi A d}, \tag{2.70}$$

where A is the ring laser area. Equation 2.70 implies that an effective reduction of the frequency 'lock-in' region can be achieved via geometric-upscaling of the laser cavity, and via the employment of super-polished mirrors which lower the magnitude of the scattering.

Analytical Methods for the Quantification of Backscatter Perturbations

Practical schemes for the quantification and correction of backscatter perturbations on the measured Sagnac frequencies have been proposed by various researchers [47, 85]. A description of the multi oscillator coupling dynamics begins with three essential, nonlinear-coupled differential equations which describe the dynamics of the intra-cavity beam intensities (I_1, I_2) and the Sagnac phase (ψ), as mentioned in [47, 86–88]:

$$\dot{I}_1 = I_1 \nu_{FSR}[\alpha - \beta I_1 - \theta I_2 + 2r_2\sqrt{I_2/I_1}\cos\psi], \tag{2.71}$$

$$\dot{I}_2 = I_2 \nu_{FSR}[\alpha - \beta I_2 - \theta I_1 + 2r_1\sqrt{I_1/I_2}\cos(\psi+\zeta)], \tag{2.72}$$

$$\dot{\psi} = \omega_S - \nu_{FSR}[r_1\sqrt{I_1/I_2}\sin(\psi+\zeta) + r_2\sqrt{I_2/I_1}\sin\psi] + \kappa(I_2 - I_1)/\tau. \tag{2.73}$$

α, β, θ and τ are dimensionless Lamb parameters which symbolise the (single-pass) gain, self-saturation, cross-saturation[7] and photon lifetime (cold-cavity ringdown time), respectively; κ is a coefficient describing the differential frequency shift due to differential intensity-related dispersion in the gain medium (cross-dispersion); ν_{FSR} is the cavity FSR and ω_S is the unperturbed, ideal Sagnac angular frequency having $\omega_S = 2\pi\delta f_s$. The most crucial parameters r_1, r_2 represent the fractional backscatter-coupled amplitudes of the two beams and ζ denotes the backscatter phase. It should be kept in mind that $\dot{I}_1$, $\dot{I}_2$ and $\dot{\psi}$ are all time-dependent.

However, the laser dynamics formulated as in Equations 2.71 to 2.73 somehow complicate the analytical method, as the backscatter perturbations mainly arise from linear properties. For simplicity, a linear analysis can be presented to demonstrate the essentials. Firstly, it is assumed that the ring cavity is passive and driven by an external excitation source. Then based on this assumption, all Lamb parameters related to the laser dynamics can be removed. Afterwards, a simplified mathematical expression for the backscatter-induced bias ($\Delta\omega$) can be given by:

$$\Delta\omega = \Delta(\omega_2 - \omega_1) \approx \frac{-2\mu\omega_S Re(r_1 r_2)}{(1-\mu)^2 + \mu^2(\omega_S/\nu_{FSR})^2}, \tag{2.74}$$

where ω_1 and ω_2 denote the perturbations on the two nominally independent resonance frequencies of beam 1 and beam 2, and μ (< 1) is the real-valued amplitude propagation factor for one travel-cycle of the monobeam. In other words, the term $(1-\mu)$ represents the fractional round-trip loss of the monobeam amplitude. Note that Equation 2.74 is derived by assuming that both travelling-beams experience the same losses ($\mu_1 = \mu_2 = \mu$) and the frequency perturbations on each beam are fairly small with $(1-\mu)$ close to zero. It should be highlighted that r_1 and r_2 in Equation 2.74 are complex rather than real values.

[7] Normally it is denoted as θ_{mn}: the nth mode cross-saturation coefficient arising from the presence of mode m; the definition and calculation of this Lamb coefficient are introduced in refs. [86, 89].

Following Equation 2.74, the passive system is converted into an active one to analyse the frequency perturbation ($\Delta\omega$) with a further approximation. With the inclusion of the gain medium, steady-state lasing occurs with two self-sustaining beams. This means the increment of the fractional amplitude should be equal to the round-trip fractional amplitude loss at any time. Therefore, the backscatter perturbation on the optical frequency of any monobeam is given by:

$$\Delta\omega_2 = -\frac{\nu_{FSR}^2 Re(r_1 r_2)}{\omega_S + \Delta\omega_2} + \frac{\nu_{FSR}^4 (Im(r_1 r_2))^2}{(\omega_S + \Delta\omega_2)^3}. \tag{2.75}$$

With the approximation that $\Delta\omega_2 = -\Delta\omega_1$, the overall Sagnac frequency bias provided by the backscatter effect is $2\Delta\omega_2$.

Applicable Solutions for Backscatter Corrections

As implied by Equation 2.75, a key element for any bias correction is to identify r_1 and r_2. In fact, they can be experimentally determined from the intensity modulations of the two counter-propagating beams. Due to backscatter-coupling, each beam contains a small proportion of the other beam. Given this beam-mixing effect, the Sagnac beat signal induced from two slightly different resonant frequencies is observable on the single beam output. The factor of $r_1 r_2$ can be obtained via:

$$r_1 r_2 = \frac{m_1 m_2 S^2 (\omega_S + \Delta\omega_2)^2}{4\nu_{FSR}^2}, \tag{2.76}$$

where m_1 and m_2 are the fractional intensity modulations of the two beams, and S represents the factor $1 + j\mathrm{Im}(r_1 r_2)\nu_{FSR}^2/(\omega_S + \Delta\omega_2)^2$. Considering that both $(\omega_S + \Delta\omega_2)^2$ and $4\nu_{FSR}^2$ are real values, $r_1 r_2$ have to be equal to $m_1 m_2 S^2$. With this argument, the backscatter phase ζ (mentioned in Equation 2.71 - 2.73) turns up as the phase difference between the beat modulations of two beams. By merging Equation 2.75 and 2.76, a relation between the ideal (ω_S) and the measured Sagnac frequency (ω_{mea}) is found:

$$\omega_S = \omega_{mea}(4 + M)/(4 - M), \tag{2.77}$$

where M denotes the complex factor of $\mathrm{Re}(m_1 m_2 S^2)$ - $[\mathrm{Im}(m_1 m_2 S^2)]^2/4$. It is worth mentioning that Equation 2.76 and 2.77 are derived without the inclusion of gain saturation[8]. Once it is considered, the beam intensity modulations can be represented for two separate cases - common-mode (CM) and differential-mode (DM) operation, via two expressions with complex amplitudes:

$$m_C = (m_1 + m_2)/2; \quad m_D = (m_1 - m_2)/2. \tag{2.78}$$

[8]Gain saturation can potentially affect the amplitudes of the monobeam modulations (m_1,m_2) as well as the Sagnac perturbation.

As for the squares of the common-mode and differential-mode modulations they can be calculated by:

$$m_C^2 = (m_1^2 + m_2^2 + 2m_1 m_2 \cos\phi)/4; \quad m_D^2 = (m_1^2 + m_2^2 - 2m_1 m_2 \cos\varphi)/4, \tag{2.79}$$

where ϕ and φ are the phase differences between the two beams. Note that the monobeam modulation amplitudes m_1 and m_2 in Equation 2.79 are real amplitudes. The term M (in Equation 2.77) can be re-formed using real rather than complex arithmetic:

$$M = m_C^2 - m_D^2 + (m_1^2 m_2^2 \sin^2\phi)^{1/4}. \tag{2.80}$$

By inserting Equations 2.79 and 2.80 into Equation 2.77, ultimately we can quantify the backscatter-induced frequency perturbation to a very good approximation as:

$$\delta f_{bs} = \delta f_s \cdot \frac{2M}{4-M} \approx \frac{1}{2}\delta f_s m_1 m_2 \cos\phi, \tag{2.81}$$

where δf_s is the measured Sagnac beat frequency (in unit of Hz) and the ϕ is the backscatter phase (in unit of rad). This approach is sufficient for backscatter correction with a resolution of the integration at a few parts per billion of the Sagnac frequency [47]. But we note that this resolution is achievable only under certain conditions: the ring laser is in common-mode operation; the monobeam modulations are smaller than 2%; the laser intensities of two beams are equal[9].

2.8 Frequency Noise on the Sagnac Signal and Noise Processes

Variations in the Sagnac frequency arise from various types of noise. The δf_s frequency is primarily perturbed by instrument noise and quantum noise. The raw Sagnac waveform (interferogram) of the combined beams can be written in terms of the DC voltage as:

$$V(t) = (V_0 + \varepsilon(t))\sin[2\pi\delta f_s t + \varphi(t)], \tag{2.82}$$

where $V(t)$ is the time dependent DC voltage signal, V_0 is the nominal peak voltage, $\varepsilon(t)$ is the deviation of amplitude contributed by the noise, δf_s is the theoretical Sagnac frequency and $\varphi(t)$ is the deviation of the phase over time. In the absence of any noise and mode instability, $\varepsilon(t)$ and $\varphi(t)$ are zero all the time. However, this is not reality. The environmental instability of pressure, temperature, and mechanical shock can lead to frequency drift in a certain range through perturbations in the amplitude and phase of the measured δf_s. The noise classifications and the analytical method of noise processing will be elaborated in the following.

[9] A ring laser cavity filled with 50:50 neon (with an equal mix of isotopes ^{20}Ne and ^{22}Ne) generates near equal intensities for the counter-propagating beams.

2.8.1 'Quantum-Limited' Noise

When one considers the laser gain properties, the influence of spontaneous emission is normally ignored as the stimulated emission makes a greater contribution to the measurable photon flux. However, spontaneous emission cannot be neglected during an analysis of the operating frequency. Spontaneous emission introduces noise via the prescence of photons of random phase, and thereby perturbs the operating frequency and limits the highest obtainable precision of the δf_s. Assuming a full population inversion ($n_k/\Delta n \approx 1$) for single-mode oscillation, the full width of the Lorentzian laser line[10] determined by the irreducible quantum-limited noise can be expressed by [90, 91]:

$$\Delta\nu_{laser} = \frac{2\pi h f_0 (\Delta\nu_R)^2}{P_o} = \frac{2\pi h f_0^3}{Q^2 P_o}, \tag{2.83}$$

where h is Plank's constant, f_0 is the nominal operating frequency, $\Delta\nu_R$ is the cavity linewidth given in Equation 2.64, and P_o is the power loss per mode. The parameter $\Delta\nu_{laser}$ can also be considered as the quantum noise contribution to the full-width-at-half-maximum power of the Sagnac beat signal. The spontaneous emission is a random signal contributing equal intensity at different frequencies. Therefore it imposes 'white' noise on the laser frequency as well as on the Sagnac beat frequency. Associated with Equation 2.83, the precision (variance) of the measured Saganc frequency $\Delta(\delta f_s)$, can be written as [83, 92]

$$\Delta(\delta f_s) = \sqrt{\frac{h f_0^3}{Q^2 P_o t}}, \tag{2.84}$$

where t is the observation time of the laser oscillation frequency. The highest precision of the δf_s is obtainable only if all of the potential impact factors are strictly excluded. Further, the measurement precision can be enhanced with longer integration times or operating the laser at higher power. Equation 2.84 yields a quantum-limited rotational sensitivity Ω_s, given by [83]:

$$\Omega_s = \frac{cP}{4AQ}\sqrt{\frac{h f_0}{P_o t}}, \tag{2.85}$$

where A is the enclosed area and P is the perimeter of the cavity. Equation 2.85 demonstrates that raising Q, A and P_o permits a lower quantum limit and the potential for higher sensitivity.

2.8.2 Instrument Noise

Instrument noise results from various sources, including the electronic noise (shot noise, thermal noise and $1/f$ noise) and the quantization noise (A/D conversion noise).

[10] Refer back to Figure 2.1.

Electronic Noise

Shot noise typically occurs in electronic circuits and photon detectors, due to the discrete nature of photons and electron charges. The magnitude of shot noise increases with the average current intensity or average light intensity. However, the signal-to-noise ratio can be improved with a higher current (light) intensity, due to the fact that the signal increases faster than the shot noise.

Two other noise sources of greater influence in the electronic circuits are thermal noise (Johnson-Nyquist noise) and frequency-dependent flicker noise. As opposed to shot noise, thermal noise is present in all electronic circuits regardless of the applied voltage due to the thermal agitation of charge carriers inside a resistive element. The power spectral density of the thermal noise is nearly constant throughout the frequency spectrum, therefore this type of noise is an approximate 'white' noise. Flicker noise ($1/f$ noise) can be generated from a variety of mechanisms, including unevenness on the surface of the photocathode and impurities in a conductive channel (conductance fluctuations). This type of noise has a power spectral density inversely proportional to the frequency. It shows up as a low-frequency phenomenon and introduces slow random fluctuation of the emitted electrons.

Quantization Noise

Quantization noise (error) occurs in analogue to digital (A/D) signal processing, and is attributable to the discrete nature of A/D conversion. As a continuous signal is sampled in amplitude into discrete steps, it generates small rounding errors between the input analogue voltage and the output digitized voltage. The resolution of the A/D converter is presented by the number of discrete digital values for a given analogue signal. For an input signal of lower amplitude, these discrete steps are more apparent, and the quantization noise and signal distortion becomes more critical. For an input signal with a high amplitude and a wide frequency spectrum, quantization noise is assumed to be 'white' for an even distribution in the frequency range.

2.8.3 Sensor Stability and Noise Source Analysis

Sensor stability is a crucial index for the characterisation of gyroscopic performance. The conventional definition of a standard deviation (SD) presents difficulties in determining the fluctuating quantities with correlations. As such, Allan variance (AVAR) is widely adopted for analysing output frequency fluctuations in the time-domain. It measures the frequency variation of an oscillator between one sample interval and the next interval with no dead time [93]. A prominent feature of the AVAR is the capability to identify the dispersive noise sources for more than just classical white noise [94]. Denoted as $\sigma_A^2(\tau)$, the Allan variance is mathematically expressed as:

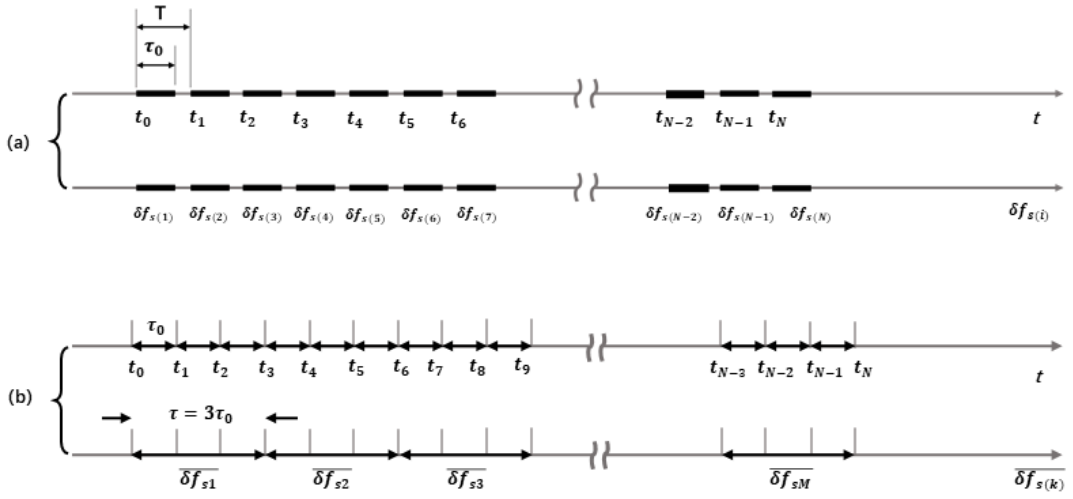

Figure 2.7: A schematic demonstrating the measurement cycle of a Sagnac frequency signal; (a) illustrates the frequency measurements with dead time, as the measuring time τ_0 of a single sample is different from the time T between consecutive measurements. In our actual data acquisition, the dead time is removed via setting $T = \tau_0$, as shown in (b).

$$\sigma_A^2(\tau) = \frac{1}{2(M-1)} \sum_{k=1}^{M-1} (f_{k+1} - f_k)^2, \tag{2.86}$$

where τ is the integration time, M is an integer multiple symbolising the number of clusters, and f_k is the mean value of a consecutive measurement averaged over the duration of τ. To calculate the AVAR of the Sagnac frequency in practice, a discrete set of $\delta f_{s(i)} (i = 1, 2..., N)$ is acquired. The total number of the collected δf_s data is denoted as N, and the measurement time-base of every single frequency is specified as τ_0.

As an alternative approach, the Allan deviation (ADEV) is applied for the evaluation of δf_s stability. Expressed in the square root of the AVAR, the Allan deviation can be written as:

$$\sigma_A(\tau) = \sqrt{\frac{1}{2(M-1)} \sum_{k=1}^{M-1} (\overline{\delta f_{s(k+1)}} - \overline{\delta f_{s(k)}})^2}, \tag{2.87}$$

where τ is expressed as $\tau = n\tau_0$ with the n ($< (N-1)/2$) as an averaging factor. An increase of the measurement time τ (or averaging factor n), reduces the number of clusters M available in the fixed data length N. An example is given in the Figure 2.7. If we set an integration time at $\tau = 3\tau_0$ for analysing a long data series, the consecutive mean frequency of $\overline{\delta f_{s1}} = (\delta f_{s(1)} + \delta f_{s(2)} + \delta f_{s(3)})/3$, $\overline{\delta f_{s2}} = (\delta f_{s(4)} + \delta f_{s(5)} + \delta f_{s(6)})/3$, etc, are used to calculate the Allan deviation for the integration time $\tau = 3\tau_0$. Repeating this procedure for all other τ can yield an ADEV plot as displayed in Figure 2.8. Note that a zero dead time is guaranteed

throughout the data acquisition.

The features of the Allan deviation plot are demonstrated in Figure 2.8. In the ADEV plot, noise is distinguished and classified into white phase, flicker phase, white frequency, flicker frequency, and random walk frequency noise by their power laws. Referring to the paper by Ng and Pines [95], the source of the noise perturbations in ring laser operation and data acquisition, are listed below:

- White phase noise ($\sigma_A(\tau) \propto \tau^{-1}$): electronic noise rise from the broadband amplifiers and electronics, and the A/D conversion apparatus.
- Flicker phase noise ($\sigma_A(\tau) \propto \tau^{-1}$): electronic noise due to the thermal effects, also denoted as thermal noise or Johnson-Nyquist noise.
- White frequency noise ($\sigma_A(\tau) \propto \tau^{-1/2}$): quantum noise due to spontaneous emission, and this is the only source which obeys this power law. The nature of the quantum noise leads to a random walk in the phase of the lasing mode.
- Flicker frequency noise ($\sigma_A(\tau) \propto \tau^{0}$): noise arises from the discharge assembly due to unknown non-reciprocal effects.
- Random walk frequency noise ($\sigma_A(\tau) \propto \tau^{1/2}$): mechanical shocks which alter the operating parameters of the ring laser. Typical sources of mechanical shocks are vibrations, micro-seisms, temperature and pressure fluctuations.

It is noticeable in Figure 2.8 that the ADEV at a short integration time τ is high due to the noise contributions. However, it decreases as the noise averages out with a longer τ. A turning point of the $\sigma_A(\tau)$ occurs when the long integration time τ reaches a certain limit. This suggests an ultimate drift of the measured frequency given by the mechanical shocks of laser operation. In the characterisation of gyroscopic performance the 'turning point' which implies the quantum-limited gyroscopic sensitivity and the sensor stability, is of the greatest interest.

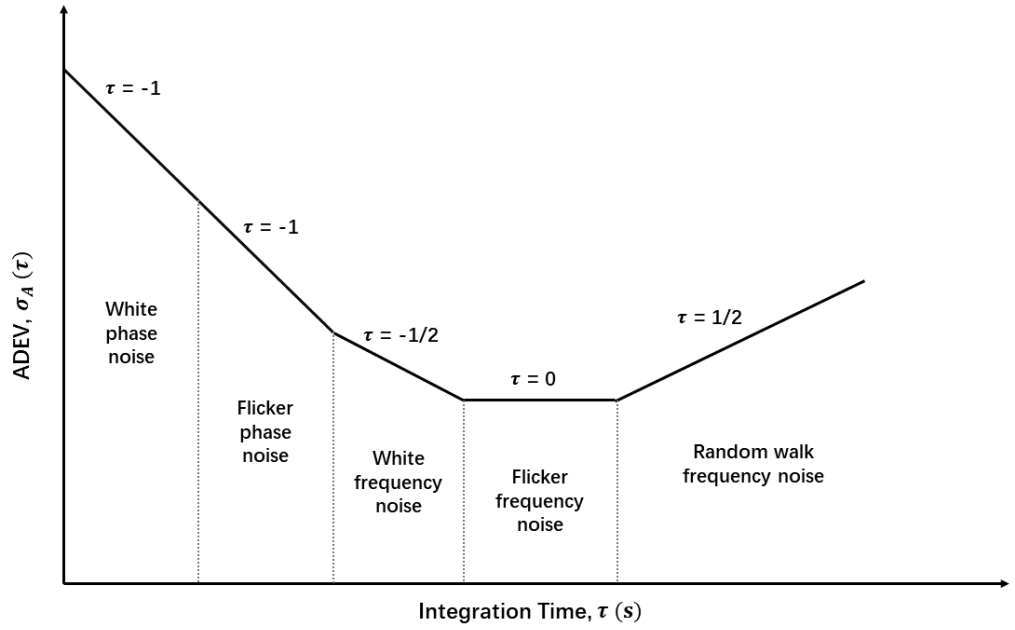

Figure 2.8: The different noise types give rise to integer or half integer power laws for the Allan deviation.

3 Operational Procedures for Large Laser Gyros and Interferometric Measurements on a 2.56 m^2 Ring Cavity

In this chapter, we describe work conducted on a 2.56 m^2 ring laser known in the literature as PR-1, or Physics Ring - 1. This heterolithic laser gyro was vertically mounted on the wall of a second-floor laboratory in an eight-story building (the West Building) at the University of Canterbury's Ilam campus. We begin this chapter by a discussion of the technical details and an introduction to the operation procedures applicable for any Canterbury ring laser. We outline the gyroscopic performance obtained from two independent experiments performed in the visible and invisible (infrared) wavelength regions. The main goal of this chapter is to explore the feasibility of a multi-oscillator gyroscope for simultaneous operation on the 611.8, 604.6 and 593.9 nm neon transitions and to investigate the functionality of commercially-sourced mirrors in the use of Earth rotation sensing.

3.1 PR-1 Technical Details and Operation Specification

3.1.1 Gyro Configuration Details

The overall design of the 1.6 m by 1.6 m ring cavity is shown in Figure 3.1. As one can see that the square-shaped ring cavity is formed by several independent components. Four mirrors are housed in mirror holders which are situated in stainless steel mirror chambers. The lower right laser corner is used for a detailed view of the mechanics as shown in Figure 3.2. The movement of the mirror holder in each corner is controlled by an individual lever arm system. Four micrometres on the folded lever arm allow precise mirror adjustments in both vertical tilt and horizontal rotation. The lever system and the mirror chamber are both firmly attached to the solid corner box made of a granite-epoxy compound[1].

The cavity, with a perimeter of 6.4 m (having a free spectral range of 46.875 MHz), is enclosed by mechanically-decoupled stainless steel tubes, with a section replaced by the gain tube. A form of mechanical decoupling is achieved through the use of a bellows placed between the corner box and the stainless steel tubes which enclose the laser cavity. In Figure

[1]Epoxy granite is used for better vibration damping (mechanical stability).

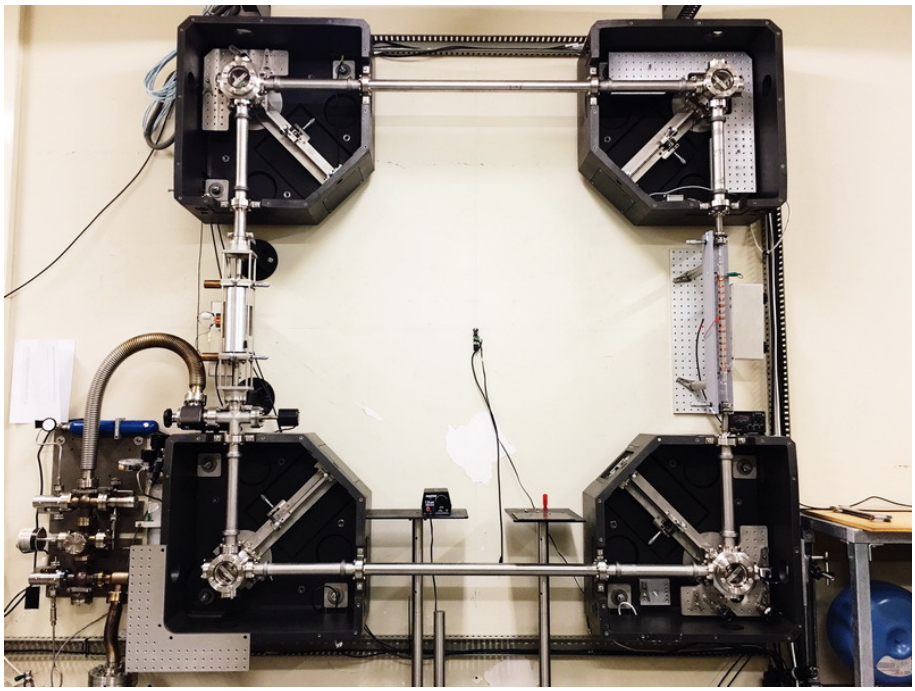

Figure 3.1: Vertically mounted PR-1 ring cavity with all ancillary equipment aside from the pumping station removed for clarity.

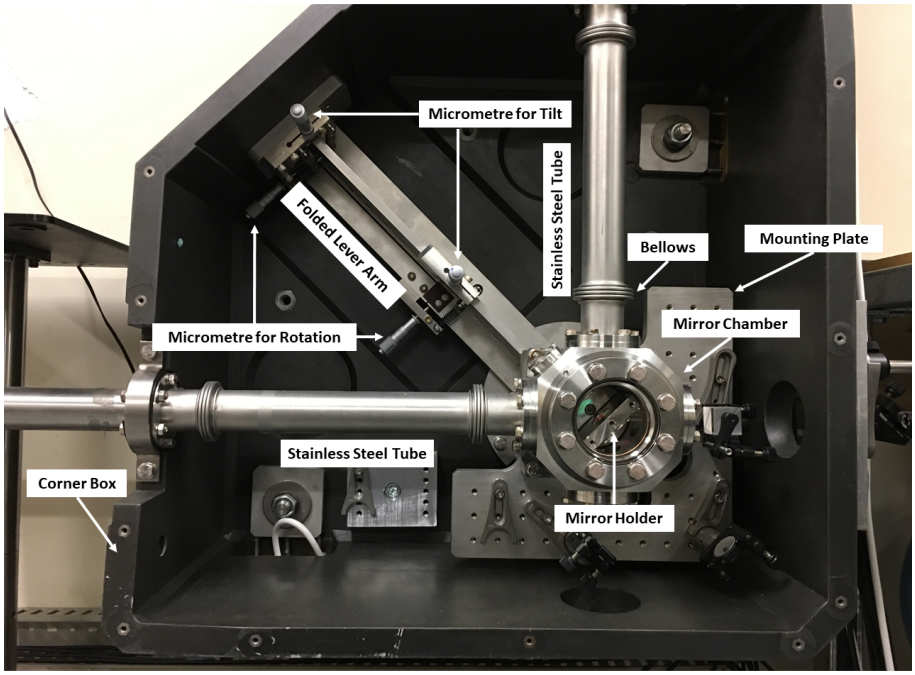

Figure 3.2: A photo demonstration of the PR-1 corner box with the cavity components housed within.

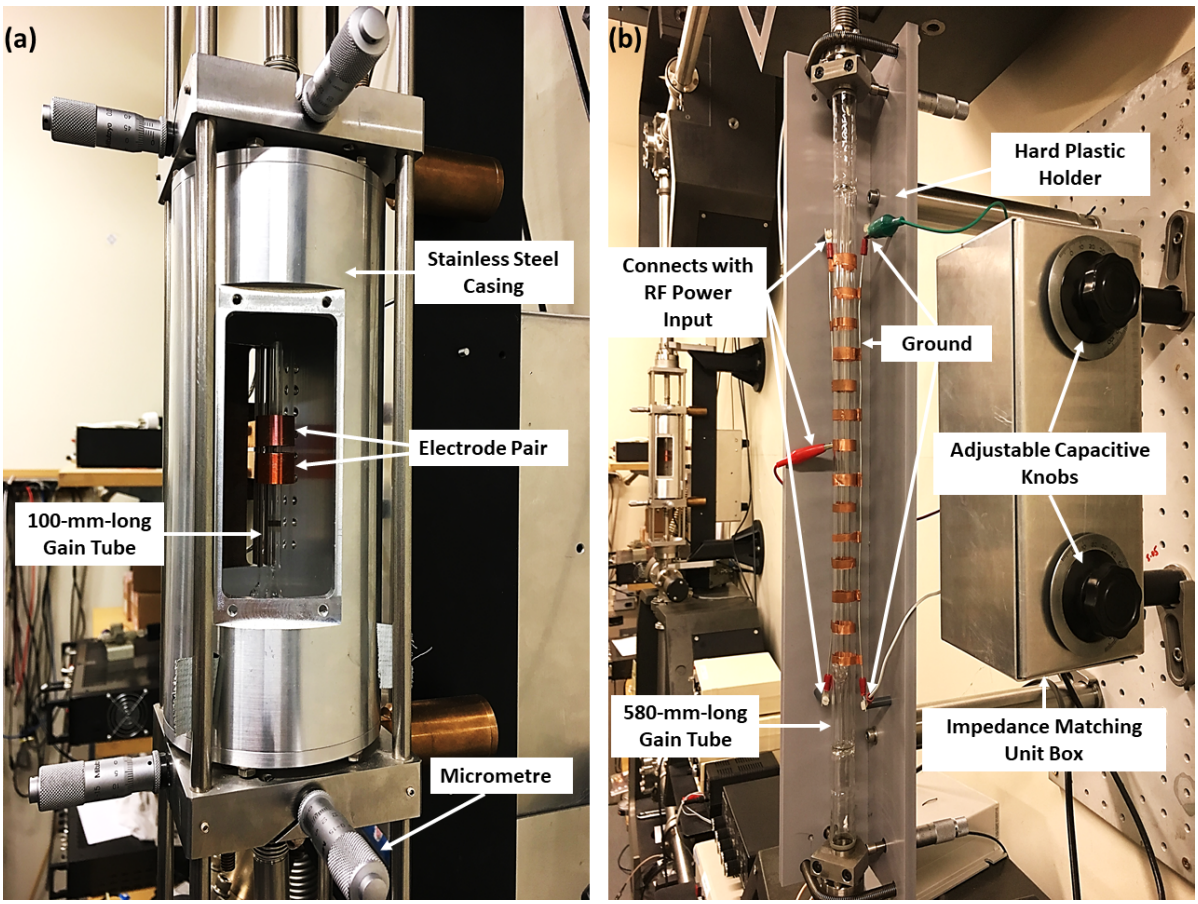

Figure 3.3: Gain tubes of (a) 100 mm in length and (b) 580 mm in length which are mounted on opposite sides of the cavity.

3.1, two fused silica (Pyrex)[2] discharge tubes of 100 and 580 mm in length have the same inner diameter at 4 mm. Both capillaries are mounted in the middle of two adjacent mirror chambers. The short one in the left is housed in a stainless steel casing and the other long one in the right is held by a hard plastic holder made out of polyvinyl chloride (see Figure 3.3). We note that normally the long gain tube is not mounted unless it is required for operation on a low gain neon transition. For the capillary, its translational movements in the vertical and horizontal planes are controlled by two sets of micrometres at each end of the gain tube.

By coupling the 80 MHz radio frequency (RF) power into the He-Ne gain medium through the electrode sets[3] that wrapped around the gain tube, laser excitation is obtained. Each electrode pair has a cathode and an anode when one is grounded while the other connected to the input RF power. The spacings between each electrode are adjusted to be equal for a

[2]Pyrex has a low thermal expansion coefficient and it can tolerate the high temperature generated from gas discharge.

[3]The electrodes are made by copper sheets in similar width and thickness.

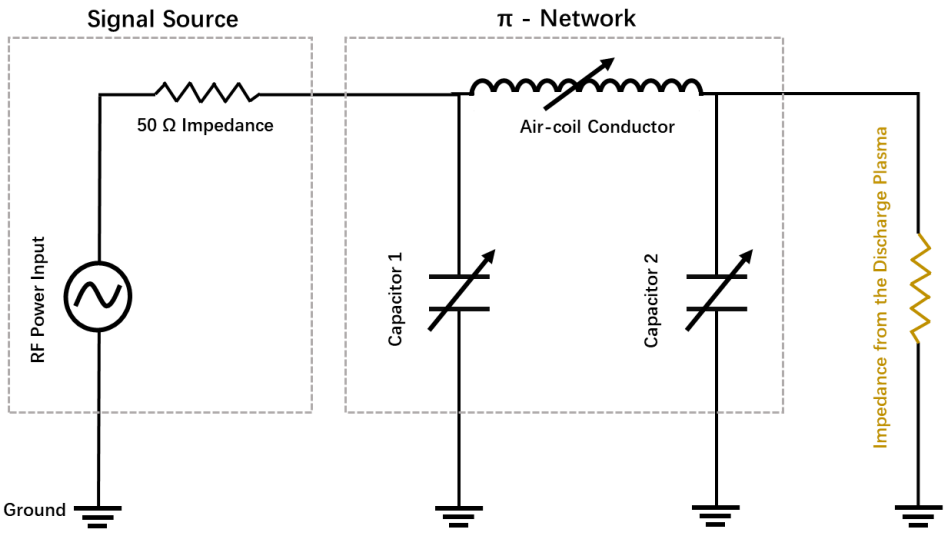

Figure 3.4: A schematic of the impedance matching unit between the 80 MHz RF transmitter and the discharge tube.

uniform plasma distribution, if more than one electrode pair is used.

The RF power is provided by an 80 MHz Tait Radio Communication (Tait T800) transmitter which delivers a maximum of 30 W of RF power. Since the RF transmitter transfers its power to a 50 Ω load, an impedance matching unit is required to match the transmitter impedance to the load-impedance generated by the gain tube and gas discharge. Specifically, the gain tube exhibits inherent capacitive and inductive properties as the distance which separates the gain tube wall and the grounding surface is effectively a double plate capacitor. Furthermore, the gas discharge generates an unknown impedance dependent on the plasma density distribution which varies from different gas pressures [96, 97]. The transmitter is connected to the impedance matching unit with an RF power meter (RS W520)[4] in between. Afterwards, the output of the matching unit is connected to the electrode pairs.

Considering that the ring laser normally operates with a pressure which varies between 2 to 13 mbar, our impedance matching unit adopts a 'π' network configuration as it permits a wider adjustable impedance ratio for the RF source compared to other matching networks [98, 99]. The 'π' matching unit configured as an LC circuit is demonstrated in Figure 3.4. It consists of two capacitors with their capacitance variable in the same range and one air-coil inductor (about 17 mm in diameter and 150 mm in length) with its total inductance determined by the location of the taps on the coil. The impedance matching units and electrode pairs served respectively for the 100 and 580 mm long gain tubes were optimally configured for operational pressures up to 13 mbar. The parameter details are listed in Table 3.1. By

[4]The RF power meter is employed to monitor the power being delivered and reflected between the transmitter and the impedance matching unit.

Parameters	100-mm-long Tube	580-mm-long Tube
Capacitance (pF)	8-150	2-100
Inductance (μH)	0.3	0.08
Electrode Pairs	1	8
Electrodes Widths (mm)	15	8
Electrode Spacing (mm)	3	20

Table 3.1: Core parameters of the optimally-designed impedance matching units and electrode pairs for the respective 100 mm and 580 mm long gain tubes [13].

adjusting the capacitive knobs on the impedance matching unit box (Figure 3.3 (b)), the highest RF excitation efficiency is achieved when the RF reflected power is tuned to 0 W with the longest possible plasma discharge length.

3.1.2 The Vacuum Pump System and General Gas Fill Procedures

Figure 3.5 provides a schematic to fully demonstrate the vacuum pump system. An external vacuum pump system is attached to the cavity via an isolation value 'A' located near the short gain tube. A second isolation valve 'B' isolates the vacuum system from atmosphere. The whole pump system consists of a rotary vane pump and a turbomolecular pump, and connects to three gas cylinders with each containing natural neon (^{20}Ne:^{22}Ne = 90:10), 50:50 neon (^{20}Ne:^{22}Ne = 50:50) and helium (^{4}He).

Before any gas-fill procedure, the initial step is to evacuate the gas in the vacuum system. This guarantees that no impurities are left in the vacuum system which could enter the cavity during the gas-fill. Therefore, the isolation valve 'A' should be closed tightly before turning on the rotary vane pump. Once the pump starts working, the isolation valve 'B' is opened to release the evacuated gas to the atmosphere. When the pressure gauge 'B' indicates a vacuum system pressure below 0.0053 mbar (0.004 torr), the turbomolecular pump starts working. Later on, the leak valves[5] of the helium gas cylinder are opened for the evacuation of helium residuals along the gas delivery pipe. Once the helium gas in the vacuum system is fully evacuated, the leak valves of the two neon gas cylinders are opened to pump out the neon residuals. After this, the isolation valve 'A' is opened by a slight amount to allow a slow and steady evacuation of the cavity gas. This procedure is handled carefully to avoid sudden, violent gas turbulence and protect the vacuum system from impurities transferred from the cavity. When the pressure gauge 'A' drops to zero, it indicates that the cavity gas is fully removed. However, the vacuum status cannot be confirmed solely by a zero reading of the pressure gauge when the long gain tube is mounted. The long, narrow gain tube can easily trap gas residuals in particular for an extreme low-pressure situation. Under this circumstance, it takes a long time for a complete gas evacuation. Therefore, the safest way

[5] All leak valves along the gas line pipes in Figure 3.5 are variable.

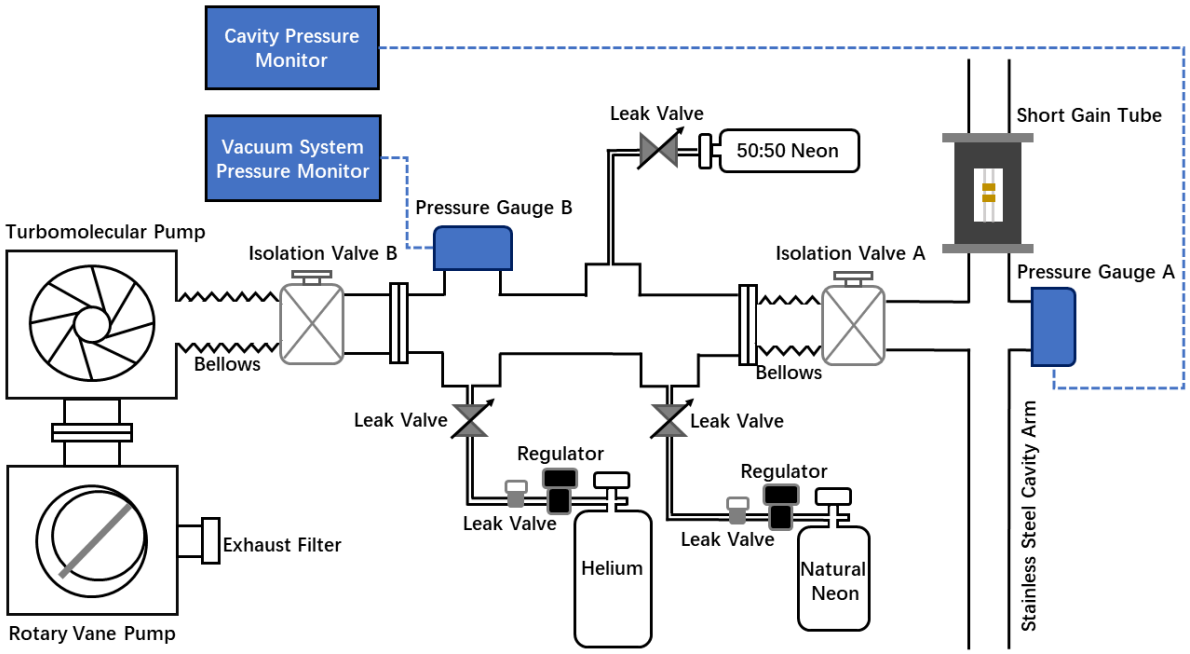

Figure 3.5: A schematic shows the vacuum pump system assembled for PR-1.

to ensure a high vacuum environment is to turn on the RF excitation and monitor the gas discharge. The cavity is under vacuum if no gas discharge can be observed while the maximal RF power is applied.

When both the pumping system and ring cavity reach a high vacuum status, all leak valves for the gas cylinders and gas pipes and the isolation valve 'B' are closed, leaving only isolation valve 'A' completely opened. Then, the valve[6] of the neon gas cylinder is opened by a small amount and closed very soon. This allows a small quantity of the neon gas to fill the gas line pipes. Later, the leak valves are opened to allow neon to fill up the cavity until the required pressure is reached. When the desired neon pressure is obtained, the leak valves are closed and the same procedures applicable for the helium gas fill are repeated. Once the desired cavity pressure is reached, the isolation valve 'A' is closed tightly to avoid any undesired gas exchange between the vacuum system and the cavity. Ultimately, all leak valves are re-opened for the gas evacuation in the vacuum pump system as a precaution.

[6]Cylinder valves for the helium and natural neon gas bottles are equipped with regulators which are used to reduce the high pressure from a gas cylinder to a low-pressure system.

3.2 A Multi-Wavelength Gyro Operating on Three Neon Transitions in the Visible Region

Precision measurement of length of day fluctuations without gaps or data latency has long been desired for advancing navigational technologies. Meanwhile, information on the absolute Earth rotation rate is the key to achieve detection of general relativistic precessions using terrestrial interferometry. Here, we demonstrate a multi-wavelength laser gyro which allows for simultaneous operation on dual or triple neon transitions. This novel approach to gyroscopic operation paves the way for accurate calibration of the measured Earth rotation rate in the presence of unavoidable biases and systematic uncertainties within the laser. To be more specific, simultaneous acquisition of Sagnac time series yielded from one wavelength can be used to make corrections for dispersion within, and the refractive index of, the gain medium and optical penetration into the mirror structure (the Goos-Hänschen effect) [43] when compared to the signal from the other wavelengths. In brief, multi-wavelength operation can provide a convenient check of corrections to systematic errors since the inferred rotation rate as measured at any wavelength should reduce to the same (time-dependent) value at any measurement time.

Wavelength (nm)	Neon Transition	Scale Factor Variation	Sagnac Frequency (Hz)
632.8	$3s_2 \rightarrow 2p_4$	1	113.38
611.8	$3s_2 \rightarrow 2p_6$	1.0343	117.27
604.6	$3s_2 \rightarrow 2p_7$	1.0466	118.67
593.9	$3s_2 \rightarrow 2p_8$	1.0655	120.81

Table 3.2: Neon transitions, corresponding energy level notations, scale factor variations relative to a 632.8 nm laser gyro and the expected Sagnac frequencies for PR-1 operation at 632.8, 611.8, 604.6 and 593.9 nm.

Generally, He-Ne ring lasers worldwide adopt the 632.8 nm wavelength for operation as its neon transition $3s_2 \rightarrow 2p_4$ obtains the highest gain in the visible region. As shown by Equation 2.85, an increase of the gyroscopic sensitivity can be achieved by a shorter operating wavelength. Therefore, we constructed the PR-1 cavity to yield laser output on rarely explored shorter wavelengths at 611.8, 604.6 and 593.9 nm. These wavelengths were used not only for testing the practicality of dual or triple wavelength operation but also for upgrading the rotational resolution. When the same PR-1 system operates on shorter wavelengths, the laser scale factor ($4A/\lambda P$) is improved as shown in Table 3.2. The up-scaled Sagnac frequencies are at 117.27, 118.67 and 120.81 Hz, respectively. As the PR-1 device is located at the latitude, φ = -43.52° and with a tilt θ_T of 32° east of the north, the Sagnac frequency demonstrated in Equation 2.47 can be calculated via a rewritten form of:

$$\delta f_s = \frac{4A}{\lambda P}\Omega_E \cos\varphi \ \cos\theta_T, \tag{3.1}$$

where Ω_E is the Earth rotation rate of 7.2921159×10^{-5} rad/s (≈ 73 μrad/s).

3.2.1 Experimental Details

In this work, we have employed latest generation ion beam sputtered (IBS) supermirrors provided by Research Electro-Optics (REO). These IBS-coated mirrors have 3 m radius of curvature (ROC), with a specified transmission loss (per mirror) of 6 ppm at 593.9 nm, 32 ppm at 604.6 nm and 158 ppm at 611.8 nm, at 45 degrees angle of incidence (AOI) in the s-polarization direction.

While the exact gain difference among the three neon transitions is dependent upon the precise dimensions of the gain tube as well as the gas ratio, isotopic composition, and excitation density, a good approximation is that the 604.6 nm transition has half the gain of the 611.8 nm transition while the 593.9 nm transition has one-third [100], following the transition probability A_{ki} of the three transitions provided by NIST (Table 2.3). Therefore, one additional 580-mm-long gain tube was assembled (shown in Figure 3.1) to provide additional gain in particular for the low-gain transitions at 604.6 and 593.9 nm. Two 80 MHz RF transmitters were separately connected to two different impedance matching units for coupling to the 580-mm-long and 100-mm-long gain tubes. The 580-mm-long gain tube had eight pairs of electrodes (with 20 mm spacing between each electrode) and can generate a maximum plasma discharge length of 330 mm.

Signal Detection and Data Acquisition System

Figure 3.6 shows a simplified diagram of the experimental setup. A non-polarising 50:50 beam splitter (Thorlabs, 1100-1600 nm) was mounted at the lower-right (LR) corner to combine the two counter-propagating beams for the detection of rotation signals (δf_s). This combined beam was detected by a photomultiplier tube (Hamamatsu R3896) PMT 1, and the raw Sagnac interferogram was observed by an oscilloscope (Tektronix TDS 220 100 MHz) and an FFT spectrum analyser (Model SR770). Two high gain photodiodes labelled as PD 1 and PD 2 (HUV-1100B) were mounted at the top-right (TR) corner to monitor the fractional intensity modulations of the CCW and CW beams (m_1, m_2). An optical power meter (Coherent FieldMaxII-TO) equipped with a silicon sensor (OP-2 VIS) was mounted on the top-left (TL) corner to measure the laser output power. The CCW beam transmitted from the lower-left (LL) corner box was directed into a Fabry-Perot interferometer (Coherent 33-6305-001) for observation of longitudinal mode structures via a fast oscilloscope. Meanwhile, the CW beam was fed into a spectrometer (Ocean Optics USB2000+ UV-Vis-NIR) via a fibre optic cable for the measurement of laser spectrum. A flip mirror was mounted in front of the optical fibre to guide the CW laser beam into PMT 3 as required. The AC signal of this beam was fed into an RF spectrum analyser (Hewlett Packard ESA-L1500A) for identifying the FSR beat frequencies induced by any set of longitudinal modes.

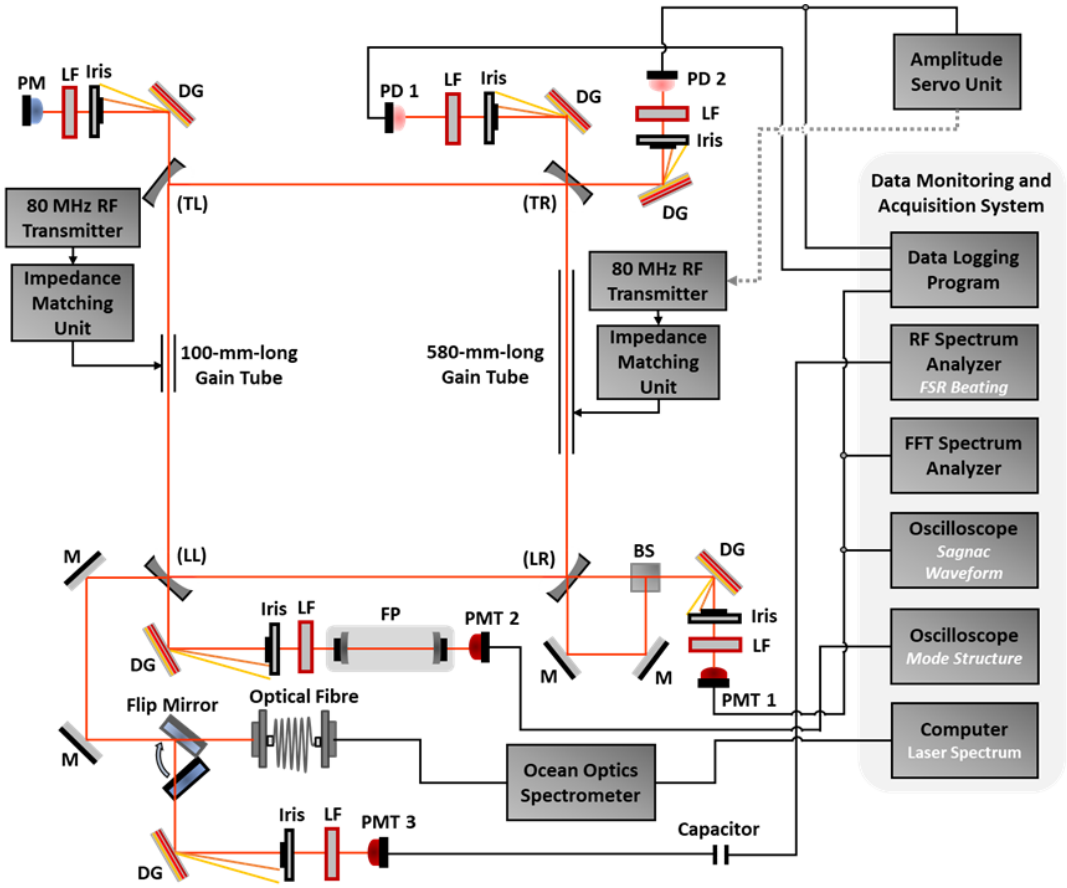

Figure 3.6: Simplified diagram of the experimental setup, where, M: dielectric mirror; PMT: photomultiplier tube; PD: photodiode; PM: power meter; FP: Fabry-Perot interferometer; DG: diffraction grating; LF: line filter; BS: beam splitter; TL: top-left corner; TR: top-right corner; LL: lower-left corner; LR: lower-right corner.

Diffraction gratings were employed in front of each photodetector to disperse the laser output into the three laser beams at different wavelengths. Meanwhile, narrow laser line-filters and irises were applied to prevent simultaneous detection of multiple laser beams or signal contamination from the plasma light. The CW and CCW beam modulations and Sagnac beat signals were fed to a National Instrument LabVIEW data acquisition board (USB NI-6216 BNC) for data logging. Continuous data acquisition was realised by a LabVIEW program written by Caroline L. Anyi.

Stable and sustainable laser operation was maintained by an intensity control system. As shown in Figure 3.6, the laser output power in the CW direction was detected (via PD 2) and fed into an amplitude servo system which consists of a simple PID unit. The error signals induced by the subtraction of the set voltage and the detected voltages were used as feedback signals to regulate the 80 MHz RF transmitter for compensating any drift in the laser intensity. Note that the error signals in terms of DC voltages were proportional to the differences between the actual laser powers and the desired laser power. Note that for this experiment the amplitude servo unit was only applied to the RF transmitter driver for the long gain tube.

3.2.2 Gas Pressure Optimisation and Some Optical Properties

Figure 3.7 (a) shows a bright red-orange beam spot on the supermirror which was obtained from using maximum excitation (in both gain tubes), and a gas-mixture with 0.2 mbar of natural neon partial pressure and 1.8 mbar of helium partial pressure. Figure 3.7 (b) shows the laser spectrum including the 611.8 nm, 604.6 nm and 593.9 nm transitions.

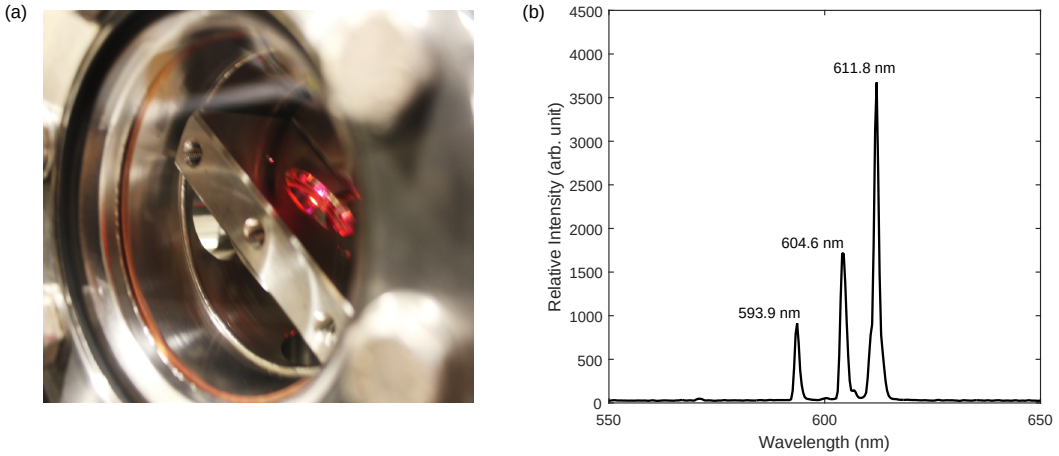

Figure 3.7: (a) Beam spot on the supermirror; (b) low-resolution laser spectrum illustrating simultaneous oscillation on the 611.8, 604.6, and 593.9 nm transitions.

Initially, we investigated the optimal He-Ne gas ratios for lasing on all three transitions.

Figure 3.8 shows the laser output powers as a function of the total gas pressure when a constant RF power of 60 W was applied to two gain tubes (30 W for each). Initially, we filled the cavity with a fixed natural neon partial pressure ranging from 0.1 to 0.5 mbar before adding helium gas to vary the total cavity pressure between 1 to 4 mbar. In general, all three laser transitions yielded their highest output powers with natural neon partial pressures in the range of 0.2 to 0.3 mbar and total gas pressures of 2 to 3 mbar. The maximum output power achieved at 611.8 nm was 290 μW, while the maximum powers obtained at 604.6 nm and 593.9 nm were 33 μW and 8 μW, respectively. For any laser system equipped with a 4-mm-diameter capillary, optimum neon partial pressures for gyroscopic operation at 632.8 nm ($3s_2 \rightarrow 2p_4$) and 1152.3 nm ($2s_2 \rightarrow 2p_4$) have been reported to be between 0.2 and 0.3 mbar [101, 102]. However, it is notable that the operable gas pressures for these three wavelengths were all lower than that for the 632.8 nm and 1152.3 nm transitions [103]. Lasing at 611.8 nm, 604.6 nm or 593.9 nm wavelength was only observable with a cavity pressure of no more than 5.5 mbar, 4.5 mbar or 3.5 mbar, respectively. However, lasing at 632.8 nm and 1152.3 nm is achievable at any pressure up to 12 mbar or even beyond.

The relative gain of the 611.8 nm, 604.6 nm and 593.9 nm transitions for various He-Ne gas compositions is demonstrated in Figure 3.9. The laser output power ratios of 611.8 to 604.6 nm and 611.8 to 593.9 nm drop notably when total cavity pressures are at 2 to 3 mbar. In this region, laser gain for the 604.6 nm and 593.9 nm laser transitions increases by larger amounts than that for 611.8 nm. When the intensity of the 611.8 nm wavelength is minimised (at 2 mbar of cavity pressure with 0.3 mbar of natural neon partial pressure), the ratio of the laser output powers of 593.9 nm: 604.6 nm: 611.8 nm is 1: 3.7: 37 (under 60 W of RF excitation).

We measured the cold cavity ring-down time (τ) at a total pressure of 2 mbar with a natural neon partial pressure of 0.25 mbar as all laser transitions can be sustained solely by the gas discharge in the 580-mm-long gain tube. Coupling 30 W of RF excitation power to this gas-mixture, the output powers for the three transitions are 593.9 nm: 604.6 nm: 611.8 nm = 1: 4.4: 97.6. As shown in Figure 3.10, the ring-down time measurement was done by connecting a coaxial relay to the RF transmitter which was coupled to the 580-mm gain tube. Using a diffraction grating in front of the PMT, the ring-down time at the three wavelengths could be measured separately. A laser line-filter and a slit was used for discrimination. The temporal signal output of the PMT was connected to a storage oscilloscope (Tektronix PPO 7104 Digital Phosphor) via a short coaxial cable. The photon-decay trend was recorded on the oscilloscope following a trigger signal provided by the switch. Note that the 1 MΩ resistor inserted in parallel between the PMT and oscilloscope can further reduce the resistance and the RC time constant. Therefore, we made sure that the observed transient was a true reflection of the photon decay.

Table 3.3 tabulates the measured ring-down time, τ, and the corresponding quality factor

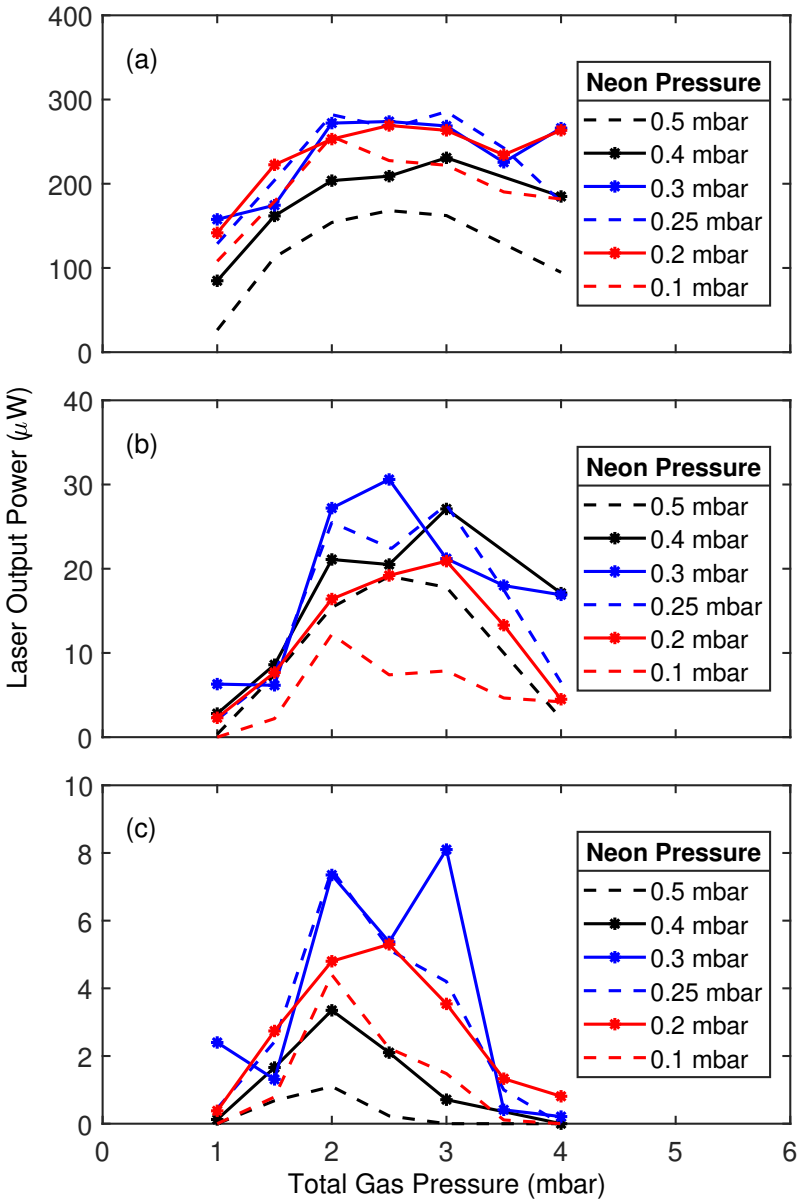

Figure 3.8: Measured laser output powers of (a) 611.8 nm, (b) 604.6 nm, and (c) 593.9 nm, as a function of total gas pressures from 1 to 4 mbar (with natural neon partial pressures fixed in a range of 0.1 and 0.5 mbar). The RF power delivered to each tube was fixed at 30 W.

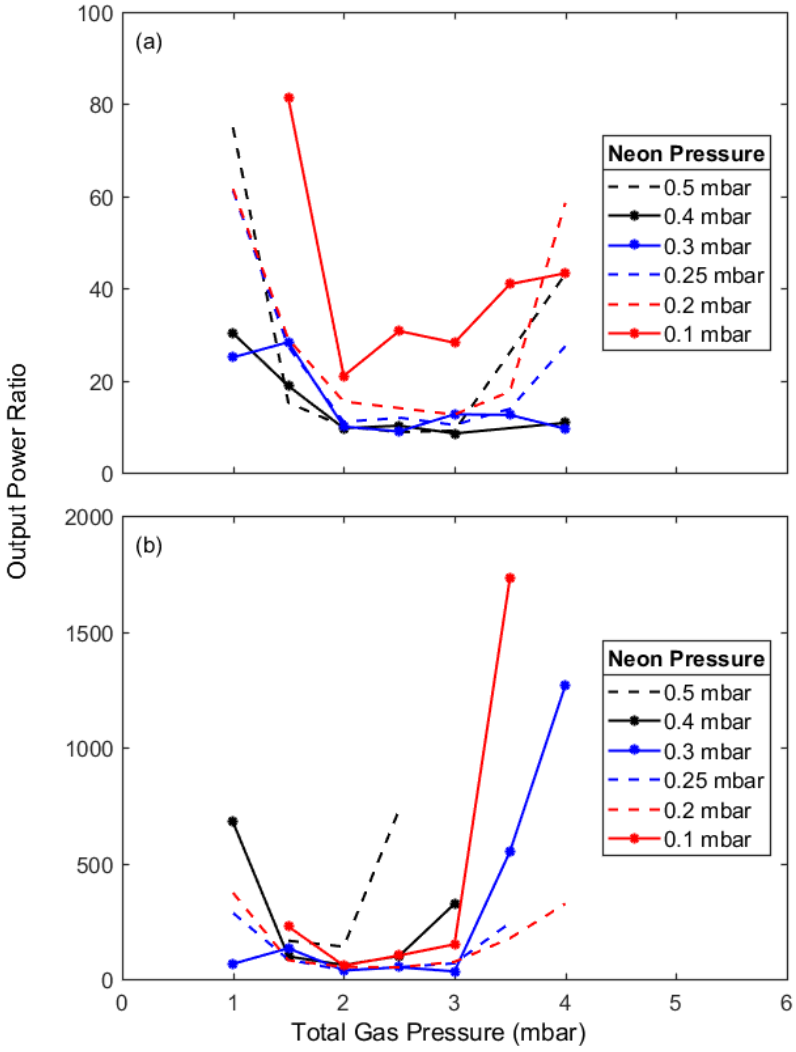

Figure 3.9: Laser output power ratios of (a) 611.8 to 604.6 nm and (b) 611.8 to 594.5 nm as a function of total gas pressures from 1 to 4 mbar, with natural neon partial pressures fixed between 0.1 and 0.5 mbar; a constant RF power of 30 W was applied to each discharge tube.

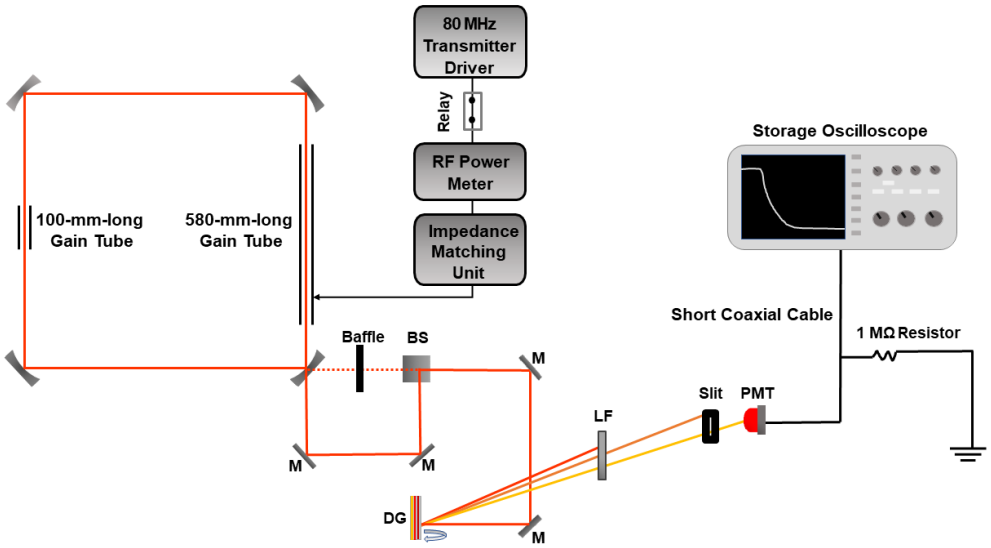

Figure 3.10: Experimental setup to measure the cold cavity ring-down, τ at the 611.8, 604.6 and 593.9 nm wavelengths via the CW beam transmitted from the lower left corner; the CCW beam was blocked by a baffle in front of the beam splitter. In the schematic, it has M: dielectric mirror; BS: beam splitter; DG: diffraction grating; LF: line filter; PMT: photomultiplier tube.

Q[7], total cavity loss[8], $L = (\tau \times \nu_{FSR})^{-1}$, and finesse[9], F = $\lambda Q/P$ at λ = 611.8 nm, 604.6 nm and 593.9 nm. For the 611.8 nm wavelength, a cold cavity ring-down time was measured at 38 μs, this yields a total cavity loss at 561 parts per million (ppm), a cavity Q at 1.2×10^{11} and finesse at 1.1×10^4. We note that the cavity finesse achieved at 611.8 nm was about 3.5 times lower than that at 632.8 nm (τ = 135 μs, L = 158 ppm, Q = 4×10^{11}, and F = 4×10^4) [13]. This is attributed to the relatively high mirror transmission loss. Normally the actual mirror losses are greater than the manufacturer's stated transmission losses since the scattering loss usually dominates. However, a measured loss per mirror at 140 ppm indicated that the mirror transmission loss at the 611.8 nm was lower than the specified value at 158 ppm. As for the 418 ppm of total loss measured at 604.6 nm (for τ = 51 μs), this translates to cavity Q of 1.6×10^{11} and finesse of 1.5×10^4. For the 593.9 nm transition, the measured ring-down time of 64 μs translates to a total loss at 333 ppm, a factor Q at 2.0×10^{11}, and a finesse at 1.9×10^4.

[7]The definition and calculation of cavity factor Q were introduced in Section 2.6.3.

[8]Total cavity loss (L) refers to the optical loss per round trip; it is also denoted as the optical loss coefficient δ as mentioned in Section 2.6.2.

[9]The finesse (F) of a resonator is defined as the free spectral range divided by the bandwidth of the resonance (cavity linewidth): $F = \nu_{FSR}/\Delta\nu_R$; the cavity linewidth, $\Delta\nu_R$, is equal to $1/2\pi\tau$ as introduced in Equation 2.63.

Wavelength, λ (nm)	611.8	604.6	593.9
Optical frequency, ν_0 (THz)	490	496	505
Ring-down time, τ (μs)	38	51	64
Total loss, L (ppm)	561	418	333
Quality factor, Q	1.2×10^{11}	1.6×10^{11}	2.0×10^{11}
Finesse, F	1.1×10^4	1.5×10^4	1.9×10^4

Table 3.3: Measured ring-down time and the derived total loss, quality factor Q, and finesse F achieved at λ = 611.8 nm, 604.6 nm and 593.9 nm.

3.2.3 Mode Configurations at the 611.8, 604.6 and 593.9 nm Wavelengths

611.8 nm

We examine the single-mode and phase-locked regimes for stable laser operation at 611.8 nm. The RF transmitter for the short gain tube was switched off for the following experiment and we only used the 580-mm-long gain tube for excitation of the three transitions as permitted by specific gas compositions. The amplitude servo system was set to the manual mode and we controlled the RF input power by turning the knob on the servo driver. The CCW laser beam was monitored with an FP interferometer (FSR = 300 MHz). The longitudinal mode structures obtained at various RF powers were monitored via an oscilloscope. Simultaneously, the CW beam output of each mode structure was measured by a power meter (refer to Figure 3.6). Examples of the 611.8 nm longitudinal mode output obtained using a cavity pressure of 3 mbar are shown in Figure 3.11. One can see that more longitudinal modes are present at increasing laser powers and mode-locked structures are obtained for a laser power region of 700 - 1100 nW. Noticeable imbalances of the laser intensities of the side-mode pairs are due to the asymmetric gain curve for natural neon. However, this intensity imbalance will be reduced with laser operation using 50:50 neon.

Figure 3.12 (a) and (b) compare the measured laser output power as a function of total gas pressures for different neon isotopic mixtures: 50:50 neon and natural neon, at a fixed neon partial pressure of 0.3 mbar. The grey-shaded area, labelled as (i) in the figure is indicating the laser is operating on a single-mode structure, the 'hatched' area indicates the laser is running in the 'stable' multi-mode (phase-locked) regime, and the area labelled as (iii) is where the laser is running in chaotic multimode (no stable δf_s observed in this operating regime). As seen from the figure, the power region to operate the laser on a single-mode configuration increases as the total gas pressure increases. Therefore, the phase-locked threshold rises as the pressure-dependent homogeneous broadening increases as well.

604.6 nm and 593.9 nm

By a careful attenuation of the RF excitation power, we managed to control and maintain lasing at the 604.6 and 593.9 nm wavelengths on the edge of the lasing thresholds. We found

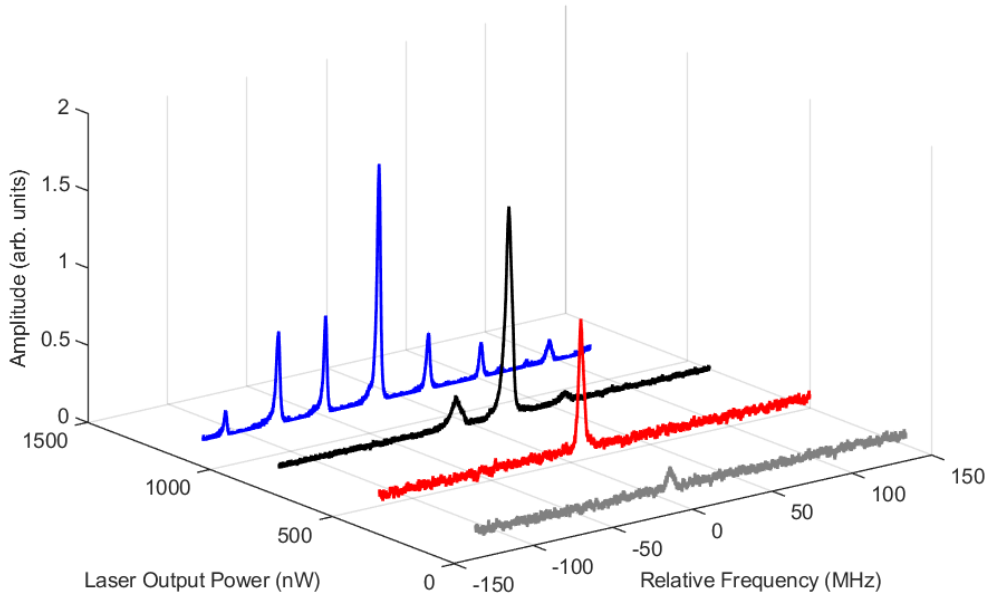

Figure 3.11: Evolution of the 611.8 nm longitudinal mode structure when the laser output power is increased from 0 to 1500 nW; the laser was operating with a cavity pressure at 3 mbar with a natural neon partial pressure at 0.3 mbar.

that the regimes of single-mode, phase-locked and chaotic multi-mode were indistinguishable for both wavelengths. The 604.6 and 593.9 nm transitions either did not lase or lased with multiple modes with the intensity and relative phase of the oscillating modes time varying (shown in Figure 3.13). Regardless of the gas compositions, lasing at these two wavelengths was normally with a minimum of 7 modes with one centre mode and three pairs of side-modes located at 1, 2, 3 FSR away. As confirmed by an RF spectrum analyser, the 604.6 nm and 593.9 nm wavelengths generated at least 3 FSR beat frequencies when they were operated just beyond the lasing thresholds. This implies that no stable gyroscopic performance can be acquired by operation on the 604.6 nm and 593.9 nm transitions, due to the gain competition, as the 611.8 nm transition always dominates. However, earlier work using a linear cavity has demonstrated the simultaneous operation of these transitions with good frequency stability [104]; thus, there is every reason to believe that these results can be improved using appropriately optimised mirrors and neon isotopic composition. If the employed cavity mirrors were able to control the loss (lasing threshold) of all neon transitions by providing an unequal mirror loss for each output-wavelength (with much higher transmission loss at 611.8 nm and much lower transmission losses at 604.6 nm and 593.9 nm), the overall gain competition will be reduced to the greatest extent. In that case, we might have a chance to operate the gyro at 604.6 nm and 593.9 nm for stable rotation sensing.

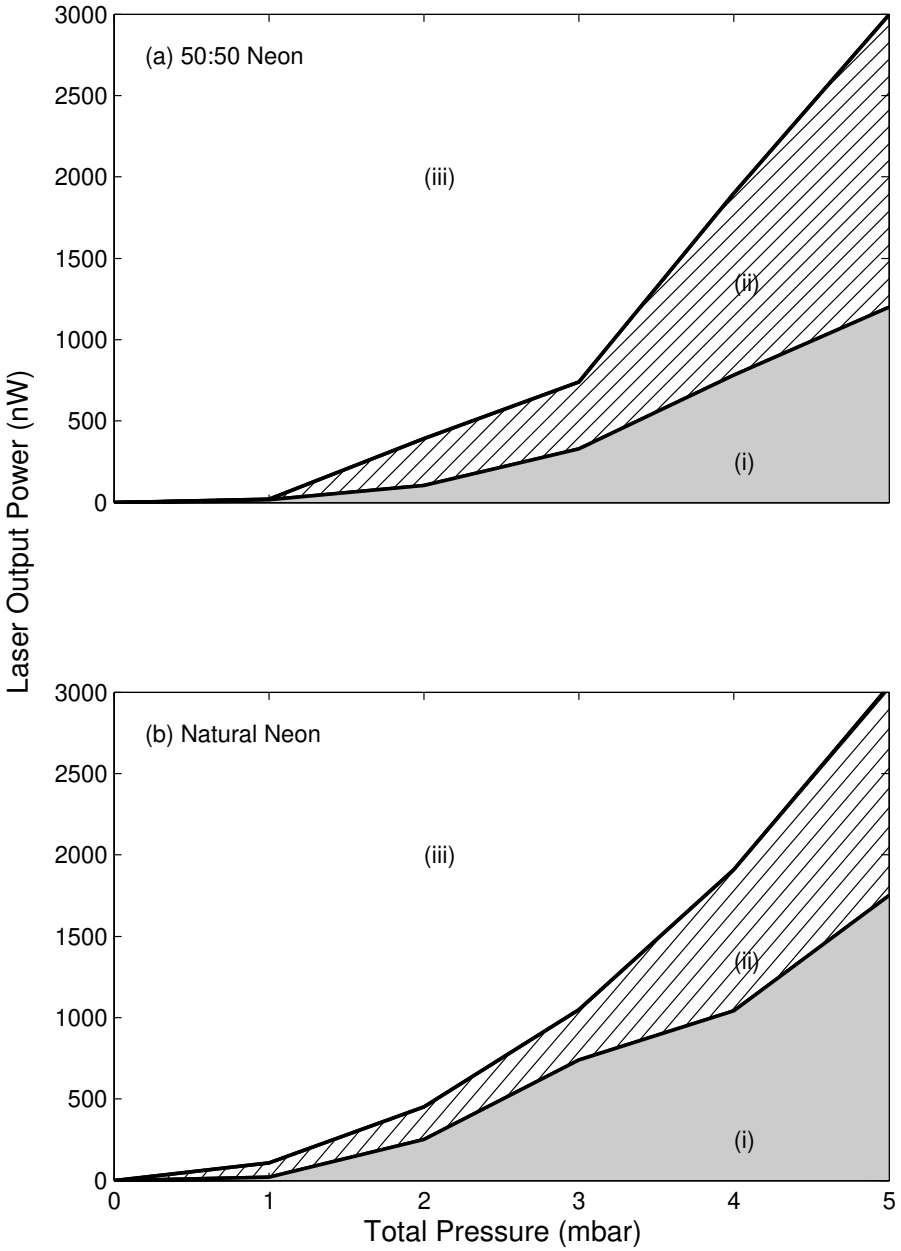

Figure 3.12: Laser output power as a function of total gas pressure for a fixed neon partial pressure of (a) 50:50 neon and (b) natural neon at 0.3 mbar where (i) indicates an area of guaranteed single-mode operation; (ii) indicates where the laser is running in a phase-coupled, multimode regime; and (iii) is a region where the chaotic multimode operation is observed.

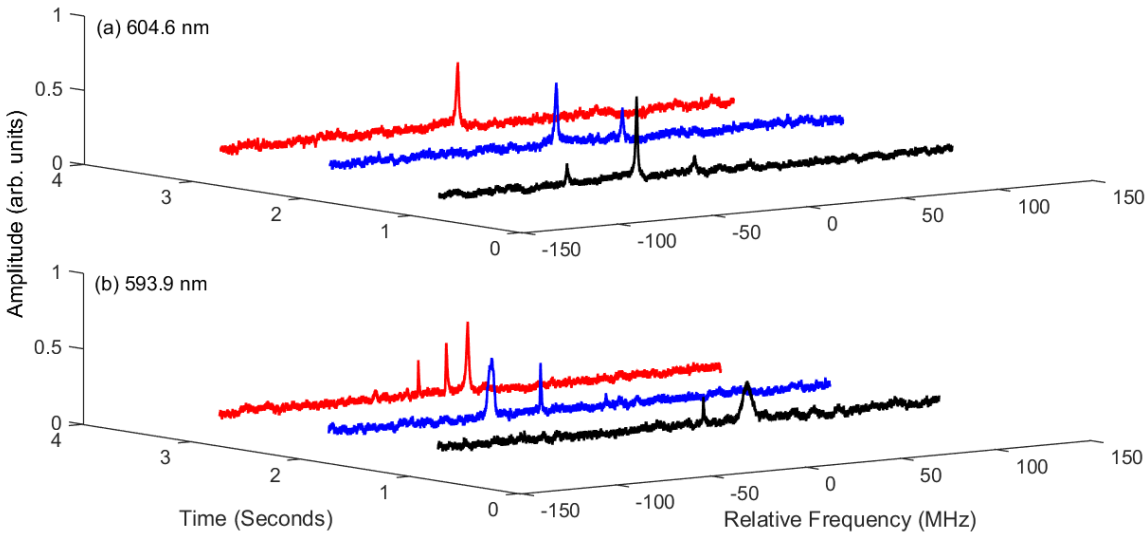

Figure 3.13: Mode structures scanned at (a) 604.6 nm and (b) 593.9 nm when their output powers were attenuated to be 0 - 300 nW higher than the lasing thresholds; the cavity pressure was at 3 mbar with natural neon partial pressure at 0.3 mbar. The mode structure was scanned several times at a rate of once per second.

3.2.4 Gyroscopic Operation on Three Different Neon Transitions

As mentioned previously, the expected Sagnac frequency for 611.8 nm operation is 117.27 Hz and for 604.6 nm and 593.9 nm operation is 118.67 Hz and 120.81 Hz, respectively. When PR-1 was operating separately at the 611.8, 604.6 and 593.9 nm wavelengths with the laser power slightly beyond the lasing threshold, the oscilloscope traces of the combined counter-propagating beams at the lower right corner of the PR-1 ring cavity (see Figure 3.6) observed at 611.8 nm, 604.6 nm, and 593.9 nm are shown in Figure 3.14 (a) to (c). The corresponding FFT power spectra observed via an FFT spectrum analyser (Model SR770) are depicted in Figure 3.15 (a) to (c). Figure 3.14 and 3.15 demonstrate that the ring laser readily unlocked on the bias provided by Earth's rotation at all of the three laser wavelengths.

Despite a high cavity loss at 611.8 nm, laser operation at this wavelength can monitor the Earth rotation rate yielding a stable, clear, and strong interferogram attributed to the availability of stable single-mode output. This was evidenced by a high Sagnac contrast ratio[10] of about 60% from the combined beams as shown in Figure 3.14 (a). As seen from Figure 3.15 (a), the Sagnac frequency obtained at 611.8 nm is centred at 117.4 Hz and accompanied by two side-bands located 2 to 3 Hz away from the centre frequency. These side-bands were generated from the natural oscillation of the West building. A 130 mHz offset between the

[10]The Sagnac contrast is defined by the ratio of the peak to peak AC amplitude to the DC amplitude measured from the combined CW and CCW beams.

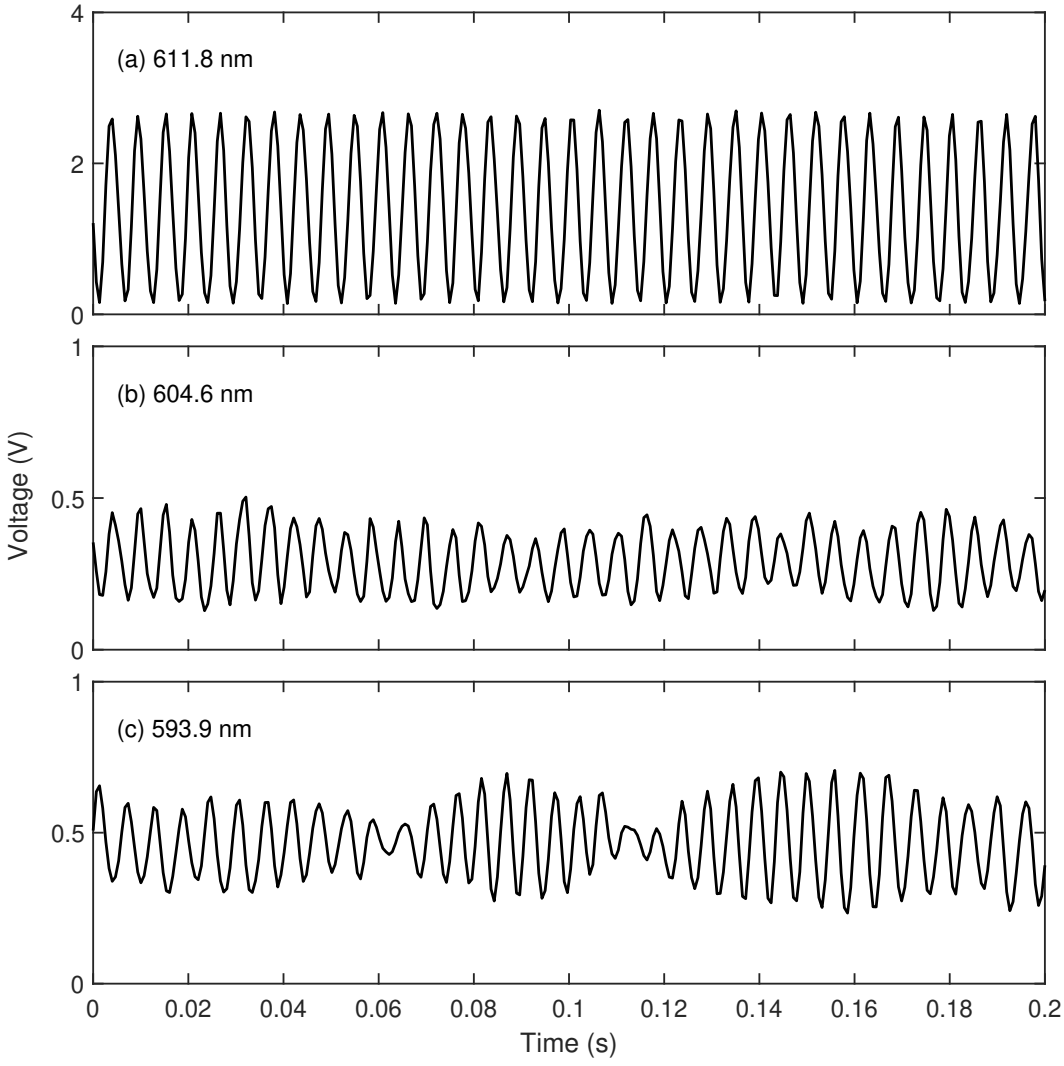

Figure 3.14: Sagnac waveforms for rotation sensing at (a) 611.8 nm, (b) 604.6 nm, and (c) 593.9 nm.

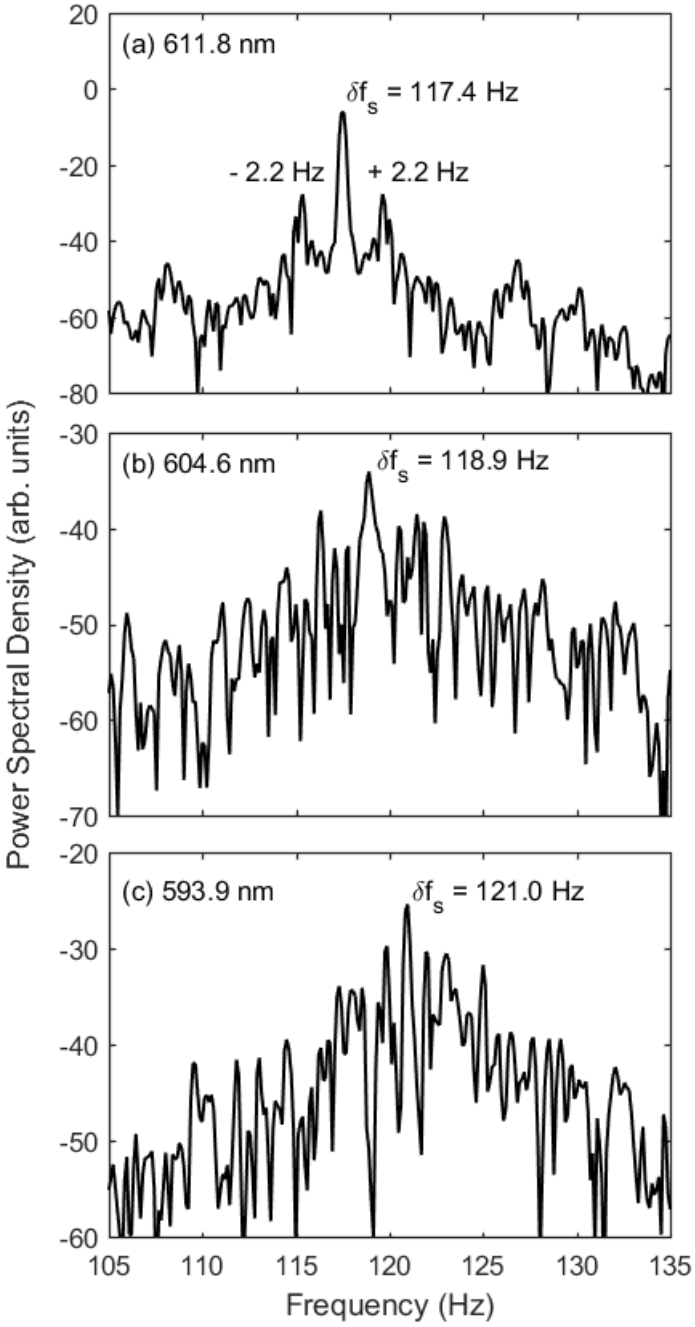

Figure 3.15: Typical power spectra obtained for operation at (a) 611.8 nm, (b) 604.6 nm, and (c) 593.9 nm; the vertical scale is expressed in decibels. In (a), the Earth line appears at 117.4 Hz with two sidebands due to mechanical building motion.

nominal and experimentally-obtained Sagnac frequency can be induced from the frequency pulling and pushing effect due to dispersion and backscatter-coupling, or from the minor uncertainties of the scale factor or cavity orientation [80].

As shown in Figure 3.14 (b) and (c), at 604.6 nm and 593.3 nm the laser was able to unlock on Earth rotation with clear δf_s interferogram. The AC amplitudes of the Sagnac waveform varied over time due to the inconsistent mode structures of the two beams (see Figure 3.13). Therefore, Figure 3.15 (b) and (c) shows the averaged power spectra of the Sagnac beat signal as contributed by various longitudinal modes (or says multiple frequency components), with the frequency maximum drifting in the vicinity of 118.9 and 121.0 Hz.

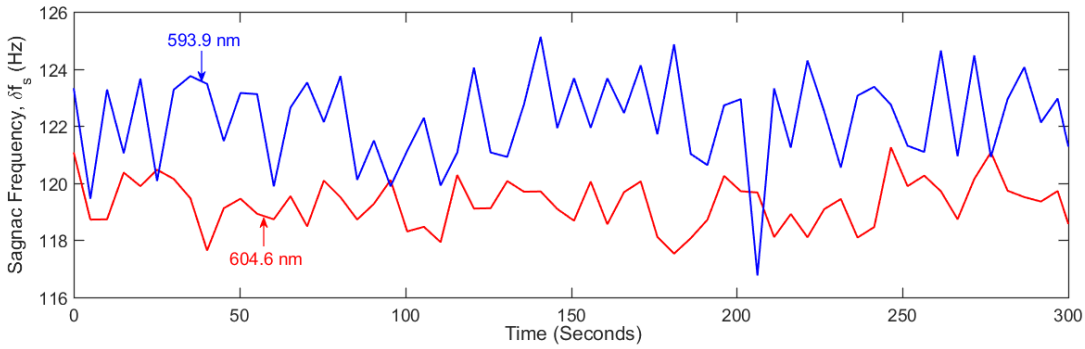

Figure 3.16: Sagnac time series in 300 s time-scale for demonstrating the laser performance from dual-wavelength operation (604.6 and 593.9 nm); PR-1 was operating with a cavity pressure of 3 mbar (with 0.2 mbar of natural neon partial pressure). The frequency write-out was 5 sec/data.

It is notable that for operation at a cavity pressure of 3 mbar, the 604.6 nm and 593.9 nm wavelengths can be tuned to yield similar laser powers. Dual-wavelength operation is shown in Figure 3.16. At the same time, the 611.8 nm wavelength was completely unstable as many modes occurred within the gain curve. Figure 3.16 shows that the 604.6 nm and 593.9 nm wavelengths yielded Sagnac frequencies of around 119 Hz and 122 Hz, with their overall frequency excursions at 4 and 6 Hz, respectively. The averaged Sagnac contrast ratios given by the 604.6 and 593.9 nm transitions were 27% and 18%, respectively. These reductions in the Sagnac contrasts (compared to a contrast ratio of 60% for the 611.8 nm output) were due to free-running multi-mode operation.

3.2.5 Gyroscopic Performance for Operation at 611.8 nm

Figure 3.17 (a) shows a representative Sagnac frequency as logged for 5000 s with the sample write-out at 5 seconds/data (0.2 Hz) for laser operation at 611.8 nm. For this purpose, we have used a gas fill of 0.3 mbar 50:50 neon partial pressure at a total pressure of 5 mbar.

Note that PR-1 was solely operating on the 611.8 nm wavelength with the single longitudinal mode structure, at an output power of 300 nW. Neither the 604.6 nm nor the 593.9 nm transitions had enough gain to oscillate under this condition. Figure 3.17 (b) and (c) present the dynamics of the Sagnac contrast ratio measured from the combined beams and the monobeam modulations (m_1, m_2) derived from the two counter-travelling beams. As shown in Figure 3.17 (a), the occurrence of mode-hops influence the frequency measurement by introducing sudden step-ups or step-downs in the Sagnac frequency by 0.1 - 1.0 Hz. Similarly, mode-hops also led to discontinuities in the Sagnac contrast and intensity modulations. Mode splitting also occurred once during the observation period. As the two longitudinal modes of the two counter-propagating beams settled down at different mode indexes, the optical beat completely disappeared as the two operating frequencies were too far apart and the Sagnac contrast ratio (also monobeam modulations) dropped to 0%.

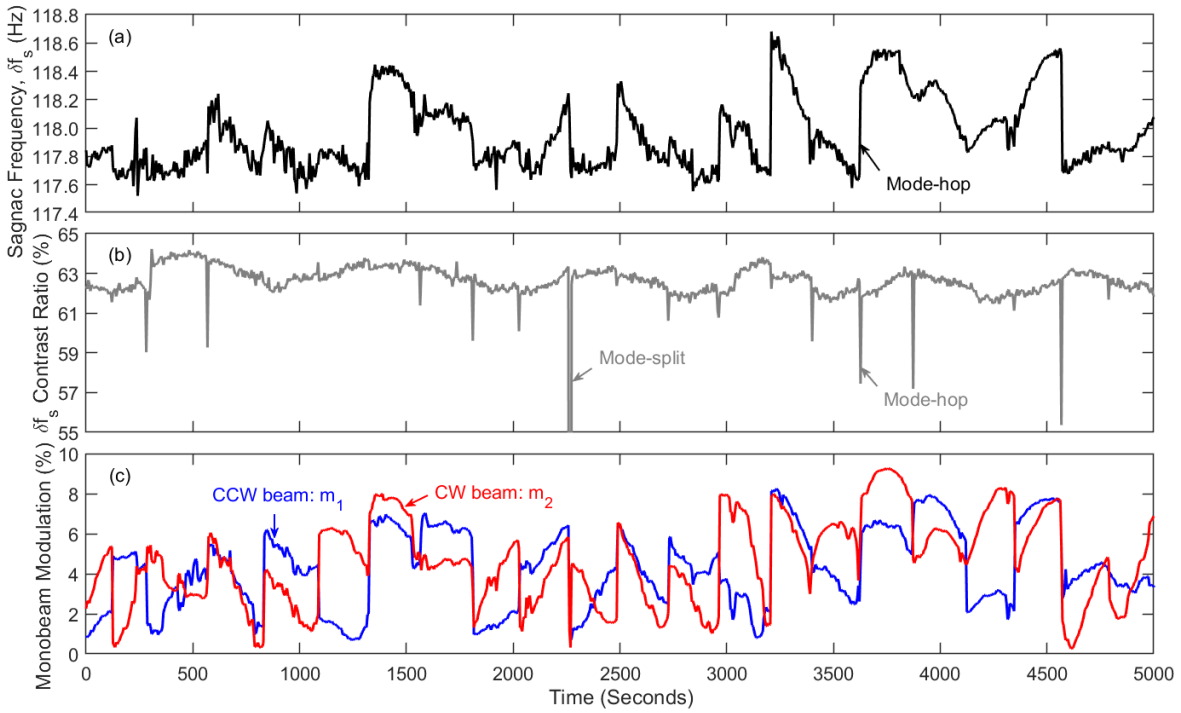

Figure 3.17: Typical long-term Sagnac signal detected for over 5000 s, where the logged time series of (a) shows the Sagnac frequency (black trace); (b) shows the δf_s contrast ratio (grey trace); (c) shows the monobeam modulations (m_1, m_2) for the CCW (blue trace) and CW (red trace) beams over time. The laser output power was maintained at 300 nW by an amplitude servo system. All sample write-out is presented in 5 seconds/data (0.2 Hz). The laser was operating at a total pressure of 5 mbar with 50:50 neon partial pressure at 0.3 mbar.

Figure 3.17 (a) shows that the Sagnac frequency is pushed and pulled by backscatter-coupling over time. The magnitudes of backscatter effects for both beams were reasonably

high and monobeam modulations measured from two directions were varied in a similar range up to 9%. This introduces significant frequency pushing and pulling effects on the two operating modes and leads to large Sagnac frequency excursions over 1.2 Hz (in a wide range of 117.5 - 118.7 Hz). It is noticeable that the gyro readout bias is proportional to the backscatter level. Sagnac frequency excursions in the time-periods of 1300 - 1800 s and 3600 - 4600 s were the largest, as the detected monobeam modulations were the highest throughout the range. Furthermore, the operating mode jumped every 200 to 300 seconds as revealed by instant changes in the contrast ratio by 0.5 - 7.0% and monobeam modulations by 1 - 7%. Frequent mode-hops were prominent for PR-1 laser operation as the cavity was subject to geometric expansion and compression due to the variation of wall temperature.

We further note that the long plasma discharge was stabilised by 8 low-field permanent magnets deployed along the 580-mm-long gain tube. It is noticed that the efficiency of power transfer from the RF source to the plasma is increased under such an arrangement. This is because that the collision probability between electrons and atoms is greatly increased due to the lengthened trajectories of the electrons [105]. As such, a higher atomic excitation rate was generated. Other than that, the implementation of magnets was crucial as it prevented the long plasma from pulsing and flickering. A static magnetic field is able to increase the discharge stability by introducing better homogeneity of the plasma as it confines the diffusion of the electrons in the plane that is perpendicular to the magnetic field [106]. The impacts of magnetic fields on the gyroscopic performance remain to be fully explored.

Figure 3.18 (a) and (b) shows the logged δf_s time series yielded from 611.8 nm operation with gas fills of 0.2 mbar natural neon partial pressure at a total pressure of 3 mbar, and 0.2 mbar 50:50 neon partial pressure at a total pressure of 4 mbar, respectively. The short-term Sagnac signals presented in Figure 3.18 were obtained between two mode-hops without split modes occurring during the measurement periods. The noise-limited Sagnac frequency excursions in Figure 3.18 (a) are 150 to 250 mHz while in Figure 3.18 (b) they are an average of 300 mHz. It was observed that the frequency pushing and pulling effect induced by natural neon operation was much more obvious than that observed for 50:50 neon operation. As a 90:10 mixture of the ^{20}Ne and ^{22}Ne isotopes gives rise to an unsymmetrical gain curve, gain competition between the bidirectional-travelling beams is more prominent. Therefore, the associated mode pushing and pulling phenomena is much more evident. The induced gyro bias errors are notably larger than those obtained from 50:50 neon operation. One can see from Figure 3.18 that the time interval between two mode-hops are much larger when compared to those seen in Figure 3.17 since no mode-hop occurred within the 1800 and 2500 s time-periods. This is because the data in Figure 3.18 was obtained between 1 to 4 a.m.

Figure 3.19 shows Allan deviation (ADEV) plots normalized to the Earth rotation rate (Ω_E). The ADEV plots compare the laser stability logged over 1500 - 3000 s, which were obtained from single-mode operation with four different gas-fills. Note that the ADEV trends for two gas fills of 0.2 mbar natural neon partial pressure with a total pressure of 3 mbar, and 0.2 mbar

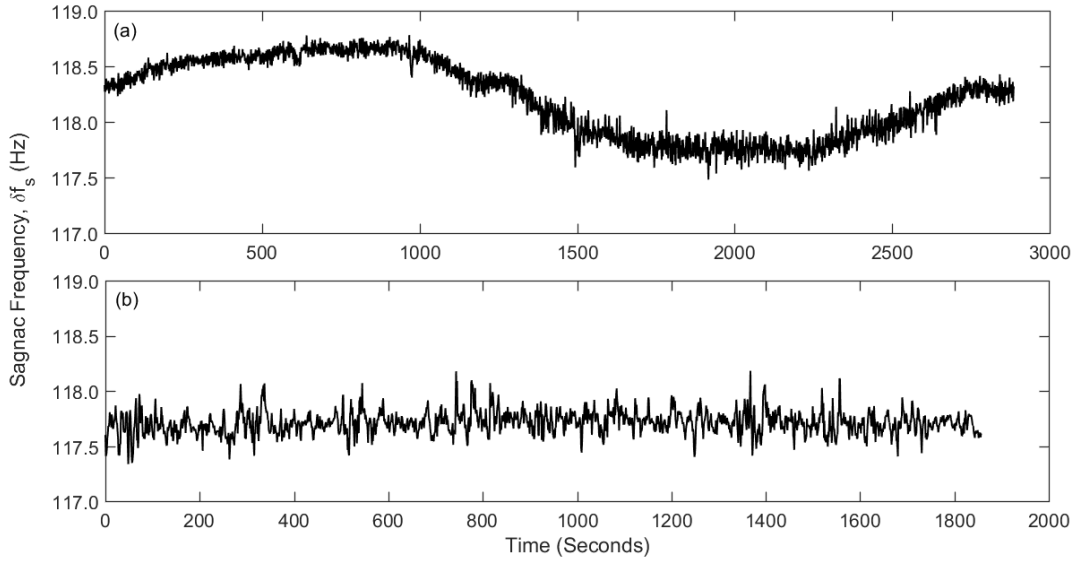

Figure 3.18: Sagnac frequency signal logged over 1800 s (without mode-hops or mode splitting) for the operation with gas fills with (a) 0.2 mbar natural neon partial pressure with a total pressure of 3 mbar; (b) 0.2 mbar 50:50 neon partial pressure with a total pressure of 4 mbar. The frequency write-out was set to be once per second (1 Hz).

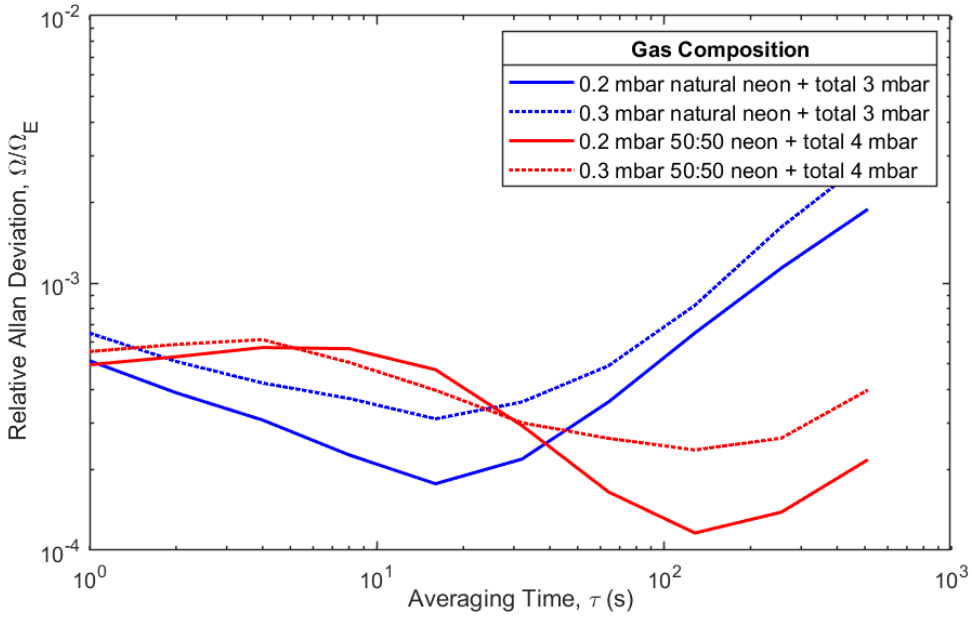

Figure 3.19: Comparison of the relative Allan deviations for 611.8 nm single-mode operation on 4 different gas mixtures. The laser output power is fixed at 500 nW.

50:50 neon partial pressure with a total pressure of 4 mbar, are plotted with the Sagnac time series presented in Figure 3.18 (a) and (b). Figure 3.19 shows that operation on the 611.8 nm transition can achieve the highest rotational resolution of $1.2\times\ 10^{-4}\ \Omega_E$ (8.8 nrad/s) at a measurement time τ of 128 s using single-mode operation at 4 mbar of gas pressure with 0.2 mbar of 50:50 partial pressure. For this gas fill, the laser was operating with a stabilised output power of 500 nW, and intensity modulations of the two beams fell into a range of 0.6 to 1.5%. The backscatter-induced frequency errors were roughly estimated at around 5 mHz by using $\delta f_{bs} \approx \frac{1}{2}\delta f_s m_1 m_2$ (a simplified form of Equation 2.81). Using Equation 2.85, the quantum-limited laser sensitivity was calculated at 1.11×10^{-10} rad/s/$\sqrt{\text{Hz}}$ with an observation time of 128 s, and the raw sensitivity was 1.26×10^{-9} rad/s/$\sqrt{\text{Hz}}$ as calculated by 1 s of integration time. Note that the rotational resolution achieved for 632.8 nm PR-1 operation was slightly better, at $9 \times 10^{-5}\Omega_E$ (6.6 nrad/s) [13]. However, it still suggests that the ring laser operated well as a gyroscope at 611.8 nm. Although the cavity factor Q at 611.8 nm was relatively low (due to the high mirror transmission loss), this setback was compensated for by a higher operable power in comparison to that of the 632.8 nm single-mode operation (below 200 nW).

3.2.6 Conclusion

In summary, we have demonstrated the initial gyroscopic operation of a large multi-wavelength ring laser operating on the 611.8 nm, 604.6 nm, and 593.9 nm neon transitions. The optimum cavity pressure for rotation sensing at 611.8 nm was 4 mbar with 0.2 mbar 50:50 neon partial pressure. Operation at 611.8 nm achieved stable laser performance and the ability to unlock on Earth rotation with a Sagnac beat frequency of 117.4 Hz. The ion beam sputtered supermirrors equipped for multi-wavelength operation yielded a cavity factor Q of 1.2×10^{11} for 611.8 nm, 1.6×10^{11} for 604.6 nm, and 2.0×10^{11} for the 593.9 nm transition. The high transmission loss at 611.8 nm enabled the laser to operate with a high output power of 500 nW. The sensor performance was comparable to that obtained from 632.8 nm, giving the highest rotational resolution at 8.8 nrad/s with an averaging time at 128 s. There were no stable mode structures available using 604.6 and 593.9 nm transitions due to gain competition. Stable rotational sensing via these two transitions could be achievable if the employed resonant mirrors provide lower transmission losses at the 604.6 and 593.9 nm wavelengths while allowing higher transmission loss at 611.8 nm.

3.3 Near-Infrared Operation with Commercially-Sourced Mirrors

As mentioned earlier, the first He-Ne ring laser gyro developed by Macek and Davis [3] was operated using the 1.15 μm neon transition. However, it failed to detect the subtle Earth rotation background due to the mirror quality available. PR-1 has previously demonstrated the capability of unlocking on the bias provided by Earth rotation, using operation at the 1152.27 nm wavelength (the $2s_2 \rightarrow 2p_4$ neon transition) via using four custom-designed crystalline-coated[11] supermirrors [103]. We revisited the near-infrared operation using four commercially sourced, standard laser mirrors of high transmission loss. This type of unexplored cost-saving[12] Bragg stack mirrors with their surfaces and substrates commercially polished are more likely to introduce a severe backscatter effect which makes unlocking on Earth rotation impossible. This opportunistic experiment was performed to see whether commercially sourced mirrors can be used to detect Earth rotation at all. Visual comparisons between the custom-designed crystalline-coated and commercially-sourced standard infrared mirrors are demonstrated in Figure 3.20 (a) and (b).

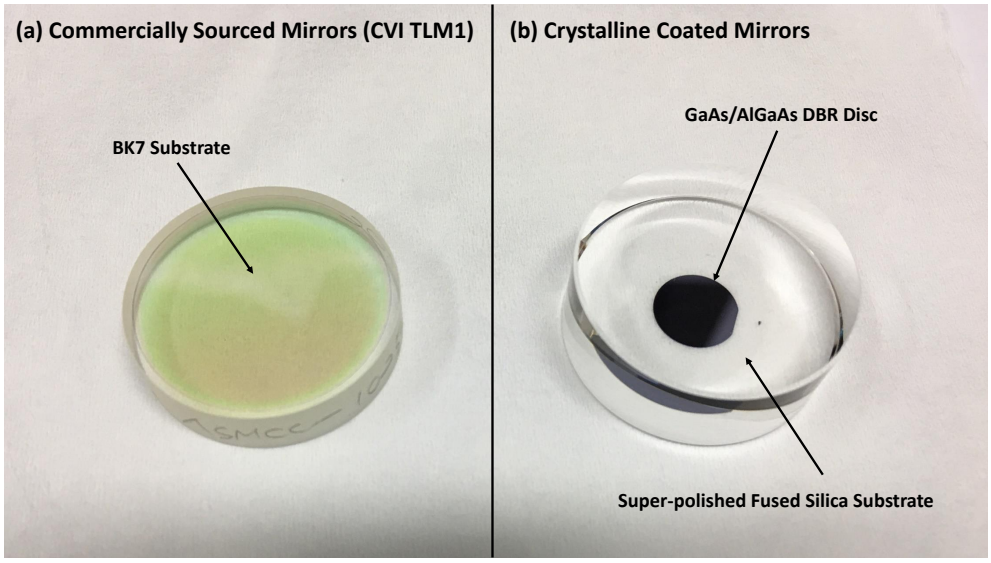

Figure 3.20: Comparison between (a) a commercially-sourced mirror having a BK7 substrate and (b) a crystalline-coated mirror comprising an 8 mm diameter GaAs/AlGaAs mirror pad and super-polished fused silica substrate.

The commercial mirrors (CVI TLM1) have an N-BK7 substrate and a radius of curvature at 1.5 m (details in Table 3.4). The transmission of N-BK7 at the 1.15 μm operating wavelength was not specified by the manufacturer (CVI Laser Optics). However, we estimate it at

[11] Second-generation crystalline-coated mirrors can potentially take thermal noise out of the measurement frequencies [102, 107].

[12] The commercially sourced standard mirrors (500 US dollars for four pieces) are about 40 times cheaper than customised crystallised-coated supermirrors (20,000 Euros for four pieces).

about 0.92 near 1.15 μm according to the optical transmission calculator and parameters published by Schott Glass (sample thickness of 6.35 mm, calculation method: including multiple reflections).

Parameter	Value
Diameter (mm)	25.4
Radius of curvature (m)	1.5
Substrate material	N-BK7
Angle of incidence	45°
Reflectance	R≥98.5 at 45°, P-Pol
Center wavelength (nm)	1030
Mirror bandwidth (nm)	74

Table 3.4: Specifications for the commercially-sourced mirrors used in the near-infrared operation.

3.3.1 Experimental Set-Up

The experimental set-up for PR-1 operation at a near-infrared wavelength is given in Figure 3.21. Initially, we utilised two gain tubes (100 and 580 mm long) to provide maximum laser power for cavity alignment purposes. The gain media in both tubes were excited by an 80 MHz radio frequency transmitter. Only one short gain tube was used to provide laser gain during gyroscopic operation. Considering that the laser beams were invisible, we used a silicon-based CCD camera (Pacom) and a NIR detector card (ThorLabs, VRC5) to observe the lasing phenomenon. In the lower right corner, a 50:50 beam splitter was used to combine the clockwise and counterclockwise beams. The combined beams were detected by a thermo-electrically cooled InGaAs photodetector (PD 1, Hamamatsu G6126) and its voltage output was fed into an oscilloscope and an FFT spectrum analyser for the detection of optical beats. Besides, the externally-overlapped laser beam was also fed into a CCD camera. The clockwise beam transmitted from the top right corner was detected by an IR photodiode, PD 2 (10 MHz New Focus Adjustable InGaAs Photoreceiver), and connected to a LabVIEW data acquisition system for data logging and an amplitude servo system for providing a feedback signal for the intensity control. In the lower-left corner, an infrared power meter (Coherent, OP-2-IR) was assembled for the beam power measurement.

In this experiment, an RF spectrum analyser was used (instead of a Fabry-Perot scanning system[13]) to identify the single-mode, phase-locked, and unstable free-running multi-mode regimes. As shown in Figure 3.21, the counterclockwise beam transmitted from the top right corner was detected by a New Focus 125 MHz InGaAs photoreceiver (PD 3). The AC signal of

[13]This is because an infrared PMT having a high responsivity at 1.15 μm for our Fabry-Perot scanning system (Thorlabs SA200-8B, FSR = 1.5 GHz) was unavailable throughout our experiment period.

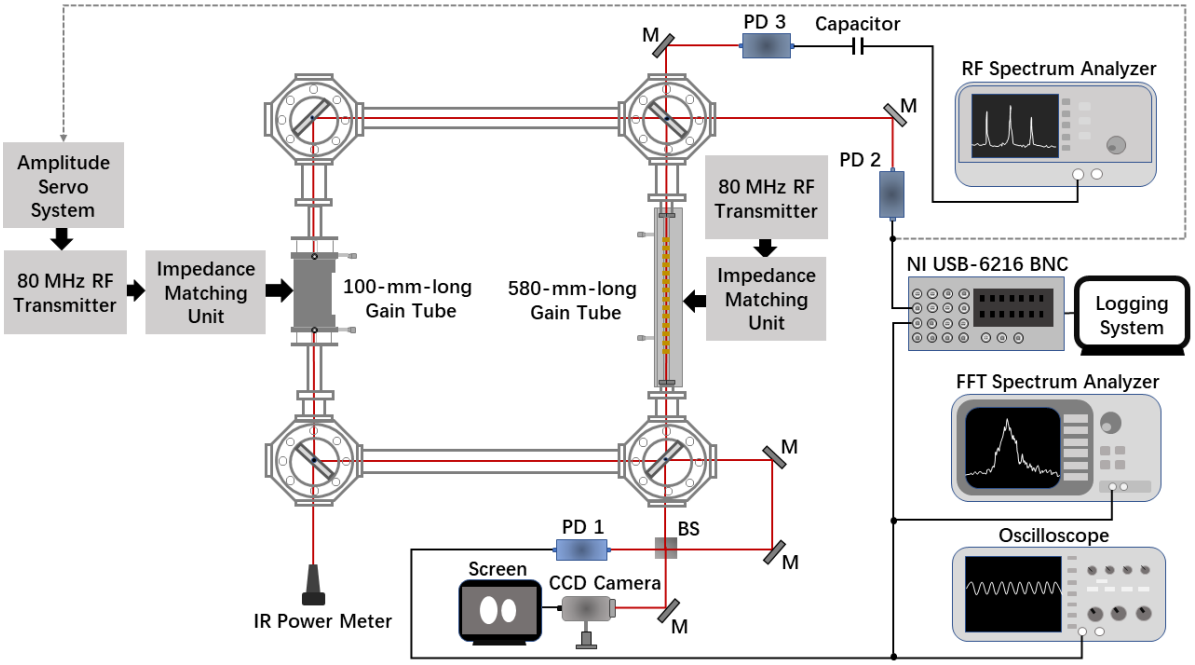

Figure 3.21: Experimental set-up and data acquisition for PR-1 operation in the near-infrared region; in this simplified schematic, the following labelling scheme applies where M: broadband dielectric mirrors with a 99.5% reflectance at 1.15 μm (Thorlabs BB1-EO3); PD 1: thermo-electrically cooled type infrared photodetector; PD 2: 10 MHz Adjustable InGaAs Photodetector; PD 3: 125 MHz InGaAs Photodetector.

the photoreceiver output was extracted by a capacitor and fed into the RF spectrum analyser for monitoring the FSR beat among different longitudinal modes. When no FSR beat signal occurs, it indicates that PR-1 yields a single-mode output, while the presence of a beat signal indicates a multi-mode laser output. A stable phase-locked mode configuration is obtained when the RF spectrum analyser detects an FSR beat signal and the oscilloscope shows a clear and well-defined Sagnac waveform signal, and the FFT spectrum analyser shows an unperturbed FFT spectrum.

3.3.2 Oscillator Parameters Determined Using the Commercially-Sourced Mirrors

The cavity was filled with 1 mbar of total pressure with 0.2 mbar of natural neon partial pressure. After optimising the cavity alignment, the ring-down was measured to determine the optical loss. The measured ring-down time (τ) was 30 μs, and this translates into a Q of 4.9×10^{10}, a finesse of 8835, and a total cavity loss of 712 ppm (see Table 3.5). We note that the short ring-down time can be introduced by not only the mirror quality but also the

assembly of the long gain tube[14].

Parameter	Value
Ring-down time, τ (μs)	30
Total loss, L (ppm)	712
Quality factor, Q	4.9×10^{10}
Finesse, F	8835

Table 3.5: The cavity ring-down time τ, total loss, quality factor Q, and finesse determined from the infrared PR-1 oscillator configured from four commercially-sourced mirrors.

3.3.3 Gas Pressure Optimisation and Laser Efficiency Measurement

As the 100-mm gain tube can provide adequate gain for the 1.15 μm transition, the long gain tube was not used for the following experiments. 1.15 μm lasing can be obtained without any helium gas. In this case, the neon doublet split by 51 GHz - both the $2s_2 \rightarrow 2p_4$ and $2s_4 \rightarrow 2p_7$ neon transitions with respective wavelengths of 1152.27 nm and 1152.50 nm (see Figure 2.2) will oscillate simultaneously. Figure 3.22 shows the laser output power as a function of natural neon pressure in the absence of helium. It is noticeable that near-infrared lasing is only achieved with pure neon at a pressure between 0.1 and 0.6 mbar, with the highest output power of 7 μW obtained at 0.2 mbar.

A sufficient amount of helium was added to eliminate the gain competition between two neon transitions and secure a lasing on the $2s_2 \rightarrow 2p_4$ transition (1152.27 nm). The helium atoms assist in terminating the $2s_4 \rightarrow 2p_7$ transition via an elevation of the atomic population at the $2p_7$ level. According to [108], the 1152.50 nm neon transition is quenched when the helium concentration surpasses 0.0665 mbar. To investigate the laser gain for various gas-mixtures, we filled the cavity with a natural neon partial pressure fixed between 0.2 to 0.4 mbar before adding helium gas to vary a total gas pressure within 2 to 12 mbar. Unlike other neon transitions in the visible region offering a variable laser gain for different gas-mix ratios, the infrared laser gain did not show much pressure-dependence as shown in Figure 3.23. Laser output powers obtained from a natural neon partial pressure of 0.4 mbar seemed higher than those from a neon pressure lower than 0.4 mbar. The highest power measured was at 23.4 μW, obtained from 6 mbar of cavity pressure.

We investigated the laser input-and-output efficiencies for various gas compositions before implementing the amplitude servo system. The laser efficiency is defined as $\eta = \Delta P_{out}/\Delta P_{in}$, where ΔP_{out} is the increment of the measured laser output power and ΔP_{in} is the increment

[14]The 580 mm discharge tube (with a 4 mm diameter) in the 1.6 m cavity sidearm is likely to introduce considerable diffraction loss.

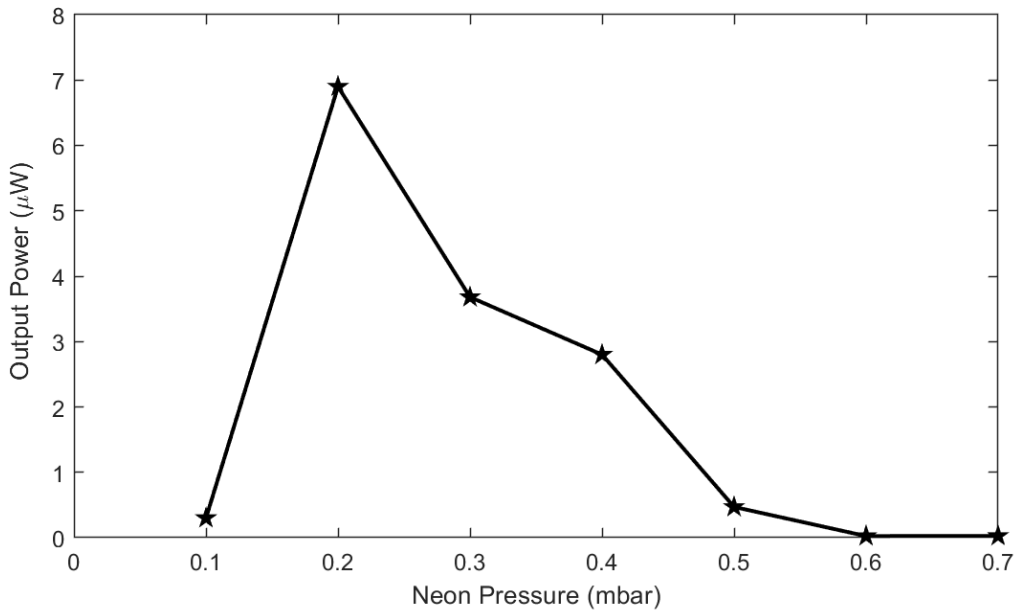

Figure 3.22: Laser output power as a function of natural neon pressure for a constant RF input power at 30 W.

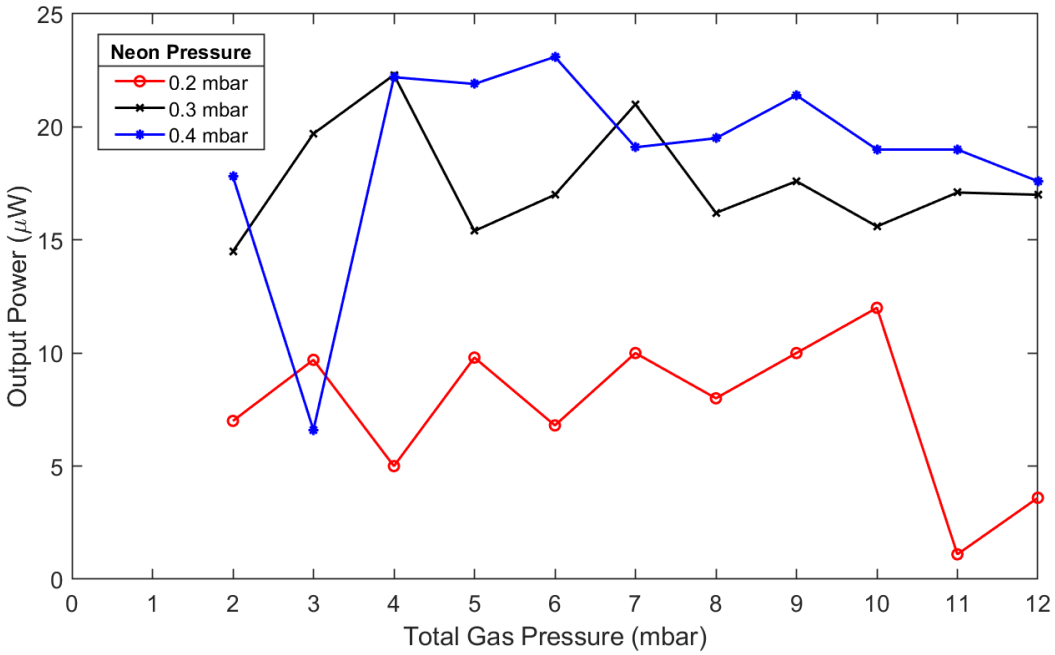

Figure 3.23: Laser output power as a function of total gas pressure; the RF input powers were fixed at 30 W; the natural neon partial pressure was fixed between 0.2 and 0.4 mbar.

of RF input power. There exists a possibility that the servo has two different slopes (both positive and negative) near the peak of the gain curve. If the RF power was set to maintain a laser power close to the centre of the gain curve, the servo control system becomes ineffective as it fluctuates between positive and negative feedback. Therefore, it is of great importance to explore the laser output power as a function of RF input power for different gas mixtures to guarantee effective servo control.

The laser efficiency was characterised for a pressure region between 2 mbar and 12 mbar, with the natural neon partial pressure fixed at 0.3 and 0.4 mbar. As shown in Figure 3.24, the RF excitation power and laser output power did not follow a linear relationship. The laser efficiency seemed to be relatively high using a total gas pressure below 6 mbar, while the input-and-output efficiency trend became less obvious for an operating pressure beyond 6 mbar. It is noticeable that the slope of laser efficiency always remained positive for the whole excitation region. As a consequence, the functionality and efficiency of the amplitude servo system was guaranteed.

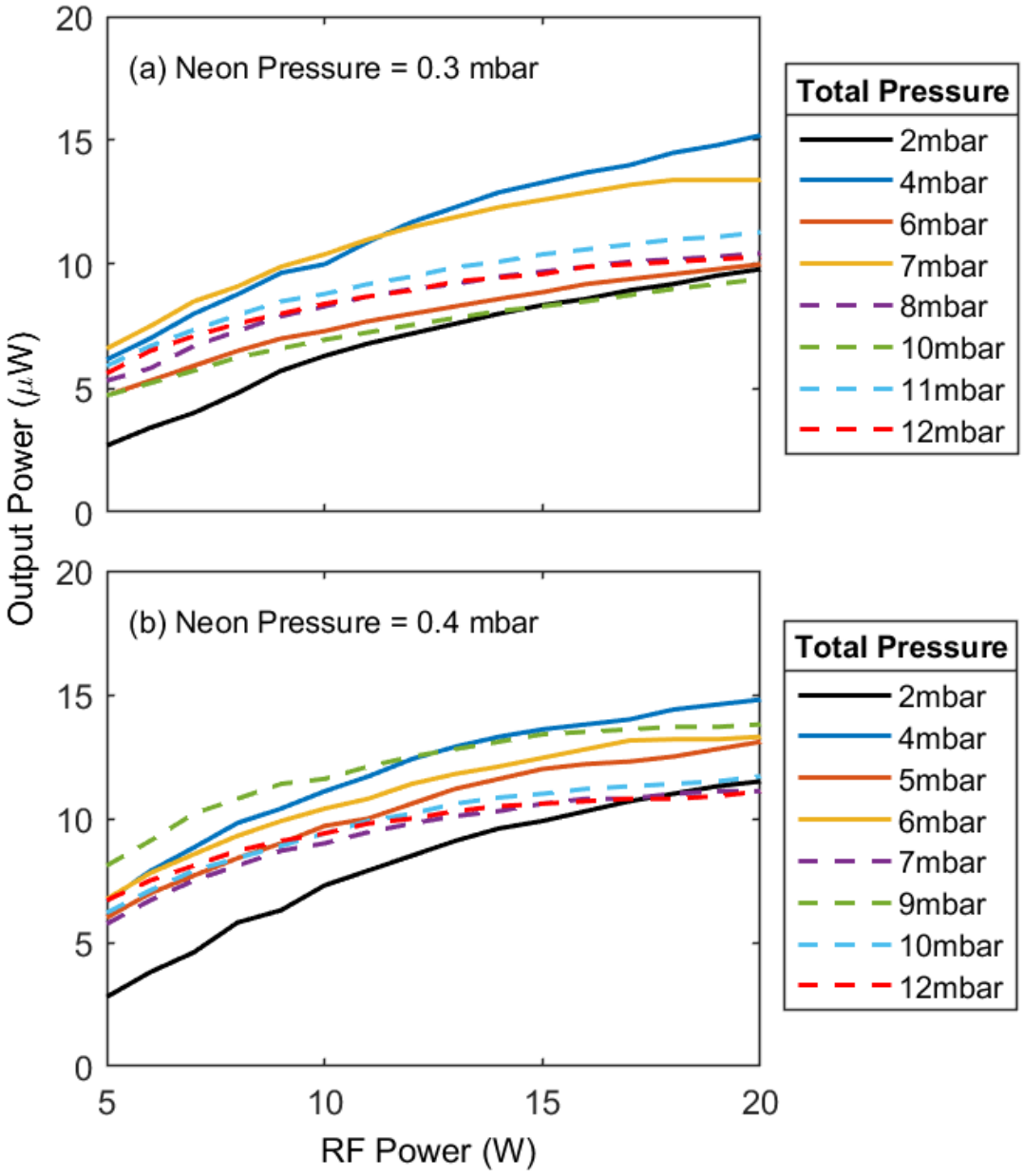

Figure 3.24: Laser output power as a function of RF excitation power; the natural neon partial pressure was fixed at 0.3 and 0.4 mbar and the cavity pressure was in a range of 2 to 12 mabr.

3.3.4 Gyroscopic Performance at the 1152.3 nm Wavelength

Typical Sagnac waveform patterns obtained during frequency-unlocked, single-mode laser operation and frequency 'lock-in' period are demonstrated in Figure 3.25 (a) and (b), respectively. The interferogram in Figure 3.25 (a) demonstrates the capability of a commercial-mirror equipped gyro in unlocking on the Earth's rotation. We remark that the phase-locked regime was not identifiable due to strong backscatter coupling. Regardless, we explored the possible operational laser output region for single-mode operation at different excitation densities since single-mode output was our priority. As shown in Figure 3.26, the single-mode regime can persist at a higher laser power at a higher cavity pressure. The maximum operable laser power for this regime was 240 nW, which was obtained from a gas composition with 0.4 mbar of natural neon partial pressure and 12 mbar of total pressure. Note that a single-mode region of 0 to 58 nW obtained from the operation with low-loss crystalline-coated supermirrors was four times smaller by comparison.

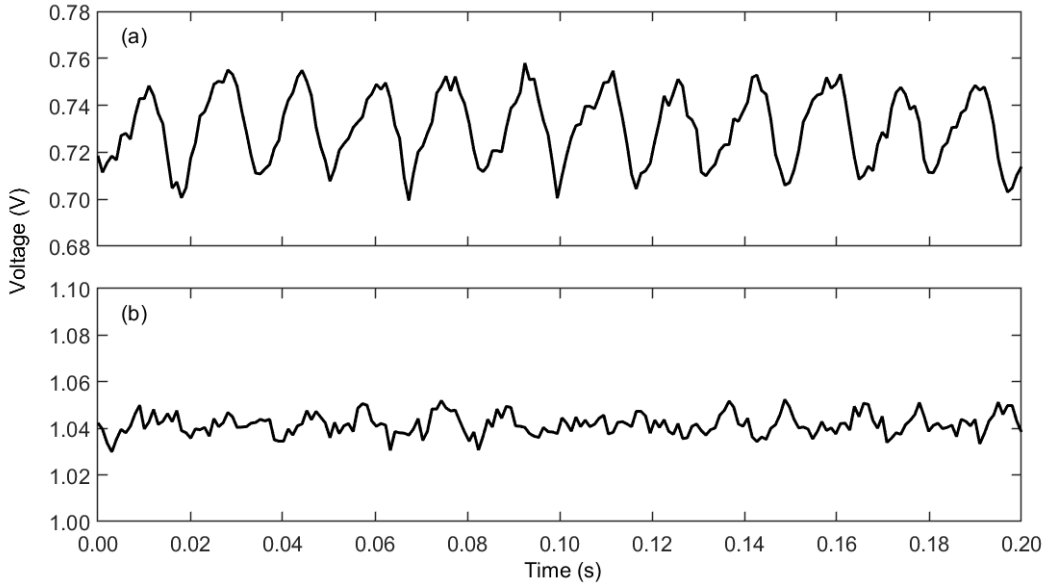

Figure 3.25: Oscilloscope-trace waveforms of the combined beams when PR-1 was (a) operating on a single longitudinal mode; (b) in the frequency-locked regime.

To characterise single-mode laser performance, the PR-1 cavity was filled with a natural neon partial pressure of 0.2 mbar with a total pressure of 10 mbar. Controlled by an amplitude servo unit, the laser output was maintained at around 100 nW (calculated intra-cavity power: 14 μW) throughout the operation period. Ideally, 1150.27 nm operation should generate a Sagnac frequency at 62.38 Hz as calculated by Equation 3.1. However, Figure 3.27 (a) shows large, fast time varying biases in the rotational signal as the observed Sagnac frequency drifted in a wide range from 50 to 80 Hz within 1800 s. This result was consistent with the raw interferogram previously demonstrated in Figure 3.25. An absence of the Sagnac beat

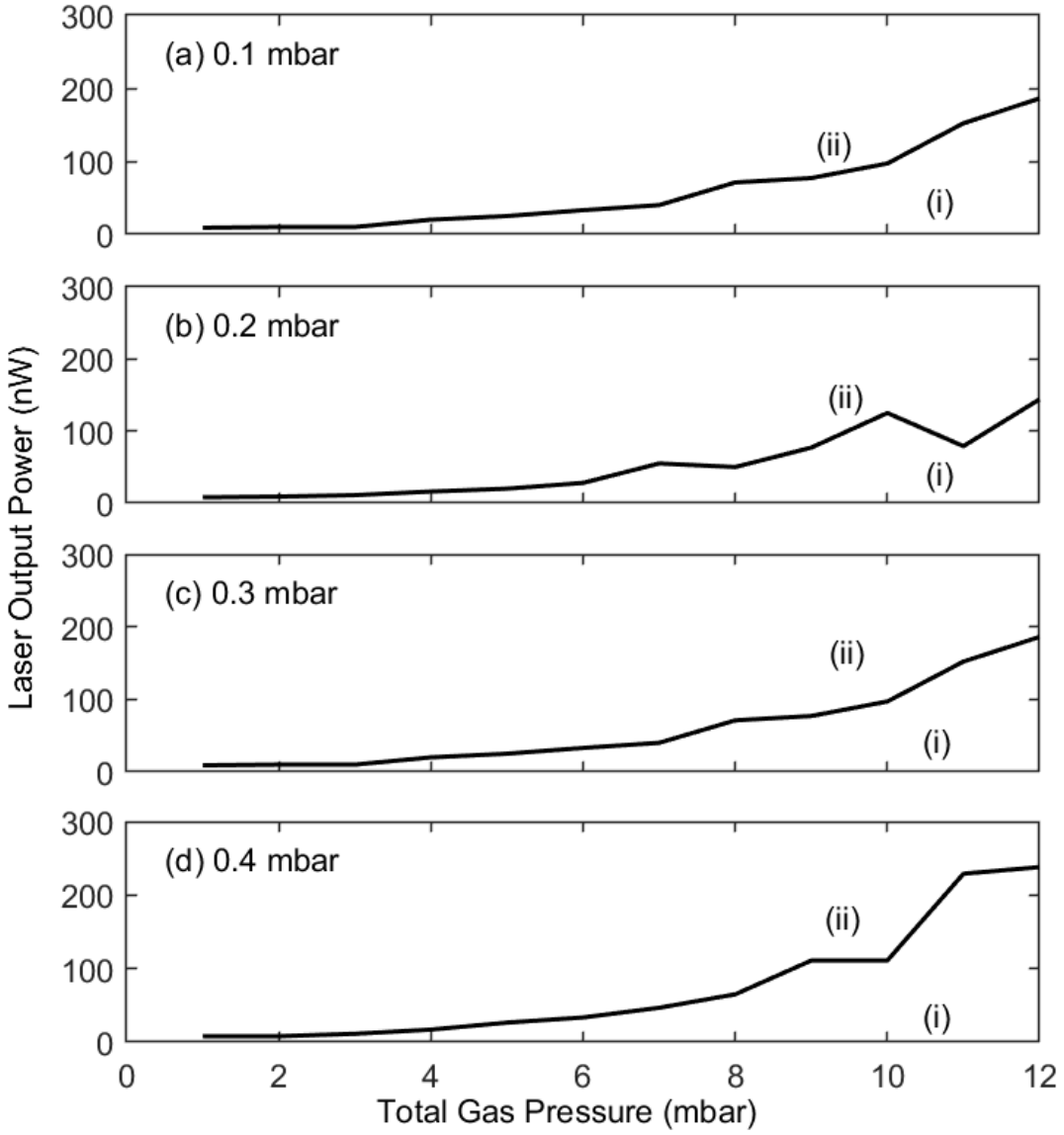

Figure 3.26: The multimode threshold (black curve) as a function of total gas pressure ranging from 1 to 12 mbar, with a natural neon partial pressure fixed at (a) 0.1 mbar, (b) 0.2 mbar, (c) 0.3 mbar, and (d) 0.4 mbar; the labelled region (i) indicates a single-mode operational regime and (ii) marks out a multi-mode regime.

signal within a period of 500 - 900 s in Figure 3.27 (a) can be given by either mode splitting or frequency lock-in. When the Sagnac frequency dropped to zero for either of these two reasons, the monobeam modulations and Sagnac contrast also exhibited a sharp decline. The low Sagnac contrast ratio measured in a range of 2 - 5% (Figure 3.27 (b)) is due to an extreme beam power inequality (with the CW beam critically weak). Figure 3.27 (c) exemplifies the strong backscatter-coupling effects that occurred in both beams by a measured CW beam modulation up to 40%. The gyroscope drifted in and out of the lock-in region as the cavity geometry varied.

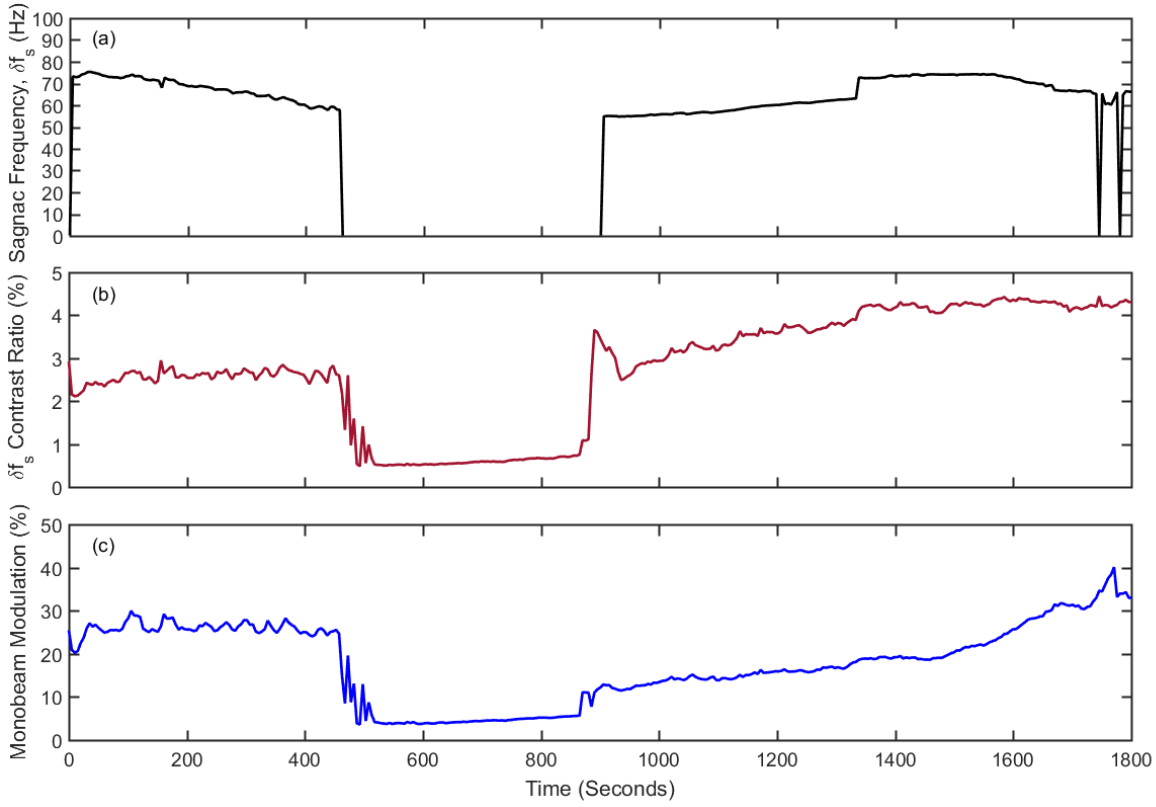

Figure 3.27: Time series of (a) Sagnac frequency, (b) Sagnac contrast ratio and (c) CW beam intensity modulation measured in a 1800 s time-period.

Figure 3.27 shows the stable single-mode laser performance limited to a short period of 140 s. Figure 3.28 (a) shows the Sagnac frequency varies by 1 Hz centred around 63 Hz. The Sagnac contrast and the CW beam modulation are shown in Figure 3.28 (b) and (c). An FFT power spectrum derived within this stable period is shown in Figure 3.29.

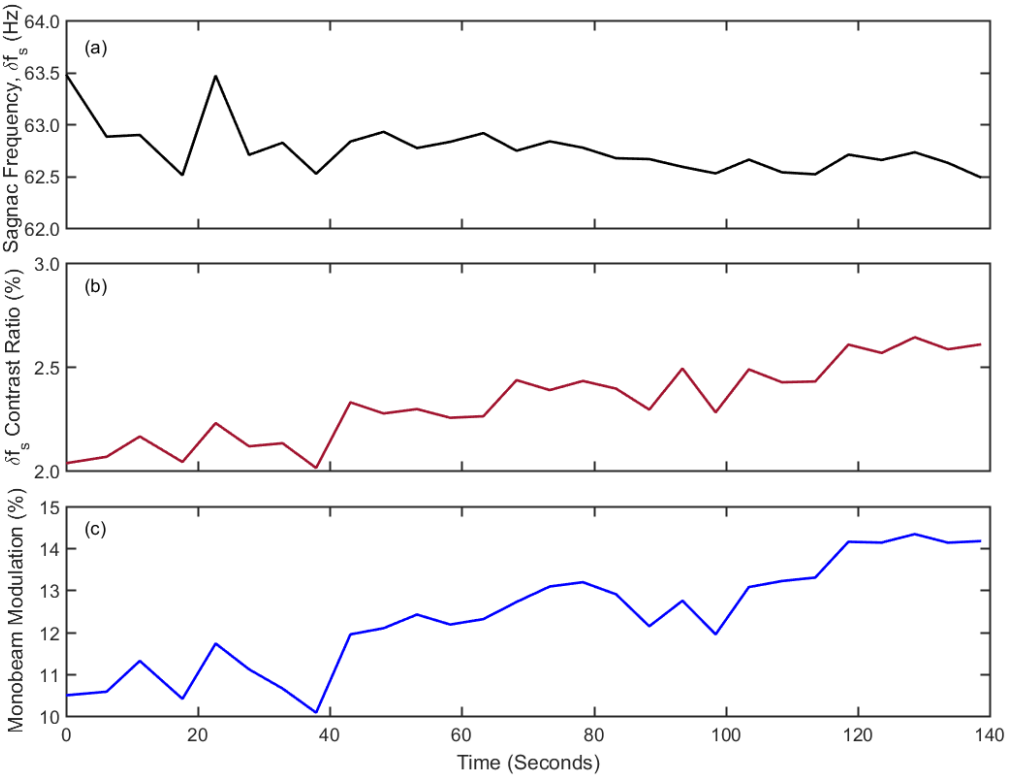

Figure 3.28: Best single-mode laser performance obtained from the near-infrared gyroscopic operation in a short time-period of 140 s, where the data series of (a) is the δf_s frequency; (b) is the δf_s contrast ratio; (c) is the measured CW beam modulation. The laser output was stabilised at 100 nW, and the cavity was filled with 10 mbar of total pressure with a natural neon partial pressure at 0.2 mbar.

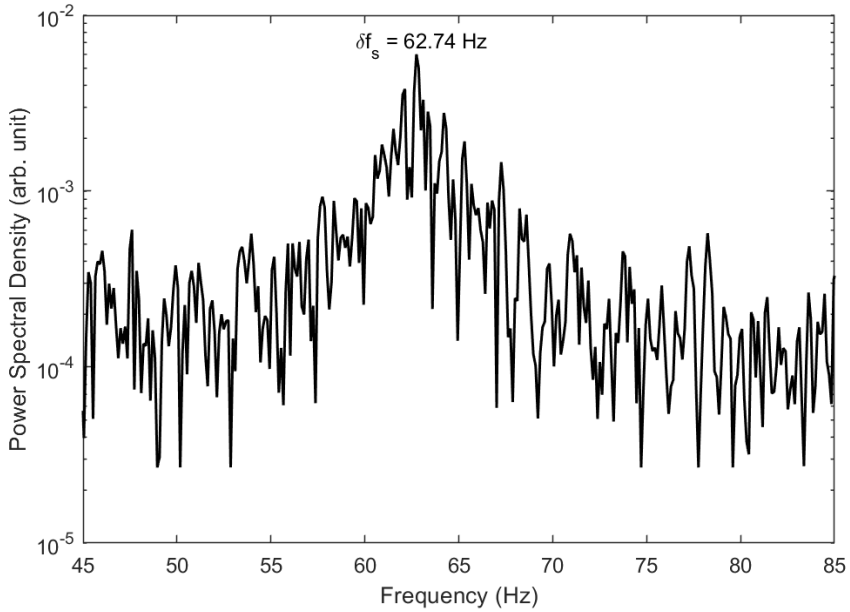

Figure 3.29: An FFT power spectrum obtained from the stable operation period; Earth rotation yields a Sagnac frequency at around 62.74 Hz.

3.3.5 Conclusion

The gyroscopic performance of a commercial-mirror-equipped ring laser operating at the near-infrared wavelength of 1152.27 nm was evaluated using the 2.56 m^2 PR-1 cavity. The standard laser mirrors (CVI TLM1) having a commercially-polished BK-7 substrate with a high transmission loss estimated at 0.92 ppm, are fundamentally different from custom-designed supermirrors. Given this cavity configuration, the photon decay time was 30 μs, the total optical loss was 712 ppm, and the finesse was 8835. The single-mode lasing yielded the highest laser output power at 240 nW for a cavity pressure of 12 mbar with a natural neon partial pressure of 0.2 mbar.

The Sagnac frequency was significantly pulled and pushed in a wide range between 50 Hz and 80 Hz. This is due to the large backscatter-coupling effect as evidenced by the time-varying CW beam modulation reaching 40% and a Sagnac contrast below 4.5%. We observed that a 1 Hz variation of the Sagnac frequency within 140 s correlated to a 4% variation of the monobeam modulation. PR-1 proved its ability to unlock on the Earth rotation background continuously for 100 - 1000 s (between mode splitting) despite yielding large systematic errors. We are not aware of previous reports of Earth rotation measurement using standard mirrors.

4 The Development of a 10 Metre Perimeter Ring Laser in the Ernest Rutherford Building

We demonstrate a new heterolithic large ring laser ER-1 (Ernest Rutherford 1) developed from its predecessor PR-1 with a geometrically-upscaled cavity. Located in a purpose-built laboratory on the ground floor of the Ernest Rutherford Building (at the Ilam campus of the University of Canterbury in Christchurch, New Zealand), this square-shaped laser encloses an area of 6.25 m^2 and is rigidly connected to a 3 m thick concrete floor. In comparison to PR-1, ER-1 has an enlarged cavity, which is expected to reduce the frequency pushing and pulling effects introduced by backscatter perturbations and yield a narrow laser linewidth of about 431 Hz under a stable operating environment. This chapter begins with an introduction to the laser construction and technical details, followed by the experimental set-up and cavity characterisation. The main goal of this chapter is to demonstrate the laser performance under different operational conditions and evaluate the overall gyroscopic sensitivity and stability. We also report a self-referenced perimeter stabilisation technique and backscatter correction on the raw Sagnac frequency to improve the accuracy of the Earth rotation data.

4.1 ER-1 Construction and Technical Details

4.1.1 Preliminary Works for the Laser Construction

Prior to ER-1's construction on the concrete foundation, two preliminary tasks were to mark out the exact positions of four mounting plates and label the relative height of each corner plate. A tape ruler was used to guarantee a distance of 2.5 m between two adjacent mirrors and a distance of 3.536 m between two diagonally-placed mirrors within a 1 mm uncertainty range. Both a levelling rotary laser and a bubble level ruler were employed to determine the relative height and tilt of each plate. Initially, four mounting plates were set down on the marked areas (shown in Figure 4.1 (a)), and the rotary laser level was placed in the centre area for laser construction. A ruler placed vertically on the top of the mounting plate read the position scanned by the rotary laser, and the relative height of each corner plate was recorded individually. As the height of each plate yielded a different reading, it is concluded that the ground floor has a minor slope from one end to the other and it is uneven in each location. To guarantee a planar ring laser cavity, we lifted the mirror mounting plates and put washers into the four bolts of each laser corner as appropriate (shown in Figure 4.1 (b)) until all mounting

plates were situated in one horizontal plane. The gap between the washer-lifted mounting plates and the concrete foundation might give rise to undesired mechanical vibrations. To avoid mechanical instability induced by loose connections between the plate and the concrete floor, an adhesive (Sika Sikadur 31) was applied to bridge the gap. The adhesive was mixed homogeneously, poured onto the concrete floor and spread out evenly, as shown in Figure 4.1 (c). Afterwards, mounting plates were put back to the laser corners and settled on the top of the adhesive, as shown in Figure 4.1 (d). After 12 hours of curing, the altitude and tilt of each corner plate were entirely fixed.

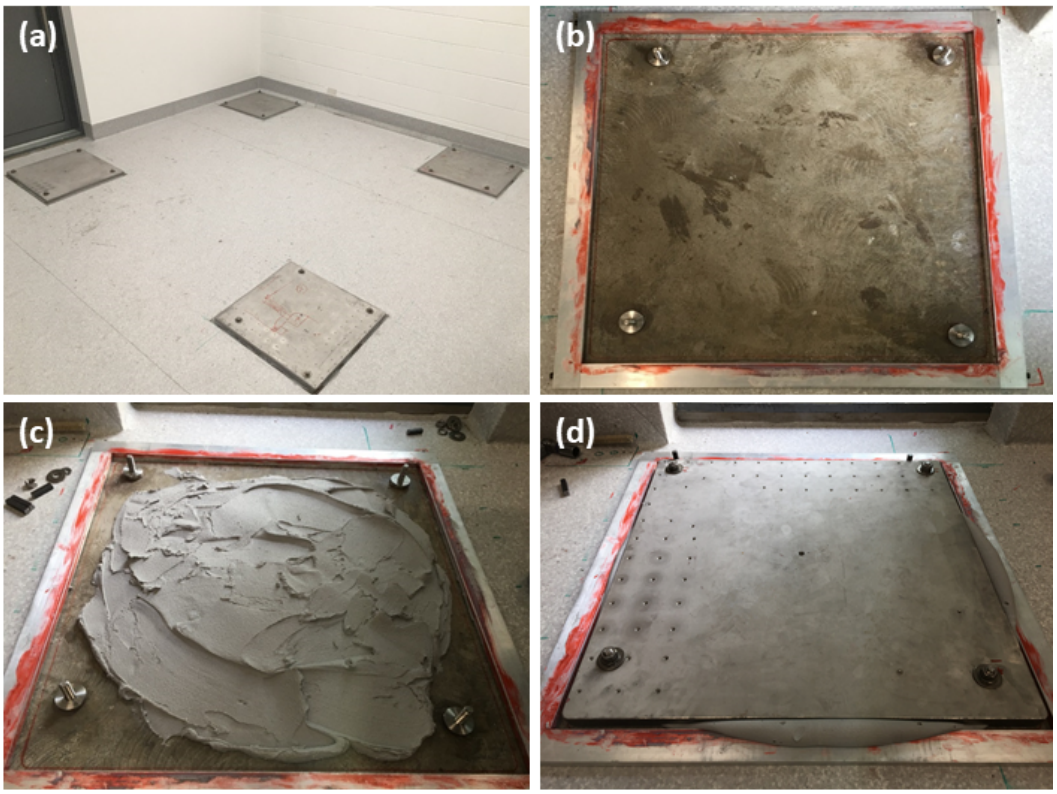

Figure 4.1: Preparation work done for ER-1 construction, where (a) shows the position labelling of four mounting plates before the laser construction; (b) shows a laser corner before the mounting plate was bolted down; (c) shows the adhesive applied for bridging the gap between the concrete floor and the mounting plate; (d) shows a ground-bolted corner plate waiting for an entirely-fixed settlement (once the adhesive completely dries out). Note that the temporary aluminum dam shown in these pictures was used to stop the adhesive from flowing out from underneath the plates.

4.1.2 Construction Procedure

The construction of ER-1 started with the installation of the mirror chambers and lever arms, followed by the assembly of stainless steel tube arms. Examples of the mounting plate bolted into the foundations and the mirror corner are in Figure 4.2 (a) and (b). The ER-1 cavity is configured mainly from mechanically-decoupled stainless steel tubes as shown in Figure 4.2 (c). Compared to the PR-1 cavity, this cavity is extremely robust against mechanical vibrations. ER-1 is mechanically improved not only because all corner plates are rigidly attached to the large concrete foundation but also because the free movement or wobbling of the cavity arms is prevented using a set of spatially fixed stainless steel tube holders connected to the floor. For a pre-alignment of the ER-1 laser, we left the cavity unsealed (without mounting the gain tube section) in an open environment and deployed a set of 632.8 nm supermirrors into the cavity. Two green alignment lasers were mounted in the SE and NW corners separately (see Figure 4.2 (d)) for injecting the alignment beams into the cavity in the counter-clockwise (CCW) and clockwise (CW) directions. Optimisation of the cavity alignment was achieved by fine-tuning the four micrometers of the lever system situated on each corner plate. The cavity was approximately aligned when the two green alignment beams could travel a complete circuit around the ring cavity with their output beams spatially overlapped. As shown in Figure 4.2 (e), the ring cavity was completely closed once the gain tube was installed. Afterwards, the gas fill and vacuum systems (details elaborated in Figure 3.5) were assembled on the nearest wall and attached to the laser cavity via an isolation valve located at the south cavity arm. As the construction work was complete, the cavity seal was assessed via a console leak detector (AdixenASM 192TD+, resolution limit of 10^{-12} l/s) and a helium spray gun. As presented in Figure 4.2 (f), the leak detection system was connected to the cavity to evacuate the gas inside. As shown in Figure 4.2 (g), a spray pistol (attached with a helium gas cylinder) was used to test for any leak in each junction of the stainless steel tube pipes. The wall-mounted gas fill and vacuum pump system and a final layout of the completed ER-1 cavity are shown in Figure 4.3 (a) and (b).

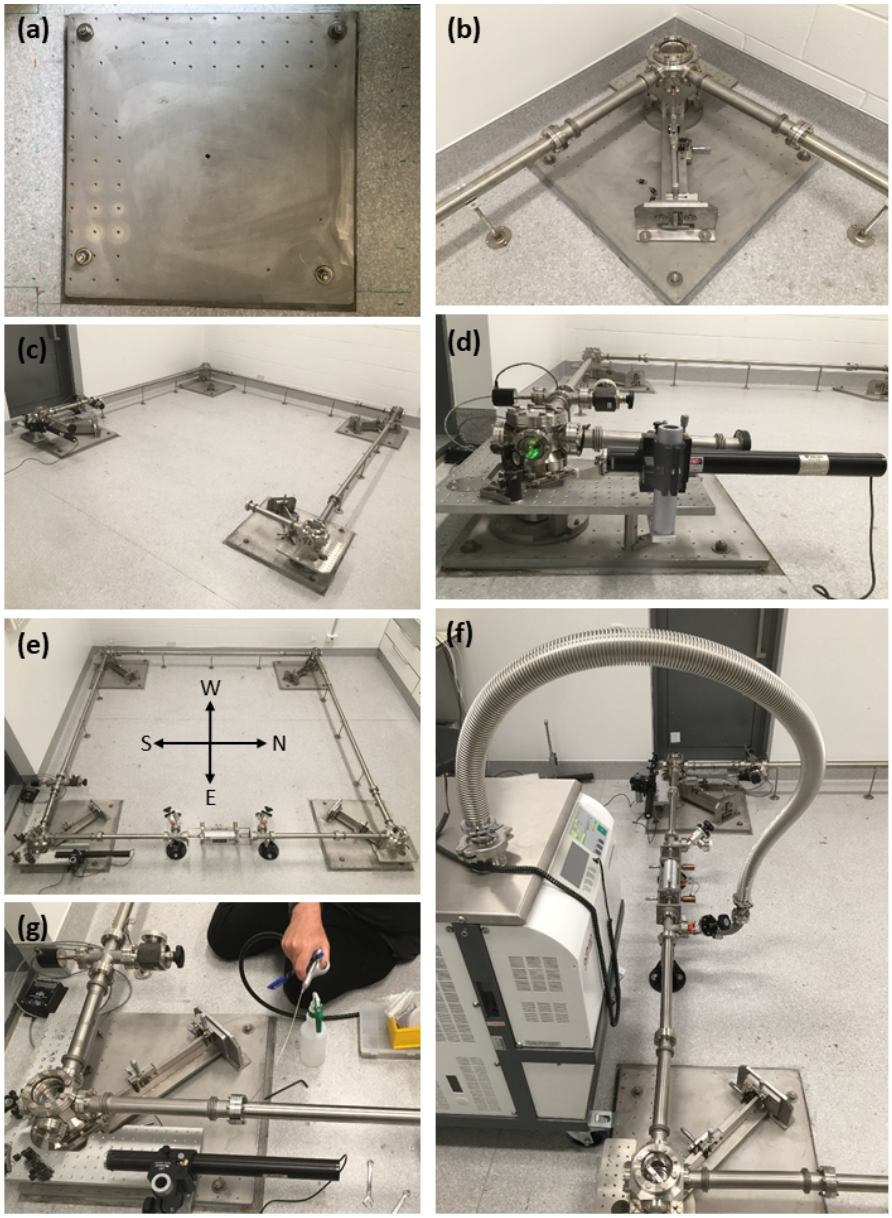

Figure 4.2: Construction procedure for the ER-1 ring laser, where (a) shows the mounting plate rigidly connected to the 3 m thick concrete floor, (b) gives an example of the mirror chamber and the associated lever arm system (from the SW corner) mounted on the corner plate; (c) shows the open laser cavity before the gain tube section was assembled; (d) shows the green alignment laser mounted in the SE corner for the pre-alignment work; (e) shows a well-aligned and enclosed ring cavity before connecting to the ancillary equipment; (f) shows the leak detection system coupled to the cavity for gas evacuation and leak test; (g) shows a leak test near the pipe junction.

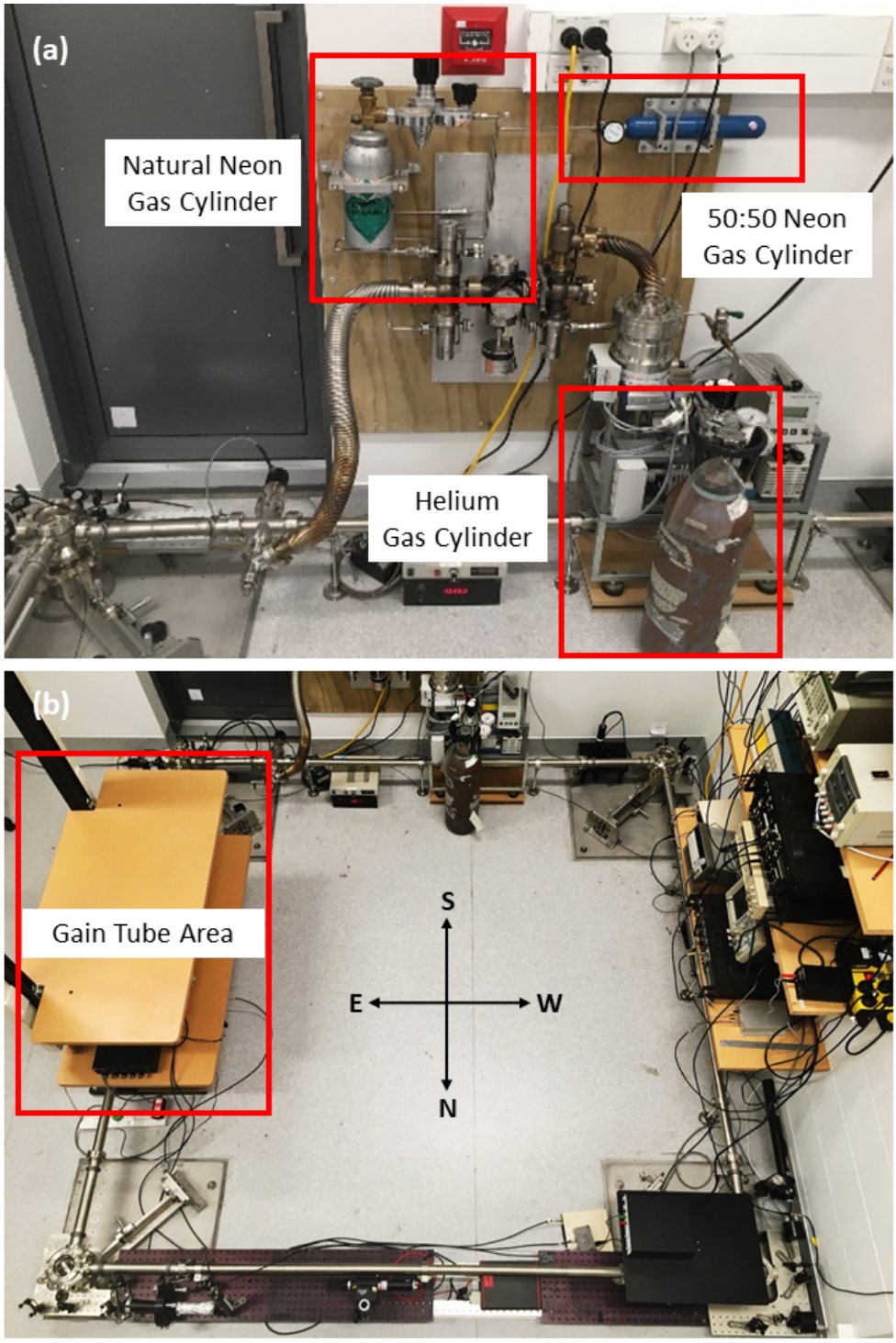

Figure 4.3: The final layout of (a) the wall-mounted gas fill and vacuum pump system and (b) the completed ER-1 laser cavity and its associated ancillary equipment (the gain tube is obscured by an equipment shelf).

4.2 Experimental Set-Up and Cavity Characterisation

Laser excitation was obtained within a Pyrex capillary of 100-mm-in-length (having a diameter of 4 mm), with the input drive for the gas discharge supplied by a 160 MHz RF transmitter. Compared to the 80 MHz RF transmitter conventionally adopted by other large ring lasers, the 160 MHz RF transmitter provides for a lower RF modulated noise, as well as a higher RF coupling efficiency due to better impedance matching. Manufactured by Research Electro-Optics (REO), a set of IBS-coated supermirrors (with radius of curvature, ROC = 4 m) with a specified transmission loss of 1.54 ppm and a total loss of 5.1 ppm per mirror were employed for 632.8 nm laser operation.

4.2.1 Signal Detection and Data Acquisition System

Figure 4.4 shows the experimental set-up, data monitoring and acquisition systems. In the SW corner, a beam splitter (BS 1) is used to combine the output laser beams to generate a Sagnac beat signal, which is detected by a photomultiplier tube (PMT 1) and monitored by an oscilloscope. In the NW corner, two photodiodes (PDs) are applied to estimate the magnitude of backscatter effects for two counter-propagating beams. In the SE corner, a power meter (PM) is used to observe the laser output power of the CW beam, with an iris mounted in the front to reduce the plasma background light. The CCW beam transmitted in this corner is used for monitoring the FSR beat frequency (ν_{fsr}) induced by two longitudinal modes (via PMT 3). In the NE corner, a Fabry-Perot interferometer (FP) having an FSR of 300 MHz is employed to observe the mode structure of the CCW beam. An iris placed in front of the FP guaranteed a clear and unperturbed mode structure detected by the photodetector (PMT 2). This spatial filter can substantially cut off the beam back reflected from multiple optical surfaces and reduce the perturbation from other light sources.

A frequency-stabilised SIOS[1] laser is used as an external reference to assist in the monitoring of mode behaviour (mode-hops or split-mode operation). An isolator (IS) mounted in front of the SIOS is used to avoid optical feedback[2]. A variable attenuator (AT) is used to attenuate the intensity of the SIOS laser. A beam splitter (BS 2) is used to combine the laser beams from the SIOS and ER-1 systems. Therefore the relative phase variation between the operating mode of ER-1 and the SIOS laser can be observed via an oscilloscope.

[1] This reference laser is a SL-03-Series stabilised He-Ne-lasers provided by SIOS Meßtechnik GmBH. The highest achievable frequency stability is $\pm\ 2 \times 10^{-9}$ at 1 hour of integration time. The absolute frequency of this SIOS laser is 473612547.1 MHz with an uncertainty of $\pm$5 MHz.

[2] The light reflected from multiple surfaces can potentially introduce frequency jitter of the SIOS laser

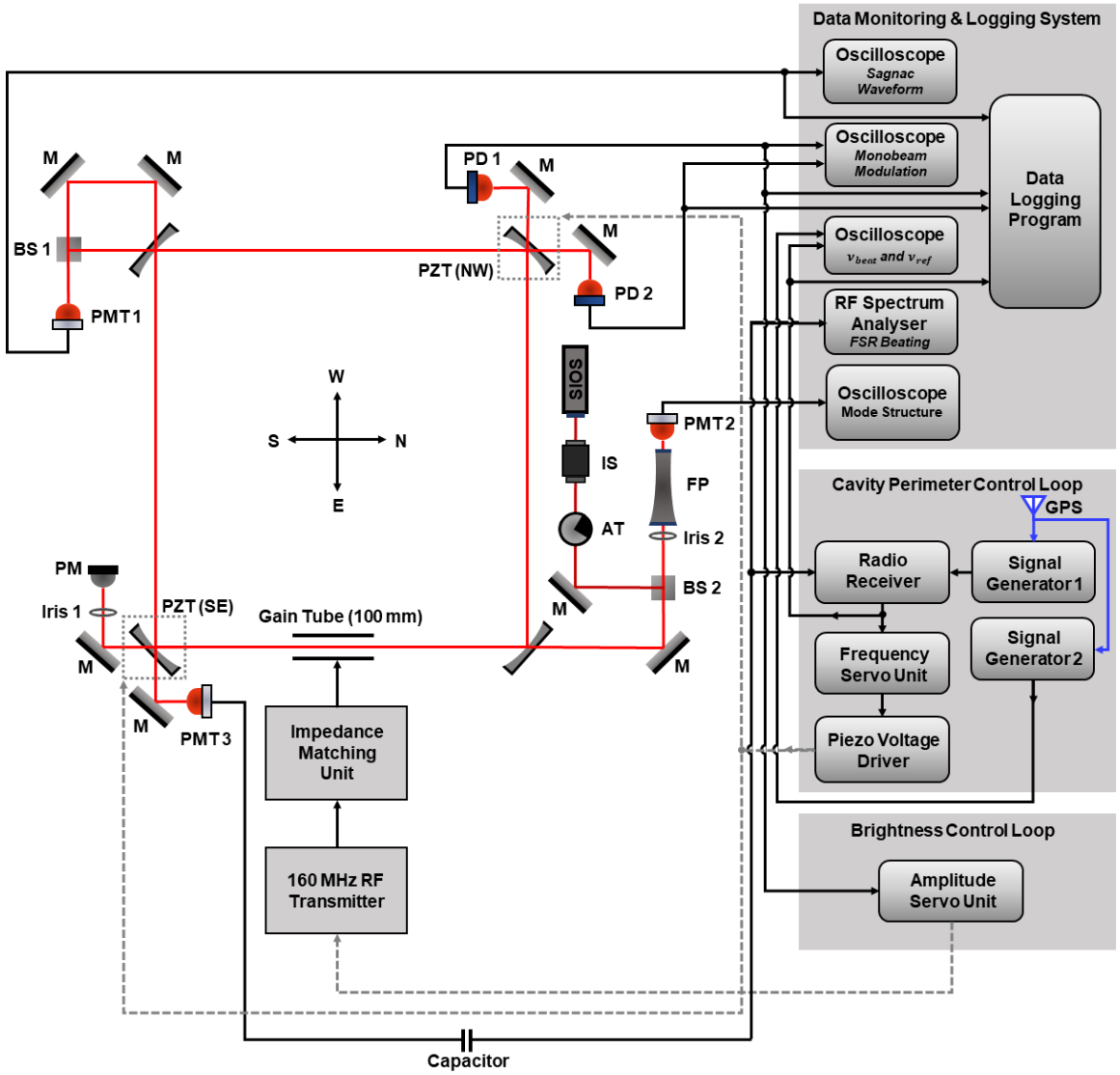

Figure 4.4: A simplified schematic of the experimental set-up, data acquisition (DAQ) and control system of the ER-1 ring laser. The following labelling scheme applies: M, dielectric mirror; BS, beam splitter; PMT, photomultiplier tube; PD, photodiode; PM, power meter; IS, isolator; AT, attenuator; FP, Fabry-Perot interferometer; PZT, piezoelectric transducers. All data is acquired via a National Instrument LabVIEW data acquisition board (USB NI 6216 BNC); the sampling rate of the DAQ was set to be 5000 samples/sec and the data write-out is set to be once per second.

4.2.2 Brightness and Cavity Perimeter Control System

Stable and sustainable ER-1 operation is maintained by both the intensity and the cavity perimeter control systems. As indicated in Figure 4.4, the laser output power of the CCW direction is detected (via PD 1) and fed into the amplitude servo unit in a closed-loop operation. The error signal induced by the subtraction of the set voltage and the detected voltage is used as a feedback signal to regulate the 160 MHz RF transmitter for compensating any drift in the laser intensity.

Cavity perimeter stabilisation is achieved via two piezoelectric translators (PZTs) which are embedded in the two diagonally opposite corners (SE and NW corners). The detected FSR beat frequency ν_{fsr} is filtered by a capacitor, leaving only the AC signals to be fed into an RF spectrum analyzer and a radio receiver (Yaesu VR-5000). A global positioning system (GPS) stabilised 'signal generator 1' (Hewlett Packard 8684A) is set to yield a stable reference signal ν_{ref}, with a frequency output about 2 kHz higher than the ν_{fsr} frequency. Both the ν_{fsr} and ν_{ref} signals are injected into the radio receiver to get a down-shifted beat frequency ν_{beat}. This heterodyned beat signal is amplified via a built-in amplifier in the radio receiver and afterwards fed into a frequency servo unit (with a set frequency of 2 kHz) as the feedback signal for self-referenced cavity perimeter control.

In a similar fashion to the amplitude servo unit (previously discussed in Section 3.2.1), the frequency servo unit comprises a counter, a comparator and a PI (proportional-integral) micro-controller, where ν_{beat} is counted by the frequency counter and the value is compared with the set frequency via the comparator. Proportional to the frequency difference between the pre-set and detected value, the output of the PI unit in terms of modulation voltage V_{mod} is coupled into the piezo voltage driver to generate a control voltage output V_{con}. Thereafter, the control voltage drives PZTs to actively compensate any drift in cavity length, via maintaining a constant ν_{beat}. As shown in Figure 4.4, both the heterodyned ν_{beat} output and the second reference ν_{ref} signal (from 'signal generator 2') are coupled to an oscilloscope. The cavity regulation process can be visualised via the on-going variations of the relative phase between the variable ν_{beat} and the fixed ν_{ref} observable from an oscilloscope.

4.2.3 Determining the Cavity Parameters

To characterise the overall optical losses and cavity finesse, the ring cavity alignment is optimised to yield a clean TEM_{00} mode with a maximised laser output. As tabulated in Table 4.1, a clean and optimally-aligned ER-1 cavity yields a quality factor Q of 1.1×10^{12}, as determined by a measured ring-down time (τ) of 375 μs. An associated total cavity loss of 88.9 ppm and a cavity finesse of 7.1×10^4 are calculated correspondingly.

Parameter	Value
Ring-down time, τ (μs)	375
Total loss, L (ppm)	88.9
Quality factor, Q	1.1×10^{12}
Finesse, F	7.1×10^{4}

Table 4.1: Measured ring-down time and the corresponding total loss, quality factor Q, and finesse of the ER-1 ring cavity.

4.3 Standard Operation at 632.8 nm Wavelength

Located at a precise latitude of φ = 43.522° S, ER-1 operating on the 632.8 nm wavelength can be anticipated to yield a Sagnac frequency at 198.38 Hz calculated from the re-written form of Equation 2.26:

$$\delta f_s = \frac{4A}{\lambda P}\Omega_E \cos(90 - \varphi). \tag{4.1}$$

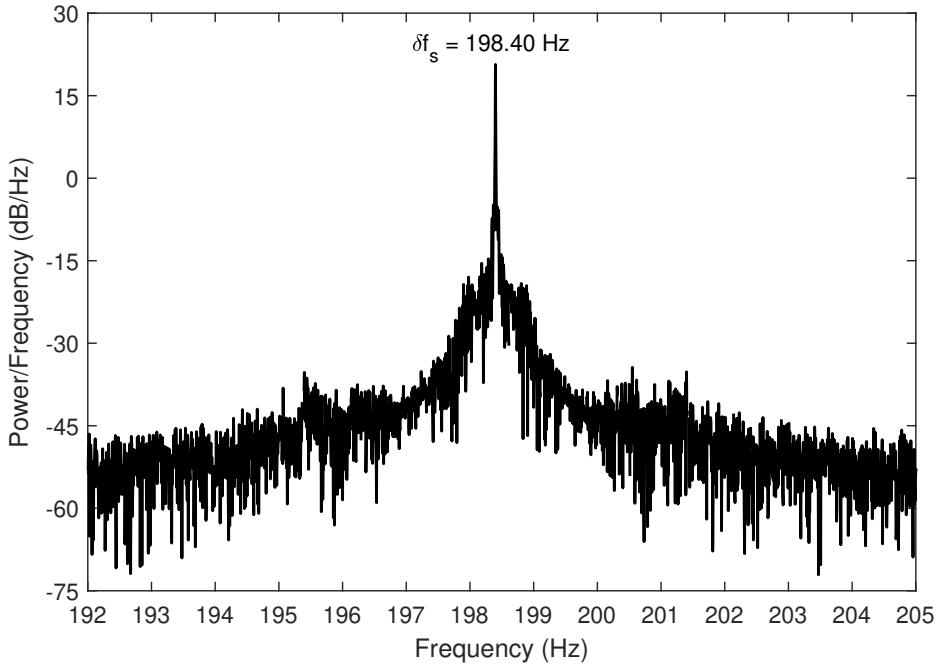

Figure 4.5: The FFT power spectrum obtained for the operation at 632.8 nm wavelength, it shows the Sagnac frequency (δf_s) with an Earth line at 198.40 Hz.

Measured via an RF spectrum analyser, the beat frequency between adjacent longitudinal modes yields an FSR at 29.970 MHz. From this, we infer an actual cavity perimeter at about

10.003 m with a scale factor construction error of approximately 0.03%. This measured cavity perimeter gives an updated nominal Sagnac frequency at 198.32 Hz. An example of the FFT power spectrum of δf_s derived from the raw Sagnac waveform is shown in Figure 4.5. It shows the Earth line at a frequency of 198.40 Hz. The 80 mHz deviation between the nominal ideal and the measured Sagnac frequency, is assumed to be associated with frequency pulling induced by residual backscattering effects on the intra-cavity mirror surfaces and any minor orientational uncertainties.

4.3.1 Stable Operational Regimes

Laser operation at a high photon flux increases gyroscopic sensitivity. In particular, for a phase-locked mode configuration set up for cavity stabilisation, higher operational power contributes a better signal-to-noise ratio of the ν_{fsr} (or ν_{beat}), which guarantees a more efficient feedback signal for the self-referenced perimeter control. To explore the optimal laser power, the mode behaviour for various intra-cavity gas pressures was investigated.

As previously demonstrated in Section 2.5.1, high gas pressure assists single-mode operation via the reduction of mode competition by providing increased homogeneous broadening and a weaker saturation at high laser power. As evidenced by the measured results in Table 4.2, stable operation at a high laser power is more accessible in the high-pressure region. As such, characterisation of the sensor stability and sensitivity was performed using laser operation at cavity pressures between 8 and 10 mbar.

Pressure (mbar)	Mode Structure	Laser Power (nW)
6	Single Mode	0-35
	Phase-locked	35-58
8	Single Mode	0-80
	Phase-locked	80-370
10	Single Mode	0-135
	Phase-locked	135-970

Table 4.2: ER-1 operational regimes for the single-mode and phase-locked mode configurations at various cavity pressures; neon partial pressures were all fixed at 0.2 mbar (with a 50:50 isotopic mixture).

4.3.2 Gyroscopic Performance without Cavity Stabilisation

Figure 4.6 (a) demonstrates typical laser performance in long-term Earth rotation sensing. Mode-hops are observed periodically as the uncontrolled cavity is affected by thermal-and-pressure-induced expansion and contraction. As shown in Figure 4.6 (b), every mode-hop yields a 10 - 30 mHz step-up or step-down in the Sagnac frequency, as well as a sudden change in the Sagnac contrast ratio at 5 - 13%.

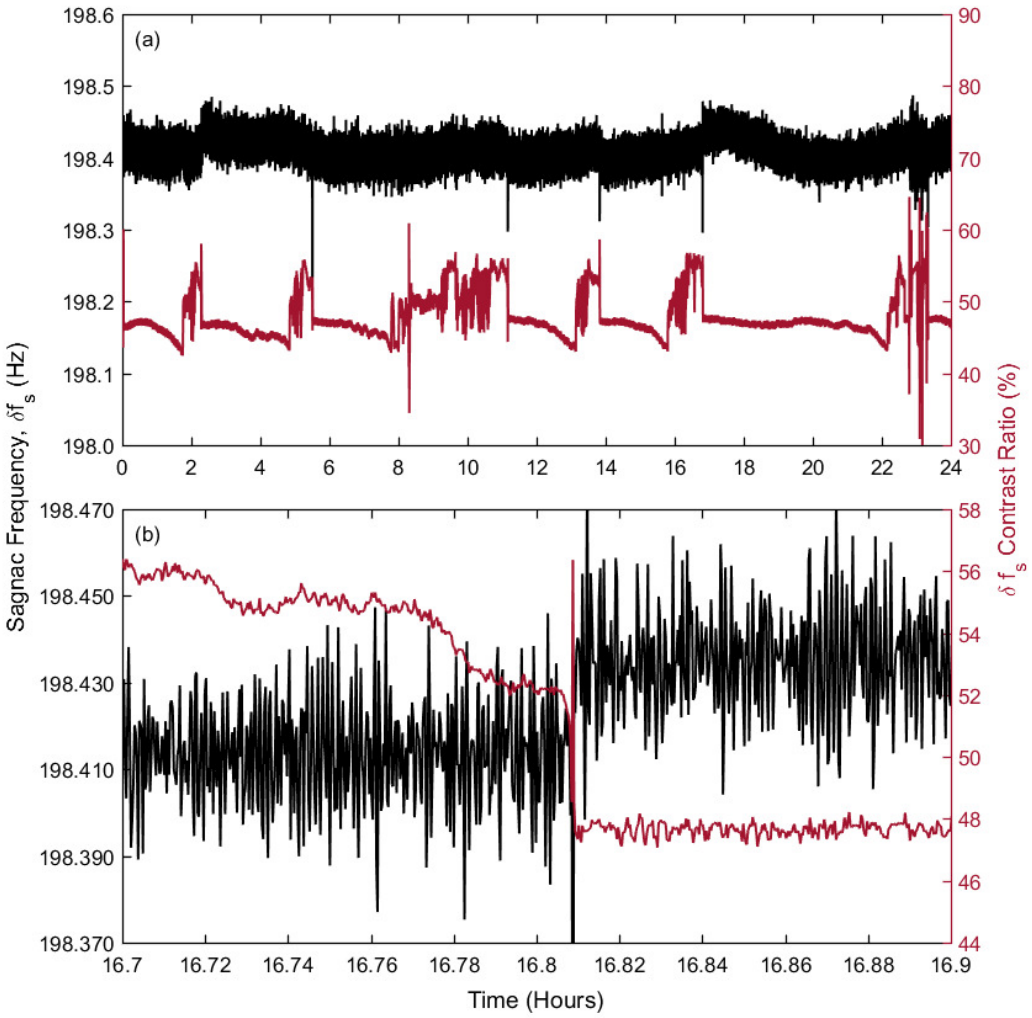

Figure 4.6: Gyroscopic operation at a cavity pressure of 8 mbar with a 50:50 neon partial pressure of 0.2 mbar, where (a) shows the laser performance over 24 hrs (with an output power stabilised at 103 nW); (b) shows an expanded view of a mode-hop induced by perimeter variations.

The rotational resolution for operation on both single-mode and phase-locked mode configurations were analysed using the Allan deviation (ADEV) normalised to the Earth's rotation rate Ω_E (see Figure 4.7). For single-mode operation at 10 mbar pressure with a laser output power of 100 nW, the minimum deviation achieved was at $\Omega/\Omega_E = 1.5 \times 10^{-6}$ with a measurement time of 256 s, giving a usable sensitivity of 1.2×10^{-11} rad/s/$\sqrt{\text{Hz}}$. The lowest normalised deviation achieved was 4.9×10^{-7} with an integration time of $\tau = 512$ s, obtained by stable phase-locked operation at 8 mbar pressure with a laser output power of 113 nW. This implies a highest sensitivity of 7.9×10^{-12} rad/s/$\sqrt{\text{Hz}}$ obtainable with 632.8 nm operation. With a normalised ADEV lower than 10^{-6}, ER-1 has a promising future for the observation of low-frequency signals in geophysics and geodesy, such as diurnal polar motion and Earth tides [14]. Meanwhile, ER-1 also proved to be a useful tool for seismic monitoring in the active Canterbury plains and, in particular, for the Darfield earthquake swarms [12].

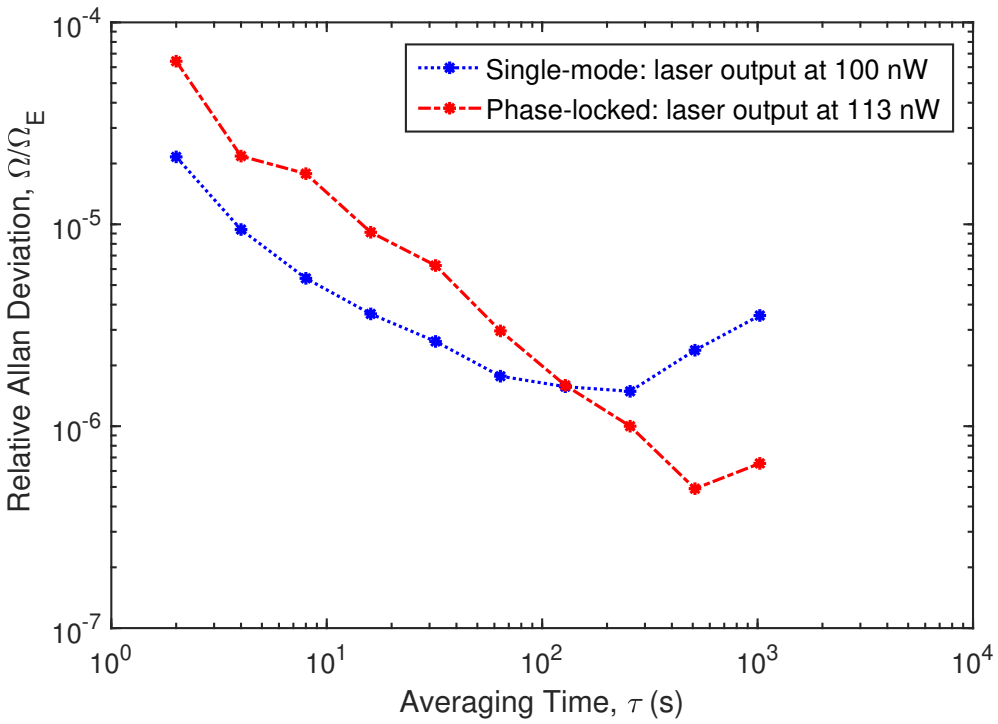

Figure 4.7: Best ER-1 gyroscopic performance operating on the single-mode and the phase-locked mode configurations; the relative Allan deviation plots selected a continuous time series of one hour in length for stability analysis.

4.3.3 Laser Performance Using a Self-Referenced Perimeter Control Mechanism

The laser power was tuned to sustain a phase-locked mode configuration to investigate the cavity perimeter drift induced by ambient thermal-and-pressure fluctuations. An example of the mode structure is given in Figure 4.8. The centre mode and two longitudinal modes 5 FSR away can be maintained in a stable configuration. As indicated in Figure 4.9, the daily perimeter variation of the ER-1 cavity was measured in the range of 2.7 to 5 μm as derived from the logged data of ν_{beat} (method explained in the preceding Section 4.2.2).

The linear expansion coefficient (α) of concrete, $\alpha = 10 \times 10^{-6}/K$, suggests a temperature fluctuation[3] of the concrete base of 27 to 50 mK/day. The calculated geometric variation rate was in the range of 0.001 to 0.25 nm/sec with an average of about 0.08 nm/sec. This suggests mode-hops will occur every 1 to 5 hours following the compression and expansion of the cavity length.

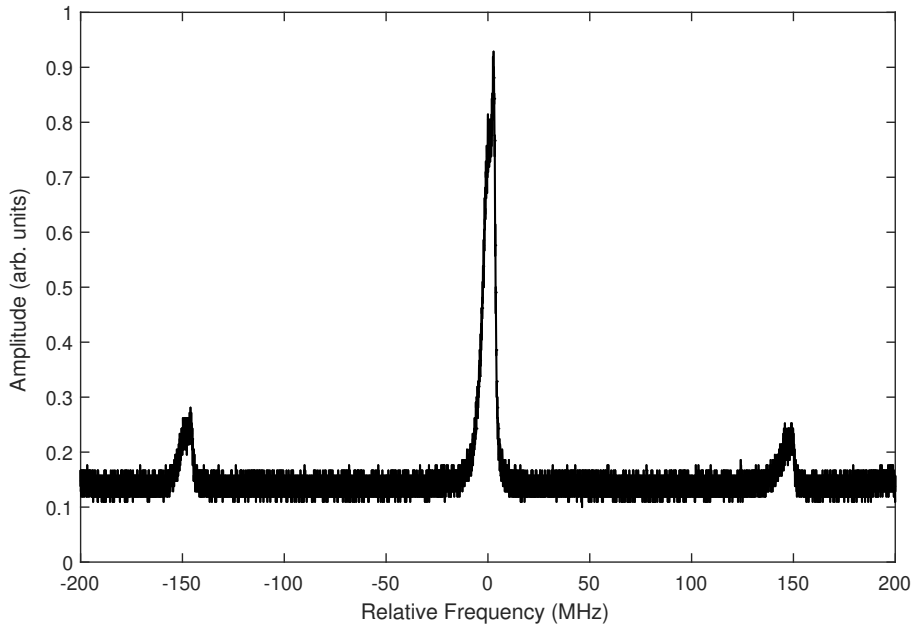

Figure 4.8: Laser mode structure as scanned by an F-P interferometer while ER-1 was operating in a phase-locked mode configuration.

Given the modest perimeter variation and a slow perimeter drift, only one PZT (in the NW corner) was activated for cavity regulation. For an optimisation of the parameter settings of

[3]The temperature probes were also implemented to roughly measure the temperature of the corner plates and the ground. However, the temperature read-outs of the probes were only able to give a highest precision of 0.01 kelvin. To precisely determine the small temperature variation over time, the logged cavity FSR is the most useful tool as it can reveal the mild temperature effect in the millikelvin scale.

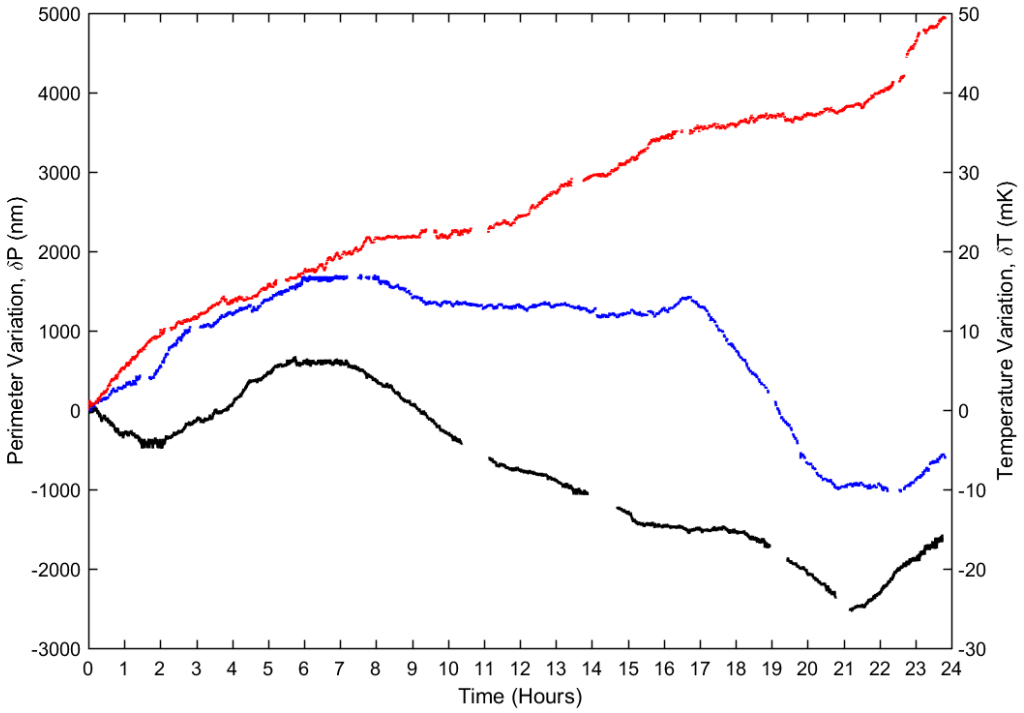

Figure 4.9: The perimeter variation (left y-axis) and the derived temperature variation of the concrete base (right y-axis) over 24 hrs from three separate measurements all starting at 11:15 am of the day.

the frequency servo unit, a preparatory characterisation of the PZT motion was performed. As shown in Figure 4.10, the modulation voltage and the perimeter change exhibit a non-linear relationship. Since the hysteresis and non-linear response of the piezoelectric ceramics are proportional to the control voltage, we set the PZT driver to operate with a low modulation voltage between 0 and 1 V with an initial point starting at 0.5 V. The piezo-actuator was expected to compensate cavity compression and expansion within a 7.4 μm variation range.

For the frequency servo unit, the integration time of the frequency estimator and the loop time for the frequency control were both set to be 15 s, to guarantee a higher resolution of the ν_{beat} estimation and a slower PZT movement to avoid frequent perturbations on cavity regulation progress. Prolonged laser performance without the occurrence of mode-hops was achieved. As shown in Figure 4.11 (a), the frequency excursion over 12 hours of operation was 150 mHz with the δf_s contrast ratio held at a constant 50%. The measured monobeam modulations ($m_{1,2}$) were varied in a small range between 0.5 to 1.5% (Figure 4.11 (b)). As shown in Figure 4.11 (c), the cavity FSR was stabilised to within 0.6 Hz, which is equivalent to a perimeter held within a 200 nm variation. As stated in [109], long-term perimeter stabilisation over 2 hours for the PR-1 ring laser was not possible as the PZT stages frequently went out of range due to fast variation of the laser perimeter over a wide range. Therefore,

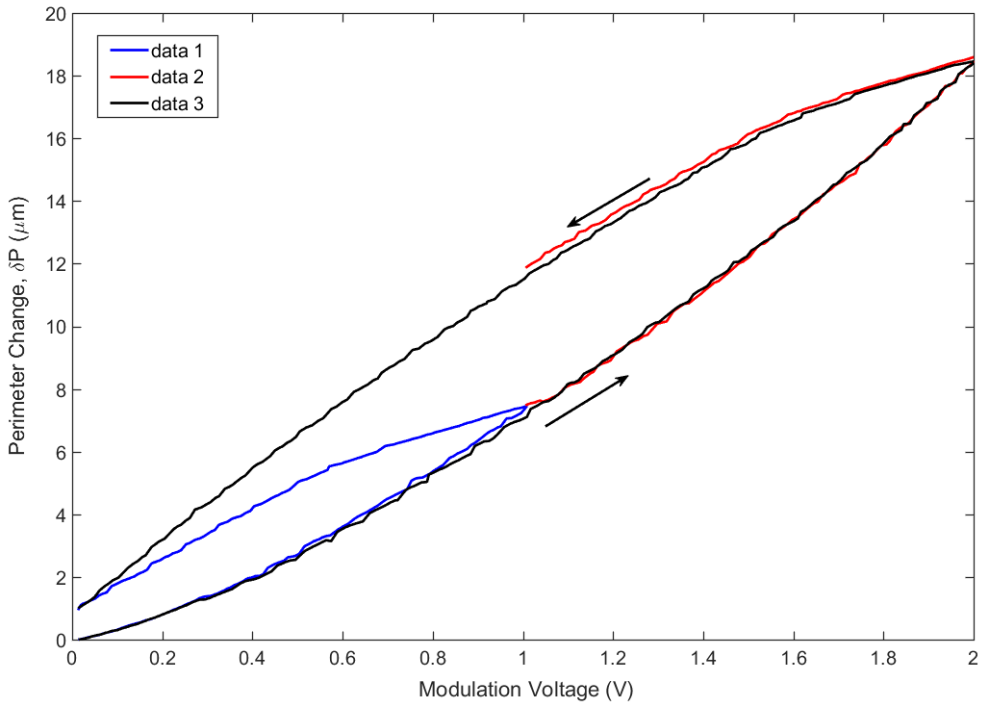

Figure 4.10: Calibration of the piezoelectric actuator for an optimisation of the PI control unit. The characterisations were done for three voltage ranges of 0-1 V (blue trace), 1-2 V (red trace) and 0-2 V (black trace), respectively. Firstly, the modulation voltage was increased and then decreased to its initial voltage setting with a 10 mV step for every 10 s, at the same time, the detected ν_{beat} was recorded and the induced perimeter change (δP) was obtained.

long-term perimeter control of ER-1 is significantly assisted by the more stable laboratory environment.

Despite effective control of the cavity perimeter, the external closed-loop frequency-stabilising system introduced extra noise to the measurement signal during the cavity regulation progress. As observed from a data write-out at once per second, the short-term frequency excursion of the Sagnac signal is approximately 50 - 70 mHz without the implementation of cavity stabilisation (Figure 4.6), increasing to 80 - 100 mHz (Figure 4.11) after the active regulation control is applied. Currently, gyroscopic performance is limited by RF transmitter noise passing through the electronic circuits ultimately affecting the precise output of the modulation voltage (V_{mod} resolution at 0.1 mV). Also, the sensor stability is limited by the non-linear response of the piezo stage which tends to overcompensate the perimeter drift.

The non-linear mechanical response of the piezoelectric stage, and the uneven translation of the mirror position, are believed to be the limiting factors in the perimeter-stabilised

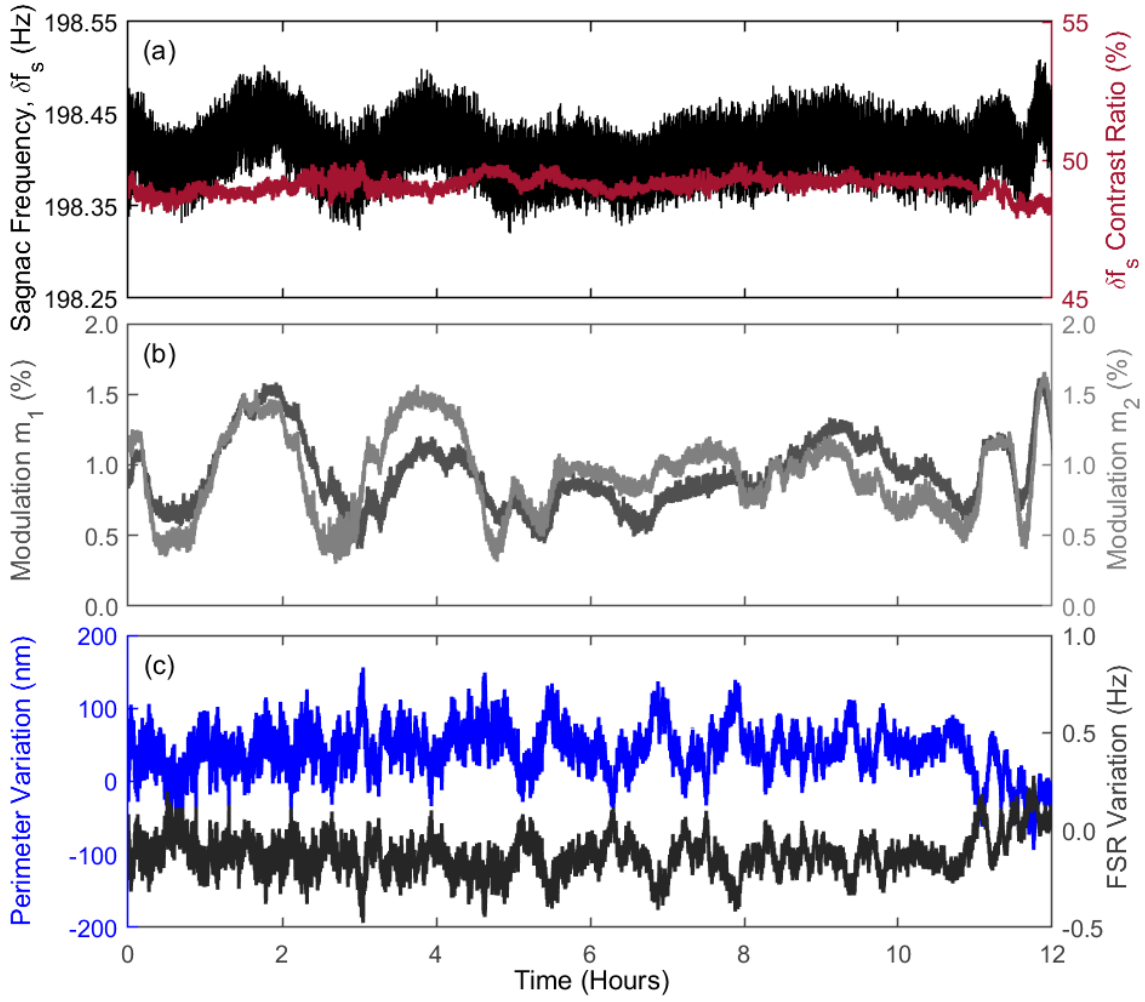

Figure 4.11: ER-1 gyroscopic performance over 12 hours duration, where (a) demonstrates stable operation with a small δf_s frequency variation of 150 mHz; (b) shows the monobeam modulations (m_1, m_2) over a perimeter-controlled period; (c) indicates the FSR variations and the associated perimeter changes given by a geometry-stabilised laser cavity.

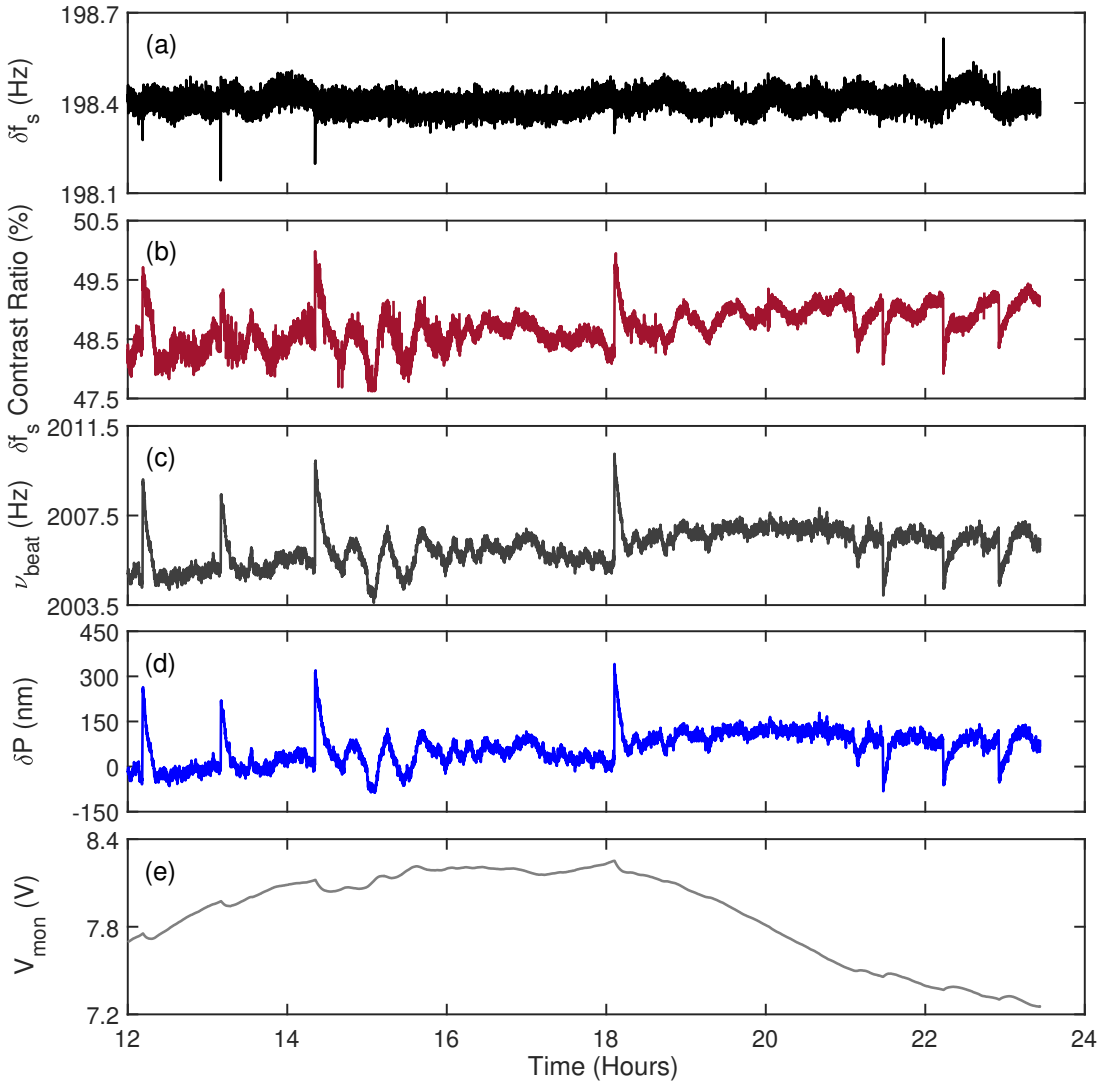

Figure 4.12: A 12 hours laser performance used to show the outcome of non-linear PZT response, where (a) shows the raw Sagnac frequency time series yielded from the operation implemented with a self-referenced perimeter control; (b) shows the measured Sagnac contrast ratio; (c) presents the beat frequency (ν_{beat}) induced by ν_{fsr} and ν_{ref} which was used as a feedback signal for the cavity control; (d) shows the dynamic of perimeter variation during the cavity regulation; (e) shows the dynamics of the monitor voltage that symbolised the PZT control voltage.

laser performance over one day. Supporting evidence can be seen in the 12 hour gyroscopic performance shown in Figure 4.12. Failure to stabilise ν_{beat} at the set value happened on occasions as the instantaneous jumps of ν_{beat} and the perimeter variation δP were recorded in the laser operation (see Figure 4.12 (c) and (d)). One possibility is that the PZT does not transform smoothly when driven by a voltage increment with rapidly changing direction. As a consequence, it introduces mechanical noise on the mirror position and thus leads to a transient change of the cavity length. As shown in Figure 4.12 (e), a sudden step-up or step-down of the ν_{beat} occurs whenever the monitor voltage (V_{mon}) displays a sharp increase or decrease.

We note that the piezoelectric stacks were not directly acting on the back of the supermirrors but the mirror holders located at the laser corners. Hence, another plausible explanation for the sudden change that occurs in the cavity length, is that the mirror position is not only driven by the mechanical deformation of the PZT but also affected by tensile stress from the lever arm used for the adjustment of the mirror holder. To be more specific, there exists turning-points where mechanical hysteresis of mirror movement occurs, induced by slow and inconsistent reactions of the spring strain.

Figure 4.13 demonstrates the best gyroscopic performances obtained from the perimeter-controlled laser cavity at gas pressures of 6, 8 and 10 mbar. All relative ADEV plots were analysed using a time series with a fixed data-length of either 5 hours or 12 hours. The 5 hour Sagnac frequency data series is from the time-periods where the perimeter was strictly controlled within a variation range of 100 - 150 nm while the 12 hours data series includes the time-periods where occasional and abrupt perimeter deformations occurred. The crucial laser parameters are summarised in Table 4.3.

Table 4.3 indicates that 8 mbar cavity pressure provides the most appropriate condition for developing self-referenced perimeter control. By contrast, a perimeter-stabilised ER-1 operating at a low operating pressure of 6 mbar yields the least sensitivity and stability. Compared to Figure 4.7, the decreased rotational resolution and mechanical stability in Figure 4.13 suggests that further technical improvement of the cavity stabilisation system needs to be considered. An alternative approach, might be a scheme based on the direct control of optical frequency via locking it to an external laser reference such as the SIOS laser. The heterodyne frequency produced by the optical frequency of ER-1 and the absolute frequency of the SIOS laser would be amplified and transferred to the frequency servo unit as a feedback signal.

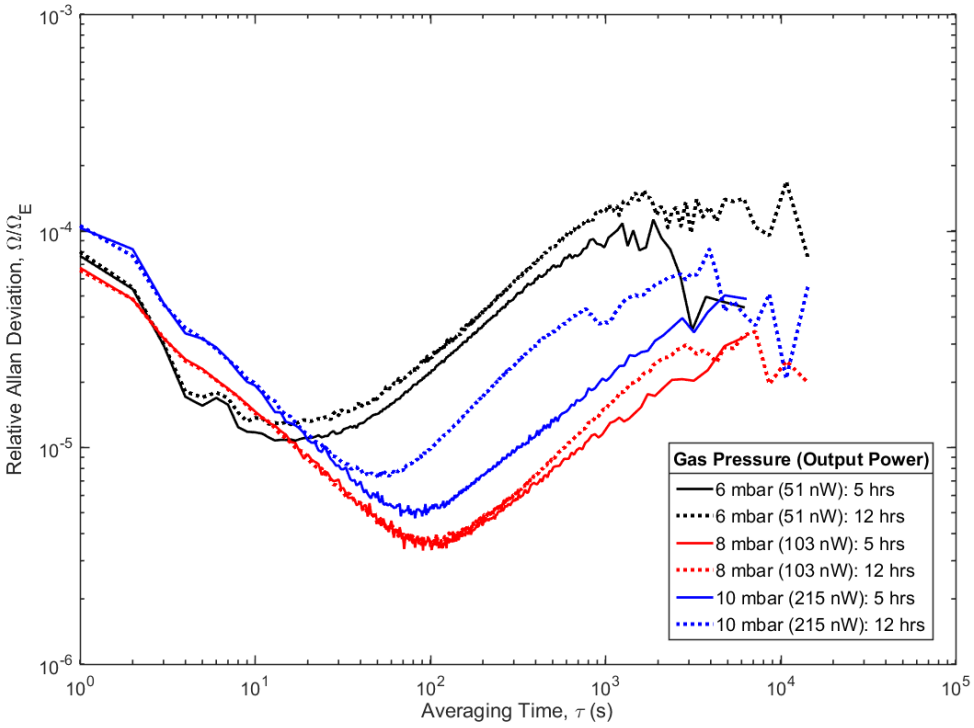

Figure 4.13: Relative ADEV plots used for the analysis of the gyroscopic sensitivity and stability obtained from laser operation with the self-referenced cavity stabilisation system.

Length L (hrs)	Pressure P (mbar)	Integration Time τ (s)	ADEV (Ω/Ω_E)	Resolution $\Delta\Omega$ (prad/s)	Usable Sensitivity Ω_s $(rad/s/\sqrt{Hz})$
5	6	17	1.1×10^{-5}	803	6.5×10^{-11}
	8	102	3.4×10^{-6}	248	1.9×10^{-11}
	10	82	4.7×10^{-6}	343	1.4×10^{-11}
12	6	16	1.3×10^{-5}	949	6.7×10^{-11}
	8	94	3.6×10^{-6}	263	1.9×10^{-11}
	10	51	7.2×10^{-6}	526	1.8×10^{-11}

Table 4.3: The crucial laser parameters obtained for a perimeter-controlled ER-1 operation at various cavity pressures.

4.4 Data Corrections for the Effects of Backscatter

The backscatter-coupling between two counter-propagating beams has long been recognised as the dominant mechanism by which a null shift bias causes gyro readout errors and thus deviation from absolute rotation rate sensing. In our large cavities, this is a small, time-varying effect which is nonetheless significant. We applied an error correction by using the linear analysis stated in Section 2.7.3. The backscatter perturbations on the measured δf_s are calculated as:

$$\delta f_{bs} = \frac{1}{2} m_1 m_2 \delta f_s \cos(\epsilon_1 - \epsilon_2), \tag{4.2}$$

where m_1 and m_2 are the fractional intensity modulations of the two beams, and ϵ_1 and ϵ_2 are their respective phase angles. The backscatter phase is denoted as $\varphi = \epsilon_1 - \epsilon_2$. These parameters were obtained via the DAQ system, which digitized the phase and amplitude signals detected from the photodetectors (PD 1 and PD 2 in Figure 4.4).

As shown in Figure 4.14, backscatter corrections were applied to post-process the Sagnac time series (using a five-day data length) obtained from single-mode operation. As stated previously, the perimeter control designed for long-term stability is still under development. Therefore, the active perimeter control was not in use. The raw δf_s frequency excursions displayed in Figure 4.14 (a) are visibly perturbed by instantaneous mode-hops and slow frequency pushing and pulling induced by the perimeter-dependent backscatter effect. However, these undesired perturbations are substantially reduced after bias corrections are applied, as shown in Figure 4.14 (b). In the corrected data, the Sagnac frequency maintains better consistency over time at a higher accuracy. Figure 4.14 (c) quantifies the time-varying frequency variation inferred from the bias correction. It also shows that occasional mode-hops led to a sudden change of the backscatter perturbation of 50 - 90 mHz.

Figure 4.15 characterises the typical sensor resolution before and after the backscatter corrections were applied. It is noticeable that the data is improved. This is evidenced by the longer averaging time from 57 s to 140 s, alongside an enhanced gyroscopic sensitivity from 2.6×10^{-11} rad/s/$\sqrt{\text{Hz}}$ to 1.6×10^{-11} rad/s/$\sqrt{\text{Hz}}$ (or equivalently, a rotational resolution of Ω/Ω_E increased from 5.6×10^{-6} (409 prad/s) to 2.8×10^{-6} (204 prad/s)). One can notice that the overall sensitivity obtained here is lower than that given in Figure 4.7 in the preceding section. Firstly, this is because the intra-cavity mirror cleanliness is slightly degraded after multiple gas refills at the time of measurement. The purpose of Figure 4.15 is to demonstrate laser stability during long-term operation. Therefore, Figure 4.15 used a Sagnac frequency time series over a 2 day period. However, we emphasise that invalid data measured from mode-hops were deleted, and interpolations were performed to bridge the data gaps to form a continuous and analysable data-set.

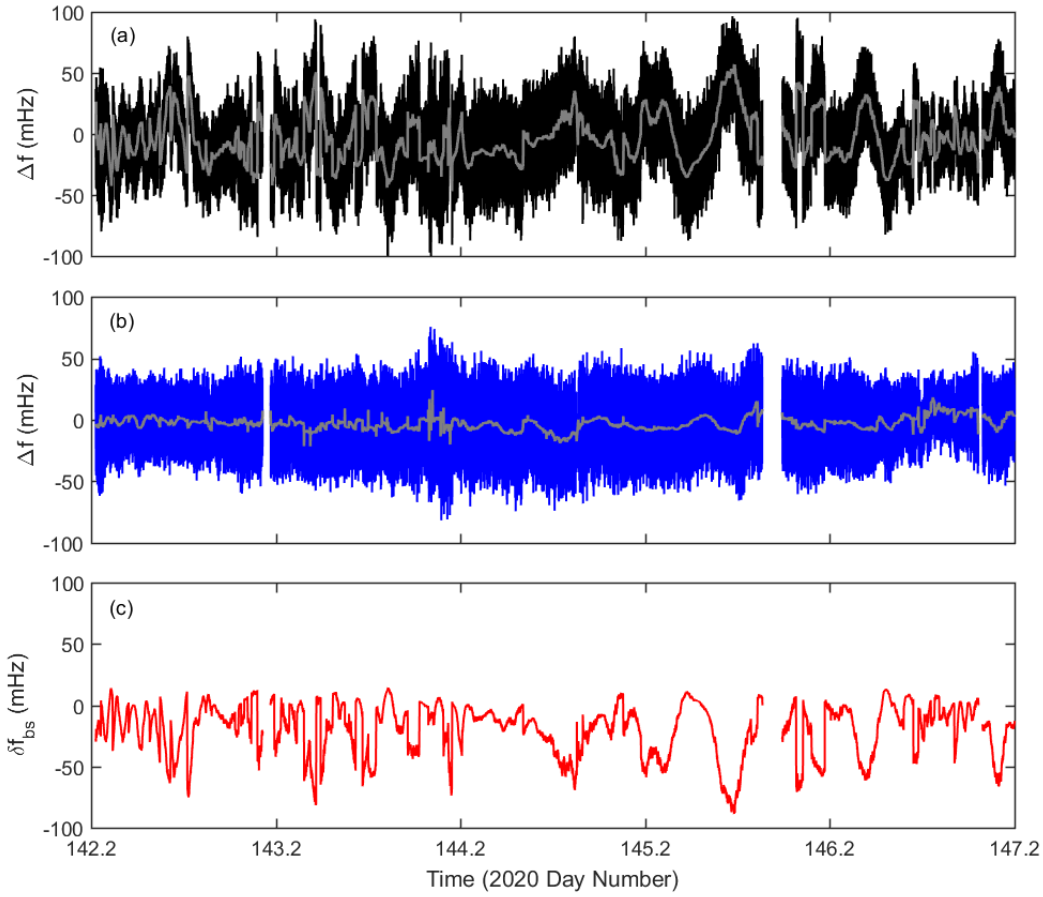

Figure 4.14: Backscatter corrections to the Sagnac frequency data series over a 5 day period. The Sagnac frequency (mean-reduced) write-outs are presented by 1 s (bold traces) and 60 s average (thin traces). In this figure, (a) shows the raw δf_s frequency excursions with no corrections applied (black trace); (b) shows the frequency excursions with backscatter perturbations reduced (blue trace); (c) quantifies the frequency-bias corrected from the backscatter-coupling effect (red trace). The x-axis is Coordinated Universal Time (UTC) with the number of days in 2020; the gaps in data-sets are from invalid time-periods due to split-mode operation.

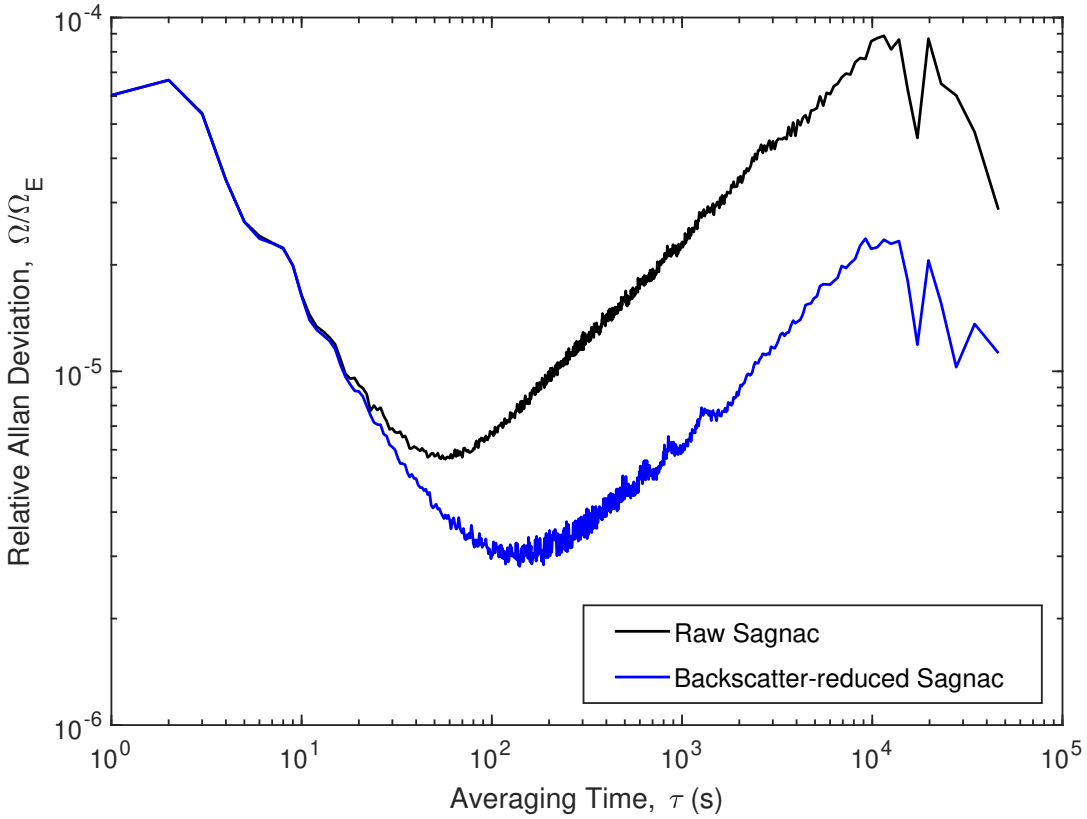

Figure 4.15: Relative ADEV plots of the raw and the backscatter-corrected Sagnac frequency used for characterising the gyroscopic performance during long-term operation.

4.5 ER-1 Applications in the Geo-Sciences

4.5.1 Marine Microseisms

Land-sea-interactions with an on-going energy exchange from ocean swells into the surf zone generate marine microseisms observable as periodic ground displacements and rotations [110]. Large ring lasers located in the near-ocean area have a greater chance of sensing oceanic microseisms compared to those located inland. Therefore, Canterbury laser gyros such as the UG-series, C-2 and G-0 have successfully detected microseismic activities.

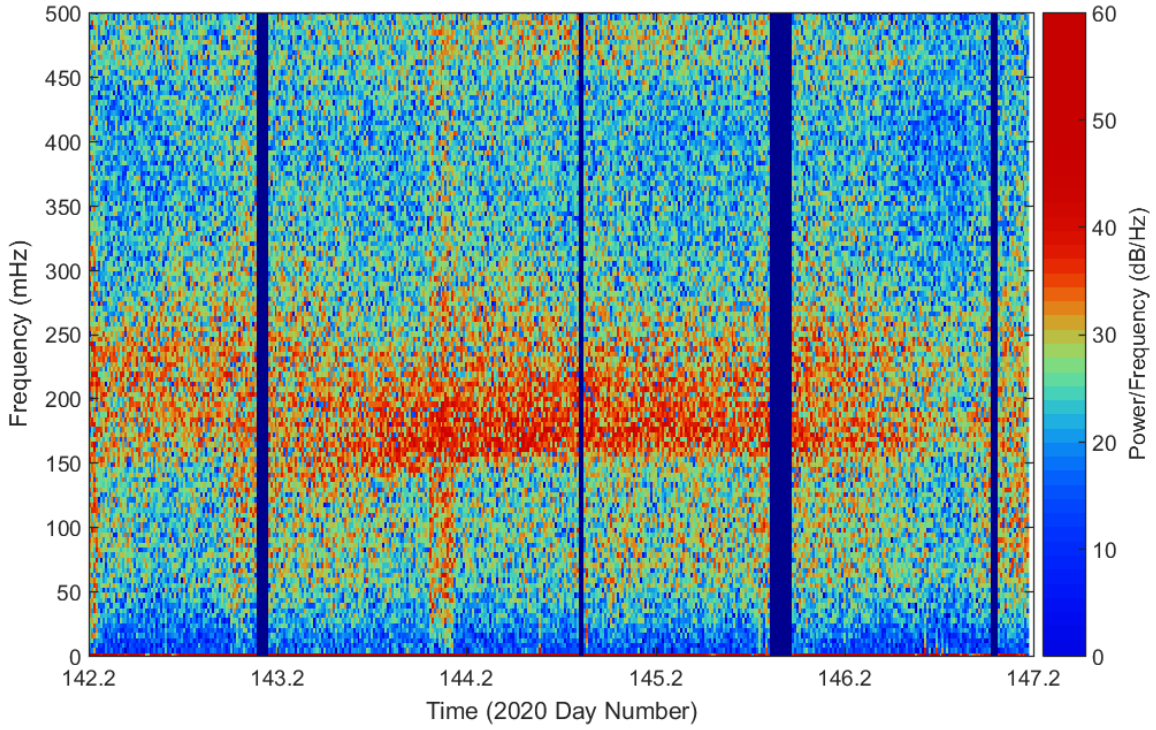

Figure 4.16: Periodic microseismic fluctuations as sensed by the ER-1 laser; the spectrogram presents a power spectral density probability function for the microseismic velocity data over 5 days. Partial time series for the earthquake and split-mode operation periods were excluded in order to show the clearest pattern of the marine microseisms. Note that the spectrogram was plotted from the time series of the backscatter-and-mean-reduced Sagnac frequency. The base sample rate was 1 Hz and the window length setting was 1024 s.

Owing to a relatively stable operational environment, a high rotational sensitivity, and an advantageous locality, ER-1 is ideally placed for continuous detection of marine microseisms. Figure 4.16 shows the long-standing and irreducible microseismic noise at the milliherz level via a time-based power spectrum of the Earth-rotation-reduced Sagnac frequencies. It reveals

that ground oscillations induced by the ocean swell activity always fall into a frequency band between 150 and 250 mHz. It is, however, notable that the exact period and amplitude varies on a daily basis. Therefore, ER-1 functions as an efficient tool for the study of geophysical signals of microseismic activities. We note that near day 144.0, the strong wind activity gave rise to the slow oscillation signal in a full frequency band of 0 - 500 mHz.

4.5.2 Ground Rotational Motions Induced by the Earthquake Event

It is well-known in seismology that a shallow earthquake can generate both body waves and surface waves detectable by different types of the instruments. Body waves like the P and S waves mainly produce the linear ground motions observable by classical seismometers, whereas surface waves introduce rotational ground motions, which can be sensed by ring lasers [38]. As a horizontally-placed laser gyro, ER-1 has great potential for measuring rotational motion around the vertical axis. Therefore, rotations around a vertical axis induced by the propagation of Love waves along the surface are the most prominent signals in any observation period.

An earthquake (M = 5.8) that occurred at 19:53:33 UTC on 24th May 2020 was clearly detected by ER-1 during the observation period. The distance from the epicentre (Northwest of Levin, New Zealand) to the observation location is about 395 km. In spite of an under-sampled measurement in Sagnac frequency (the recorded rate at 1 sec/sample), the arrival of seismic waves was clearly identified from the strong variations of the Sagnac frequencies (backscatter and Earth rotation background reduced) shown in Figure 4.17 (a) and (c). The S-waves and surface waves (or Love waves) occurred with a respective time delay of 92 s and 114 s, giving rise to energy bands observable in the earthquake spectrogram presented in Figure 4.17 (c). This suggests a phase velocity for the S-waves of 4.3 km/s and the Love wave of 3.5 km/s. Both of these measured velocities fit into the expected range. As indicated in Figure 4.17 (a), the maximum ground rotation rate given by this seismic event is 254 nrad/s.

We note that the backscatter perturbation varied by about 40 mHz (within 10 s) when the S-waves passed by, as shown in Figure 4.17 (b). The S-wave impact on the cavity scale factor decreased after 30 s, and correspondingly the magnitude of backscatter returned to its previous level. By referring to Figure 4.14 (c), it is obvious that a 40 mHz variation of the backscatter perturbation is comparable to the instantaneous backscatter variations observed during mode-hops. We assume that the sudden jump of the backscatter degree is attributable to a geometric variation within one wavelength (about 633 nm), and suggest that the installation is suitable for local seismic measurements.

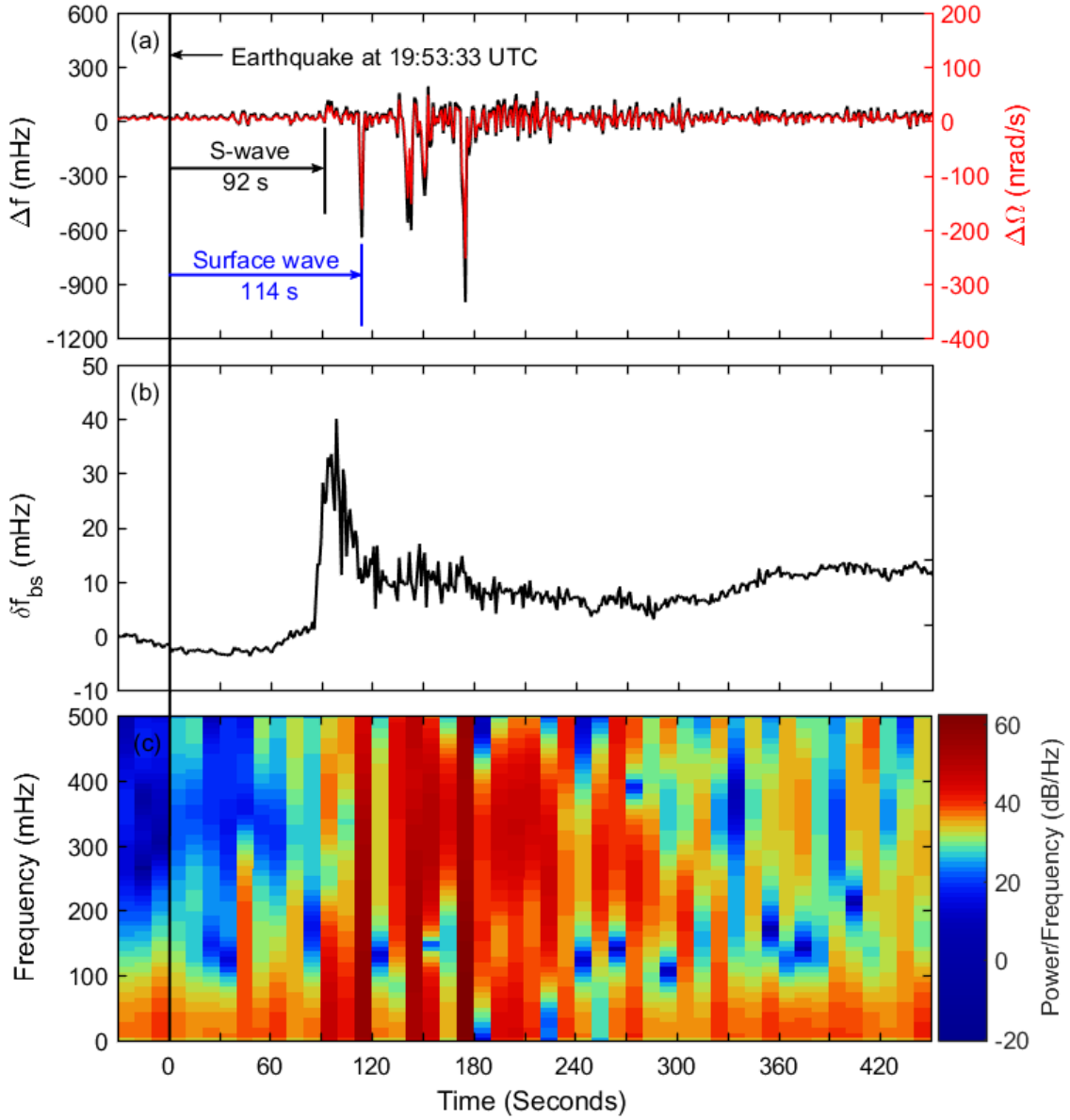

Figure 4.17: Earthquake on 24th May 2020, 19:53:33 at NW Levin, NZ as measured by the ER-1 ring laser, where (a) shows the Sagnac frequency variations Δf with black trace (left y-axis) and the converted ground rotation rates $\Delta\Omega$ with red trace (right y-axis); (b) shows the frequency error (δf_{bs}) contributed by the backscatter effect; (c) shows the correlated earthquake spectrogram. The timestamp in the x-axis is expressed by 'seconds since earthquake'. Note that the unusual shape of the earthquake signal was due to the significant undersampling.

4.6 Conclusion

We have presented first operational results from a 10 m perimeter, He–Ne based heterolithic ring laser located on the ground floor of a five-storey building. The results are promising and certainly the best we have achieved for a rotation sensor housed within a substantive building structure. As the laser itself is rigidly constructed on a 3 m thick, massive concrete base, the laser cavity is stable against the ambient temperature and pressure changes experiencing only modest thermal variations to its observed linear dimensions (2.7 to 5 μm per day). Having total optical losses of 88.9 ppm, the laser operating at the 632.8 nm wavelength with an optimised gas pressure between 8 and 10 mbar, obtained the highest rotational resolution of 36 prad/s at a measurement time of 512 s. This translates to a highest raw sensitivity at 1.8×10^{-10} rad/s/$\sqrt{\text{Hz}}$ obtainable with an integral time of 1 s. With the implementation of a slow self-referenced perimeter stabilisation technique, stable gyroscopic operation was continuously achieved for more than one day. Finally, we have demonstrated the observation of both ocean-generated microseismic signals in the 150 - 250 mHz frequency band as well as medium-sized, regional earthquakes, inferring phase velocities for the S-waves and Love waves consistent with expectations.

5 Operation of a 10 Metre Perimeter Ring Laser on the 611.8 nm Neon Transition

In this chapter, we present the gyroscopic performance of ER-1 in a frequency-upscaled operational regime (from 474 THz to 490 THz). Two sets of IBS-coated supermirrors having the same centre wavelength of 611.8 nm but a different focal length of either 3 m or 10 m are employed to explore ER-1's scientific potential. This experiment is highly useful as it demonstrates how different mirror configurations would influence the gyroscopic performance of a large ring laser. We begin with calculations of laser beam profiles to evaluate the beam stability obtained from different cavity configurations. Later, we separately describe the oscillator parameters, operational conditions, and overall laser performance obtained from each cavity configuration. The main objective is to evaluate the practical implementation of sensitivity upgrade through the operation on a shorter optical wavelength.

5.1 Laser Beam Profiles Obtained from Two Mirror Configurations

The ER-1 cavity was configured using four concave mirrors with the same radius of curvature (ROC) at either 4 $\times$ 3 m or 4 $\times$ 10 m. Beam parameters such as the waist sizes and waist positions for these two configurations are calculated and compared in Table 5.1. For the 3 metre ROC symmetric mirror configuration, the beam waist focused at the mid-arm is calculated to be 0.90 mm in-plane and 1.22 mm out-of-plane, and the waist size on the mirrors is calculated to be 1.40 mm in-plane and 1.46 mm out-of-plane. For the 10 m configuration, the calculated beam waist is 1.45 mm in-plane and 1.77 mm out-of-plane, and the waist size on the mirrors is 1.60 mm in-plane and 1.85 mm out-of-plane. The beam size at the waist and mirror surface are all reported as 2 times the $1/e^2$ beam intensity radius.

It is shown that the beam sizes obtained using the 10 metre ROC mirrors are much larger than those obtained using the 3 metre ROC mirrors. Since the gain tube used for the experiments is 4-mm-in-diameter, these mirrors seem to be suitable for our experiment as the beam waist obtained from either configuration is smaller than the 4 mm diameter aperture size. As the intra-cavity diffraction loss is proportional to the waist size, the cavity photon lifetime measured from a configuration using the 3 m ROC mirrors should be longer than that obtained from the other configuration.

A fundamental condition for a stable cavity configuration is that the plane-waves as formed can converge after travelling a round trip allowing for the build-up of a stable Gaussian

Parameter	ROC = 3 m		ROC = 10 m	
	in-plane	out-of-plane	in-plane	out-of-plane
Beam waist size (mm)	0.90	1.22	1.45	1.77
Beam size on mirrors (mm)	1.40	1.46	1.60	1.85
Waist position (m)	0	0	0	0
Bilger-Stedman stability, k	1.51	-0.24	-1.89	-1.49
Rigrod stability, L/f	0.49	2.24	3.89	3.49

Table 5.1: The location and size of the beam waist, beam size on the mirrors, Bilger Stedman Stability, and Rigrod Stability, calculated for two cavity configurations as formed by four concave mirrors with ROC of either 3 m or 10 m. Note that the waist positions are reported in a clockwise manner starting from the mid-point of the relevant side; all beam sizes reported are two times the $1/e^2$ beam intensity radius. These calculations were done using a program originally developed by Dr. Bob Dunn and Prof. Geoff Stedman to calculate the beam stability for planar rectangular cavities.

mode. As such, two independent criteria denoted as the Bilger-Stedman Stability [111] and the Rigrod stability [112, 113] are introduced to evaluate whether the cavity is stable. Rigrod and Pierce demonstrated that the stability condition for a quadrilateral resonator made from spherical mirrors is: $0 < \frac{L}{f} < 4$, where L is the spacing of the mirrors and f is the focal length of the mirrors [112, 113]. This stability index ($\frac{L}{f}$) is specifically applied to evaluate the boundary condition for the travelling-waves of a Gaussian beam while considering the astigmatism induced using spherical mirrors at 45°. However, stability evaluations of a large planar ring laser should not depend solely on this criterion. The accuracy of the beam steering and tolerance of the beam deviation to the designed path should also be assessed. For this reason, a stability parameter (denoted as factor 'k') as stated by Bilger and Stedman is adopted to assess the sensitivity of beam steering with regards to the mirror misalignment [111]. In brief, within certain limits the beam deviation relative to ideal ray propagation in an optimally-aligned ring is tolerable if the stability condition of $-2 < k < 2$ is satisfied. It is emphasised that the selected mirrors in respect of their conic section and radii of curvature should avoid yielding a positive criticality at $k = 2$ since the beam steering tends to diverge in this unstable regime.

As shown in Table 5.1, both the 3 m and 10 m ROC mirrors can be used to create a ring cavity within the beam stability regimes. ER-1 operating with mirrors having 3 m ROC seem to provide a more stable cavity, as the stability parameters given by this configuration are much further away from the critical edges marked for unstable regimes. The experimental results provided by these two resonant configurations will be reported and discussed in the following sections.

5.2 A Cavity Configuration with Four Spherical Mirrors of 3 m ROC

5.2.1 Cavity Parameters Obtained from Two Different Alignments

ER-1 was aligned to yield a maximised laser output power for a minimised plasma discharge power. Under this circumstance, the longest ring-down time was measured at 510 μs as obtained from a TEM_{01} output. This ring-down time indicates a Q of 1.6×10^{12}, a minimum cavity loss of 65.4 ppm, and a finesse of 9.6×10^4. We then realigned the cavity and gain tube to yield TEM_{00} output. The cavity parameters as characterised from both alignments are given in Table 5.2.

Parameter	TEM_{01}	TEM_{00}
Ring-down time, τ (μs)	510	485
Total loss, L (ppm)	65.4	68.7
Quality factor, Q	1.6×10^{12}	1.5×10^{12}
Finesse, F	9.6×10^4	9.1×10^4

Table 5.2: Ring-down time, total cavity loss, quality factor Q, and finesse F, as measured from laser output having either TEM_{01} or TEM_{00} mode patterns.

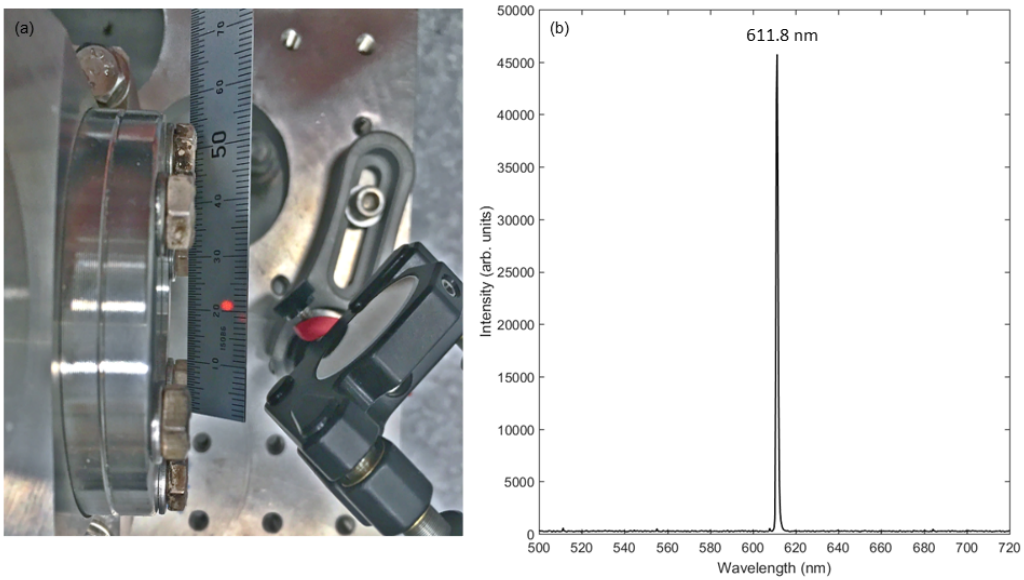

Figure 5.1: The laser beam output in a TEM_{00} pattern and the spectrum detected from a spectrometer: where (a) shows an observed beam diameter at around 1.6 mm; (b) shows lasing at 611.8 nm.

In principle, high-order transverse modes should only have sufficient gain with a large diameter gain tube which is well centred around the modal volume. Only when the centre axis of the narrow gain tube and the optical axis of the four supermirrors are aligned, the laser gain is maximised, and the overall diffraction loss induced by the aperture effect is minimised [114, 115]. Figure 5.1 (a) shows the TEM_{00} laser output with an observed beam diameter of approximately 1.6 mm. Figure 5.1 (b) presents a laser spectrum as measured by a spectrometer, with only the 611.8 nm transition observed. In the following sections, ER-1 operation using these two transverse modes will be compared and discussed.

5.2.2 Essential Features of 611.8 nm ER-1 Operation

As previously stated in Section 3.2.6, 611.8 nm operation gives promising performance comparable to that given by operation at 632.8 nm. To fully explore the 611.8 nm laser potential, the lasing behaviour, operable gas pressure regions, and RF excitation efficiency were investigated. We emphasise that laser operation at a cavity pressure beyond 7.5 mbar is impracticable because lasing ceased after the He-Ne gain medium was evenly mixed about 2 hours after the gas fill. The operable laser powers using a cavity pressure between 5.5 to 7.5 mbar are given in Table 5.3.

Gas pressure (mbar)	Single-mode (nW)	Phase-locked mode (nW)
5.5	0-69	69-108
6.5	0-82	82-225
7.5	0-100	100-545

Table 5.3: Operable laser powers for stable gyroscopic operation as measured for cavity pressures of 5.5, 6.5 and 7.5 mbar respectively.

Figure 5.2 shows the relationship between the RF input power and the laser output for various cavity pressures. It indicates that the plasma discharge was extremely efficient with an RF input power below 5 W, and higher gain was obtainable using a lower cavity pressure. Moreover, the measured output powers from the TEM_{01} mode were generally two times higher than those measured from the TEM_{00} mode when the same RF excitation power was applied. RF input powers required for minimum lasing with a TEM_{01} mode at a cavity pressure of 5.5, 6.5 and 7.5 mbar, were measured at 0.5, 1.2 and 1.4 W, respectively. As for the minimum lasing with a TEM_{00} pattern, the RF power required was 0.7, 0.8, and 1 W respectively.

As calculated from Equation 4.1, 611.8 nm ER-1 operation is expected to yield a Sagnac frequency in the vicinity of 205.14 Hz. Figure 5.3 presents an FFT power spectrum with an Earth rotation peak at approximately 205.23 Hz. It is noticeable that RF transmitter noise can

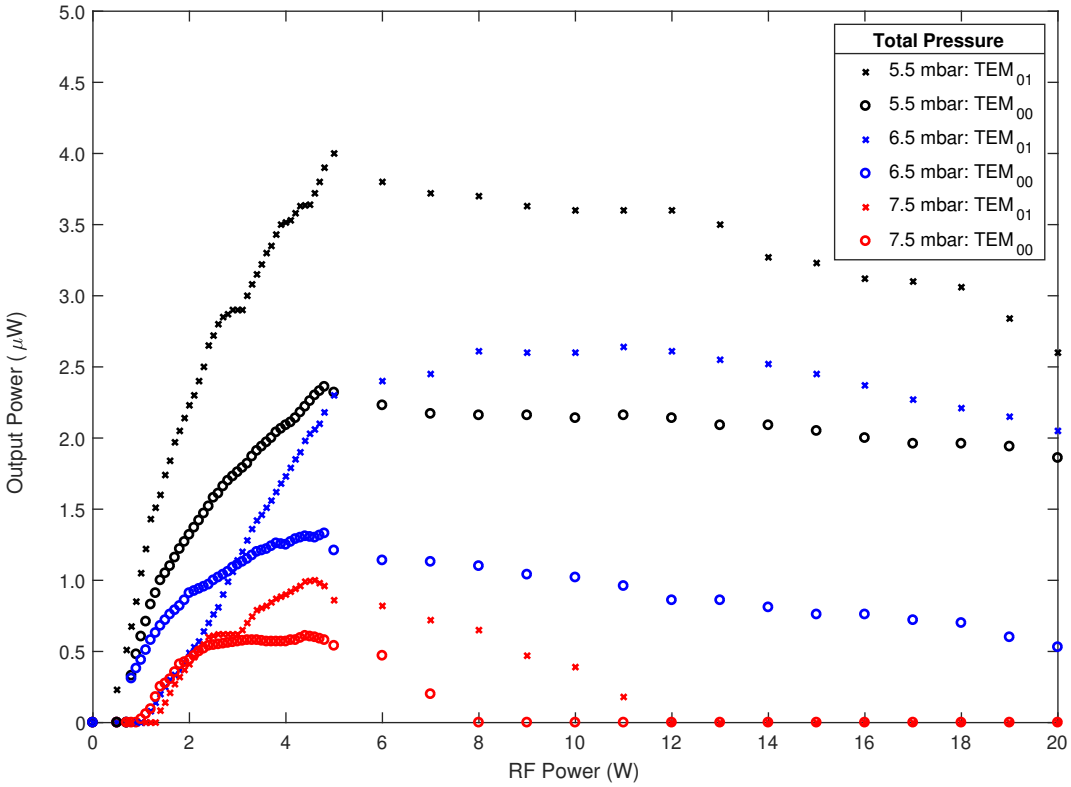

Figure 5.2: Laser output power as a function of RF input power. The laser efficiencies were determined from operation on either the TEM_{01} or the TEM_{00} modes. Measurements were performed for three different cavity pressures at 5.5, 6.5, and 7.5 mbar; the 50:50 neon partial pressures were all fixed at 0.3 mbar. We note that the laser efficiency for a 7.5 mbar gas pressure was measured within 2 hours of the gas fill. After this time, laser action ceased.

be observed in the FFT spectrum. This is because the RF power required for 611.8 nm lasing is higher than that for 632.8 nm and due to imperfect RF shielding.

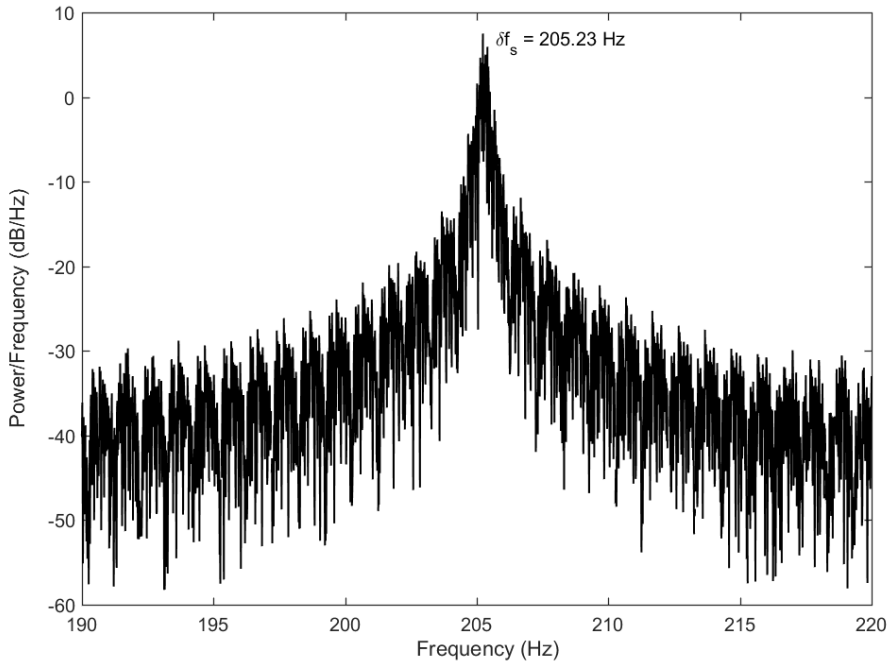

Figure 5.3: The FFT power spectrum shows the Earthline at a frequency of 205.23 Hz.

5.2.3 Gyroscopic Operation using the TEM_{01} and TEM_{00} Transverse Modes

The laser performance was obtained from operation at the highest operable pressure of 6.5 mbar. Figure 5.4 compares laser performance over a 48 hour period as obtained from both TEM_{01} and TEM_{00} operation in either the single-mode or the phase-locked mode configurations. All essential parameters provided by these four independent operational regimes are summarised in Table 5.4. The Sagnac time series presented in Figure 5.4 (a) and (b) suggest that operation with a high-order transverse mode is more likely to be disrupted by mode splitting.

From observation, it is noticed that high-order transverse modes are more susceptible to alignment variations and mechanical vibrations of the cavity, when compared to the lowest order transverse mode. Furthermore, higher order modes tend to split longitudinal mode operation more often. Mode splitting is introduced by non-reciprocal effects. Essentially, it occurs as the two oppositely-directed modes experience unequal frequency pulling effects. This is likely due to the larger waist size at the gain tube and on the mirrors. In addition, operation on higher order modes yields a larger deviation from the theoretical value. We note that a similar phenomenon was also reported by Graham [116]. Referring back to Figure 5.4, the mean Sagnac frequencies measured from TEM_{01} and TEM_{00} operation are 205.38 and 205.27 Hz, respectively. The 0.11 Hz Sagnac frequency offset implies that the actual operating frequency of the TEM_{01} mode was 254 GHz higher than that of the TEM_{00} mode. The TEM_{00} mode offers the smallest beam size at the mirrors and thereby the lowest

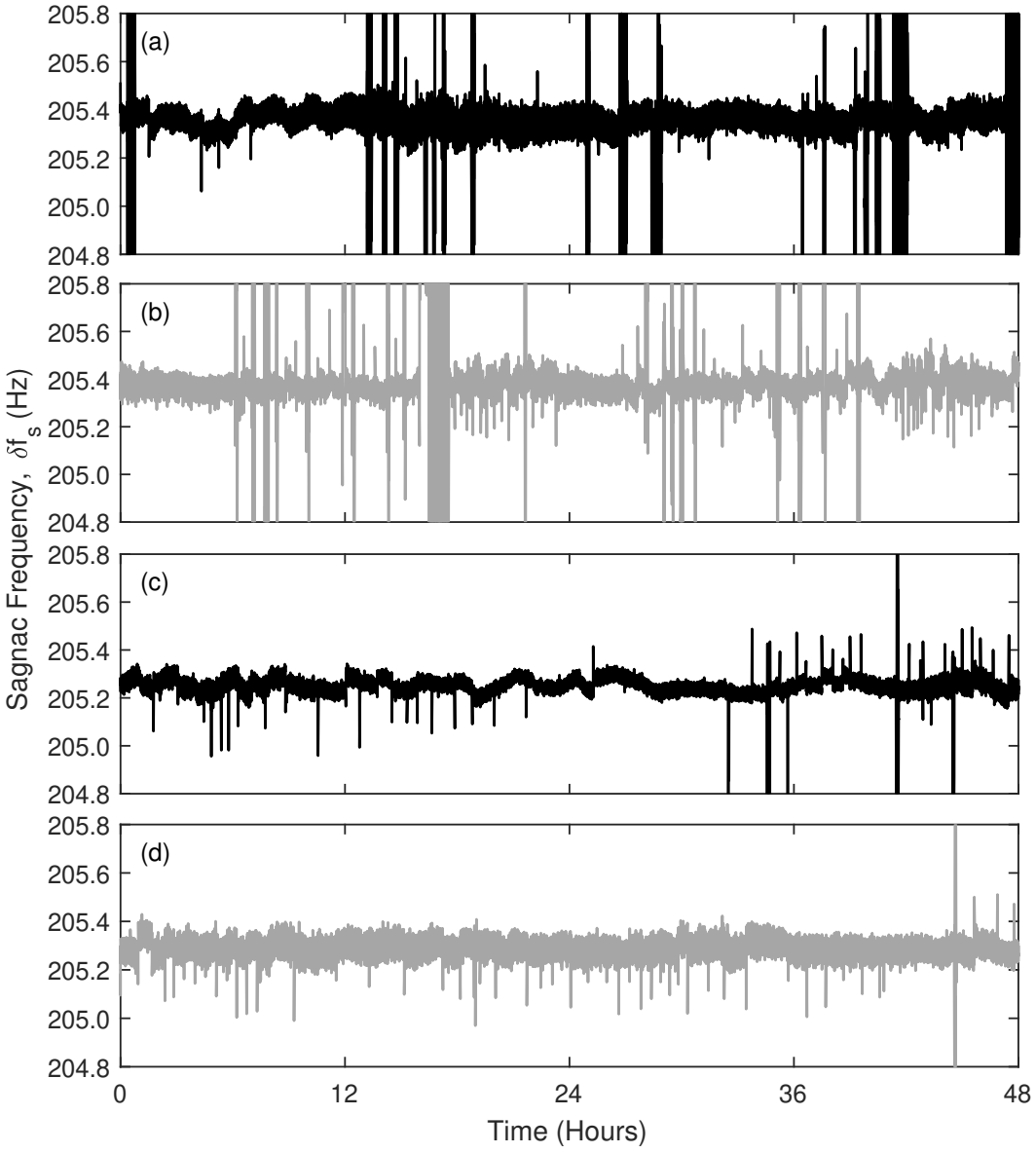

Figure 5.4: Sagnac frequency (raw) time series as obtained from operation in (a) single-mode with a TEM_{01} pattern, (b) phase-locked mode with a TEM_{01} pattern, (c) single-mode with a TEM_{00} pattern, and (d) phase-locked mode with a TEM_{00} pattern. The black traces show the single-mode performance, while the grey traces denote the phase-locked mode performance. The sampling rate of the DAQ system was at 5 kHz, and the frequency write-outs were 1 sec/sample.

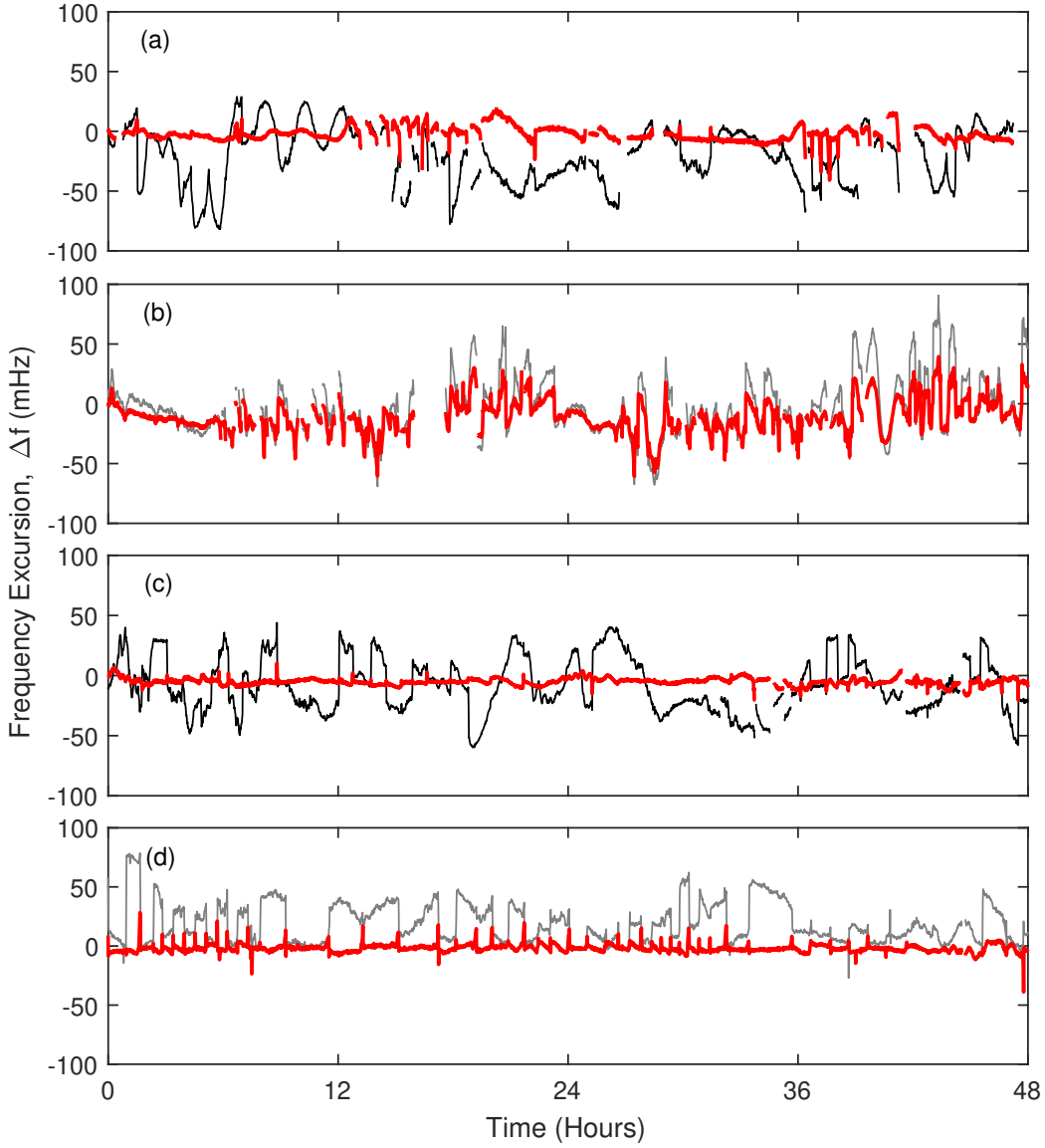

Figure 5.5: Mean-subtracted data series of the raw and backscatter-corrected Sagnac frequency. The presented mean-subtracted frequencies were from laser operation in (a): single-mode with a TEM_{01} pattern, (b): phase-locked mode with a TEM_{01} pattern, (c): single-mode with a TEM_{00} pattern, and (d): phase-locked mode with a TEM_{00} pattern. The raw δf_s frequencies obtained from the single-mode and the phase-locked mode operation are denoted by black traces and grey traces, respectively; all backscatter-and-mean-reduced δf_s are marked out by the red traces; the sample write-outs here are presented as a 60 s average.

	TEM_{01}		TEM_{00}	
Parameter	Single mode	Phase-locked	Single mode	Phase-locked
Output power (nW)	105	135	60	85
CCW beam modulation (%)	0-4.1	0-2.2	0-2.7	0-3.0
CW beam modulation (%)	0-4.7	0-3.3	0-3.5	0-4.0
δf_s contrast ratio (%)	62-66	56-61	73-77	74-77
Frequency excursion (mHz)	111	138	108	87
Occurrence of mode splitting	19	20	4	1

Table 5.4: The output powers, monobeam modulations, Sagnac contrast ratios, overall frequency excursions, and occurrence of mode splitting given by 48 hours laser operation on various conditions are summarised for a comparison.

backscatter perturbation. In addition, TEM_{00} has higher cross-sectional coherence. Therefore all gyroscopic performance in the following is analysed using 611.8 nm operation with a TEM_{00} output.

Figure 5.5 (a) to (d) presents the Earth-rotation-normalised Sagnac frequency. The four selected data-series (with the backscatter perturbations either included or excluded) are all consistent with those presented in Figure 5.4. We know fairly well that backscatter-coupling is the biggest source for frequency noise as it is responsible for at least 90% of the total systematic bias. Nevertheless, the majority of the frequency error bias can be reduced via backscatter corrections. As evidenced by Figure 5.6 and Table 5.5, the backscatter correction can double the rotational resolution. We note that the current mathematical model applied for backscatter corrections was originally developed for single-frequency operation [47]. Therefore, backscatter corrections only work well for single mode, TEM_{00} operation. It can be seen that the backscatter-removed TEM_{01} laser performance in terms of the frequency stability and sensitivity was scarcely enhanced. Models for backscatter corrections in the presence of multiple optical frequencies are not available. This is because in the context of multiple-frequency operation the backscatter phase of each mode is unknown and only the central mode can be estimated.

For phase-locked mode operation, the detected signal has contributions not only from a strong central mode but also from two weaker side modes. It is conceivable that the superposition of these three independent signals leads to a less accurate averaging of backscatter phase and the AC and DC amplitudes of the single beam. Hence, backscatter-induced frequency errors cannot be evaluated and ruled out precisely due to the (relatively) large uncertainty in parameter estimations. Moreover, the amplitude servo unit uses the intensity integral as the feedback signal. Therefore, a well-sustained operational power would not guarantee an absolutely constant intensity for each of the modes.

No perimeter control was used for 611.8 nm operation. Under such circumstances, mode-

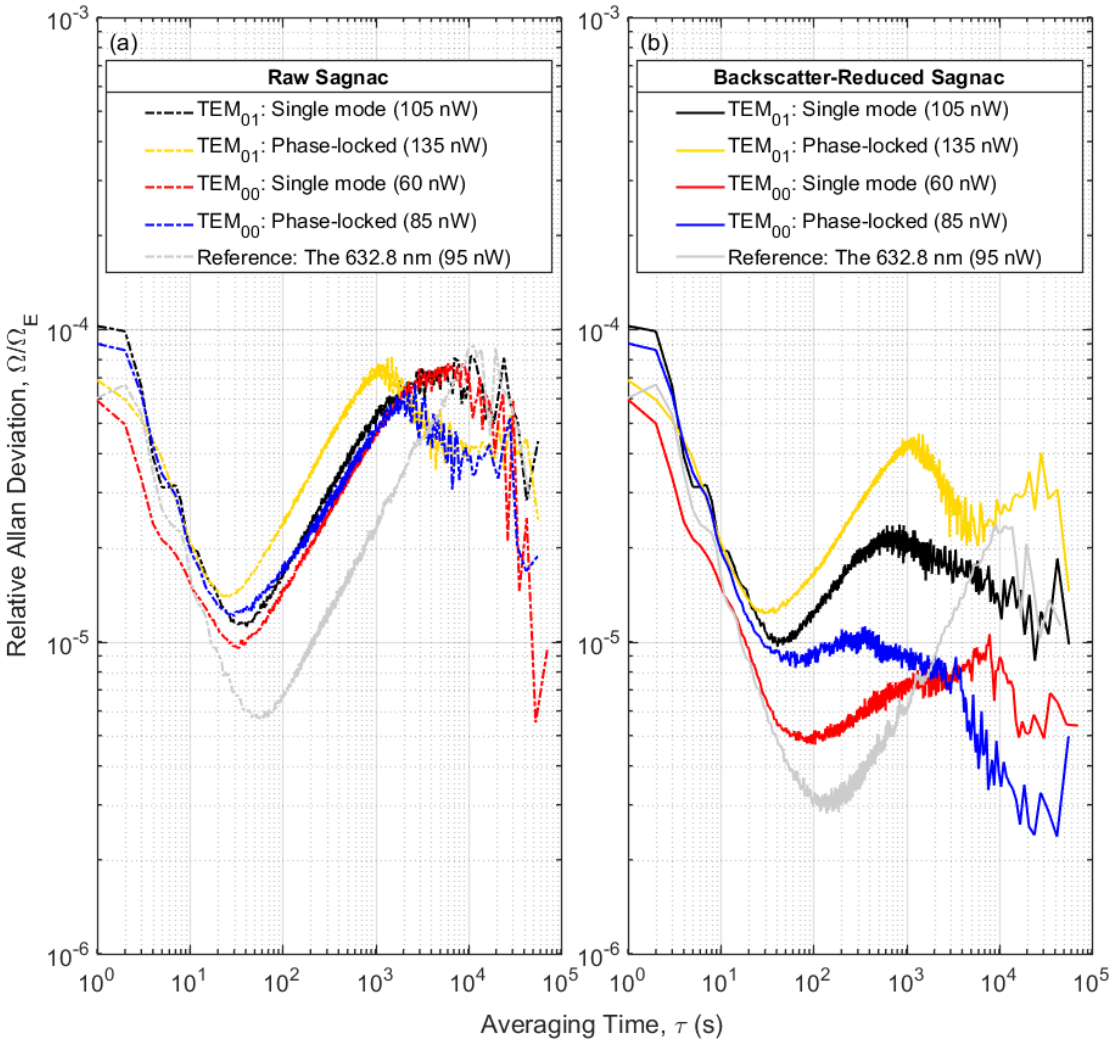

Figure 5.6: Relative Allan deviation plots over a 48 hour period as yielded from operation: single-mode with a TEM_{01} pattern, phase-locked mode with a TEM_{01} pattern, single-mode with a TEM_{00} pattern, and phase-locked mode with a TEM_{00} pattern. The subplot (a) presents the raw sensing capabilities via the uncorrected Sagnac time series, while (b) shows the improved sensor behaviour by using the backscatter-corrected frequency.

Operation		Sensor Stability and Resolution					
Mode Structure		Raw Sagnac			Backscatter-reduced Sagnac		
Transverse Mode	Longitudinal Mode	τ (s)	ADEV (Ω/Ω_E)	Resolution (prad/s)	τ (s)	ADEV (Ω/Ω_E)	Resolution (prad/s)
TEM_{01}	Single	41	1.1×10^{-5}	803	41	9.6×10^{-6}	701
	Phase-locked	26	1.4×10^{-5}	1022	29	1.2×10^{-5}	876
TEM_{00}	Single	34	9.5×10^{-6}	694	104	4.7×10^{-6}	343
	Phase-locked	30	1.2×10^{-5}	876	64	8.2×10^{-6}	599

Table 5.5: The 611.8 nm laser parameters including the longest integration times, ADEV normalised to the Earth rotation rate, and usable sensor resolutions obtained from independent operation in various mode configurations.

hops inevitably occurred, and the rate at which they occur can affect the overall appearance of the Allan deviation plot. Thus, the number of mode-hops in the Sagnac data series is the major impact factor for the Allan deviation at a longer averaging time.

It has been well-studied that high cavity pressure allows the laser to drift through a wide range of optical frequencies before jumping to the next mode index. Due to the low operable gas pressures, the 611.8 nm laser experienced mode-hops more frequently and therefore generated more frequency noise than using 632.8 nm operation. In terms of long-term laser operation, the 611.8 nm gyroscopic performance was slightly inferior to the 632.8 nm performance, as shown in Figure 5.6.

Operation		Sensor Stability and Resolution					
Mode Structure		Raw Sagnac			Backscatter-reduced Sagnac		
Transverse Mode	Longitudinal Mode	τ (s)	ADEV (Ω/Ω_E)	Resolution (prad/s)	τ (s)	ADEV (Ω/Ω_E)	Resolution (prad/s)
TEM_{01}	Single	101	4.1×10^{-6}	299	228	1.8×10^{-6}	131
TEM_{01}	Phase-locked	74	4.8×10^{-6}	350	137	2.5×10^{-6}	182
TEM_{00}	Single	52	5.3×10^{-6}	387	225	1.1×10^{-6}	80
TEM_{00}	Phase-locked	74	4.7×10^{-6}	343	135	2.0×10^{-6}	146

Table 5.6: The 611.8 nm laser parameters obtained from operation on various mode configurations. The frequency stability (denoted by the integration time at the lowest ADEV), the ADEV normalised to the Earth rotation rate, and the highest usable sensor resolution are listed and compared to investigate the short-term gyroscopic performance.

As the phase changes randomly and discontinuously when a mode-hop occurs, any Sagnac frequency estimated from the mode-hop-included time interval is invalid. Therefore, we

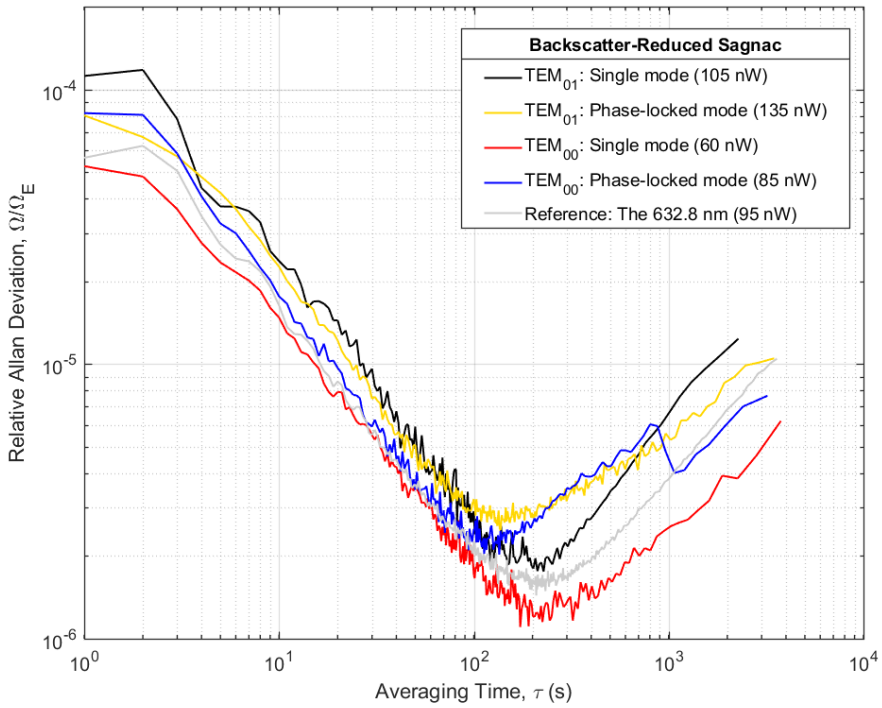

Figure 5.7: Relative Allan deviation. The ADEV used the backscatter-reduced Sagnac frequency time series obtained from laser operation at single-mode with a TEM_{01} pattern, phase-locked mode with a TEM_{01} pattern, single-mode with a TEM_{00} pattern, and phase-locked mode with a TEM_{00} pattern. Note that the best short-term 632.8 nm performance was also provided here (grey traces) as a reference.

present another ADEV plot (Figure 5.7) using mode-hop excluded Sagnac data to demonstrate short-term gyroscopic performance which is primarily limited by the ambient building noise. As shown in Figure 5.7, gyroscopic sensitivity and stability of 611.8 nm operation is comparable to that of 632.8 nm operation. As shown in Table 5.6, the usable rotational resolution provided by 611.8 nm ER-1 operation was determined to be $1.1 \times 10^{-6}\Omega_E$ (80 prad/s) at an integral time of 225 s. This result proved the feasibility of high-sensitivity rotation sensing using a frequency-upscaled 611.8 nm neon transition.

5.2.4 The 611.8 nm Frequency-Upscaled Laser Gyro in Seismological Detection

Revealing a Repetition of the Microseismic Patterns

Sagnac phase fluctuations caused by marine microseisms can yield features in the ADEV plot which can be observed in Figure 5.6 between 2 to 5 s. This microseismic signal can be seen in the two spectrograms demonstrated by Figure 5.8 (a) and (b). It is observed that both spectrograms present a 'tree branch' pattern even though they were separately obtained on different days. It is clear that a continuous excitation of the primary frequency content was in the range of 180 - 250 mHz. On top of that, a second frequency component at 350 mHz was excited at around mid-day of the UTC frame (midnight New Zealand local time) in both cases. This secondary frequency decreased within 4 to 7 hours and eventually merged with the fundamental one being continuously excited. As there is an observation gap between day number 204 and 219, we cannot conclude the minimum repeat cycle required for this pattern.

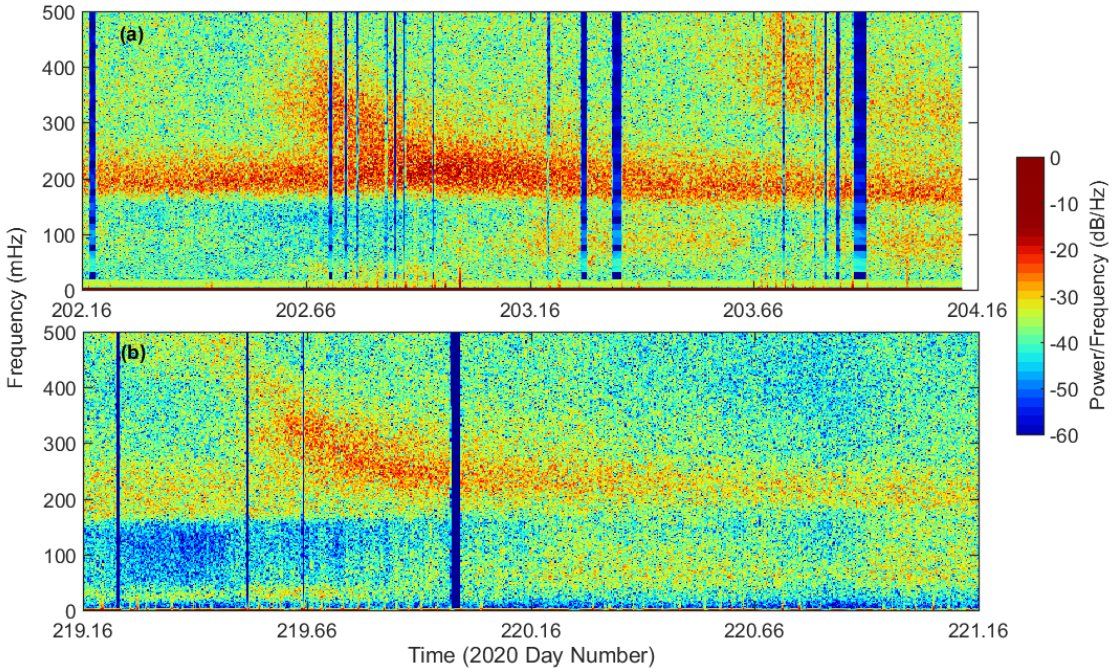

Figure 5.8: The marine microseismic patterns as observed in (a) TEM_{01} and (b) TEM_{00}. The x-axis is expressed in the Coordinated Universal Time (UTC) with the decimal day in 2020.

We point out that this microseismic pattern can be initiated from a continuous event or a secondary source as given by the meteorological pattern. Moreover, the origin of this excitation might be located far away. A determination of the origin of the excitation is technically feasible via a noise analysis of the rotational and translational motion [110]. This noise information can be measured by an auxiliary instrument such as a seismometer or other

extended environment observations. In the absence of such additional measurements, one plausible assumption is that the observed patterns originate from tectonic plate activity, such as slow earthquakes that occur with a randomly matched timing during the day. This unique pattern appears to be interesting for further study in the seismology field.

Earthquake Measurements

A shallow earthquake event (magnitude = 5.4, depth = 5 km) occurred at the UTC 10:16:45 on August 12th of 2020 and was detected by ER-1 while it was operating on the frequency-upscaled 611.8 nm transition (see Figure 5.9). The epicentre was located at 35 km west of Milford Sound in New Zealand, about 425 km away from the observation location. Compared to the last seismic event detected using 632.8 nm operation (refer to Figure 4.17), the horizontal ground rotational motions detected for this event were observed with higher quality. One can see that the orientation of Sagnac amplitudes which denotes clockwise or counter-clockwise rotational motion, was measured in a more evenly distributed manner.

As indicated in Figure 5.9 (a), the S-waves and Love waves were detected with a respective time delay of 99 s and 127 s. Therefore, the propagation velocities for the S-waves and Love waves were calculated as 4.3 km/s and 3.3 km/s, respectively. As converted from a 317 mHz maximum variation of the Sagnac frequency, this seismic event induced a highest ground rotation rate of 78 nrad/s. Figure 5.9 (b) implies that the shear waves did not deform the cavity geometry even by a slight amount, as the backscatter contribution is maintained at a consistent level throughout the observation period. The δf_{bs} variation that generally occurred with a low oscillation frequency between 133 mHz to 183 mHz (8 - 11 cycles per minute) is related to the microseismic background (introducing periodic tilt or rotational motion).

Table 5.7 compares two earthquakes respectively detected using the standard 632.8 nm and frequency-upscaled 611.8 nm gyroscopic systems. These two seismic events have epicentres at a similar distance to the ER-1 site (see Figure 5.10). As compared in Table 5.7, the magnitude of the earthquake at Milford Sound was 0.4 ($\pm$0.2) smaller than that of the one at Levin. Based on the definition of Richter magnitude scale (M) [117], the amplitude of the seismic waves and the energy released from the epicentre at Milford Sound, should be approximately 4 times smaller than those from the other. Our measurement results are in agreement with this expectation. The ground rotation rates derived from the earthquake at M = 5.4 are 3 $\sim$ 4 times smaller than those induced from the earthquake at M = 5.8. Demonstrated by Figure 5.9 and Table 5.7, the shear-waves generated from Milford Sound seemed to have a more powerful influence on the ground deformations when compared to those generated from Levin. Despite that the earthquake at Milford Sound has a smaller magnitude, the S-waves introduced transient ground movements (about 46.2 nrad/s) to a greater extent when compared to the ground motion (32.3 nrad/s) as induced by the S-waves from Levin. This result is explainable as the earthquake at M = 5.4 was activated at a shallower depth (5 km) compared to the other at M = 5.8 (depth = 37 km).

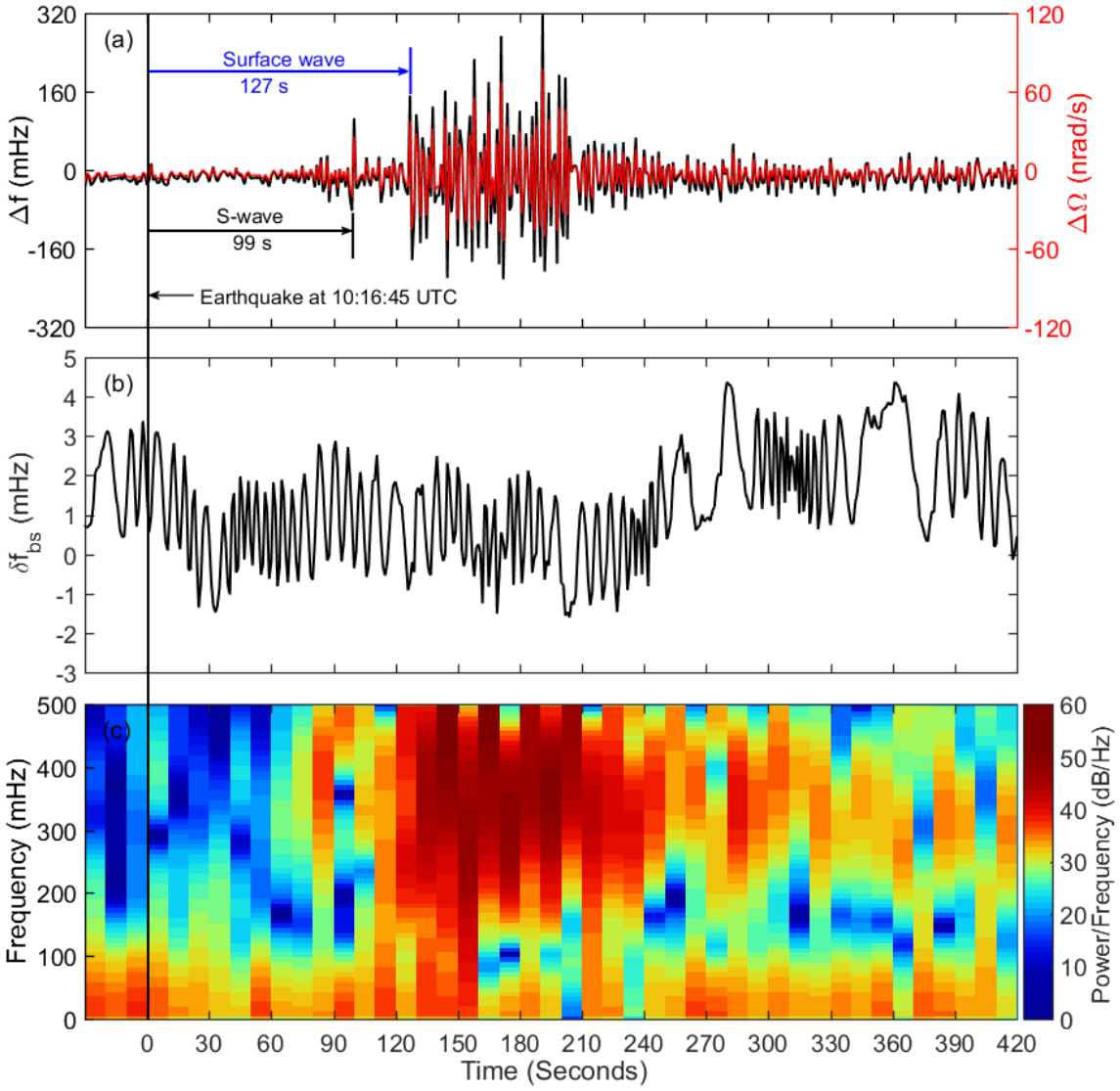

Figure 5.9: An earthquake event as sensed by the 611.8 nm ER-1 system, where (a) shows the Sagnac frequency variations Δf with black trace (left y-axis) and the converted ground rotation rates $\Delta\Omega$ with red trace (right y-axis); (b) shows the frequency error (δf_{bs}) contributed by the backscatter effect; (c) shows the correlated earthquake spectrogram. The timestamp in the x-axis is expressed by 'seconds since earthquake'. During the observation time, ER-1 was operating in a phase-locked mode configuration at 95 nW output power. Note that the sample write-out was 1 sec/data.

Earthquake detail	Gyro operating wavelength	
Parameter	611.8 nm	632.8 nm
Epicentre	Milford Sound	Levin
Distance to sensor (km)	425 ± 4	395 ± 3
Magnitude (M)	5.4 ± 0.2	5.8 ± 0.0
Depth (km)	5 ± 0	37 ± 4
S-wave velocity (km/s)	4.293 ± 0.040	4.293 ± 0.031
Love wave velocity (km/s)	3.346 ± 0.033	3.465 ± 0.026
S-wave-induced ground motion, $\Delta\Omega_S$ (nrad/s)	46.2	32.3
Maximum backscatter perturbation (mHz)	5	40
Maximum δf_s variation, Δf_{max} (mHz)	317	1000
Maximum ground rotation rate, Ω_{max} (nrad/s)	78	254

Table 5.7: Two earthquake events respectively observed by the 611.8 and 632.8 nm ER-1 system.

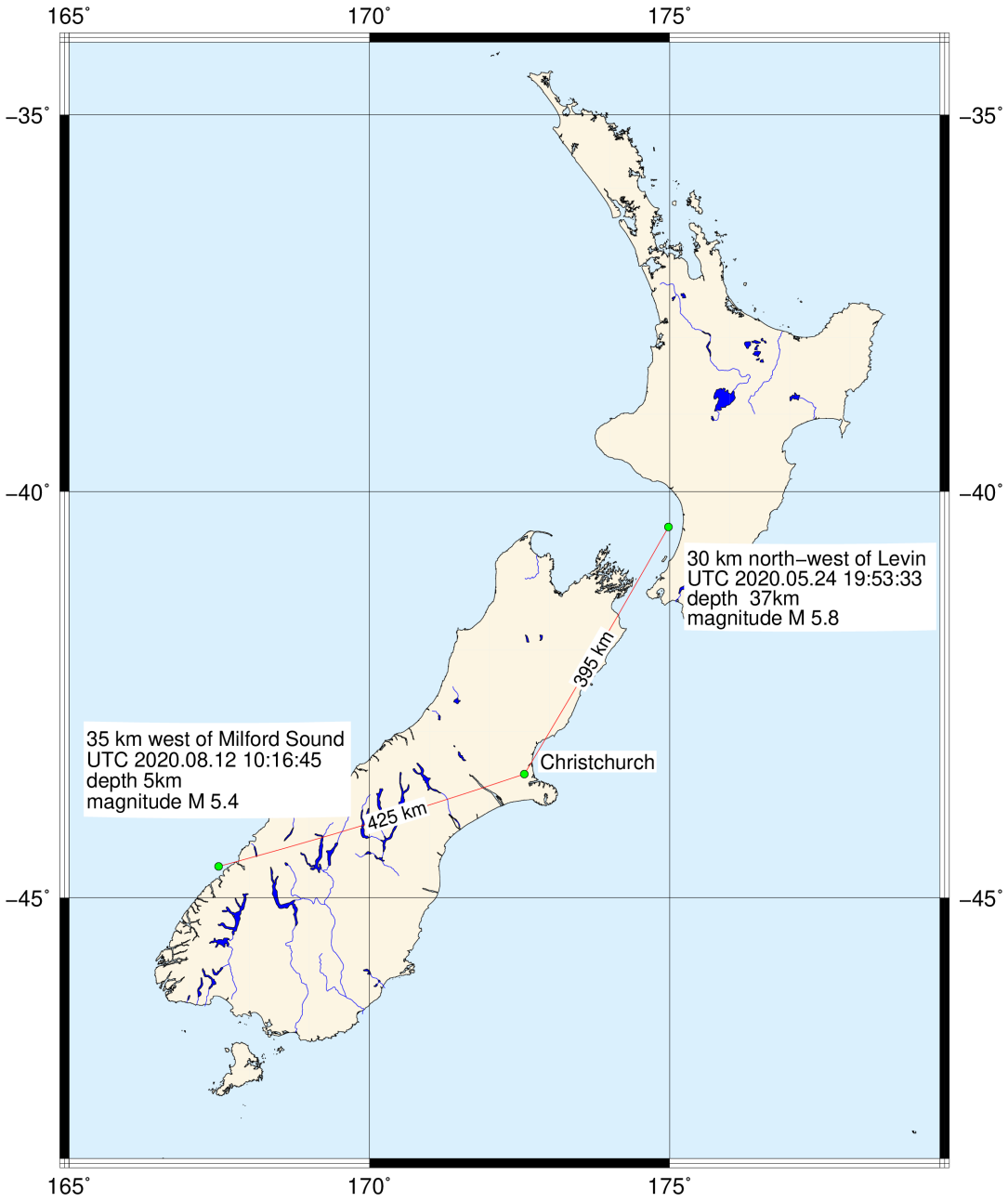

Figure 5.10: The epicentres of two detected earthquakes marked out on the map. The seismic event as sensed by the 611.8 nm operation was at 35 km west of Milford Sound in the South Island of New Zealand (about 425 km away from the ER-1 location); that detected by 632.8 nm operation was at 30 km north-west of Levin in the North Island of New Zealand (about 395 km away from the ER-1 location).

5.3 A Cavity Configuration Using Supermirrors with 10 m ROC

We now explore gyroscopic operation using four 10 metre ROC mirrors. As shown in Table 5.8, the ring-down time defined by such a cavity configuration was measured at 226 μs. This corresponds to a Q of 7.0×10^{11}, an overall optical loss of 147.5 ppm, and a finesse of 4.3×10^4. These values are lower than those obtained using the 3 m ROC mirrors (refer to Table 5.2). This is due to the larger beam waist yielding higher diffraction losses.

Parameter	Value
Ring-down time, τ (μs)	226
Total loss, L (ppm)	147.5
Quality factor, Q	7.0×10^{11}
Finesse, F	4.3×10^4

Table 5.8: Ring-down time, total cavity loss, quality factor Q, and finesse as measured from a cavity formation using four concave supermirrors of 10 m ROC.

5.3.1 Operational Regime and Beam Stability Analysis

Given this cavity Q, lasing at 611.8 nm was only possible with a cavity pressure of no more than 4.5 mbar. Lasing was not sustainable beyond this pressure boundary as the gain was insufficient to overcome the cavity loss. For studies of the frequency pulling effect, we operated ER-1 with the highest operable pressure at 4.5 mbar since it provides the widest tunable regimes for single-mode (0 - 54 nW) and phase-locked (55 - 75 nW) operation.

Figure 5.11 demonstrates a typical laser performance (over 23 hours) obtained from this cavity configuration. As concluded in Table 5.9, the noise-reduced Sagnac time series (denoted by the data write-outs in a 60 s average) over a 23 hour period presented a frequency variation of about 104 mHz and the backscatter-coupling contributed a systematic bias up to 114 mHz. Referring to Table 5.4, it is noticeable that the backscatter amplitude given by this mirror configuration showed no difference to those measured from the previous cavity configuration (using mirrors at 3 m ROC). However, mode splitting was more common than that obtained using the 3 m ROC mirrors. This phenomenon can be traced back to a higher beam power inequality observed with this cavity configuration. As indicated by Table 5.9, the clockwise and counter-clockwise beams exhibit a nearly 50% difference between their monobeam modulations. The imbalance of the two intensity modulations is considerable when compared to that measured from the previous configuration (see Table 5.4).

We analysed the gyroscopic sensitivity by picking the Sagnac time series in two different lengths. The long data series includes the frequencies estimated within the mode-hop-included time interval. The short one was selected from the stablest period (between two adjacent mode-hops) during long-term laser operation, as such, its relative ADEV can

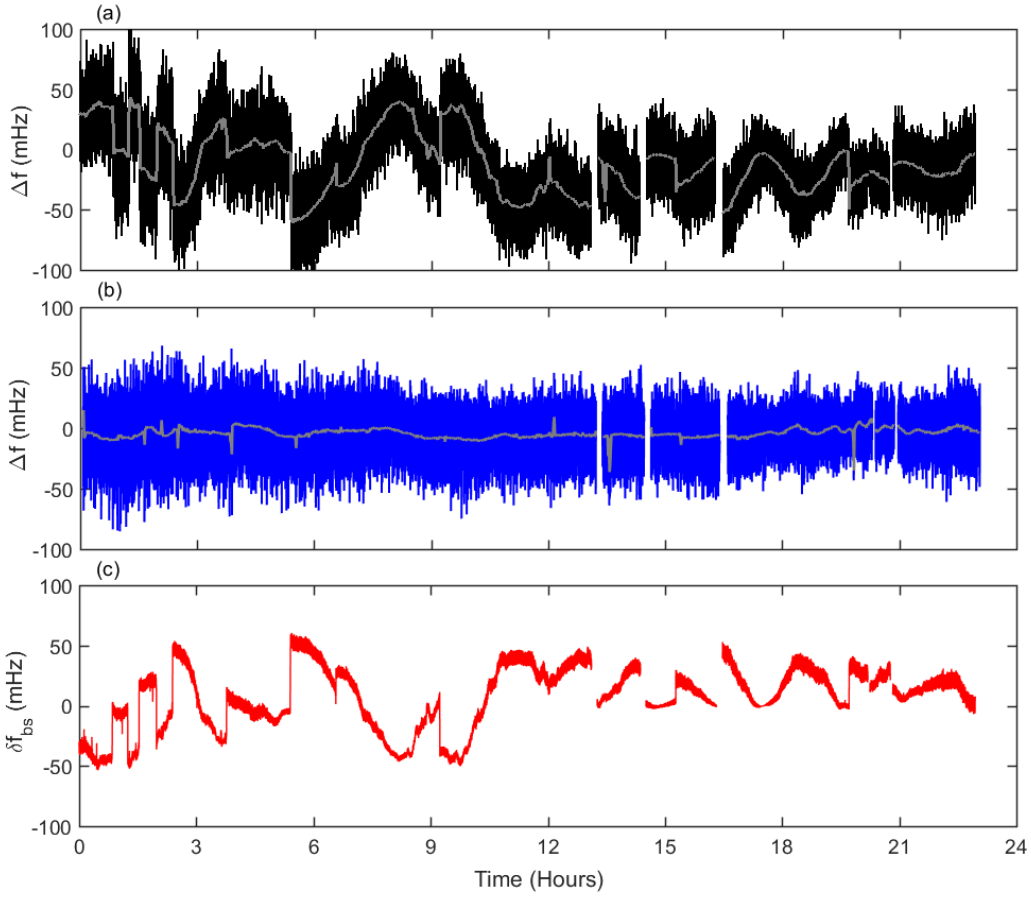

Figure 5.11: Laser performance obtained from single-mode operation at 25 nW over 23 hours. Sagnac frequencies obtained using a sample write-out of 1 s (bold traces) are overlapped by a down-sampled frequency data series with a recorded rate at 60 s (thin traces). In this figure, (a) shows the raw Sagnac frequency variation (black trace), (b) shows the backscatter-removed frequency variation (blue trace), and (c) shows the frequency bias as corrected from backscatter-coupling effects (red trace); the gaps in data-sets symbolise the invalid time-periods due to split-mode operation.

Parameter	Value
Data length (hours)	23
Occurrence of mode splitting	5
Laser output power (nW)	25
δf_s Contrast ratio (%)	58 - 62
CCW beam modulation (%)	0 - 2.3
CW beam modulation (%)	0 - 4.4
Frequency excursion (mHz)	104
Backscatter perturbation (mHz)	114

Table 5.9: Gyroscopic parameters as obtained from the laser performance.

demonstrate the best obtainable performance given by the current mirror configuration. The relative Allan deviation plots as analysed from these two data series are shown in Figure 5.12. The best short-term laser performance yields a highest achievable sensor resolution at 131 prad, inferred from a lowest ADEV of 1.8×10^{-6} at a measurement time of 128 s. The typical sensor resolution for long-term operation was measured at $7.9 \times 10^{-6}\Omega_E$ (577 prad) at an integration time of 71 s. One can see that the laser stability and sensitivity derived from either the short-term or long-term operation (summarised in Table 5.10) were inferior to the best laser parameters previously achieved from the 611.8 nm system using 3 m ROC mirrors (see Tables 5.5 and 5.6). Essentially, this is because ER-1 configured with the 10 m ROC mirrors provides neither optimal beam stability nor minimal cavity loss. Therefore, this cavity configuration does not maximise the potential of 611.8 nm operation.

Moreover, we noticed that the gyroscopic performance cannot be improved solely by an increase in the operational powers. Initially, we attempted to operate the laser at a high output power between 40 to 50 nW below the phase-locked multi-mode threshold. However, the laser performance was continuously interrupted by mode splitting, and thus the data series were extremely limited for a long analysable length. It might indicate that the larger beam size created greater beam power imbalance, which was already evidenced by the significant inequality between the two intensity modulations. Thus, a larger non-reciprocal effect is associated with a higher frequency of split-mode operation.

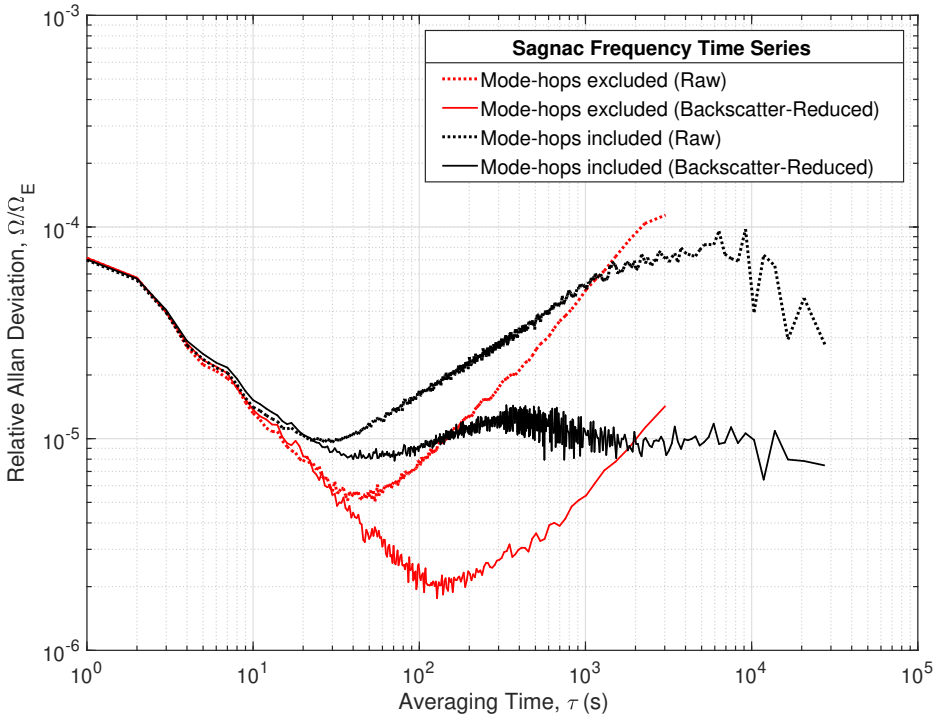

Figure 5.12: Relative Allan deviation plotted from Sagnac frequency time series in two different lengths. The dot-traces were analysed from the raw Sagnac frequency, while the solid-traces were from the backscatter-removed frequency.

Sagnac Time Series	Raw Sagnac			Backscatter-reduced Sagnac		
Data Length (Hours)	τ (s)	ADEV (Ω/Ω_E)	Resolution (prad/s)	τ (s)	ADEV (Ω/Ω_E)	Resolution (prad/s)
2.5	54	5.1×10^{-6}	372	128	1.8×10^{-6}	131
23	30	9.6×10^{-6}	701	71	7.9×10^{-6}	577

Table 5.10: The gyroscopic parameters summarized from the relative ADEV plots. The Sagnac time series of 2.5 hours in length was selected to present the best short-term laser performance while the time series of 23 hours in full length represents the typical laser performance during a long-run.

5.4 Conclusions

We have assessed the laser performance of a geometrically-upscaled ER-1 gyro operating on the frequency-upscaled neon transition of $3s_2 \rightarrow 2p_6$ using two different cavity configurations. Four spherical IBS-coated supermirrors employed in the 611.8 nm system were of either 3 m or 10 m ROC. The oscillator configured using the 3 m ROC mirrors experienced less optical loss than that using the 10 m ROC mirrors, since the photon decay time of 510 μs measured from a 3-m-ROC-mirror-configured cavity (Q = 1.6×10^{12}, L = 65.4 ppm) was more than two times the 226 μs obtained from the other one (Q = 7.0×10^{11}, L = 147.5 ppm). These results are also in line with the beam profile calculations, which show that the waist size formed by the 3 m ROC mirrors is on average about 35% smaller than that obtained with the 10 m ROC mirrors. With a 50:50 neon partial pressure fixed at 0.2 mbar, the highest operable cavity pressures obtained from the 3 m and 10 m ROC mirror configurations were at 6.5 and 4.5 mbar, respectively. Laser operation at 6.5 mbar yielded the widest single-mode and stable phase-locked regimes with the operable output powers up to 82 nW and 225 nW, respectively.

For TEM_{00} single-mode operation (using 3 m ROC mirrors), the magnitude of backscatter effects (having intensity modulations $m_{1,2}$ below 3.5 %) was similar to that measured from the previous 632.8 nm system (having $m_{1,2}$ below 3.3 %). As such the maximum Sagnac frequency excursion measured at 108 mHz (over 48 hours operation) was comparable to the 100 mHz frequency variation obtained from the 632.8 nm system. We also compared the 611.8 nm laser performance using four different mode regimes - TEM_{01} single-mode, TEM_{01} phase-locked mode, TEM_{00} single-mode, and TEM_{00} phase-locked mode. The TEM_{00} single-mode output offered the best sensor resolution and stability over time. This is because the backscatter correction works efficiently on the raw Sagnac frequencies when only one optical frequency is present. Hence, the systematic errors yielded by TEM_{00} single-mode operation were most efficiently reduced, and thus the measurement of Earth rotation rate performed with better accuracy. An increase in the operating frequency from 474 THz (632.8 nm) to 490 THz (611.8 nm) yields an upscaled Sagnac frequency at 205.23 Hz.

In general, mode-hops and the mode splitting phenomena seemed to perturb 611.8 nm laser performance more frequently than at 632.8 nm. Fundamentally, this is because the homogeneous line-broadening in the low operational pressure of 6.5 mbar was insufficient. Therefore, the hole burning of the 611.8 nm spectral lineshape was narrower than the spectral hole 'burnt' in the 632.8 nm one. As a result, mode competition for 611.8 nm operation was stronger as the 611.8 nm gain curve has a more prominent curvature at the saturation point. Consequently, mode-hops frequently occurred and thus the possibility of mode splitting also increased. Short term operation at 611.8 nm yielded a sensor resolution of 80 prad/s (1.1×10^{-6} Ω_E, measured from an integration time τ of 225 s), comparable to or even slightly better than that obtained from short-term 632.8 nm performance. This translates into a building-noise-limited laser sensitivity of 1.25×10^{-11} rad/s/$\sqrt{\text{Hz}}$ and a raw sensitivity of 1.87×10^{-10} rad/s/$\sqrt{\text{Hz}}$ (at 1 s of integral time).

A medium-size (M = 5.4, depth = 5 km) earthquake with an epicentre located 425 km from the sensor location was detected by the ER-1 system while operating on the 611.8 nm wavelength. All measured phase velocities of the S-waves and Love waves fell into the expected ranges. It is encouraging to observe that the surface-wave-induced ground rotations from this earthquake were 3 - 4 times smaller than that generated from the M = 5.8 earthquake mentioned in Chapter 4. The difference between the ground rotations measured respectively from the two seismic events matched perfectly with the difference in the energies released individually from two earthquakes.

6 Gyroscopic Operation Using the Highest Optical Frequency Available from the Helium-Neon Gain Medium

In this chapter, we investigate the operation of ER-1 on the shortest usable wavelength of 543.4 nm in the visible region. We begin this chapter by introducing some preliminary work for the 543.4 nm operational environment. To provide sufficient gain for this neon transition of $3s_2 \rightarrow 2p_{10}$, one of the ER-1 cavity arms was partially modified for the assembly of a secondary 400-mm-long capillary of either 3 mm or 4 mm in diameter. The pros and cons in regards to the selection of an extra gain tube with larger or smaller diameter, and the optimisation of gain excitation (the plasma discharge) in a long gain tube, are investigated via the parameters obtained from a 632.8 nm ER-1 cavity. For this frequency-upscaled gyroscopic operation, a set of IBS-coated supermirrors with an ultra-low transmission loss of 0.2 ppm per mirror are employed to reduce the backscatter perturbation as well as improve the cavity Q factor. We summarise the general operational environment, laser output behaviour, and technical challenges which apply to all large ring lasers while using the 543.4 nm wavelength. Lastly, we present the gyroscopic performance obtained and the ability of the laser to unlock on Earth rotation with an increased Sagnac frequency of around 230.96 Hz.

6.1 Preparatory Investigations Using the 632.8 nm Transition

6.1.1 Evaluations for the Assembly of a Secondary Capillary

As mentioned in Chapter 3, achieving laser operation at a wavelength of 543.4 nm in the helium-neon gain medium is challenging due to the inherently low gain of the neon transition ($3s_2 \rightarrow 2p_{10}$). Therefore, the gain tube employed should be long enough to enable a long plasma discharge length to provide a sufficient gain. The use of an extra gain tube will inevitably introduce greater diffraction loss via the introduction of an additional aperture. With this configuration, even a slight misalignment of the gain tube can significantly reduce the gain through obstruction of the beam profile.

Initially, we configured the ER-1 cavity with four 632.8 nm supermirrors (ROC = 4 m, the same mirrors used in Chapter 4) and one additional long gain tube to achieve a discharge length over 45 cm. To simulate the operational condition for the 543.4 nm, two long gain tubes with the same effective length at 400 mm but different inner-diameters respectively at 3 mm

and 4 mm were assembled in turn. After mounting the long gain tube, we deployed two green alignment lasers at the opposite Northwest and Southeast mirror corners for injecting the laser beams into the sealed ring cavity in both the CW and CCW directions. Once the two beams propagating in the CW and CCW directions were overlapped[1] inside the cavity, we considered that the cavity along with the two gain tubes was aligned. Following this, the cavity was filled to a total pressure of 2 mbar with a natural neon partial pressure at 0.2 mbar. As expected, 632.8 nm lasing occurred with bright laser output. Afterwards, we utilised the 632.8 nm laser beam output for fine-tuning of the alignment[2] of the gain tube and mirror corners. Once the alignment was optimised, we began to characterise the oscillator parameters and the cavity loss induced by the use of a secondary discharge tube.

The essential cavity parameters obtained from a configuration using either of the two gain tubes are tabulated in Table 6.1. It is clear that the implementation of a long capillary with a narrower diameter of 3 mm introduced a larger optical loss. This is clear from the low ring-down time measured of 20 μs. By contrast, the capillary of 4-mm-in-diameter yielded a much lower optical loss, as it provided a ring-down time of 197 μs.

Parameter	3 mm Diameter	4 mm Diameter
Ring-down time, τ (μs)	20	197
Total loss, L (ppm)	1666.7	169.2
Quality factor, Q	6.2×10^{10}	6.1×10^{11}
Finesse, F	3.8×10^{3}	3.7×10^{4}

Table 6.1: Ring-down time, total cavity loss, quality factor Q and finesse F measured from the ER-1 cavity configured with an extra 400-mm-long gain tube of either 3 mm or 4 mm in diameter.

While the cavity was configured with the 3 mm diameter gain tube, we measured the maximum tolerance of the capillary misalignment for minimum lasing action, through an adjustment of the 100-mm-long short gain tube (4-mm-in-diameter). Two micrometres assembled on a capillary holder for the alignment of the horizontal plane were tuned by an equal amount. By doing this, we created a displacement in the 'in-and-out' direction with respect to the vertical axis of the ring cavity. It showed that a horizontal displacement within 0.6 mm (in total 1.2 mm) departure from the starting point (where the beam waist located in the centre of the cross-section of the capillary) was still able to maintain the laser action. However, beyond this tolerance limit, the lasing stopped. The measured result indicates that even with the 4 mm discharge tube a cut-off of the beam profile is still unavoidable.

[1] A spatial overlap of the two externally-injected alignment lasers introduced interference fringes observable in the mono-beam output transmitted from the window.

[2] An optimal cavity alignment was achieved when the DC voltage of the monobeam output as measured by a photodetector reached to its highest.

The long ring-down time of 375 μs obtained from the cavity configuration with only the 100 mm-long gain tube, suggests that both long gain tubes seem to be non-ideal in terms of the losses they introduce. The configuration with a 4 mm diameter gain tube appears to be more suitable for 543.4 nm operation considering the reasonable cavity Q it provides. Therefore, initially we configured the ER-1 cavity with the 4 mm diameter tube for practical evaluation of 543.4 nm operation.

6.1.2 Maximisation of the Total Plasma Discharge Length

As mentioned in Chapter 3.1, the impedance matching between the RF transmitter and the gain tube is varied in accordance to the plasma density. Following previous characterisation using the 2.56 m^2 PR-1 cavity (assembled with the 400-mm-long gain tube of 3-mm-in-diameter), a total pressure of 0.8 mbar with a natural neon partial pressure of 0.2 mbar seems to be ideal as the maximum gain for the 543.4 nm neon transition was achieved with this gas composition [13]. Therefore, we pre-filled the cavity with this gas-mixture to maximise the plasma discharge length, and also adjusted the number of the electrodes and the spacing among them. We also employed eight permanent magnets along the tube to help stabilise the plasma discharge between each pair of copper electrodes [105]. As shown in Figure 6.1, the longest plasma discharge obtained was able to fully cover the effective capillary range (400 mm long) with a full RF input power of 30 W.

The RF transmitter, impedance matching unit, RF coupling electrodes, and associated wires and nearby metal structures form a lumped circuit with its resonant frequency determined by the formula: $f_0 = \frac{1}{2\pi\sqrt{LC}}$ (L: total inductance[3], C: total capacitance[4]). When the 400-mm-long capillary[5] was wrapped with 11 electrodes in a multi-dipole configuration (connected alternately with a 10 mm spacing between each pair), the measured resonant frequency[6] was in the vicinity of 89 MHz. Note that the exact resonance value was changed when the quantity and structure of the electrodes and the associated wiring was re-arranged. Nevertheless, it was generally at around 80 MHz. If the RF transmitter was off, the load impedance[7] is estimated to be higher than 10k ohm as the gain tube and gas medium exhibit a higher impedance feature when no plasma is generated. It is necessary to use an RF transmitter frequency near the resonant frequency to transfer maximum energy from the RF source (and

[3]The total inductance (L) represents a sum of the inductance generated from multiple parts: the cable wiring between the RF transmitter and the matching unit, coupling wires from the matching unit to electrodes, and coupling wires between each pair of electrodes.

[4]The total capacitance (C) represents a sum of capacitance generated at multiple parts: the spacing between each pair of electrodes (dominant capacitance), the spacing between the gain tube and gain tube holder (there is no stray capacitance if the holder is not metallic), and the spacing between the gain tube and ground (stray capacitance).

[5]Compared to the short gain tube, the long one introduced a higher load impedance since capacitance along the gain tube increased with an increasing number of electrodes.

[6]The resonant frequency was measured by an MFJ-269C-pro frequency meter.

[7]The load impedance falls to near zero when the plasma strike occurs as the plasma is conductive.

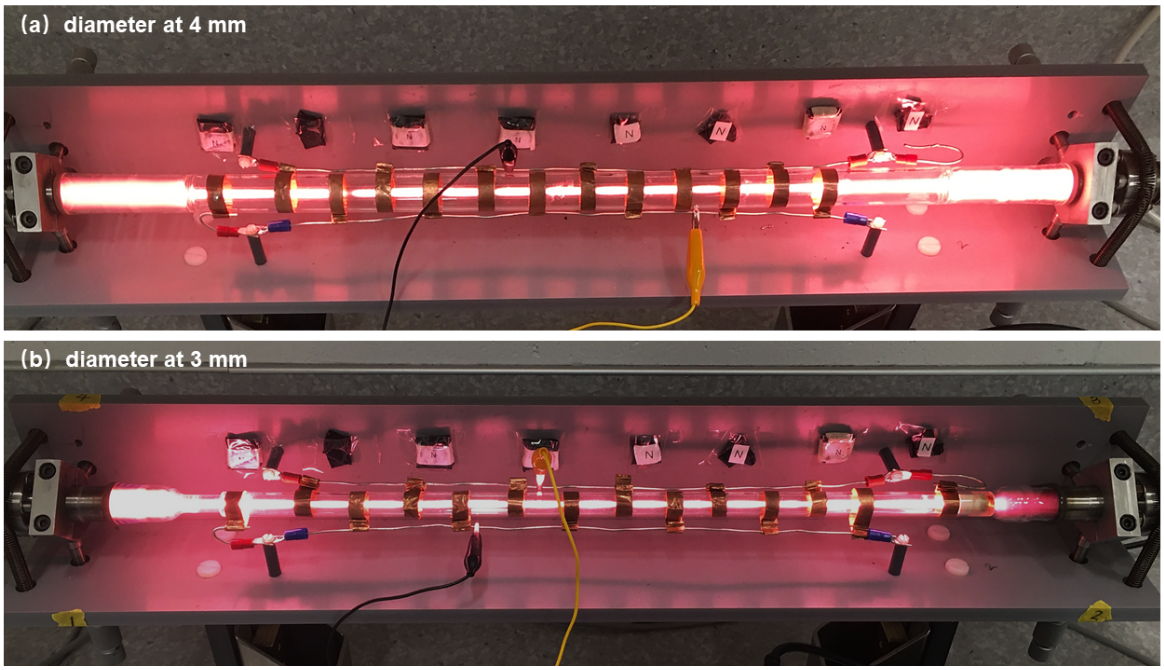

Figure 6.1: The optimised plasma discharge in the 400-mm-long gain tubes of (a) 4 mm-in-diameter, and (b) 3 mm-in-diameter, given by the maximally designed electrode configuration and impedance matching unit; eight magnets which spread out along the 400 mm effective discharge range yield better stability of the plasma discharge.

the matching unit) to the gain medium. Therefore, for the RF coupling to the long gain tube, we employed the 80 MHz RF transmitter rather than the 160 MHz transmitter which would have been outside the resonant frequency required.

6.2 Laser Operation Using a 4 mm Diameter Capillary

After the 543.4 nm supermirrors were cleaned and inserted into the cavity, we carefully filled the cavity with a natural neon partial pressure of 0.2 mbar and a helium partial pressure of 0.6 mbar (He: Ne = 3:1). The employed IBS-coated supermirrors were provided by Five-Nine Optics. They all have a ROC of 3 m, effective plane diameter of 25.4 mm, and mirror thickness of 10.0 mm. As shown in Table 6.2, the measured mirror transmission loss at the centre wavelength of 543.4 nm is the lowest, at 0.05 to 0.3 ppm, while transmission losses for other undesired wavelengths are very high, more than 10000 ppm.

Wavelength (nm)	Transmission (ppm)	Total loss (ppm)
543.4	0.05-0.3	< 12
593.9	> 10000	-
604.6	> 10000	-
611.8	> 10000	-

Table 6.2: Specifications for the ultra low-loss, IBS-coated superimirrors with a centre wavelength at the 543.4 nm. Parameters are characterised at a 45° angle of incidence in the s-polarisation direction.

At the initial stage of the laser characterisation, natural neon was used, as it can provide higher gain compared to 50:50 neon under the same operational conditions (such as the same He-Ne gas ratio, total cavity pressure, and length and diameter of the discharge tube). The gas fill for 543.4 nm operation was handled with extreme care to avoid any undesired gas turbulence[8]. With this predetermined optimal gas composition, lasing at 543.4 nm was achieved using solely the long gain tube. As shown in Figure 6.2 (a), the green laser beam-spot was situated at the centre of the supermirror surface. The dim, pink background light spread out around the beam-spot is from the plasma discharge. Figure 6.2 (b) shows the spectrum of the laser output detected by a spectrometer.

The cold cavity ring-down time measured was 200 μs. This translates into a quality factor Q of 6.9×10^{11}, a cavity finesse of 3.8×10^4 and a total optical loss of 167 ppm. One can see that the cavity ring-down time obtained from the 543.4 nm oscillator is quite similar to the one (197 μs) obtained from the previous 632.8 nm oscillator (refer to Table 6.1).

6.2.1 Instrumental and Optical Layout for 543.4 nm Operation

A simplified schematic of the experimental set-up, data acquisition and laser intensity control system is shown in Figure 6.3. The cavity is configured having both the 400 mm and 100 mm

[8]Gas turbulence during the gas fill or evacuation can potentially introduce dust or impurities to the centre of the mirror surface and thereby terminate the laser action. A gas fill to 0.8 to 2 mbar pressure normally took about one hour.

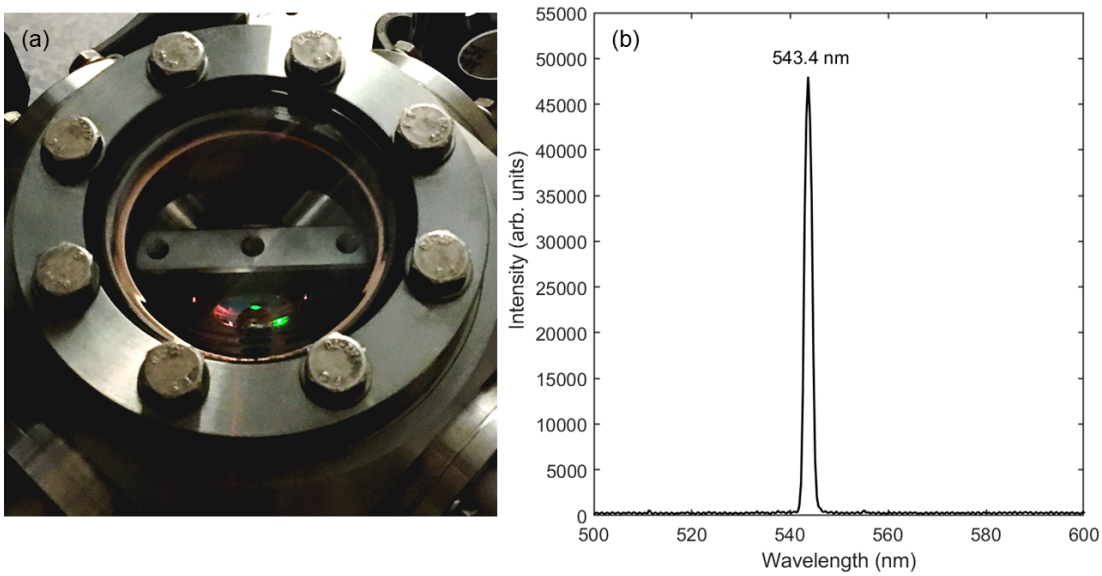

Figure 6.2: ER-1 laser using the green neon transition: (a) a photo taken from the northeast mirror corner shows the lasing phenomenon with the green colour; (b) a spectrum of the laser output shows only lasing at the 543.4 nm wavelength.

long gain tubes which are oppositely mounted in the west and east arms and coupled by RF transmitters at 80 MHz and 160 MHz, respectively. As the 543.4 nm transition has a much lower gain relative to that of 632.8 nm, the RF input powers required for a long plasma discharge length were expected to be reasonably high. Taking this into consideration, the amplitude servo unit for the laser intensity control was placed far away from the 80 MHz RF transmitter. This scheme was beneficial as it potentially reduced the impact of large stray RF fields on the amplitude feedback control loop. The CW beam transmitted from the Northeast (NE) corner was detected by a high gain photomultiplier tube (PMT 3). In particular, its DC voltage was measured and used as a feedback signal to attenuate the laser excitation power (provided by the 80 MHz RF transmitter) for maintaining stable mode operation. The AC signal from this beam was also utilised for the measurement of FSR beat frequencies induced from a multi-mode regime via an RF spectrum analyser (Keysight N9000B CXA Signal Analyser)[9]. The longitudinal mode configurations were measured using the CCW beam output (detected via PMT 2) from the NE corner with an F-P interferometer. Two photodiodes (PD 1 and PD 2) mounted in the Southeast (SE) corner were used to monitor the magnitudes of the backscatter perturbation. A power meter (PM) mounted in the Northwest (NW) corner was used to measure the laser output power of the CCW beam without interference from plasma background light contributed by the 400-mm-long capillary. The Sagnac beat signal from the combined beams was obtained from the Southwest (SW) corner. Note that 543.4 nm line

[9] An RF spectrum analyser of high resolution can easily identify the weak oscillations of side modes located far away from the centre mode.

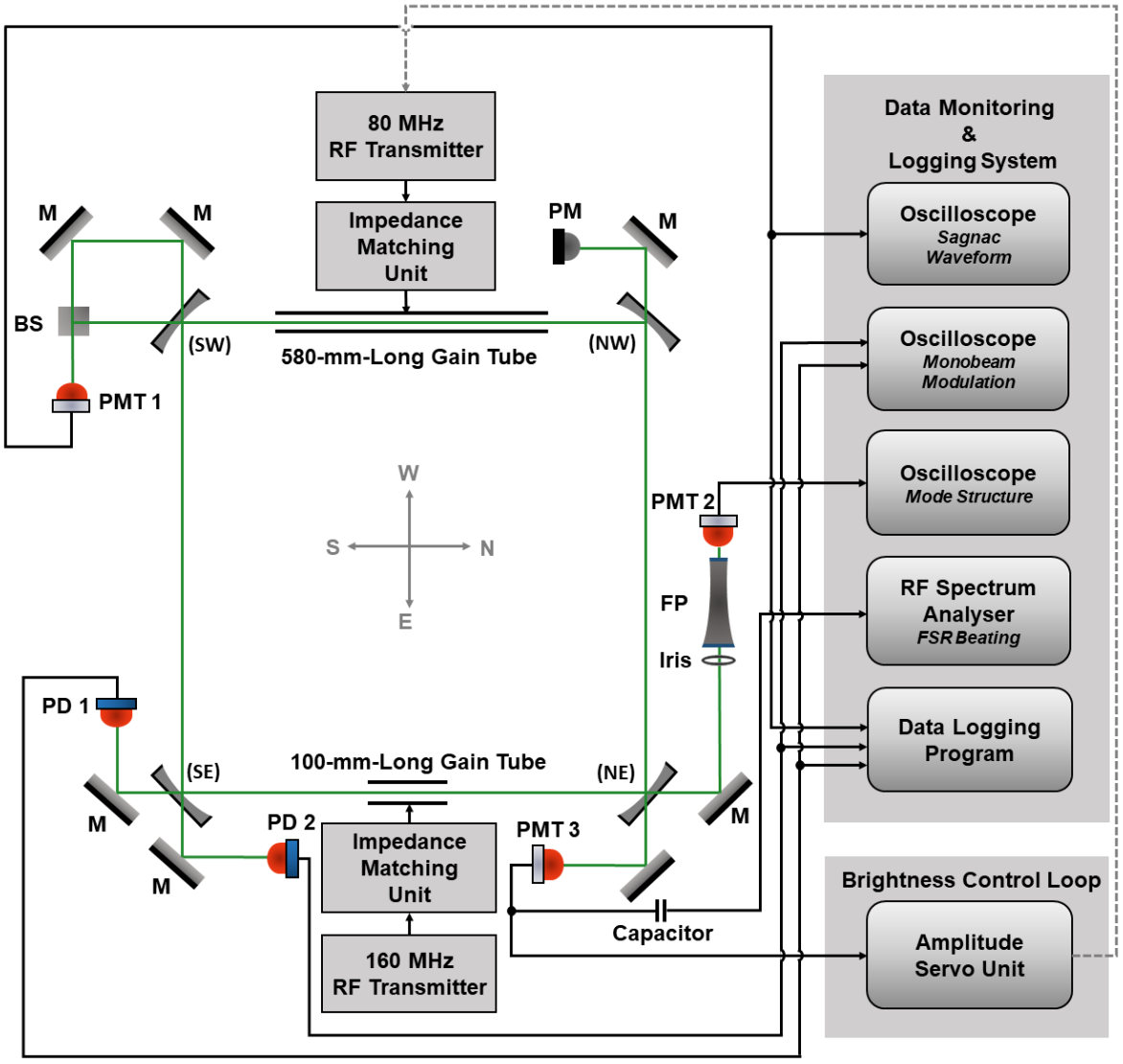

Figure 6.3: The experimental set-up, data monitoring and acquisition layout for 543.4 nm gyroscopic operation. The following labelling scheme applies: M, dielectric mirror; BS, beam splitter; PMT, photomultiplier tube; PD, photodiode; PM, power meter; FP, Fabry-Perot interferometer. Data logging was obtained via a National Instrument LabVIEW data acquisition board (USB NI 6216 BNC); the sampling rate of the DAQ was set to be 5000 samples/sec and the data write-out was set to be once per second.

filters (Thorlab, FL543.5-10) were placed in front of four photodetectors of PMT 1, PMT 3, PD 1 and PD 2 to avoid signal contamination from other light sources (mainly residual room light and plasma light).

6.2.2 Laser Performance

Laser operation with a natural neon pressure of 0.2 mbar and total pressure of 0.8 mbar yielded a maximum laser output power of 208 - 212 nW and a TEM_{00} beam diameter of 2.4 - 2.7 mm (with a full RF input power at 30 W). An RF input power of 16 W and a plasma discharge length of 320 mm were required to achieve lasing threshold. We note that no stable mode structures were obtainable at this low operational pressure. The minimum lasing obtained with a power output of 1 - 3 nW (beam diameter about 1.3 - 1.5 mm) yielded at least 7 longitudinal modes, as monitored from an RF spectrum analyzer (see Figure 6.4). This unstable lasing situation was also confirmed by the on-going amplitude modulations among the FSR beat frequencies.

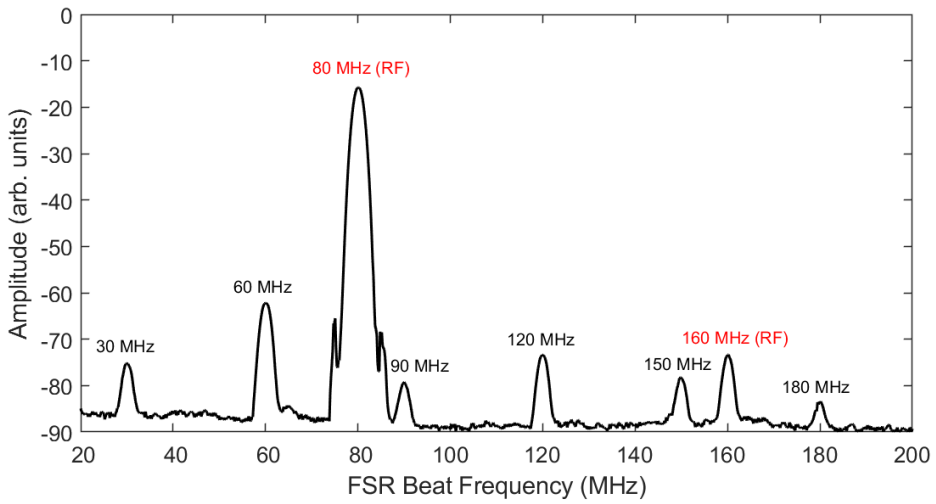

Figure 6.4: Spectrum of the FSR beat frequencies measured by an RF spectrum analyser when the laser was tuned to operate just beyond the lasing threshold. There were at least 7 longitudinal modes with unstable phases and amplitudes. The 80 MHz and 160 MHz signal were both contributed by the 80 MHz RF transmitter; the 160 MHz was given by the second harmonic of the RF frequency.

We found that 0.9 mbar was the upper pressure-limit for 543.4 nm lasing. However, this pressure was not enough to provide a sufficient pressure-broadening for the build-up of stable mode configurations. The highest laser output measured was 70 - 72 nW. It is clear that a 0.1 mbar increase of the cavity pressure reduces the laser gain by more than 50%. Despite a broad frequency band induced by multi-mode oscillations, the FFT power spectrum

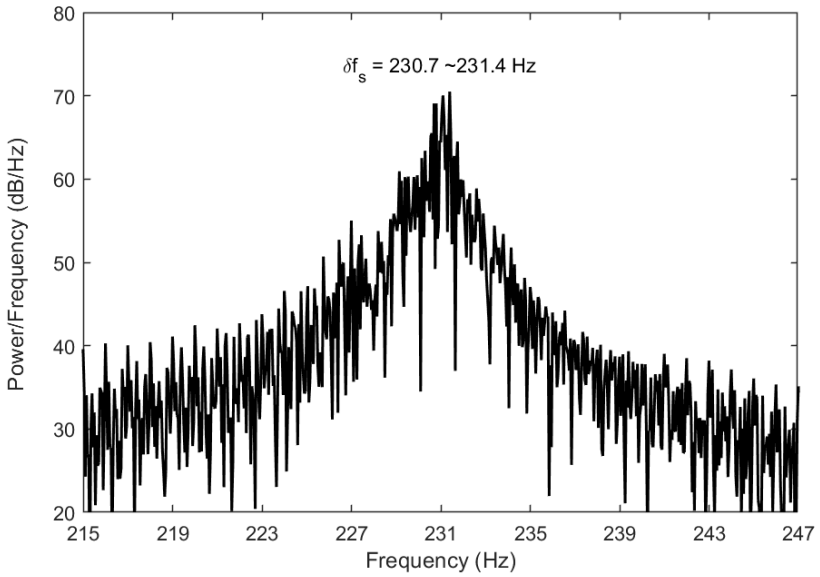

Figure 6.5: An FFT result derived from the raw Sagnac waveform (data length of 20 s). Even though the 543.4 nm laser was unable to operate with a single-mode or mode-locked structure, the FFT result still unveiled an Earth rotation background by a prominent Sagnac beat frequency at around 231 Hz.

derived from the raw Sagnac interferogram yields a peak frequency in the vicinity of 231 Hz for the Earth rotation background (see Figure 6.5). Note that the nominal Sagnac frequency (calculated via Equation 4.1) for the 543.4 nm neon transition is 230.96 Hz.

6.3 Laser Operation Using a 3 mm Diameter Capillary

As stated in Section 6.2.2, the 4 mm diameter capillary was unable to provide sufficient gain for 543.4 nm lasing with an operational pressure over 0.9 mbar. We expect that this issue can be addressed by the 3 mm diameter tube, as the discharge tube with a smaller diameter should provide higher gain for the neon transition via acceleration of the depletion of the lower energy state through wall collisions. As shown in Table 6.3, the cavity configured from a 3 mm diameter tube reduced the ring-down time by nearly one half when compared to that obtained from the configuration with a 4 mm diameter tube. The measured ring-down time of 110 μs correlates to a quality factor Q of 3.8×10^{11}, a cavity finesse of 2.1×10^4, and a total loss of 167 ppm.

Parameter	3 mm Diameter	4 mm Diameter
Ring-down time, τ (μs)	110	200
Total loss, L (ppm)	303.0	166.7
Quality factor, Q	3.8×10^{11}	6.9×10^{11}
Finesse, F	2.1×10^4	3.8×10^4

Table 6.3: Ring-down time, total cavity loss, quality factor Q and finesse F measured using a laser wavelength of 543.4 nm and the 3 mm diameter capillary. The results obtained using the 4 mm capillary are shown for comparison.

Using the 3 mm diameter discharge tube, the ring-down time at 543.4 nm was measured to be 5 times longer than that measured at 632.8 nm. This can be explained by the fact that the laser beam waist formed at the centre of the cavity arm using the 543.4 nm wavelength is smaller than that formed using the 632.8 nm wavelength (see Table 6.4). Therefore, the diffraction loss experienced by the 543.4 nm laser beam (at the 3 mm diameter aperture) was lower than that experienced by the 632.8 nm laser beam.

Parameter	632.8 nm, ROC = 4 m		543.4 nm, ROC = 3 m	
	in-plane	out-of-plane	in-plane	out-of-plane
Beam waist size (mm)	1.06	1.38	0.85	1.16
Beam size on mirrors (mm)	1.42	1.56	1.32	1.38
Waist position (m)	0	0	0	0

Table 6.4: Laser beam parameters including the location and size of the beam waist and the beam size on the mirrors, are calculated for the two different cavities configured with four concave mirrors with a centre wavelength at 632.8 nm (ROC = 4 m) and 543.4 nm (ROC = 3 m), respectively. Note that the waist positions referred to the middle of the relevant side are reported in a clockwise manner; all beam sizes reported are 2 times the $1/e^2$ beam intensity radius.

6.3.1 Optimisation of the Gas-Mixture and Overview of the Operation Conditions

Initially, the cavity was filled with 0.8 mbar total pressure (a natural neon pressure of 0.2 mbar). As anticipated, the plasma discharge efficiency was greatly increased using this 3 mm diameter capillary. This is shown by the fact that the minimum lasing required a much lower RF power input of 9 W and a shorter discharge length of 240 - 250 mm, in comparison to those measured in Section 6.2. Thus the additional gain available more than compensates for any higher diffraction losses. A maximum laser output measured at 140 nW (for 0.8 mbar pressure) and a ring-down of 110 μs are both lower than those measured from the previous cavity configuration in Section 6.2.

For laser operation at 0.8 mbar pressure distinguishable single-mode and phase-locked regimes could be observed with laser outputs below 3 nW. We set up the amplitude servo unit and tried to maintain stable mode configurations. Working at its lower limit, the intensity control loop was only able to roughly maintain the laser power within a widely-drifting range of 3 - 4 nW. Under such circumstances, no stable multi-mode configurations could be obtained for long-term operation. Therefore, it was impractical to control and maintain the laser intensity at this pressure, as the adjustable regime for stable operation was extremely limited. The only hope for stable gyroscopic operation at 543.4 nm lies in an efficient intensity stabilisation, which is fundamentally based on sufficient operating laser power above the servo control limit.

From time to time, we observed that 543.4 nm lasing ceased within 1 to 3 minutes of striking the plasma discharge. This phenomenon occurred regardless of the gas-mixing ratios, cavity pressures, or RF excitation powers. In most cases, this undesired lasing issue arose shortly after the gas-fill was complete, while the possibility for it to occur seemed to decrease 1 to 2 days after the gas-fill. The origin of this effect could not be identified because the laser died out even when the RF input power and the discharge length remained unchanged. However, we speculate that the discontinuity of lasing is strongly correlated to discontinuity of atomic excitation across the length of the tube over time. As such, we measured the plasma temperature variations during excitation of the gain medium (at 1 mbar of total pressure) via a non-contact infrared thermometer (Fluke 61). The thermometer was placed at a position near the gain tube. Its output laser beam penetrated through the exterior and interior of the gain tube walls and focused on the centre of plasma discharge length.

As shown in Figure 6.6, the plasma temperature increased by 20 $^{\circ}C$ for 1 - 2 minutes after the beginning of the RF excitation. Ultimately, it reached equilibrium[10] at around 281 $^{\circ}C$. It was noticed that the time required for reaching a temperature equilibrium coincided with the time that the lasing was sustained. It can happen that the total impedance varies as the temperature changes. However, the exact mechanism which leads to this lasing discontinuity

[10]The increase in the plasma temperature can be mainly related to the temperature warm-up effect of the RF electronic system.

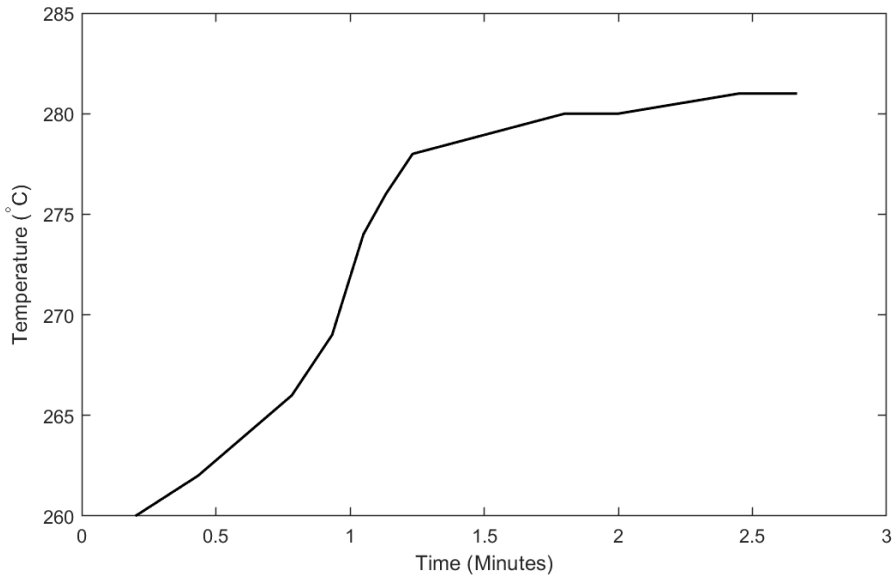

Figure 6.6: Plasma temperature measured from a non-contact infrared thermometer during the gas discharge; an RF power of 30 W was applied to fully excite the gain medium of 400-mm-in-length. This measurement was conducted with a cavity pressure of 1 mbar.

appears rather complicated and it remains an open question.

We explored the upper pressure-limit for 543.4 nm lasing at various cavity pressures with a fixed neon partial pressure at 0.2 mbar. The highest operable pressures using the natural and the 50:50 neon isotope compositions are at 1.2 and 2.2 mbar, respectively. For different cavity pressures, the maximum laser output powers achieved (with various RF input powers) are tabulated in Table 6.5. Using the natural neon isotope, an increase of the cavity pressure after 0.8 mbar tended to decrease the laser gain. As for using the 50:50 neon isotope, maximum laser output powers achieved at various gas pressures of 1.2 - 2.2 mbar were reasonably high (more than 200 nW) relative to those given by operation using the natural neon isotope (up to 140 nW).

	Natural Neon		50:50 Neon	
Pressure (mbar)	RF Power (W)	Output (nW)	RF Power (W)	Output (nW)
0.8	30	140	-	-
1.0	30	60	-	-
1.2	30	40	25	250
1.4	-	-	20	264
1.8	-	-	16	180
2.2	-	-	12	259

Table 6.5: Maximum laser output powers achieved using different cavity pressures with a neon (either the natural neon or the 50:50 neon) partial pressure fixed at 0.2 mbar; the excitation powers (from the 80 MHz RF transmitter) for the maximum gain varied for different gas compositions.

6.3.2 Gyroscopic Performance Using a 'Natural' Neon Isotopic Distribution

When the laser cavity was at 1.2 mbar pressure with a natural neon partial pressure of 0.2 mbar, the highest laser output obtained was 140 nW with an RF input of 30 W (see Table 6.5). Ten Watts of RF power and a 300 mm long plasma discharge length were required to achieve the lasing threshold. For this gas composition, an operating power of 0 - 4 nW yielded single longitudinal mode oscillation whereas at 4 - 10 nW stable phase-locked configurations were obtained. Figure 6.7 (a) and (b) show the single-mode and the phase-locked structures observed with a laser output power at 3.8 and 5.0 nW, respectively. A small but noticeable imbalance of the laser intensity between two side-modes was introduced by the asymmetric gain curve for natural neon. The photon flux for stable gyroscopic operation was still low for this 1.2 mbar pressure. Nevertheless, the enlarged stable-mode operational regime was able to make the amplitude servo control loop functional.

Sustained by a servo system (with the integration time set to an optimal value of 0.7 s), the RF power delivered to the 400-mm-long gain tube was maintained to give an output power of 3 - 4 nW. An FFT spectrum obtained from this single-mode operation is shown in Figure 6.8. It was noticed that the FFT spectrum derived from intensity-controlled single-mode performance did not show a great improvement in the resolution of the Sagnac frequency estimation when compared to that presented in Figure 6.5. Moreover, the signal-to-noise ratio of the FFT spectrum was low when compared to those previously obtained for operation at 632.8 nm and 611.8 nm using ER-1 (see Figures 4.5 and 5.3). This is because the laser intensity maintained for single-mode operation was 20 - 40 times smaller than that used for 632.8 nm (up to 135 nW) and 611.8 nm (up to 82 nW) operation. Referring to [118], one can see that the FFT spectrum derived from the '543.3 nm PR-1 system' yields the Earthline with a more distinct peak frequency. This is because the laser powers operable for PR-1 (single-mode: up to 14 nW, phase-locked: up to 26 nW) are much higher than those used by ER-1, and the amplitude control loop of PR-1 is therefore more stable than that of ER-1. Moreover, the cavity FSR of PR-1 (46.8 MHz) is 56% larger than that for ER-1 (30 MHz). Therefore, the

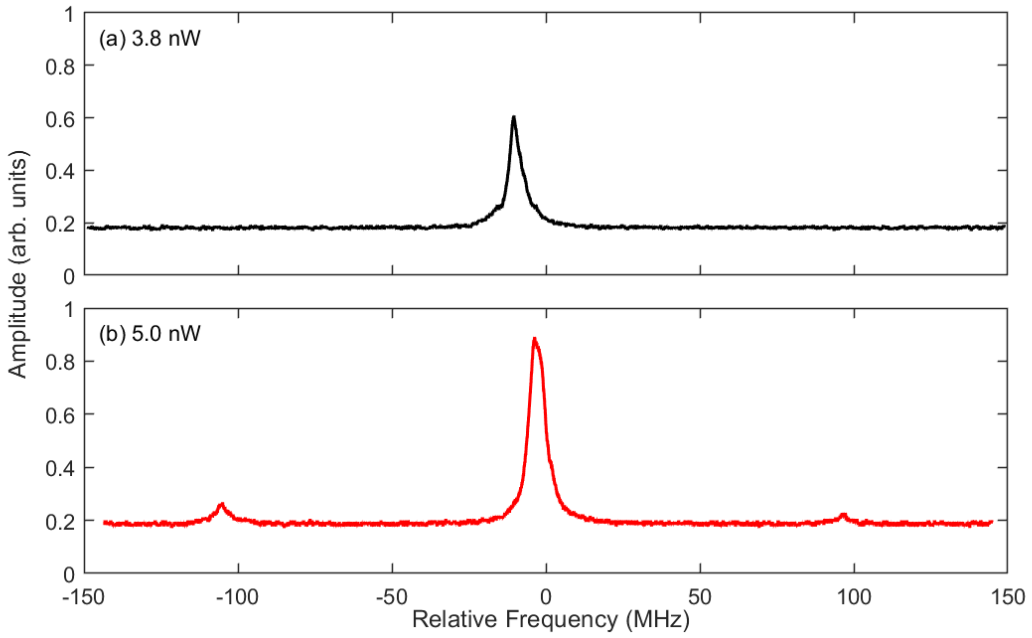

Figure 6.7: Stable mode structures scanned by the F-P interferometer, where (a) shows single-mode lasing with a laser output of 3.8 nW; (b) shows phase-locked lasing with a laser power at 5.0 nW.

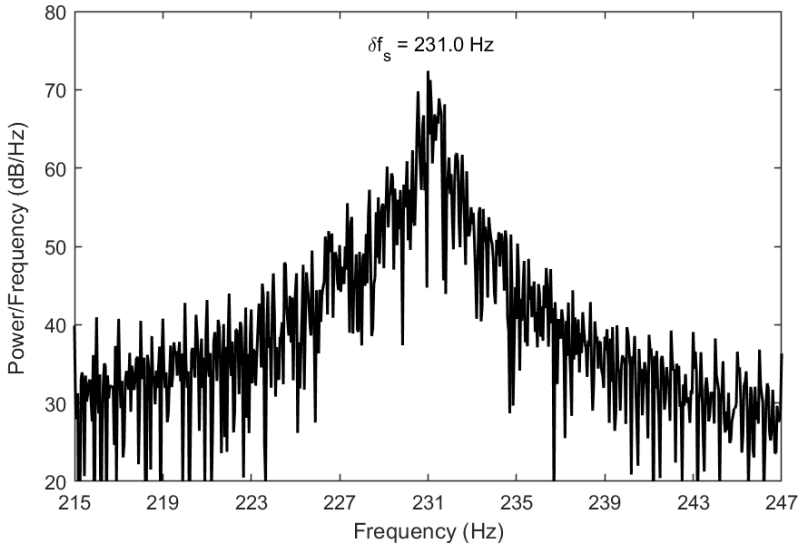

Figure 6.8: The FFT spectrum obtained from intensity-stabilized single-mode operation at a laser output power of 3-4 nW; the cavity pressure was 1.2 mbar.

wider frequency spacing (for PR-1) between each longitudinal mode can assist stable gain starvation process during the intensity control and consequently brings benefit to stable mode operation. Since the amplitude servo system of ER-1 worked with a low photon flux, it only stabilised the laser intensity to within 20% of its amplitude. As such, the Sagnac waveforms obtained were not so steady as those for high-photon-flux operation[11].

As shown in Figure 6.9 (a), the observed Sagnac frequency excursions over a period of 1400 s were fairly small, at 30-40 mHz. It is promising that the frequency excursions obtained from low-photon operation are comparable to that obtained from 632.8 nm operation (about 80 mHz) at a higher laser power of 100 nW. As shown in Figure 6.9 (b) and (c), the Sagnac contrast ratio was 62 - 63% and the monobeam modulations measured from the CCW and CW directions were 0.8 and 1.8%, respectively. One can see that the time series of the Sagnac contrast ratio and monobeam modulations all exhibit excess noise, especially after 350 s of data logging. Since the photon flux for stable gyroscopic output was quite limited, the noise level turned out to be comparably high and thereby induced a large uncertainty in the frequency and amplitude estimations for the optical output. The precision and accuracy of the monobeam signal detection turned out to be one of our greatest concerns, as any incorrectly-measured parameter can affect the backscatter correction. The backscatter-induced frequency perturbations derived from the measured backscatter phase and monobeam modulations were up to 20 mHz, as shown in Figure 6.9 (d).

A continuous data series of 560-s in length was selected (corresponding to a period of 288-847 seconds in Figure 6.9) for the relative Allan deviation plot, with some data points excluded due to mode-hops. Figure 6.10 shows the rotational resolution as a function of the averaging time induced from the raw and backscatter-reduced Sagnac frequency. It was noticed for the first time that the application of the backscatter correction deteriorated rather than improved the stability of Sagnac frequency. This is inferred from the decrease in the usable rotational resolution in Figure 6.10. The raw Sagnac frequency yielded the highest resolution of $3.1 \times 10^{-6}\Omega_E$ (226 prad) at an averaging time of 128 s, whereas the backscatter-reduced Sagnac provided a maximum resolution of $5.7 \times 10^{-6}\Omega_E$ (416 prad/s) at 64 s.

[11] The amplitude servo unit (with optimal parameter settings) can stabilise the laser intensity with an uncertainty smaller than 2% when the laser operates at an output power beyond 25 nW.

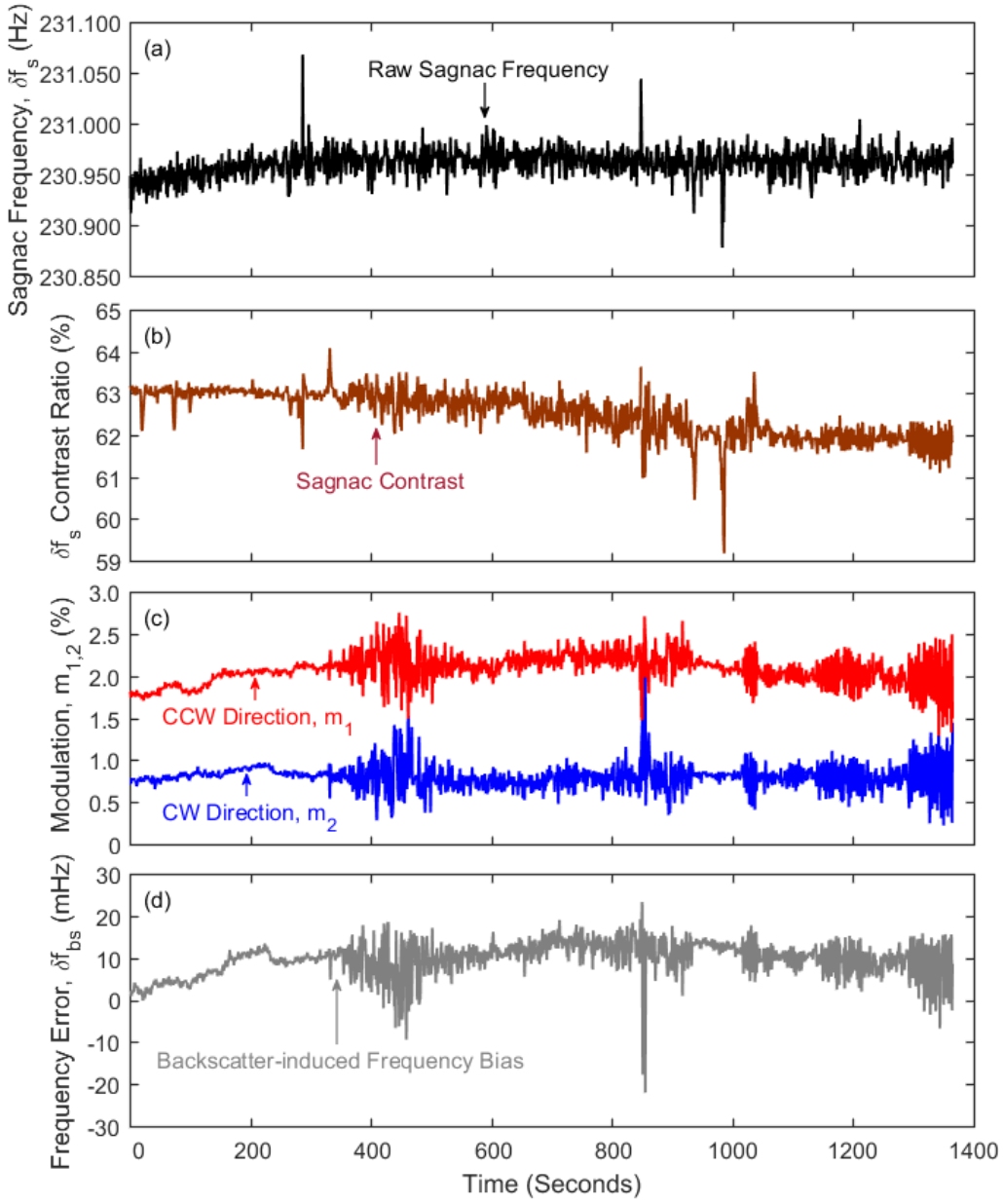

Figure 6.9: Intensity-controlled single-mode operation achieved with a cavity pressure of 1.2 mbar and a natural neon partial pressure of 0.2 mbar, where: (a) shows the raw Sagnac frequency; (b) shows the Sagnac contrast ratio; (c) shows the monobeam modulations measured from the CCW and the CW beam output; (d) shows the magnitude of the backscatter-induced frequency bias. The laser output power was stabilised within a range of 3-4 nW which was marginally above the servo limitation.

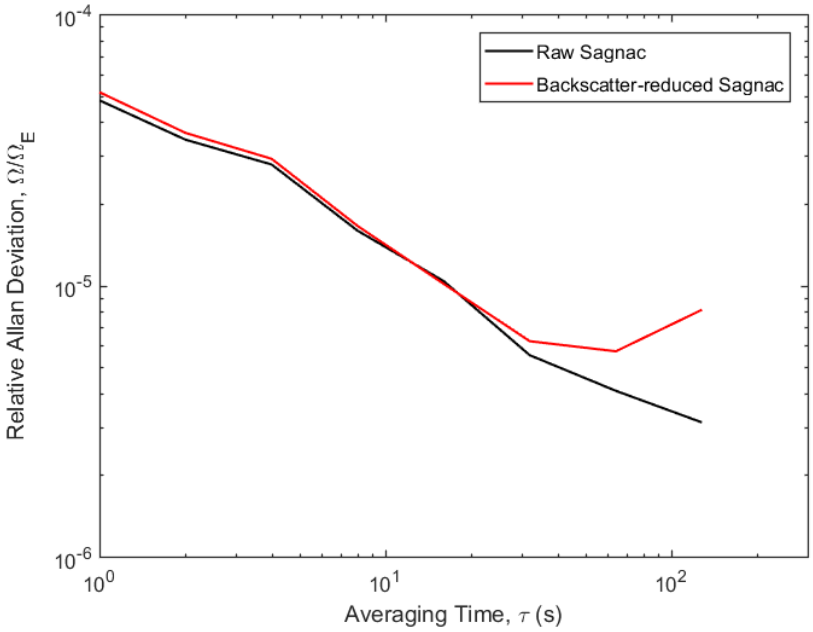

Figure 6.10: Relative ADEV plots obtained for the raw and the backscatter-corrected Sagnac frequency.

6.3.3 Gyroscopic Performance Using the 50:50 Neon Isotope

As stated previously, the upper-limit for the operable pressure was 2.2 mbar with a 0.2 mbar partial pressure of 50:50 neon. We note that the single-mode and phase-locked regimes obtained for 50:50 neon operation were relatively small compared to those given by natural neon operation under the same total cavity pressure (see Table 6.6). For example, at a cavity pressure of 1.2 mbar, the upper limits of laser power output for the single-mode and the phase-locked modes were at 2.4 and 5.3 nW, respectively.

	50:50 Neon	Natural Neon
Mode Structure	Output Power (nW)	Output Power (nW)
Single-mode	0 - 2.4	0 - 4.0
Phase-locked	2.4 - 5.3	4.0 - 10.0

Table 6.6: Comparison of the operational regimes provided by the 50:50 and natural neon isotope gas composition; the cavity pressures were both at 1.2 mbar with a fixed neon partial pressure at 0.2 mbar.

Referring back to Table 6.5, the RF power required for the maximum gain (laser output power) decreased as the total pressure increased. For operation at 2.2 mbar pressure, a maximum laser power of 259 nW was obtained with an RF input power at 12 W. In the following, we demonstrate the laser performance at this pressure since it yielded the widest

tunable power region for the respective single-mode (0 - 4 nW) and phase-locked mode (4 - 9 nW) regimes.

A challenge when operating at 543.4 nm is that the laser power, along with the plasma discharge length, cannot smoothly respond to the reduction or elevation of the RF input power when using only the 400-mm-long gain tube. As shown in Figure 6.11, significant variations in the laser power occur due to the segmented reduction of the discharge length. Therefore, we were unable to precisely or evenly adjust the long plasma discharge length in particular for the low power region. As can be seen in Figure 6.11, the plasma was extinguished once the discharge length was shorter than 180 mm or for an RF power lower than 5 W.

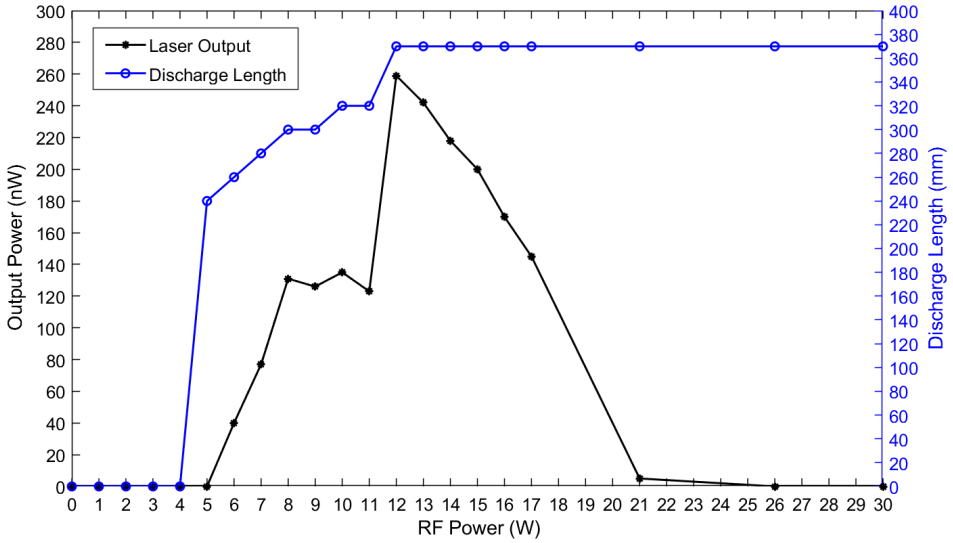

Figure 6.11: The laser output power as a function of the RF input power delivered to the 400-mm-long gain tube; the 100-mm-long gain tube was switched off and the laser gain was solely sustained by the 400-mm-long gain tube. The cavity was filled with a 50:50 neon partial pressure of 0.2 mbar with a total pressure of 2.2 mbar (He:Ne ratio = 10:1).

Given these problems, a different method was used for the intensity stabilisation. Both the 100 mm and 400 mm long gain tubes were utilised simultaneously. The amplitude servo system acted solely on the 160 MHz RF transmitter and therefore only stabilised the RF power delivered to the 100-mm-long gain tube. The RF power (from the 80 MHz transmitter) coupled to the other 400-mm-long gain tube was not controlled by the feedback system and only set to yield a reasonably fixed plasma discharge.

Firstly, we switched on the long gain tube and adjusted the RF input power to obtain a continuous plasma discharge at respective lengths of 350, 300 and 260 mm. Once a particular discharge length was established, we turned on the short gain tube with an initial RF power of

20 W. While decreasing the RF input for the short gain tube, the trend of laser output powers was documented as shown in Figure 6.12. In comparison with Figure 6.11, it is evident that the laser output power can be tuned in a smooth and continuous fashion when the discharge in the long gain tube is fixed. More importantly, the laser input-output efficiency (laser power per unit increment of RF power) can be lowered down over a wide range depending on the gain provided in the long gain tube. This allowed for the implementation of an efficient intensity control loop. It was also determined that the peak of the total gain always occurred when the RF power delivered to the short tube was 4 - 5 W, regardless of the gain provided in the long tube (Figure 6.12). This is because given any fixed cross-sectional area of the gain tube and atomic density for the gas discharge and any specified He-Ne atomic ratio, there always exists a pre-determined upper, fixed threshold for the gain per unit length (or per unit RF input power) [119].

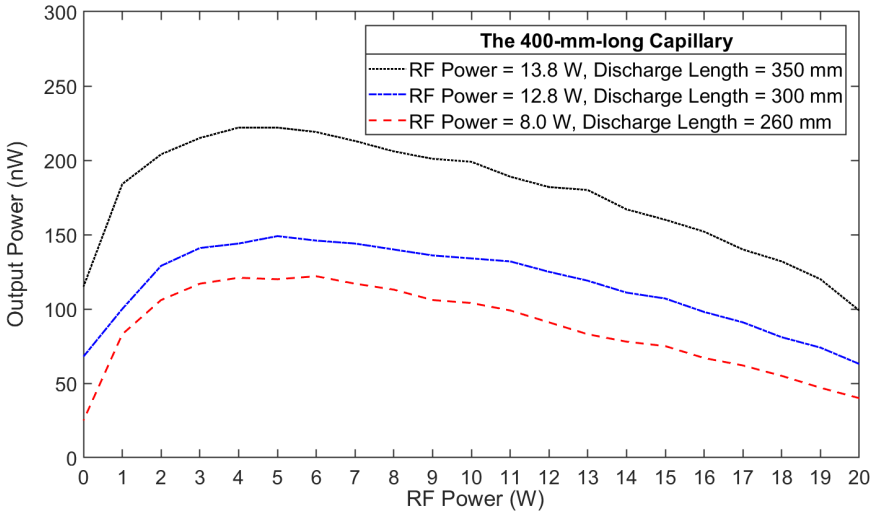

Figure 6.12: Laser output power as a function of the RF power delivered to the short gain tube; for the long gain tube, the excitation power and the plasma discharge length were fixed at certain values. This measurement was repeated three times with the discharge length in the long gain tube set to be 350, 300, and 260 mm, respectively; the cavity was filled with a 50:50 neon partial pressure of 0.2 mbar with a total pressure of 2.2 mbar (He:Ne ratio = 10:1).

Figure 6.12 shows that the overall laser output tended to roll off once the RF power surpassed 5 W. This gain reduction phenomenon is because intra-cavity photons at 543.4 nm have excited neon atoms from the terminal state ($2p_{10}$) to the upper laser state i.e. reabsorption loss.

The gain medium was excited in the long gain tube with an RF input power at 6 W for a discharge length at 200 mm. This set-up was able to yield an optimal gradient of the laser input-output efficiency within the RF power range of 0 to 5 W and guarantees an accurate response to the feedback signal. Phase-locked operation with an output power maintained

at 4 to 5 nW (just beyond the multi-mode threshold) is shown in Figure 6.13. Within 920 seconds, a mode-hop occurred and correspondingly the Sagnac contrast ratio increased by 6%. The measured frequency excursions are generally less than 50 mHz, which are similar to those obtained from natural neon operation at 1.2 mbar total pressure (Section 6.3.2). Laser action could only be sustained for about 15 minutes.

Figure 6.14 shows the ADEV plots using the data series from Figure 6.13 (a). One can see that the stability of the Sagnac frequency was slightly increased after the backscatter correction, as indicated by an improvement of the usable resolution from $9.5 \times 10^{-6}\Omega_E$ (693 prad/s) to $7.9 \times 10^{-6}\Omega_E$ (577 prad/s) with a prolonged integration time from 32 s to 64 s. This is because the frequency stability (after the backscatter correction) was improved due to better accuracy in the phase and amplitude measurements (of the monobeam signal). It is noticeable from Figure 6.13 (c) that the noise on the monobeam modulations was much smaller than those demonstrated in Figure 6.9 (c).

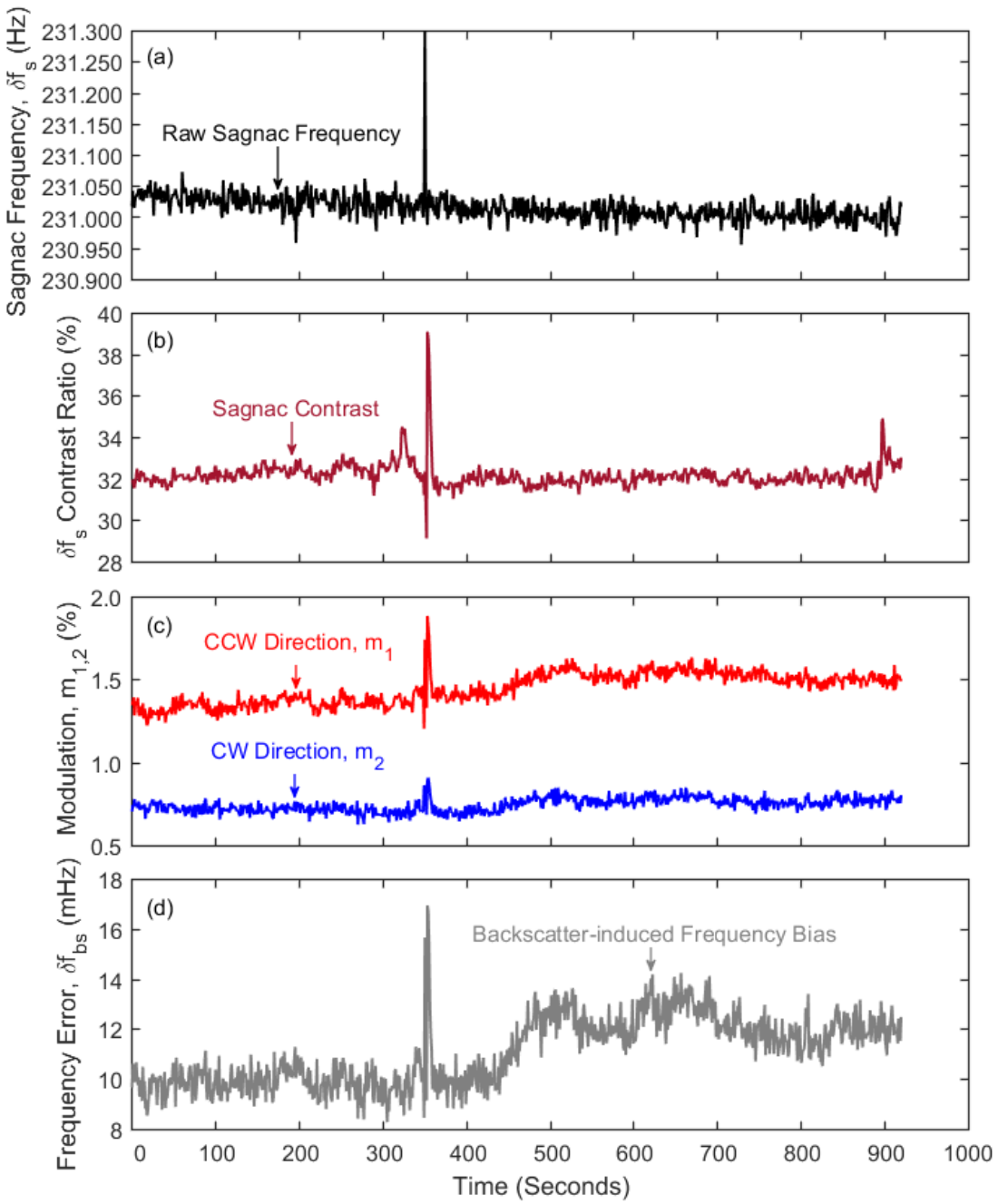

Figure 6.13: The intensity-controlled phase-locked mode performance at a cavity pressure of 2.2 mbar with a 50:50 neon partial pressure of 0.2 mbar, where (a) shows the raw Sagnac frequency; (b) shows the Sagnac contrast ratio; (c) shows the monobeam modulations measured from the CCW and CW beam output; (d) shows the magnitude of the backscatter-induced frequency bias.

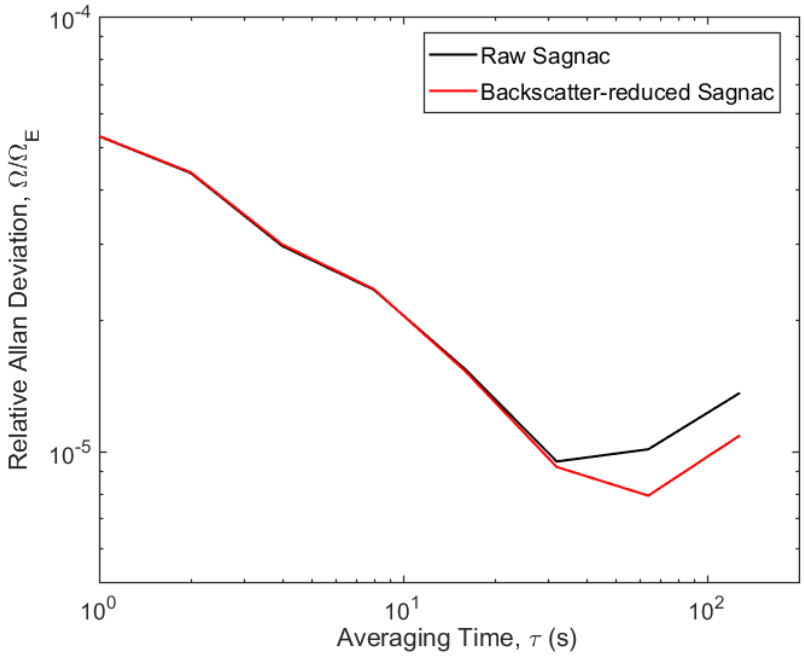

Figure 6.14: Relative ADEV plots obtained for the raw and the backscatter-reduced Sagnac frequency.

6.4 Discussions and Conclusions

Using four ultra low-loss 543.4 nm supermirrors, we demonstrate lasing and rotation sensing at the highest available optical frequency using the helium-neon gain medium. The 543.4 nm wavelength is useful for rotation sensing only when sufficient gain is provided via a long plasma discharge in an additional 400-mm-long gain tube having an inner diameter of 3 mm. A ring-down time of 110 μs and a cavity Q of 3.8×10^{11} was achieved. The 543.4 nm ER-1 laser yielded a maximum output power in the range of 140 to 264 nW depending on the use of the neon isotope ratio. Single-mode and phase-locked operation was obtained over the range of 0 - 4 nW and 4 - 10 nW, respectively. With a 50:50 neon partial pressure fixed at 0.2 mbar, the highest operable gas pressure for 543.4 nm operation (up to 2.2 mbar) was about 3 times lower than that for 611.8 nm operation (up to 6.5 mbar), and 6 times lower than that for 632.8 nm operation (up to 12 - 14 mbar). Lasing was also obtained with a 400-mm-long discharge tube with a larger diameter of 4 mm. This gave a ring-down time of 200 μs and a cavity Q of 6.9×10^{11}. However, this gain tube was not useful for gyroscopic operation as it did not provide an operable pressure beyond 0.9 mbar for the build-up of stable longitudinal mode configurations.

When operating the laser at a low cavity pressure and low output power regime, it was necessary to establish the amplitude servo unit with a short integration time. An integration time shorter than 0.8 s was the prerequisite for an effective intensity control loop. The

feedback system needed to respond reasonably fast to avoid a 'wide' drift of the laser power which might disrupt the consistency of the operating mode structure. This is because the tunable laser power for an operable mode regime was narrow (only a few nanowatts for a total cavity pressure equal to or lower than 2.2 mbar) and the plasma discharge sustained in the long gain tube was relatively unstable.

Stable gyroscopic performance longer than 25 minutes was impractical due to the instability of plasma discharge. We occasionally observed the laser extinguish when the RF excitation power and the plasma discharge remained unchanged. In addition, the lasing was not always recoverable by attenuation of the RF input. Under such circumstance, even the servo unit was unable to re-activate the laser by an elevation of the RF excitation power but only a complete turn-off of the RF transmitter and a re-excitation of the gain medium could restore laser operation. Restricted by a low-pressure environment, homogeneous broadening from the pressure effect was not sufficient, and thus the resultant spectral 'holes' were narrow. As a consequence, mode competition among adjacent longitudinal modes was fierce during the gain starvation process. For 543.4 nm operation, mode-hops occurred very frequently about every 8 to 15 minutes. Similarly, 'frequency-splitting' also occurred more often in 543.4 nm operation than for operation at the longer wavelengths. Mode-hops occurred only once every 1 to 7 hours for 632.8 nm and 611.8 nm operation in the high-pressure regime.

Nevertheless, the laser is capable of monitoring Earth rotation with an up-scaled Sagnac frequency of 230.96 Hz with a highest rotational resolution of $3.1 \times 10^{-6}\Omega_E$, or 226 prad/s (corresponds to a highest usable sensitivity of 2.85×10^{-10} rad/s/$\sqrt{\text{Hz}}$ and a raw sensitivity at 3.23×10^{-9} rad/s/$\sqrt{\text{Hz}}$). Recorded with a sample write-out rate of once per second, the Sagnac frequency excursions were in a range of 30 - 50 mHz within a short time-scale. We note that there is still space for technical and parameter improvements on the 543.4 nm ER-1 gyroscope in order to improve its stability and sensitivity. For example, a set of super-polished mirrors having a ROC smaller than 3 m but larger than 2.4 m (2.5 and 2.6 m are the ideal parameters) might enhance the overall laser behaviour. As they can form a smaller beam spot at the gain tube section without increasing the beam size on the intra-cavity mirrors. The cavity would then experience lower diffraction losses. In this case, a lower lasing threshold would permit a higher photon-flux output, which would benefit the amplitude feedback control loop.

7 Conclusion, Discussion and Future Work

This thesis examined several applicable schemes for improving the sensitivity and stability of large ring laser gyros developed for applications in geosciences. To gain comprehensive insights into the best operational regime, we have investigated the laser performance under various conditions via gyroscopic operation using:

- a wide range of optical wavelengths:
  1152.3 nm, 632.8 nm, 611.8 nm, 604.6 nm, 593.9 nm, and 543.4 nm;
- different cavity dimensions:
  PR-1: area: 2.56 m^2, perimeter: 6.25 m,
  ER-1: area: 6.25 m^2, perimeter: 10 m;
- different operational environments:
  PR-1: vertically mounted on the wall,
  ER-1: horizontally bolted down to the concrete base;
- different mirror configurations:
  mirrors with substrate and surface: commercially-polished and super-polished,
  mirrors with ROC at: 3 m, 4 m and 10 m;
- different mode configurations:
  longitudinal mode: single-mode and phase-locked modes,
  transverse mode: TEM_{00} and TEM_{01} modes.

A self-referenced cavity stabilisation technique was applied to the ER-1 ring laser to address perimeter variations caused by ambient temperature-and-pressure fluctuations. We have applied a numerical solution to correct the systematic bias errors from backscatter-coupling effects in order to enhance the rotational sensitivity. We also proposed a novel scheme useful for the calibration of the systematic biases induced from the gain medium via the development of a multi-wavelength He-Ne ring laser. The idea behind multi-wavelength operation is that rotation rates derived from Sagnac measurements by either wavelength should be the same at any time. By comparing the backscatter-perturbation-reduced Sagnac time series acquired from each wavelength, a quantification of the null-shift errors may be obtained, and thus the residual systematic biases can be removed from any signal of rotational origin for precise measurements of Earth's rotation.

7.1 Summary of Results

Initially, the vertically mounted PR-1 ring laser was equipped for simultaneous, stable operation on multiple wavelengths using a set of IBS-coated, test supermirrors having a centre wavelength of 543.4 nm but which also allowed lasing at 611.8, 604.6 and 593.9 nm. Lasing at the three wavelengths simultaneously was achieved with specific He-Ne gas ratios, cavity pressures, and plasma excitation densities. In addition, given optimised gas composition and RF excitation power, lasing at 604.6 and 593.9 nm could be achieved with very comparable output powers and similar numbers of oscillating longitudinal modes, even though the neon transitions have very dissimilar gain. In our experiments, the single-mode and the phase-locked configurations for these two wavelengths could not be obtained since the 611.8 nm transition always dominated the gain competition among the three neon transitions - since they all share the same upper energy state of $3s_2$. Nevertheless, the result is still promising because it indicates the possibility of simultaneous operation at multiple wavelengths when appropriately optimised resonant mirrors and gas composition are used.

A set of commercially polished, standard laser mirrors was used to configure a near-infrared ring laser cavity having a cavity loss of 712 ppm. PR-1 was able to unlock on the Earth rotation bias for a period of 100 to 1000 seconds yielding the Sagnac beat frequency of 62.38 Hz. Due to the backscatter induced frequency pulling effect there was a drift in the Sagnac frequency of the order of $\pm$10 Hz. We are not aware of a free space laser gyroscope which uses standard laser mirrors achieving an Earth rotation measurement.

We designed and constructed a new large ring laser ER-1 that is rigidly connected to a 3 metre thick concrete base. The massive concrete floor-base gives excellent 'protection' against ambient temperature and pressure changes. It was inferred that the temperature fluctuation of the concrete base was in a range of 27 to 50 mK/day, inferred from cavity variations of 2.7 - 5.0 μm. A self-referenced perimeter control system implemented on the ER-1 laser successfully sustained the 10 m cavity perimeter within 200 nm variation as indicated from a FSR variation of 0.6 Hz. As a result, ER-1 can sustain laser operation on a consistent mode number for over one day. Currently, stable mode operation longer than this duration can not be obtained. This is because the perimeter regulation progress encountered some undesired mechanical issues. Since the piezoelectric stack is embedded on the mirror holder, whose translation is achieved through tensile stress on the springs on the lever system, mechanical hysteresis of the mirror movement occasionally introduced sudden variations to the cavity length and thus ultimately perturbed the operating mode.

ER-1 has detected marine microseisms on a millihertz scale and measured the ocean-swell-induced ground oscillations in a frequency band between 150 and 250 mHz. It is also a valuable tool for measuring rotational ground motion (on a scale of nano-radians per second) induced by earthquake events and identifying the arrival of different seismic waves (mainly the Love waves) due to its high cavity Q and robust cavity installation. Two medium-sized, regional earthquakes having their epicentres at different locations were sensed by the ER-1

laser during the operating periods. The measured phase velocities for the S-waves and surface waves fitted well into the expected ranges. By comparing the measured results obtained from the two respective earthquakes, we noticed that the ground rotation rates derived from the Sagnac frequency excursions were in good agreement with the specified magnitude scale of the earthquake. As the measurement of earthquake-induced ground rotational motion and building motion plays a significant role in developing criteria for earthquake-proofed structures, ER-1 will be extremely useful for civil engineering studies of building deformation due to seismic motion.

Compared to PR-1, the geometrically upscaled ER-1 is also mechanically improved. This is because its cavity experiences only modest thermal variations given the construction on a large concrete foundation. In addition, ER-1 is maximally protected from mechanical vibrations since all corner plates are rigidly attached to the concrete foundation as guaranteed by an adhesive (which bridges the gap between the plate and foundation), moreover, the free movement or wobbling of the cavity arms are avoided by using a set of spatially-fixed stainless steel tube holders connected to the floor. Owing to greater mechanical stability, ER-1 reduces backscatter perturbation and obtains a narrower cavity linewidth (via an improved cavity Q), and its gyroscopic performance is significantly better. The laser sensitivity and sensor resolution of ER-1 is two orders of magnitude higher than that of PR-1 as shown in Table 7.1. From our results, the 632.8 nm wavelength offers the best operating performance when compared against others for the same laser gyro system. Frequency upscaling does not work for the transitions involved. For operation at the shortest wavelength of 543.4 nm, the low operable pressures and low photon-flux (derived from the low gain of the $3s_2 \rightarrow 2p_{10}$ neon transition) hinders the gyroscopic potential. Plasma instability within the long discharge tube and instability of the amplitude servo unit due to the week usable feedback signal remain to be addressed. Therefore, we conclude that the ultimate sensor performance depends on multiple factors rather than the scale factor of the gyroscope alone. Factors such as the gain tube diameter, and cavity length; operating photon-flux permissible by the He-Ne gas ratio and cavity pressure; as well as the mechanical stability of the cavity; and even the efficiency of amplitude servo control system.

7.2 Future Work

ER-1 performance at 543.4 nm can be improved if the resolution and other parameters of the amplitude servo unit such as the integration time are re-designed for intensity stabilisation in a low photon-flux regime. Other than that, implementing multiple short gain tube sections might prevent plasma excitation instabilities given by the long discharge length in one single gain tube.

It would be worth trying to apply a set of 'multiple-stop-band' supermirrors (providing a high transmission loss for the high-gain transition and a low loss for the low-gain one) which

Ring laser	ER-1			PR-1
Operating wavelength, λ (nm)	632.8	611.8	543.4	611.8
Optical frequency, ν_0 (THz)	474	490	552	490
Nominal Sagnac frequency, $\delta\ f_s$ (Hz)	198.32	205.14	230.96	117.27
Gain tube diameter, d (mm)	4	4	3	4
Gain tube length, l (mm)	100	100	400	100
Ring-down time, τ (μs)	375	485	110	38
Quality factor, Q	1.1×10^{12}	1.5×10^{12}	3.8×10^{11}	1.2×10^{11}
Finesse, F	7.1×10^{4}	9.1×10^{4}	2.1×10^{4}	1.1×10^{4}
Total loss, L (ppm)	88.9	68.7	303.0	561.4
Neon partial pressure, p_{ne} (mbar)	0.2	0.2	0.2	0.2
Total gas pressure, p_{total} (mbar)	8	6.5	1.2	4
Laser output power, P_{out}	113	60	3.5	500
Raw sensitivity, $\Omega_{s(raw)}$ (rad/s/$\sqrt{\text{Hz}}$)	1.8×10^{-10}	1.9×10^{-10}	3.2×10^{-9}	1.3×10^{-9}
Usable sensitivity, Ω_s (rad/s/$\sqrt{\text{Hz}}$)	7.9×10^{-12}	1.2×10^{-11}	2.8×10^{-10}	1.1×10^{-10}
Relative ADEV, Ω/Ω_E	4.9×10^{-7}	1.1×10^{-6}	3.1×10^{-6}	1.2×10^{-4}
Resolution, $\Delta\Omega$ (prad/s)	36	80	226	8750
Integration time, τ (s)	512	225	128	128
Lock-in threshold, Ω_L (μrad/s)	2	2	2	2

Table 7.1: Comparison of the best available sensor performances from ER-1 operation at three different wavelengths and PR-1 operation at 611.8 nm.

permit simultaneous and stable operation at 632.8 and 543.4 nm. This dual-wavelength ring laser gyroscope can have great potential in rotational sensing as the high-power 632.8 nm output can be used as an efficient feedback signal for both the laser intensity and cavity perimeter stabilisation systems while the 543.4 nm output can be utilised for the high-resolution measurements.

In future, the approach to achieving better gyroscopic stability and sensitivity for Earth rotation sensing lies in operation at the 632.8 nm wavelength and the implementation of a fast-responsive feedback control system for the cavity perimeter stabilisation. The piezo should be re-assembled to the back of the supermirror for controlling the mirror movement in a more precise way. Moreover, it will be advantageous to stabilise the room-and-concrete-base temperature to drift within a smaller range. This scheme would allow the perimeter control system to function efficiently in the long term. Specifically, a temperature-stabilised laboratory would minimise the thermal expansion of the cavity and ensure that the perimeter variations always fall into a compensatable range determined by our piezo-actuator. Under this condition, the mirror position would translate evenly with a reduced chance of mechanical problems. It is of equivalent importance that all the electronic circuits and wiring of the feedback control system are protected by RF shielding materials, as any undesired RF field near the feedback loop unit would affect the accuracy of the control voltage for the fine-movement of the piezo stage and perturb precise perimeter control on a large and slow-drifting cavity.

The highest sensor resolution achieved of below 10^{-6} of Earth rotation rate using 632.8 nm operation indicates ER-1's potential in the observation of subtle geophysical changes such as solid Earth tides and diurnal polar motion caused by the gravitational forces of the sun and moon. To make ER-1 able to measure these signals, the key steps are to finely stabilise the laser perimeter, avoid any discontinuity of the operating mode and acquire the Sagnac signal over certain data-lengths (longer than 10 days) with a rotational resolution consistently maintained below $10^{-6}\Omega_E$. In summary, cavity stabilisation to obtain continuous and unperturbed long-term operation would be the priority task for a full exploration of ER-1's potential.

Publications

Published Articles in Peer-Reviewed Scholarly Journals:

- **D. Zou**, R. J. Thirkettle, A. Gebauer, G. K. MacDonald, K. U. Schreiber, and J.-P. R. Wells. “Gyroscopic performance and some seismic measurements made with a 10 meter perimeter ring laser gyro housed in the Ernest Rutherford Building”. In: Applied Optics 60.6 (2021), pages 1737–1743.

- **D. Zou**, C. L. Anyi, R. J. Thirkettle, K. U. Schreiber, and J.-P. R.Wells. “Sensing Earth rotation with a helium–neon laser operating on three transitions in the visible region”. In: Applied Optics 58.28 (2019), pages 7884–7891.

- C. L. Anyi, R. J. Thirkettle, **D. Zou**, D. Follman, G. D. Cole, K. U. Schreiber, and J.-P. R. Wells. “The Macek and Davis experiment revisited: a large ring laser interferometer operating on the $2s_2 \rightarrow 2p_4$ transition of neon”. In: Applied Optics 58.2 (2019), pages 302–307.

Paper In Preparation:

- **D. Zou**, R. J. Thirkettle, K. U. Schreiber, and J.-P. R. Wells, "Short wavelength operation of a 10-metre perimeter ring laser", 2021. In preparation for Optics Letters.

Conference and Seminar Talks:

- **D. Zou**, J.-P. R. Wells, R. J. Thirkettle, and K. U. Schreiber, "ER-1: A large He-Ne ring laser with a 6.25 m^2 ground-bolted cavity", PSI (Photonic Sensors and Imaging) Seminar, Dodd-Walls Centre for Photonic and Quantum Technologies, May 2020.

- **D. Zou**, J.-P. R. Wells, R. J. Thirkettle, and K. U. Schreiber, "Initial gyroscopic operation of a large multi-oscillator ring laser for Earth rotation sensing", 12th Annual Dodd-Walls Centre Symposium, Dunedin, New Zealand, February 2019.

Bibliography

[1] E. J. Post. "Sagnac effect". In: *Reviews of Modern Physics* 39.2 (1967), page 475.

[2] A. A. Michelson. "The effect of the Earth's rotation on the velocity of light, I." In: *The Astrophysical Journal* 61 (1925), page 137.

[3] W. M. Macek and D. T. M. Davis Jr. "Rotation rate sensing with traveling-wave ring lasers". In: *Applied Physics Letters* 2.3 (1963), pages 67–68.

[4] N. I. Krobka and D. A. Türkin. "Laser gyros frequency biasing and fiber optic gyros phase biasing: Similarities and differences". In: *2017 24th Saint Petersburg International Conference on Integrated Navigation Systems (ICINS)*. IEEE. 2017, pages 1–12.

[5] R. Bergh, H. Lefevre, and H. Shaw. "An overview of fiber-optic gyroscopes". In: *Journal of Lightwave Technology* 2.2 (1984), pages 91–107.

[6] W. W. Chow, J. Gea-Banacloche, L. M. Pedrotti, V. E. Sanders, W. Schleich, and M. O. Scully. "The ring laser gyro". In: *Reviews of Modern Physics* 57.1 (1985), page 61.

[7] N. Rabeendran. "New approaches to gyroscopic lasers". PhD thesis. Department of Physics and Astronomy, University of Canterbury, 2013.

[8] Y. Liu, L. Sun, H. Qiu, Y. Wang, Q. Tian, and X. Ma. "Bidirectional operation and gyroscopic properties of passively mode-locked Nd: YVO4 ring laser". In: *Laser Physics Letters* 4.3 (2007), pages 187–190.

[9] S. Schwartz, F. Gutty, G. Feugnet, É. Loil, and J. P. Pocholle. "Solid-state ring laser gyro behaving like its helium-neon counterpart at low rotation rates". In: *Optics Letters* 34.24 (2009), pages 3884–3886.

[10] K. U. Schreiber and J.-P. R. Wells. "Invited review article: Large ring lasers for rotation sensing". In: *Review of Scientific Instruments* 84.4 (2013), page 041101.

[11] A. Velikoseltsev. "The development of a sensor model for large ring lasers and their application in seismic studies". PhD thesis. Technische Universität München, 2005.

[12] D. Zou, R. J. Thirkettle, A. Gebauer, G. K. MacDonald, K. U. Schreiber, and J.-P. R. Wells. "Gyroscopic performance and some seismic measurements made with a 10 meter perimeter ring laser gyro housed in the Ernest Rutherford Building". In: *Applied Optics* 60.6 (2021), pages 1737–1743.

[13] C. L. Anyi. "Large ring lasers: beyond the Macek and Davis experiment." PhD thesis. Department of Physics and Astronomy, University of Canterbury, 2019.

[14] G. E. Stedman, R. B. Hurst, and K. U. Schreiber. "On the potential of large ring lasers". In: *Optics Communications* 279.1 (2007), pages 124–129.

[15] A. Gebauer, M. Tercjak, K. U. Schreiber, H. Igel, J. Kodet, U. Hugentobler, J. Wassermann, F. Bernauer, C. J. Lin, S. Donner, et al. "Reconstruction of the Instantaneous Earth Rotation Vector with Sub-Arcsecond Resolution Using a Large Scale Ring Laser Array". In: *Physical Review Letters* 125.3 (2020), page 033605.

[16] A. Brotzer, F. Bernauer, K. U. Schreiber, J. Wassermann, and H. Igel. "Automated Quality Assessment of Interferometric Ring Laser Data". In: *Sensors* 21.10 (2021), page 3425.

[17] H. Igel, K. U. Schreiber, A. Gebauer, F. Bernauer, S. Egdorf, A. Simonelli, C. J. Lin, J. Wassermann, S. Donner, C. Hadziioannou, et al. "ROMY: a multicomponent ring laser for geodesy and geophysics". In: *Geophysical Journal International* 225.1 (2021), pages 684–698.

[18] J. Belfi, N. Beverini, F. Bosi, G. Carelli, A. Di Virgilio, E. Maccioni, A. Ortolan, and F. Stefani. "A 1.82 m^2 ring laser gyroscope for nano-rotational motion sensing". In: *Applied Physics B* 106.2 (2012), pages 271–281.

[19] J. Belfi, N. Beverini, F. Bosi, G. Carelli, A. Di Virgilio, D. Kolker, E. Maccioni, A. Ortolan, R. Passaquieti, and F. Stefani. "Performance of 'G-Pisa' ring laser gyro at the Virgo site". In: *Journal of Seismology* 16.4 (2012), pages 757–766.

[20] N. Rabeendran. "A study of ring laser gyroscopes". Master's thesis. Department of Physics and Astronomy, University of Canterbury, 2008.

[21] K. U. Schreiber, H. Igel, A. Cochard, A. Velikoseltsev, A. Flaws, B. Schuberth, W. Drewitz, and F. Müller. "The GEOsensor project: rotations—a new observable for seismology". In: *Observation of the Earth System from Space*. Springer, 2006, pages 427–443.

[22] J. Belfi, N. Beverini, G. Carelli, A. Di Virgilio, U. Giacomelli, E. Maccioni, A. Simonelli, F. Stefani, and G. Terreni. "Analysis of 90 day operation of the GINGERINO gyroscope". In: *Applied Optics* 57.20 (2018), pages 5844–5851.

[23] R. S. Gross. "Earth rotation variations-long period". In: *Treatise on Geophysics* 3 (2007), pages 239–294.

[24] H. Schuh and D. Behrend. "VLBI: A fascinating technique for geodesy and astrometry". In: *Journal of Geodynamics* 61 (2012), pages 68–80.

[25] R. Haas. "Investigating high-frequency Earth orientation variations with continuous geodetic VLBI campaigns". In: *IVS2006 General Meeting Proceedings*. 2006, pages 316–319.

[26] G. E. Stedman, H. R. Bilger, Z. Y. Li, M. P. Poulton, C. H. Rowe, I. Vetharaniam, and P. V. Wells. "Canterbury ring laser and tests for nonreciprocal phenomena". In: *Australian Journal of Physics* 46.1 (1993), pages 87–102.

[27] K. U. Schreiber, T. Klügel, A. Velikoseltsev, W. Schlüter, G. E. Stedman, and J.-P. R. Wells. "The large ring laser G for continuous Earth rotation monitoring". In: *Pure and Applied Geophysics* 166.8-9 (2009), pages 1485–1498.

[28] K. U. Schreiber, T. Klügel, J.-P. R. Wells, R. B. Hurst, and A. Gebauer. "How to detect the Chandler and the annual wobble of the Earth with a large ring laser gyroscope". In: *Physical Review Letters* 107.17 (2011), page 173904.

[29] T. Nilsson, J. Böhm, H. Schuh, K. U. Schreiber, A. Gebauer, and T. Klügel. "Combining VLBI and ring laser observations for determination of high frequency Earth rotation variation". In: *Journal of Geodynamics* 62 (2012), pages 69–73.

[30] K. U. Schreiber, A. Velikoseltsev, M. Rothacher, T. Klügel, G. E. Stedman, and D. L. Wiltshire. "Direct measurement of diurnal polar motion by ring laser gyroscopes". In: *Journal of Geophysical Research: Solid Earth* 109.B6 (2004).

[31] R. W. Dunn, D. E. Shabalin, R. J. Thirkettle, G. J. MacDonald, G. E. Stedman, and K. U. Schreiber. "Design and initial operation of a 367 m^2 rectangular ring laser". In: *Applied Optics* 41.9 (2002), pages 1685–1688.

[32] R. B. Hurst, G. E. Stedman, K. U. Schreiber, R. J. Thirkettle, R. D. Graham, N. Rabeendran, and J.-P. R. Wells. "Experiments with an 834 m^2 ring laser interferometer". In: *Journal of Applied Physics* 105.11 (2009), page 113115.

[33] K. U. Schreiber, H. Igel, J. Wassermann, C. J. Lin, A. Gebauer, and J.-P. R. Wells. "ROMY-the first large 3D ring laser structure for seismology and geodesy". In: *EGU General Assembly Conference Abstracts*. 2016, EPSC2016–4967.

[34] H. Igel, A. Cochard, J. Wassermann, A. Flaws, K. U. Schreiber, A. Velikoseltsev, and N. Pham Dinh. "Broad-band observations of earthquake-induced rotational ground motions". In: *Geophysical Journal International* 168.1 (2007), pages 182–196.

[35] W. H. K. Lee, H. Igel, and M. D. Trifunac. "Recent advances in rotational seismology". In: *Seismological Research Letters* 80.3 (2009), pages 479–490.

[36] D. P. McLeod, G. E. Stedman, T. H. Webb, and K. U. Schreiber. "Comparison of standard and ring laser rotational seismograms". In: *Bulletin of the Seismological Society of America* 88.6 (1998), pages 1495–1503.

[37] K. U. Schreiber, A. Velikoseltsev, G. E. Stedman, R. B. Hurst, and T. Klügel. "Large ring laser gyros as high resolution sensors for applications in geoscience". In: *Giroskopiia i Navigatsiia (Gyroscopy and Navigation)* 3, 46 (2004), pages 38–47.

[38] H. Igel, K. U. Schreiber, A. Flaws, B. Schuberth, A. Velikoseltsev, and A. Cochard. *Rotational motions induced by the M 8.1 Tokachi-oki earthquake, September, 25, 2003: Geophysical Research Letters*. 2005.

[39] K. U. Schreiber, J. N. Hautmann, A. Velikoseltsev, J. Wassermann, H. Igel, J. Otero, F. Vernon, and J.-P. R. Wells. "Ring laser measurements of ground rotations for seismology". In: *Bulletin of the Seismological Society of America* 99.2B (2009), pages 1190–1198.

[40] T. Podgorski and F. Aronowitz. "Langmuir flow effects in the laser gyro". In: *IEEE Journal of Quantum Electronics* 4.1 (1968), pages 11–18.

[41] F. Aronowitz. "Effects of radiation trapping on mode competition and dispersion in the ring laser". In: *Applied Optics* 11.10 (1972), pages 2146–2152.

[42] D. Cuccato, A. Beghi, J. Belfi, N. Beverini, A. Ortolan, and A. Di Virgilio. "Controlling the non-linear intracavity dynamics of large He–Ne laser gyroscopes". In: *Metrologia* 51.1 (2014), page 97.

[43] R. B. Hurst, M. Mayerbacher, A. Gebauer, K. U. Schreiber, and J.-P. R. Wells. "High-accuracy absolute rotation rate measurements with a large ring laser gyro: establishing the scale factor". In: *Applied Optics* 56.4 (2017), pages 1124–1130.

[44] F. Aronowitz and R. J. Collins. "Mode coupling due to Backscattering in a He–Ne traveling-wave ring laser". In: *Applied Physics Letters* 9.1 (1966), pages 55–58.

[45] C. Etrich, P. Mandel, R. C. Neelen, R. J. C. Spreeuw, and J. P. Woerdman. "Dynamics of a ring-laser gyroscope with backscattering". In: *Physical Review A* 46.1 (1992), page 525.

[46] R. B. Hurst, R. W. Dunn, K. U. Schreiber, R. J. Thirkettle, and G. K. MacDonald. "Mode behavior in ultra large ring lasers". In: *Applied Optics* 43.11 (2004), pages 2337–2346.

[47] R. B. Hurst, N. Rabeendran, K. U. Schreiber, and J.-P. R. Wells. "Correction of backscatter-induced systematic errors in ring laser gyroscopes". In: *Applied Optics* 53.31 (2014), pages 7610–7618.

[48] J. A. Stone. "Uncalibrated helium-neon lasers in length metrology". In: *NCSLI Measure* 4.3 (2009), pages 52–58.

[49] Y. I. Zaitsev and D. P. Stepanov. "Frequency fluctuation of a gas laser and determination of the natural width of its spectral line". In: *Soviet Physics Jetp* 28.5 (1969).

[50] W. R. Bennett Jr. "The physics of gas lasers". In: *NASA STI/Recon Technical Report A* 78 (1977).

[51] J. W. Knutson Jr and W. R. Bennett Jr. "Line broadening of the $3s_2 \rightarrow 2p_n$ laser transitions of neon". In: *Physical Review A* 13.1 (1976), page 318.

[52] B. V. Rybakov and A. I. Yakushev. "Investigation of the collisional broadening of the $2s_2$ –$2p_4$ neon transition line". In: *Quantum Electronics* 4.2 (1974), pages 217–219.

[53] J. J. Olivero and R. L. Longbothum. "Empirical fits to the Voigt line width: A brief review". In: *Journal of Quantitative Spectroscopy and Radiative Transfer* 17.2 (1977), pages 233–236.

[54] C. E. Moore. *Atomic energy levels as derived from the analyses of optical spectra: The spectra of hydrogen, deuterium, tritium, helium, lithium, beryllium, boron, carbon, nitrogen, oxygen, flourine, neon, sodium, magnesium, aluminum, silicon, phosphorus, sulfur, chlorine, argon, potassium, calcium, scandium, titanium, and vanadium*. Volume 1. US Department of Commerce, National Bureau of Standards, 1949.

[55] W. R. Bennett, P. J. Kindlmann, and G. N. Mercer. "Measurement of excited state relaxation rates". In: *Applied Optics* 4.101 (1965), pages 34–57.

[56] A. V. Eletskii and B. M. Smirnov. "Physical processes in gas lasers". In: *Journal of Soviet Laser Research* 7.3 (1986), pages 207–323.

[57] C. A. Kocher, J. E. Clendenin, and R. Novick. "Lifetime of the $2^2S_{\frac{1}{2}}$ state of singly ionized helium". In: *Physical Review Letters* 29.10 (1972), page 615.

[58] G. Pascoli. "The Sagnac effect and its interpretation by Paul Langevin". In: *Comptes Rendus Physique* 18.9-10 (2017), pages 563–569.

[59] R. B. Hurst, J.-P. R. Wells, and G. E. Stedman. "An elementary proof of the geometrical dependence of the Sagnac effect". In: *Journal of Optics A: Pure and Applied Optics* 9.10 (2007), page 838.

[60] S. F. Jacobs and R. Zanoni. "Laser ring gyro of arbitrary shape and rotation axis". In: *American Journal of Physics* 50.7 (1982), pages 659–660.

[61] L. H. Loomis and S. Sternberg. *Advanced calculus*. World Scientific, 1968.

[62] A. E. Siegman. *Lasers*. University Science Books, 1986.

[63] Z. Y. Li. "Optical supercavity and precision ring laser measurements". PhD thesis. Department of Physics and Astronomy, University of Canterbury, 1993.

[64] F. Aronowitz. "Theory of a traveling-wave optical maser". In: *Physical Review* 139.3A (1965), A635.

[65] T. J. Hutchings, J. Winocur, R. H. Durrett, E. D. Jacobs, and W. L. Zingery. "Amplitude and frequency characteristics of a ring laser". In: *Physical Review* 152.1 (1966), page 467.

[66] F. Aronowitz. "Single-isotope laser gyro". In: *Applied Optics* 11.2 (1972), pages 405–412.

[67] J. Holdaway, R. B. Hurst, R. Graham, N. Rabeendran, K. U. Schreiber, and J.-P. R. Wells. "Self-locked operation of large He-Ne ring laser gyroscopes". In: *Metrologia* 49.3 (2012), page 209.

[68] P. W. Smith. "Mode-locking of lasers". In: *Proceedings of the IEEE* 58.9 (1970), pages 1342–1357.

[69] A. Bambini and P. Burlamacchi. "Stability conditions for mode-locked gas lasers". In: *IEEE Journal of Quantum Electronics* 4.3 (1968), pages 101–102.

[70] D. G. C. Jones, M. D. Sayers, and L. Allen. "Mode self-locking in gas lasers". In: *Journal of Physics A: General Physics* 2.1 (1968), page 95.

[71] M. Crowell. "Characteristics of mode-coupled lasers". In: *IEEE Journal of Quantum Electronics* 1.1 (1965), pages 12–20.

[72] F. Nash. "Observations of spontaneous phase locking of TEM_{00q} modes at 0.63 μ". In: *IEEE Journal of Quantum Electronics* 3.5 (1967), pages 189–196.

[73] O. McDuff and A. L. Pardue. "Theory of laser mode coupling produced by cavity-length modulation". In: *IEEE Journal of Quantum Electronics* 4.3 (1968), pages 99–101.

[74] H. Gerhardt, H. Welling, and A. Güttner. "Measurements of the laser linewidth due to quantum phase and quantum amplitude noise above and below threshold. I". In: *Zeitschrift für Physik* 253.2 (1972), pages 113–126.

[75] T. Podgorski and F. Aronowitz. "Langmuir flow effects in the laser gyro". In: *IEEE Journal of Quantum Electronics* 3.6 (1967), pages 235–236.

[76] M. Faucheux, D. Fayoux, and J. J. Roland. "The ring laser gyro". In: *Journal of Optics* 19.3 (1988), page 101.

[77] J. D. Coccoli and S. B. Helfant. "The intrinsic stability of laser gyro scale factor". In: *NAECON'78; Proceedings of the National Aerospace and Electronics Conference*. 1978, pages 574–582.

[78] J. L. Zhang, H. Wu, I. V. Kozhevnikov, S. K. Shi, X. B. Cheng, and Z. S. Wang. "Interference suppression of light backscattering through oblique deposition of a layered reflecting coating: bi-layer on a substrate". In: *Optics Express* 27.11 (2019), pages 15262–15282.

[79] R. W. Dunn, H. H. Mahdi, and H. J. Al-Shukri. "Design of a relatively inexpensive ring laser seismic detector". In: *Bulletin of the Seismological Society of America* 99.2B (2009), pages 1437–1442.

[80] F. Aronowitz. *The laser gyro*. Academic Press, 1971.

[81] F. Aronowitz. "Loss lock-in in the ring laser". In: *Journal of Applied Physics* 41.6 (1970), pages 2453–2456.

[82] F. Aronowitz and W. Lim. "Positive scale factor correction in the laser gyro". In: *IEEE Journal of Quantum Electronics* 13.5 (1977), pages 338–343.

[83] G. E. Stedman. "Ring-laser tests of fundamental physics and geophysics". In: *Reports on Progress in Physics* 60.6 (1997), page 615.

[84] G. E. Stedman, Z. Li, C. H. Rowe, A. D. McGregor, and H. R. Bilger. "Harmonic analysis in a large ring laser with backscatter-induced pulling". In: *Physical Review A* 51.6 (1995), page 4944.

[85] A. Di Virgilio, N. Beverini, G. Carelli, D. Ciampini, F. Fuso, and E. Maccioni. "Analysis of ring laser gyroscopes including laser dynamics". In: *arXiv preprint arXiv:1904.02533* (2019).

[86] A. Beghi, J. Belfi, N. Beverini, B. Bouhadef, D. Cuccato, A. Di Virgilio, and A. Ortolan. "Compensation of the laser parameter fluctuations in large ring-laser gyros: a Kalman filter approach". In: *Applied Optics* 51.31 (2012), pages 7518–7528.

[87] L. N. Menegozzi and W. E. Lamb Jr. "Theory of a ring laser". In: *Physical Review A* 8.4 (1973), page 2103.

[88] F. Aronowitz. *Fundamentals of the ring laser gyro*. Volume 339. RTO AGARDograph, 1999.

[89] M. O. Scully and W. E. Lamb Jr. "Quantum theory of an optical maser. I. General theory". In: *Physical Review* 159.2 (1967), page 208.

[90] A. L. Schawlow and C. H. Townes. "Infrared and optical masers". In: *Physical Review* 112.6 (1958), page 1940.

[91] A. Siegman, B. Daino, and K. Manes. "Preliminary measurements of laser short-term frequency fluctuations". In: *IEEE Journal of Quantum Electronics* 3.5 (1967), pages 180–189.

[92] M. Sargent III, M. O. Scully, and W. E. Lamb Jr. *Laser physics*. Addison-Wesley, 1974.

[93] S. R. Stein. "The Allan variance-challenges and opportunities". In: *IEEE Transactions on Ultrasonics, Ferroelectrics, and Frequency Control* 57.3 (2010), pages 540–547.

[94] F. Riehle. *Frequency standards: basics and applications*. John Wiley & Sons, 2006.

[95] L. C. Ng and D. J. Pines. "Characterization of ring laser gyro performance using the Allan variance method". In: *Journal of Guidance, Control, and Dynamics* 20.1 (1997), pages 211–214.

[96] Y. P. Raizer, M. N. Shneider, and N. A. Yatsenko. *Radio-frequency capacitive discharges*. CRC press, 1995.

[97] M. A. Lieberman, A. J. Lichtenberg, et al. *Principles of plasma discharges and materials processing*. Volume 2. Wiley Online Library, 2005.

[98] G. Grammer. "Simplified design of impedance-matching networks". In: *QST* (1957), pages 38–42.

[99] C. Bowick. "RF Circuit Design Howard W. Sams & Co". In: *Inc., Indianapolis, Indiana* (1982).

[100] J. Hecht. "Helium-neon lasers flourish in face of diode-laser competition". In: *Laser Focus World* 28.11 (1992), pages 99–108.

[101] C. P. Wyss, D. N. Wright, B. T. King, D. P. McLeod, S. J. Cooper, and G. E. Stedman. "Collision broadening and quantum noise in a very large laser gyroscope". In: *Optics Communications* 174.1-4 (2000), pages 181–189.

[102] K. U. Schreiber, R. J. Thirkettle, R. B. Hurst, D. Follman, G. D. Cole, M. Aspelmeyer, and J.-P. R. Wells. "Sensing Earth's rotation with a helium–neon ring laser operating at 1.15 μm". In: *Optics Letters* 40.8 (2015), pages 1705–1708.

[103] C. L. Anyi, R. J. Thirkettle, D. Zou, D. Follman, G. D. Cole, K. U. Schreiber, and J.-P. R. Wells. "The Macek and Davis experiment revisited: a large ring laser interferometer operating on the $2s_2 \rightarrow 2p_4$ transition of neon". In: *Applied Optics* 58.2 (2019), pages 302–307.

[104] P. Franke, A. Feitisch, F. Riehle, K. Zhao, and J. Helmcke. "Simultaneous cw laser emission including a Raman line of a He-Ne laser at six wavelengths in the visible range". In: *Applied Optics* 28.17 (1989), pages 3702–3707.

[105] H. Conrads and M. Schmidt. "Plasma generation and plasma sources". In: *Plasma Sources Science and Technology* 9.4 (2000), page 441.

[106] J. Hopwood. "Review of inductively coupled plasmas for plasma processing". In: *Plasma Sources Science and Technology* 1.2 (1992), page 109.

[107] G. D. Cole, W. Zhang, B. J. Bjork, D. Follman, P. Heu, C. Deutsch, L. Sonderhouse, J. Robinson, C. Franz, A. Alexandrovski, et al. "High-performance near-and mid-infrared crystalline coatings". In: *Optica* 3.6 (2016), pages 647–656.

[108] W. R. Bennett and J. W. Knutson. "Simultaneous laser oscillation on the neon doublet at 1.1523 μm". In: *Proceedings of the IEEE* 52.7 (1964), pages 861–862.

[109] D. Zou, C. L. Anyi, R. J. Thirkettle, K. U. Schreiber, and J.-P. R. Wells. "Sensing Earth rotation with a helium–neon laser operating on three transitions in the visible region". In: *Applied Optics* 58.28 (2019), pages 7884–7891.

[110] C. Hadziioannou, P. Gaebler, K. U. Schreiber, J. Wassermann, and H. Igel. "Examining ambient noise using colocated measurements of rotational and translational motion". In: *Journal of Seismology* 16.4 (2012), pages 787–796.

[111] H. R. Bilger and G. E. Stedman. "Stability of planar ring lasers with mirror misalignment". In: *Applied Optics* 26.17 (1987), pages 3710–3716.

[112] W. W. Rigrod. "The optical ring resonator". In: *Bell System Technical Journal* 44.5 (1965), pages 907–916.

[113] J. R. Pierce. *Theory and design of electron beams*. D. Van Nostrand Co., Inc., 1954.

[114] R. D. Graham. "New concepts for operating ring laser gyroscopes". PhD thesis. Department of Physics and Astronomy, University of Canterbury, 2010.

[115] B. T. King. "Ring laser dynamics". PhD thesis. Department of Physics and Astronomy, University of Canterbury, 1999.

[116] R. D. Graham. "Ring laser gain media". Master's thesis. Department of Physics and Astronomy, University of Canterbury, 2006.

[117] C. F. Richter. "An instrumental earthquake magnitude scale". In: *Bulletin of the Seismological Society of America* 25.1 (1935), pages 1–32.

[118] C. L. Anyi, R. J. Thirkettle, G. K. MacDonald, K. U. Schreiber, and J.-P. R. Wells. "Gyroscopic operation on the $3s_2 \rightarrow 2p_{10}$ 543.3 nm transition of neon in a 2.56 m^2 ring cavity". In: *Optics Letters* 44.12 (2019), pages 3074–3077.

[119] B. S. Gray, I. D. Latimer, and S. P. Spoor. "Gain measurements at 543 nm in helium neon laser discharges". In: *Journal of Physics D: Applied Physics* 29.1 (1996), page 50.